Experiments and Inverse Analysis for Determining Non-Linear Viscoelastic Properties of Polymeric Capsules and Biological Cells

by

Nhung T. Nguyen

A dissertation submitted in partial fulfillment
of the requirements for the degree of
Doctor of Philosophy
(Mechanical Engineering)
in The University of Michigan
2014

Doctoral Committee:

Professor Anthony M. Waas, Co-Chair
Professor Alan S. Wineman, Co-Chair
Assistant Professor Jianping Fu
Professor Wei Lu
Associate Professor Veera Sundararaghavan

to my family

ACKNOWLEDGEMENTS

I would like to take this opportunity to express my sincere gratitude to my teachers, colleagues, friends, and family whose support helped to make this dissertation possible.

First of all, I would like to thank my advisor, Professor Anthony Waas, for giving me the chance to pursue my PhD study at the University of Michigan, which has been an important turning point of my life. I am also very grateful for his consistent guidance, support, patience, and encouragement during the last five years. His suggestions helped me to establish and implement many ideas in this dissertation. I would also like to extend this gratitude to my co-advisor, Professor Alan Wineman, who has helped me to improve and deepen my knowledge in many aspects of solid mechanics. I have really appreciated his time, effort, care, and enthusiasm. I feel lucky that I have had the opportunity to work with both of them.

Next, I would like to thank my committee members, Professor Jianping Fu, Professor Wei Lu, and Professor Veera Sundararaghavan, for serving in my dissertation committee and for providing me with many useful comments and suggestions. My gratitude is also expressed towards all my professors from Vietnam and from the University of Michigan who have taught me throughout my academic career.

My appreciation is also extended towards the people who contributed to the experimental part of my dissertation. I would like to thank the Electron Microbeam Analysis Laboratory at the University of Michigan for the use of Atomic Force Microscopy (AFM) and Professor Jianping Fu's Laboratory, specifically Yue Shao, for

providing samples and helping with preparations, as well as for many helpful suggestions. Remy Elbez in the Department of Chemistry, University of Michigan is also appreciated for his help with sample preparations that enabled me to get started and become familiar with the AFM indentation technique.

I am thankful for the time spent working with the members of the Composite Structures Laboratory at the University of Michigan, which has been invaluable for my research. My appreciation also goes to all the technical and administrative staff in both the Mechanical and Aerospace Engineering Departments at the University of Michigan.

I would also like to express my gratification towards all my friends who have helped and encouraged me through this journey. Specifically, I would like to thank the wonderful friends that I have met and spent time with at the University of Michigan: Anna, Corin, Sriram, Chih-Kuang, Riddhiman, Devesh, Pavana, Kalyan, Loc, Abhishek, Brian, Royan and many others. I am also grateful to all my Vietnamese friends, who are either in Vietnam or are pursuing their careers in other countries, for their support and care during my pursuit in the US. My gratification is also expressed towards the Vietnamese community in Ann Arbor and to many Vietnam Education Foundation fellows. The financial support from the Vietnam Education Foundation Fellowship is also greatly appreciated.

Last but certainly not least, this dissertation is dedicated to my family: my parents, sister, brother, little niece, and other family members. Without their unconditional love and support I would have not been able to pursue this challenging but exciting part of my life.

TABLE OF CONTENTS

LIST OF FIGURES

Figure

LIST OF TABLES

Table

LIST OF APPENDICES

Appendix

LIST OF ABBREVIATIONS

AFM Atomic Force Microscopy

MTC Magnetic Twisting Cytometry

NLV Non-Linear Viscoelastic

NLE non-linear elastic

QLV quasi-linear viscoelastic

FE Finite Element

RH ramp-hold

RR ramp-reverse

RMSE root mean square error

DS deflection sensitivity

ABSTRACT

Experiments and Inverse Analysis for Determining Non-Linear Viscoelastic Properties of Polymeric Capsules and Biological Cells

by

Nhung T. Nguyen

Co-Chairs: Anthony M. Waas and Alan S. Wineman

The mechanics of capsules and cells plays an important role in many applications, including designing and efficiency testing for drug delivery purposes, establishing potential biomarkers for disease detection, and providing insight into many cells' functions and processes. Hence, techniques like indentation, micropipette aspiration, and atomic force microscopy (AFM) based testing have been employed widely to probe their mechanical properties. Interpreting data from these experimental platforms, however, is still a challenging problem. It requires the incorporation of many factors into the model, such as contact mechanics, large deformations, nonlinearity in the material and the geometry, and history-dependent characteristics. This leads to significant computational cost associated with extracting mechanical properties. This thesis aims to address this issue by presenting a methodology to automatically and efficiently characterize non-linear viscoelastic (NLV) properties from time dependent data of polymeric capsules in compression and biological cells in AFM indentation. In addition, this thesis also investigates the possibility of utilizing the extracted NLV parameters for distinguishing cell groups.

The mechanical behavior of fluid-filled polymeric capsules was studied by compressing them between two flat, rigid, parallel plates. Displacement was controlled, and the corresponding force-time responses for ramp-reverse and ramp-hold loading were acquired. The compression process was simulated using finite element (FE) modeling, in which the capsule material is modeled by a NLV constitutive relationship as suggested by experimental data. An inverse analysis based on surrogate modeling and a Kriging estimator is employed in order to reduce the total time needed for optimizing the error between the experimental force-time data and the FE predictions. The method allows for the efficient extraction of the capsule wall's NLV parameters.

The study on polymeric capsules is a precursor to a study on biological cells, using AFM indentation technique to investigate the correlation between the NLV properties of the cells and alterations in the cytoskeletal structures. For this purpose, two approaches were utilized. In the first, breast cancer cells at the benign (MCF-10A) and malignant (MCF-7) states were indented in their culture medium using spherical probes in AFM contact mode in fluid. A two-step indentation loading input was employed. It was comprised of applying a small force to initiate the contact between the probe and the cell, followed by controlling the AFM piezo movement in a ramp-reverse and ramp-hold manner. The force-time responses of the cells were recorded and used for the extraction of the mechanical properties. The indentation experiment was also simulated using the FE method, and the same inverse technique (surrogate modeling with a Kriging estimator) was applied to extract the NLV properties of MCF-10A and MCF-7 cells. In the second approach, MCF-10A cells treated with the drug cytochalasin D to disrupt the cytoskeleton structure were studied, and their NLV parameters were characterized through the same procedure.

Comparison between the extracted NLV properties indicates that malignant cells (MCF-7) are softer and exhibit more relaxation. Disrupting the cytoskeleton using the drug cytochalasin D also results in a larger amount of relaxation in the cell's

response. These results may be useful for disease diagnosing purposes.

CHAPTER I

Introduction

The characterization of a material's mechanical properties has many important applications, such as in the design and testing of products as well as in identifying and distinguishing materials. Two approaches are often employed for the purpose of determining material properties (*Wineman et al.*, 1979). The first is a direct method in which a specimen with a specific shape is carefully prepared for traditional testing scenarios, such as uniaxial, biaxial, or shear experiments (*Boyce and Arruda*, 2000). With the assumption of homogeneous deformation, the deformed shape, and the force-deformation relationship in these tests can be obtained in an analytical/semi-analytical form and is normally not computationally expensive. Hence, the characterization of material properties can be obtained by comparing these solutions with the experimental data using a fast and efficient iterative inverse analysis. The disadvantage of this method is that sample preparation and test setups, such as the tensile grips in tension experiments, have to be precisely designed to be compatible with each other. Furthermore, for systems like biological cells, it is impractical to conduct these traditional tests. These drawbacks can be overcome by testing the actual structural shapes. This second approach assumes that the sample is an assembly of an infinite number of infinitesimal blocks and the deformation of the sample is a combination of simultaneous homogeneous deformations of these blocks. An inverse technique is

required to automatically extract the material parameters. This analysis optimizes the error between the experimental data and the calculations using an appropriately selected theoretical constitutive model. However, an experiment on real structures is often associated with time-consuming and computationally expensive modeling. In addition, the inverse approach also encounters difficulties arising from the number of unknown material parameters needed to be determined in the constitutive models, and the large amount of experimental data required for testing samples with large variations, such as biological materials. A recently developed method, surrogate modeling (*Sacks et al.*, 1989; *Lophaven et al.*, 2002; *Queipo et al.*, 2005; *Forrester et al.*, 2008), has been used to address these problems. In this thesis, an inverse analysis based on a surrogate model is employed, which reaps the benefits of testing actual structural shapes and reducing the difficulty of the inverse process. Inverse modeling in connection with surrogate modeling has been successfully used to characterize the mechanical properties of many traditional materials (*Gustafson and Waas*, 2009; *Heinrich and Waas*, 2009), however, there is still relatively little that has investigated the potential applications of this method to evaluate and understand the mechanical behavior of biological materials, such as living cells. In this thesis, the effectiveness of surrogate modeling in studying the mechanics of polymeric and biological structures is discussed in details.

In particular, this thesis focuses on synthetic polymeric and biological structures that are widely available, such as polymeric fluid-filled capsules used in the pharmaceutical industry, engineered polymeric cells and microcapsules, and biological cells. In the context of these structures, time-dependent or viscoelastic characteristics are essential mechanical features. They have been known to relate closely to the changes in the material's internal organization (*Wineman and Rajagopal*, 2000; *Bursac et al.*, 2005; *Mofrad and Kamm*, 2006). Therefore, developing a methodology to understand and characterize these properties has been an interesting subject of research.

1.1 Importance of Material Identification for Synthetic Polymeric and Biological Capsules and Cells

Polymeric capsules are common products in the pharmaceutical industry used for drug delivery. Their mechanical properties play a key role in the drug release process. For instance, as soon as the capsules are swallowed, they can undergo deformation due to mechanical interactions with the surrounding tissue environment. The amount of deformation is highly dependent on how the capsule material reacts under certain loading conditions. Hence, knowing the mechanical behavior of the capsule under contact situations leads to a more precise prediction of how much the capsule will deform upon being swallowed. Such predictions can be used in the investigation of the time of drug release and for evaluating the capsule's performance. Many of these products are made of soft gel shells and enclose a fluid. One example is the commercial vitamin capsule composed of a gelatin shell filled with fish-liver oil. The shell material exhibits typical viscoelastic properties, including stress relaxation features (*Nguyen et al.*, 2014). Understanding these features requires testing the actual objects subjected to contact interactions, modeling the tests, and incorporating an inverse process.

Commercially available pharmaceutical fluid-filled capsules might also be viewed as a macroscopic model of micro-scale structures like synthetic polymeric and biological cells. Many attempts have been made to manufacture engineered polymeric cells and microcapsules that either mimic the real cells or deliver drug and imaging particles (*Kühtreiber et al.*, 1999). For the purpose of mimicking real cells, there is a necessity of matching the mechanical properties of synthetic cells with those that are present in the blood stream. Thus, it is necessary to make synthetic cells that mechanically resemble actual cells. For example, to function properly when interacting with organs inside the body such as blood vessels, the synthetic cells should have

the same range of stiffness as the actual cells. Hence, knowledge of the mechanical behavior of both engineered and biological cells is beneficial in guiding the selection of materials for manufacturing synthetic cells as well as examining their effectiveness.

In addition to being useful for the design of synthetic polymeric microcapsule and cells, such knowledge can contribute to better quantifying the physiology of biological cells (*Bao and Suresh*, 2003; *Suresh et al.*, 2005; *Suresh*, 2006, 2007). Cell mechanics is also closely linked with alterations in cytoskeletal structures, which may be associated with invasive diseases such as cancer. For instance, several studies (*Cross et al.*, 2007; *Prabhune et al.*, 2012) have investigated the difference in cell stiffness between cancerous cells and their corresponding normal cells. Initial results indicated that certain types of diseased cells might be softer and more deformable, which may explain the spreading ability of cancerous cells within the body. Furthermore, changes in cell stiffness have been reported between different states of cancer. The studies by *Guck et al.* (2005); *Faria et al.* (2008); *Li et al.* (2008, 2009) showed that as cells transform from benign to malignant stages, the stiffness exhibits a decreasing trend. In addition to stiffness, the viscoelastic behavior of the cells has also been observed (*Darling et al.*, 2006, 2008; *Li et al.*, 2008, 2009), but this still requires further investigation, especially at the large deformation range. Preliminary results suggest that viscoelastic characteristics may be effective indicators and biomarkers for better diagnosis and treatment of this dangerous disease, and could also aid testing the efficiency of anti-cancer drugs to combat cancer. Therefore, various techniques and theoretical models have been developed to characterize the mechanical behavior of capsules and biological cells; these are summarized in the two following sections, (1.2) and (1.3).

1.2 Literature Review: Experimental Work

To study the mechanical properties of capsules and cells, various experimental methods have been employed. These are designed to imitate many aspects of the real

loading conditions. One important aspect is the contact feature that the capsules and cells are frequently subjected to. The following is an overview of some widely used techniques.

1.2.1 Compression Test

In this experiment, capsules and cells are squeezed between two flat, rigid, parallel plates as shown in Figure 1.1. The displacement of one plate is controlled while

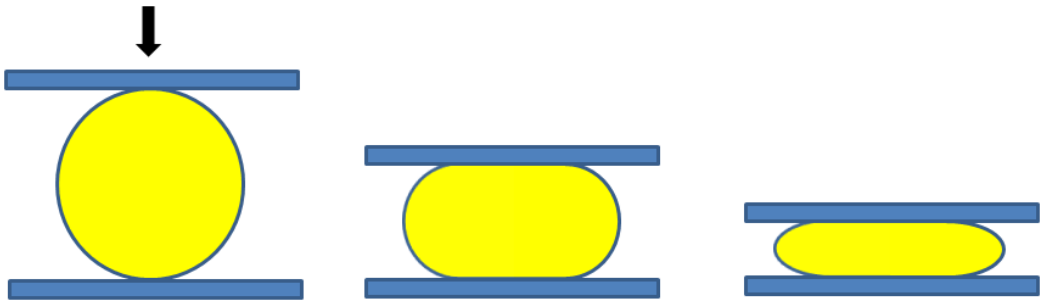

Figure 1.1: Illustration of compression test.

the other remains stationary. During the compression process, the reaction force is recorded and subsequently used to analyze the mechanical behavior of the capsules and cells. This technique was employed in the work by *Carin et al.* (2003) in order to investigate the mechanical response of liquid-filled HSA-Alginate capsules.

1.2.2 Atomic Force Microscopy (AFM)

AFM indentation, as shown in Figure 1.2, has the capability to control and measure very small forces and displacements. This is a popular tool for probing mechanical properties of various structures at the micro/nano scale (*Bao and Suresh*, 2003; *Mofrad and Kamm*, 2006). In addition, the ability to conduct experiments in fluid environments makes it applicable for testing biological samples. For indentation on cells and soft microcapsules, the AFM cantilever is often attached with a spherical particle to reduce damage to the samples during the test. The relationship

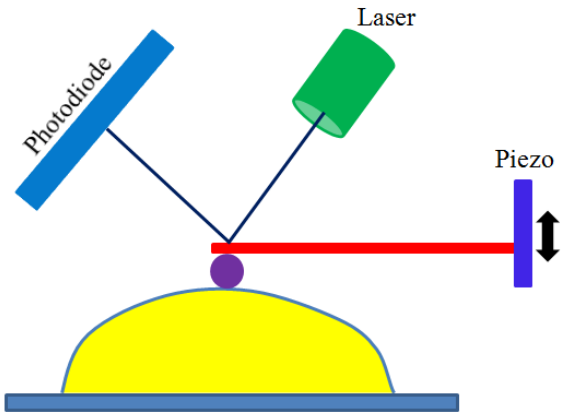

Figure 1.2: Illustration of AFM indentation test.

between the sample's reaction force, the cantilever deflection (measured through the photodiode), and the piezo's movement is utilized in the extraction of the mechanical properties. For this purpose, a model of the cell behavior must be a-priori assumed in order to interpret the mechanical data.

1.2.3 Magnetic Twisting Cytometry (MTC)

In MTC (*Karcher et al.*, 2003; *Bao and Suresh*, 2003; *Bursac et al.*, 2005), a magnetic microsphere is partially embedded in the cell surface as shown in Figure 1.3. A torque is applied to the spherical bead while its displacement is measured. The material properties of the cells are extracted from the relationship between the applied torque and this measured displacement. Again, a model of the cell behavior must be a-priori assumed in order to interpret the mechanical data.

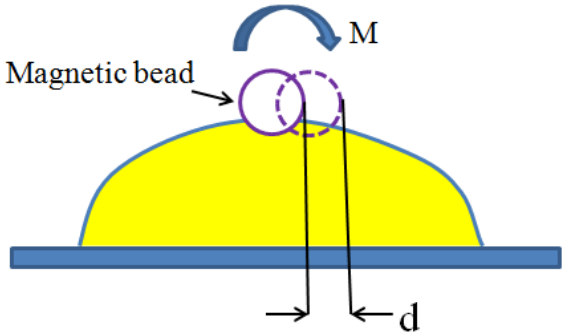

Figure 1.3: Illustration of MTC test.

1.2.4 Micropipette Aspiration

This technique was developed in order to gain insight into the squeezing process of cells through small blood vessels. For this purpose, a small diameter glass pipette is brought into contact with the cell, and a known suction pressure is applied while the rise into the pipette is recorded (*Evans and Young*, 1989; *Dong and Skalak*, 1992; *Drury and Dembo*, 2001; *Bao and Suresh*, 2003). Figure 1.4 is an illustration of the aspiration process of a cell. It is unclear whether the results of this test can provide useful information on extracting cell mechanical properties, due to the complex deformation history that the cell undergoes.

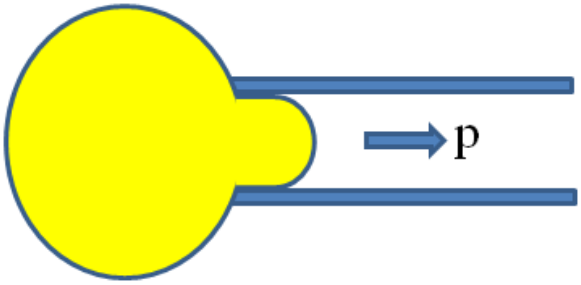

Figure 1.4: Illustration of micropipette aspiration test.

1.2.5 Optical Trap

As described in *Dao et al.* (2003), the optical trap setup is comprised of two silica microbeads diametrically bound to a cell. One bead is fixed while the other is trapped by a laser beam as shown in Figure 1.5. The movement of the free bead due to the laser beam causes the cell to stretch. The power setting of the laser determines the amount of force generated on the microbead, causing the cell to deform axially and transversely. The deformed shape is captured using a CCD camera and video recorders. The output provides important information for the study of cell mechanical behavior.

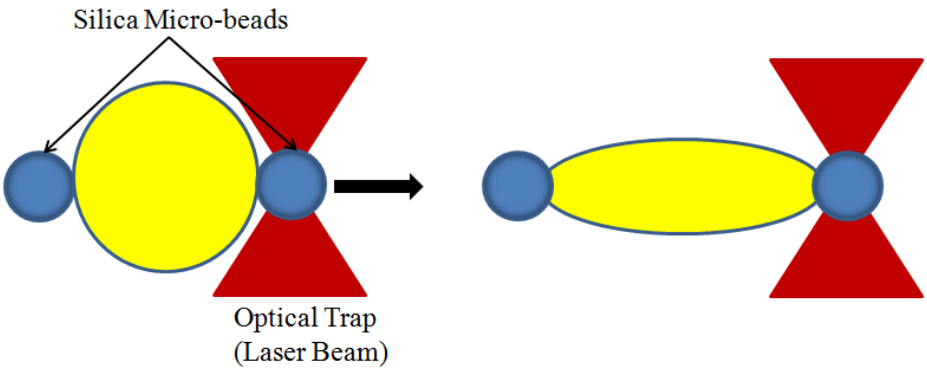

Figure 1.5: Illustration of optical trap test.

1.3 Literature Review: Theoretical Models and Inverse Techniques

Amongst the various techniques described above, it appears that contact of a capsule and a cell with a "rigid" indentor, followed by measurement of the sample response to controlled motion of the indentor, is a common technique by which the capsule and cell properties are probed. The measured data is then interpreted by formulating and solving a corresponding boundary value problem with an assumed constitutive model for the capsule and cell material. This section presents an overview and discussion of current theoretical models used in formulating such a problem, focusing on the ones pertaining to compression and AFM indentation tests that are employed in this thesis.

1.3.1 Material Property Extraction from Compression Test

Many studies have been focused on the development of theoretical constitutive models to interpret experimental data from compression tests on liquid-filled capsules, microcapsules, and cells. Earlier work by *Feng and Yang* (1973) used a non-linear elastic (NLE) model to solve the contact problem of an inflated spherical membrane with gas inside. Recent work by *Nadler* (2010) utilized the same model for a con-

tact problem of a spherical membrane enclosing an incompressible fluid. The work by *Nguyen et al.* (2013a) takes into account the non-linear history-dependent (viscoelastic) properties of a polymeric capsule's wall. However, these studies have not considered the inverse problem to determine the actual capsule shell/membrane properties from the experimental data. This material identification problem is a difficult task that requires an inverse technique to automatically extract the optimized sets of material parameters. In *Carin et al.* (2003), the mechanical properties of a liquid-filled HSA-Alginate capsule were determined by comparing the results of compression experiments to predictions from a non-linear theoretical model such as neo-Hookean non-linear elasticity. Nevertheless, the simplified inverse approach used in this study, which was based on a semi-analytical solution for the compression of spherical cells by *Lardner and Pujara* (1980), might not be applicable to study more general cases, such as those with non-spherical, non-uniform thickness capsules. Additionally, the contact area, in particular how it varies during the compression process, was not investigated.

1.3.2 Material Property Extraction from AFM Indentation

As mentioned earlier, AFM is a technique widely used to probe the mechanical properties of microcapsules and cells (*Mofrad and Kamm*, 2006; *Radmacher*, 2007; *Faria et al.*, 2008; *Li et al.*, 2008, 2009; *Fernandes et al.*, 2010). However, processing the AFM data is still a challenging problem and is highly dependent on the chosen constitutive model. In the literature, the Hertz contact model has been frequently used to analyze the data. This model examines the contact between two elastic bodies, including the case between a rigid sphere and an elastic infinite half-space. The rigid sphere of radius R is taken to be the probe of the AFM cantilever while the half-space is used to model the microcapsules and cells. As explained in *Hertz* (1882), this model predicts the relationship between the applied force F and the indentation

depth δ, in this case, as follows:

$$F = \frac{4}{3} E^* R^{1/2} \delta^{3/2}, \tag{1.1}$$

where:

$$\frac{1}{E^*} = \frac{1 - \nu_1^2}{E_1} + \frac{1 - \nu_2^2}{E_2}. \tag{1.2}$$

E_1, E_2 are the elastic moduli, and ν_1, ν_2 are the Poisson ratios of the sphere and the half-space, respectively. The sphere is rigid compared to the half-space, or $E_1 >> E_2$, thus,

$$E^* \simeq \frac{E_2}{1 - \nu_2^2}. \tag{1.3}$$

It is important to note that the Hertz contact model is only valid given the following assumptions:

- Strains are small and within the elastic limit.

- Each body can be considered to have large radii of curvature, and the length of contact is much smaller than the characteristic radius of each body.

- Surfaces are continuous, non-conforming, and frictionless.

However, in the actual context of an AFM indentation test, these assumptions are not normally satisfied. For example, polymeric microcapsules and cells cannot be treated as perfectly elastic bodies. One reason for this is the viscoelastic behavior that has been observed in experiments (*Darling et al.*, 2006, 2008; *Li et al.*, 2008, 2009; *Bernick et al.*, 2011). In addition, in many cases, the indentation depth is not sufficiently smaller than the characteristic dimension of the indenter and the cell body, and the strains are no longer small (*Bernick et al.*, 2011). Therefore, using the Hertz model to predict the relationship between force and indentation depth under these circumstances might result in inaccurate estimations of material parameters.

As polymeric capsules and cells can be subjected to large deformations, approaches, in which contact in AFM indentation tests are included in the context

of non-linear continuum mechanics, were also employed. One approach interprets the experimental data using the FE method to take into account many aspects of the indentation process, including the dimensions of the probe and the sample, contact features, and non-linear material models (*Charras and Horton*, 2002; *Bernick et al.*, 2011). This method can better capture the response at the large strain range. However, the computational cost associated with FE models is a drawback for inversely extracting material properties. Furthermore, the number of unknown material parameters needed to identify mechanical behavior and the large amount of experimental data increase the difficulty of the inverse process. In the literature, recent work by *Bernick et al.* (2011) employed an inverse FE approach for interpreting AFM experimental data; nevertheless, details related to these computational issues have still not been thoroughly discussed. Additionally, in many cases of AFM indentation, the experiment is neither force nor displacement control because of the manner by which an AFM operates. This is normally neglected during FE modeling, which is also another source of inaccuracy.

1.4 Thesis Objectives

The aim of this thesis is to present a methodology that can be applied to determine the NLV properties of materials and structures in various testing scenarios and in the large strain regime. Two specific applications related to fluid-filled polymeric capsules and biological cells are considered in order to illustrate the effectiveness of the method. Specifically, capsule and cell mechanical properties are probed by conducting compression and AFM indentation tests, respectively. The experimental force-time data is acquired and analyzed using a FE approach, which incorporates nonlinearity in both material and geometry as well as history-dependent characteristics. An inverse process is implemented to automatically determine the optimized set of material parameters that can predict the responses observed in experiments. An

inverse technique based on a surrogate model and a Kriging predictor is employed in order to overcome the computational cost problem associated with the property extraction process (*Forrester et al.*, 2008; *Gustafson and Waas*, 2009; *Heinrich and Waas*, 2009).

This thesis also includes a discussion on the use of cell relaxation response as a potential marker for cancer diagnosis. For this purpose, the above procedure is applied to analyze time-dependent AFM indentation data obtained using two approaches. The first focuses on the differences between benign and malignant breast cancer cells in terms of their viscoelastic behavior while the other studies how cytoskeletal disruption induced by drug treatment can affect this behavior. This supplements current attempts to investigate the potential use of viscoelastic features for disease detection purposes.

1.5 Thesis Outline

This thesis includes six chapters, with the introduction presented in Chapter I. Chapter II is a discussion of a NLV model to interpret time-dependent responses. The chapter serves as a forward problem in material property characterization process. It includes the development of a NLV model based on a single integral Pipkin-Rogers NLV model, the FE implementation of the model, and verification by comparison with an analytical solution. Different aspects of viscoelastic phenomena are also investigated to gain insight into the mechanics of the problem.

Chapter III is an overview of inverse analysis, utilizing surrogate modeling with a Kriging estimator to solve inverse problems. Two specific problems of interest are to determine the NLV properties using experimental data from compression and AFM indentation tests.

Chapter IV presents an experimental setup and inverse analysis for determining the NLV properties of a polymeric capsule filled with a fluid. It contains a detailed

description of compression tests on polymeric capsules and an optical arrangement for getting contact information. The error between the recorded force-displacement-time data and predictions from FE simulations of the compression process is optimized through an inverse analysis utilizing surrogate modeling and a Kriging estimator. The inverse process allows an efficient extraction of the NLV properties from compression tests.

Chapter V focuses on experiments and inverse analysis used to characterize the NLV properties of breast cancer cells. Results for two approaches are acquired with a two-step indentation procedure composed of force control and AFM piezo displacement control followed by a combination of ramp-reverse and ramp-hold piezo loading. The first approach concerns AFM indentation data from benign (MCF-10A) and malignant (MCF-7) cells. The second uses data from a drug treatment approach, including experimental force-time responses from untreated MCF-10A cells and MCF-10A cells treated with the drug cytochalasin D. The same inverse process, based on a surrogate model and a Kriging predictor, is employed to obtain the NLV properties for each cell group, allowing a quantitative comparison of the differences in their viscoelastic properties. A discussion of the use of such differences in formulating potential marker for cancer detection is also included in this chapter.

Chapter VI includes conclusions and future work.

A study of prostate cancer cells using AFM indentation technique is presented in Appendix A. Appendix B provides additional details for the AFM indentation setup, including calibration procedures that were employed. Appendix C has the expressions used in establishing governing equations for solving the forward problem in Chapter II. Appendix D contains the detailed derivation of a user material subroutine (UMAT) for implementing a NLV model in the FE ABAQUS commercial software. The source code for the UMAT subroutines are provided in Appendix E.

CHAPTER II

Non-Linear Viscoelastic Model and Forward Problem

2.1 Introduction

The process of using data obtained from the techniques described in Chapter I requires a better understanding of the forward problem, which is used to model the corresponding experiment. For such a problem, an appropriate theoretical constitutive model is selected, and the material parameters are assumed to be known in advance. A boundary value problem is then formulated and solved with an analytical and/or FE approach to predict the response of an experimental process. The obtained solutions are useful for investigating the influences of a sample's material parameters on its deformation as well as for gaining insight into the constitutive model. Another advantage is that the analytical formulation approach, if available, can be used to cross-check the FE solution. Therefore, the purpose of this chapter is to study selected forward problems that can mimic testing scenarios for material identification as well as capture important features within experiments.

One class of models for a cell or microcapsule regards them as a closed membrane containing a fluid. Such membrane-fluid structures can be modeled with the theory developed for non-linear membranes. The formulation of the theory for NLE

membranes can be found in the classic work by *Green and Adkins* (1970) (see *Fu and Ogden* (2001) for a more recent presentation). *Selvadurai* (2006) provides a very useful and thorough review of the extensive literature on NLE membranes. Much of the literature involves membranes loaded by tractions along their edges or by lateral pressure. A smaller body of work is concerned with loading by contact with a hard object. Among the earliest work in this latter category is that of *Yang and Hsu* (1971), who considered a planar membrane that is supported along a circular boundary and indented at its center with a smooth rigid sphere. This problem was revisited by *Selvadurai* (2006) and *Selvadurai and Yu* (2006), who studied off-center indentation. The membrane indentation study by *Yang and Hsu* (1971) was followed by that of *Feng and Yang* (1973), who considered a closed NLE spherical membrane containing compressible gas. The system was compressed between two rigid parallel plates. *Lardner and Pujara* (1980) subsequently carried out a similar contact study with the purpose of determining the mechanical properties of cell membranes. A system consisting of a NLE spherical membrane enclosing an incompressible fluid and compressed between smooth, rigid, parallel plates was recently studied by *Nadler* (2010). Interesting phenomena were observed with increasing plate displacements, such as the decrease in principal stresses from positive to negative and the onset of wrinkling in the contact region.

As polymeric capsules and cells have been shown to exhibit non-linear history-dependent properties, it is natural to consider the influence of non-linear viscoelasticity on their response. Until recently, the literature on NLV membranes (see *Wineman* (2007)) has been limited to loading by edge tractions or by lateral pressure. *Nguyen et al.* (2013b) presented perhaps the first study of NLV membrane contact. They extended the indentation study of *Yang and Hsu* (1971) to NLV membranes. The purpose of the present chapter is to extend the work of *Nadler* (2010) by adding non-linear viscoelasticity to the mechanical properties of the container. The results can

thus provide a useful context in which to interpret results of contact type experiments that probe the behavior of cells and microcapsules.

The viscoelastic response of the membrane is described by a non-linear single integral constitutive equation as presented in *Nguyen et al.* (2013b). Section 2.2 gives an overview of the model. A special case is a quasi-linear viscoelasticity model (*Fung*, 1981), which arises when the material properties satisfy certain conditions. The analytical formulation and solution method for the corresponding NLV membrane problem suggested in *Wineman* (2007) are implemented in section 2.3. This provides insight into the mechanical behavior of a spherical membrane containing a fluid in an axisymmetric contact problem. A discussion of the FE approach is included in section 2.4. This approach can be extended to general cases, where the problem is no longer axisymmetric. In section 2.5, specific choices for the NLV material properties are made and numerical results are presented. Many aspects of the non-linear response are also discussed, including the instantaneous and long-term equilibrium elastic response, the time-dependent transition between the two limits, and how they are affected by material properties. It is shown that, in a step deformation experiment, time dependence of the deformation indicates that the membrane should not be modeled using quasi-linear viscoelasticity. Section 2.6 contains concluding comments.

2.2 A NLV Constitutive Model

Let t denote the current time and s denote a generic time, $s \in (-\infty, t]$. It is assumed that the viscoelastic solid body occupies the same configuration at all $t < 0$, which is taken as its reference configuration. The position of a material particle is denoted by $\mathbf{X}$ in this reference configuration and by $\mathbf{x}(s)$ at a generic time $s \in (-\infty, t]$. The deformation gradient and right Cauchy-Green tensor are, respectively, $\mathbf{F}(s) = \partial\mathbf{x}(s)/\partial\mathbf{X}$ and $\mathbf{C}(s) = \mathbf{F}(s)^{\mathrm{T}}\mathbf{F}(s)$. Note that $\mathbf{x}(s) = \mathbf{X}$ and $\mathbf{F}(s) = \mathbf{C}(s) = \mathbf{I}$ for $s \in (-\infty, 0)$. The invariants of $\mathbf{C}$ are defined by $\mathrm{I}_1(\mathbf{C})$=tr($\mathbf{C}$),

and $\mathrm{I}_2(\mathbf{C}) = \frac{1}{2}\left[\mathrm{tr}(\mathbf{C})^2 - \mathrm{tr}(\mathbf{C}^2)\right]$, with $\mathrm{tr}(\mathbf{C})$ denoting the trace. For notational brevity, explicit mention of t is omitted when quantities are evaluated at the current time, i.e. $\mathbf{x}(t) = \mathbf{x}$. It is assumed that the NLV material is incompressible, isotropic and can be modeled by the Pipkin and Rogers constitutive theory (*Pipkin and Rogers*, 1968), whose form is

$$\boldsymbol{\sigma}(t) = -q\mathbf{I} + \mathbf{F}(t)\{\mathbf{R}[\mathbf{C}(t), 0] + \int_0^t \frac{\partial}{\partial(t-s)}\mathbf{R}[\mathbf{C}(s), t-s]ds\}\mathbf{F}(t)^T. \tag{2.1}$$

In the first term of (2.1), q is an arbitrary scalar that arises from the constraint of incompressibility, $\det(\mathbf{F}(s)) = \det(\mathbf{C}(s)) = 1$, $s \in [0, t]$. $\mathbf{R}[\mathbf{C}, t]$ is a tensor-valued function of the right Cauchy-Green tensor $\mathbf{C}$ and time t. For isotropic materials,

$$\mathbf{R}[\mathbf{C}, t] = \alpha_0\mathbf{I} + \alpha_1\mathbf{C} + \alpha_2\mathbf{C}^2, \tag{2.2}$$

where $\alpha_i = \alpha_i(\mathrm{I}_1(\mathbf{C}), \mathrm{I}_2(\mathbf{C}), t)$, $i = 0, 1, 2$ are scalar coefficients that represent material properties. For fixed $\mathbf{C}$, $\alpha_i = \alpha_i(\mathrm{I}_1(\mathbf{C}),\mathrm{I}_2(\mathbf{C}), t)$ monotonically decreases with t to a non-zero limit. When the material is undeformed, (2.1) and (2.2) reduce to $\boldsymbol{\sigma}(t) = (-q(t) + \alpha_0(3, 3, t) + \alpha_1(3, 3, t) + \alpha_2(3, 3, t))\mathbf{I}$. The scalar $q(t)$ can be chosen so that $\boldsymbol{\sigma}(t) = 0$.

There are three cases when the constitutive theory (2.1), (2.2) reduces to the form

$$\boldsymbol{\sigma}(t) = -q\mathbf{I} + \hat{\alpha_2}\mathbf{I} + [\hat{\alpha_0} - \mathrm{I}_2\hat{\alpha_2}]\mathbf{B} + [\hat{\alpha_0} + \mathrm{I}_1\hat{\alpha_2}]\mathbf{B}^2, \tag{2.3}$$

where $\mathbf{B} = \mathbf{F}\mathbf{F}^T$, the left Cauchy-Green tensor, I_1 and I_2 are now the invariants of $\mathbf{B}$ and the scalar coefficients $\hat{\alpha_i}$ are functions of I_1, I_2, and t. In these cases, the Pipkin-Rogers model has the general form of the constitutive equation for an incompressible non-linear isotropic elastic solid.

Note for reference that the Mooney-Rivlin material is the special case of (2.3) when

$$\begin{aligned} \hat{\alpha_0} - I_2\hat{\alpha_2} &= C_1 + I_1C_2 = C_1(1+\gamma I_1), \\ \hat{\alpha_1} + I_2\hat{\alpha_2} &= -C_2 = -C_1\gamma, \end{aligned} \tag{2.4}$$

where C_1, C_2 are positive constants. The ratio $\gamma = C_2/C_1$ is referred to as the Mooney-Rivlin parameter.

Case 1. *Instantaneous response at* $t = 0^+$

At $t = 0^+$, (2.1) and (2.2) reduce to

$$\boldsymbol{\sigma}(0) = -q(0)\mathbf{I} + \mathbf{F}(0)\{\alpha_0\mathbf{I} + \alpha_1\mathbf{C}(0) + \alpha_2\mathbf{C}(0)^2\}\mathbf{F}(0)^T, \tag{2.5}$$

in which $\alpha_i = \alpha_i(\mathrm{I}_1(\mathbf{C}(0)), \mathrm{I}_2(\mathbf{C}(0)), 0)$. Equation (2.5) reduces to the form (2.3) on introducing the left Cauchy-Green tensor $\mathbf{B}(0) = \mathbf{F}(0)\mathbf{F}(0)^T$, recalling that $\mathbf{C}(0) = \mathbf{F}(0)^T\mathbf{F}(0)$, noting that $\mathrm{I}_k(\mathbf{C}(0)) = \mathrm{I}_k(\mathbf{B}(0))$, and making use of the Cayley-Hamilton theorem.

Case 2. *Fixed deformation as* $t \to \infty$

Suppose the body approaches a fixed deformed state, i.e. $\mathbf{F}(s) \to \mathbf{F}(\infty)$ as $t \to \infty$. Then, as in linear viscoelasticity, it can be expected that (2.1) and (2.2) reduce to

$$\boldsymbol{\sigma}(\infty) = -q(\infty)\mathbf{I} + \mathbf{F}(\infty)\{\alpha_0\mathbf{I} + \alpha_1\mathbf{C}(\infty) + \alpha_2\mathbf{C}(\infty)^2\}\mathbf{F}(\infty)^T, \tag{2.6}$$

in which $\alpha_i = \alpha_i(\mathrm{I}_1(\mathbf{C}(\infty)), \mathrm{I}_2(\mathbf{C}(\infty)), \infty)$, with the notation indicating the limit as $t \to \infty$. Equation (2.6) reduces to (2.3) on introducing the left Cauchy-Green tensor $\mathbf{B}(\infty) = \mathbf{F}(\infty)(\infty)^T$, recalling that $\mathbf{C}(\infty) = \mathbf{F}(\infty)^T\mathbf{F}(\infty)$, noting that $\mathrm{I}_k(\mathbf{C}(\infty)) = \mathrm{I}_k(\mathbf{B}(\infty))$, and making using of the Cayley-Hamilton theorem.

Case 3. *Step deformation history*

Let the material undergo a step change in deformation at $t = 0$. The deformation

gradient and right Cauchy-Green tensor change from $\mathbf{F}(t) = \mathbf{C}(t) = \mathbf{I}$ for $t < 0$ to $\mathbf{F}(t) = \mathbf{F}_0$ and $\mathbf{C}(t) = \mathbf{C}_0 = \mathbf{F}_0^T\mathbf{F}_0$ for $t \geq 0$, where $\mathbf{F}_0$ is constant. The integral in (2.1) becomes:

$$\int_0^t \frac{\partial}{\partial(t-s)}\mathbf{R}[\mathbf{C}_0, t-s]ds = \mathbf{R}[\mathbf{C}_0, t] - \mathbf{R}[\mathbf{C}_0, 0], \tag{2.7}$$

and equations (2.1) and (2.2) reduce to

$$\boldsymbol{\sigma}(t) = -q(t)\mathbf{I} + \mathbf{F}_0\left\{\alpha_0\mathbf{I} + \alpha_1\mathbf{C}_0 + \alpha_2\mathbf{C}_0^2\right\}\mathbf{F}_0^T, \tag{2.8}$$

in which $\alpha_i = \alpha_i(\mathrm{I}_1(\mathbf{C}_0), \mathrm{I}_2(\mathbf{C}_0), t)$. Equation (2.8) reduces to (2.3) on introducing the left Cauchy-Green tensor $\mathbf{B}_0 = \mathbf{F}_0\mathbf{F}_0^T$, noting that $\mathrm{I}_k(\mathbf{C}_0) = \mathrm{I}_k(\mathbf{B}_0)$ and proceeding as in Cases 1 and 2. Note that the second expression in (2.8) monotonically decreases with t to a non-zero limit and thus represents deformation dependent stress relaxation. A reasonable restriction on the Pipkin-Rogers constitutive equation (2.1), (2.2) is that it reduces to the constitutive equation for an incompressible isotropic linear viscoelastic material in the limit of infinitesimal strains. To this end, let $\mathbf{x}(s) = \mathbf{X} + \mathbf{u}(s)$, $s \in [0, t]$, where $\mathbf{u}(s)$ is the displacement history. Then $\mathbf{F}(s) = \mathbf{I} + \mathbf{H}(s)$, where $\mathbf{H}(s) = \partial\mathbf{u}(s)/\partial\mathbf{X}$. Let it be assumed that $|\mathbf{H}(s)| \ll 1$, where $|\mathbf{H}(s)|$ denotes the magnitude of any component of $\mathbf{H}(s)$. The infinitesimal strain tensor is then $\mathbf{e}(s) = (\mathbf{H}(s) + \mathbf{H}(s)^T)/2$. As the material is incompressible, $\mathrm{tr}(\mathbf{e}(s)) = 0$. Retaining only first order terms in $\mathbf{H}(s)$,

$$\mathbf{C}(s) = \mathbf{I} + 2\mathbf{e}(s), \tag{2.9a}$$

$$\mathrm{I}_1(\mathbf{C}(s)) = \mathrm{I}_2(\mathbf{C}(s)) = 3. \tag{2.9b}$$

The linearized form of (2.1) and (2.2) is found to be

$$\boldsymbol{\sigma}(t) = -q\mathbf{I} + [\bar{\alpha_0}(t) + \bar{\alpha_1}(t) + \bar{\alpha_2}(t)](\mathbf{I} + 2\mathbf{e}(t)) \\ + [\bar{\alpha_1}(0) + 2\bar{\alpha_2}(0)]2\mathbf{e}(t) + \int_0^t \frac{\partial}{\partial(t-s)}[\bar{\alpha_1}(t-s) + 2\bar{\alpha_2}(t-s)]2\mathbf{e}(s)ds, \quad (2.10)$$

where $\bar{\alpha_k}(t) = \alpha_k(3, 3, t)$. Let the moduli $\bar{\alpha_k}(t)$ satisfy the condition

$$\bar{\alpha_0}(t) + \bar{\alpha_1}(t) + \bar{\alpha_2}(t) = K, \quad (2.11)$$

where K is a constant. Then, (2.10) reduces to the form

$$\boldsymbol{\sigma}(t) = (-q + K)\mathbf{I} + \mu(0)2\mathbf{e}(t) + \int_0^t \frac{\partial}{\partial(t-s)}\mu(t-s)2\mathbf{e}(s)ds. \quad (2.12)$$

in which $\mu(t) = \bar{\alpha_1}(t) + 2\bar{\alpha_2}(t) + K$. This has the form of the constitutive equation for incompressible isotropic linearized viscoelastic response in which the shear modulus is given by $\mu(t) = \bar{\alpha}_1(t) + 2\bar{\alpha}_2(t) + K$. Thus (2.11) imposes a restriction on the material scalar coefficients α_i.

A special case arises when the scalar properties have the following form,

$$\alpha_i\left(\mathrm{I}_1(\mathbf{C}), \mathrm{I}_2(\mathbf{C}), t\right) = \bar{\alpha}_i(\mathrm{I}_1(\mathbf{C}), \mathrm{I}_2(\mathbf{C}))G(t), i = 0, 1, 2, \quad (2.13)$$

where $G(t)$ is a monotonically decreasing function of t that accounts for the previously mentioned time dependence of the scalar properties α_i. Then (2.2) becomes:

$$\mathbf{R}[\mathbf{C}, t] = \mathbf{R}^E[\mathbf{C}]G(t), \quad (2.14)$$

where

$$\mathbf{R}^{(E)}[\mathbf{C}] = \bar{\alpha}_0\mathbf{I} + \bar{\alpha}_1\mathbf{C} + \bar{\alpha}_2\mathbf{C^2}. \quad (2.15)$$

The model becomes:

$$\boldsymbol{\sigma}(t) = -q\mathbf{I} + \mathbf{F}(t)\left\{\mathbf{R}^{(E)}[\mathbf{C}(t)]G(0) + \int_0^t \mathbf{R}^{(E)}[\mathbf{C}(s)]\frac{\partial G(t-s)}{\partial(t-s)}ds\right\}\mathbf{F}(t)^T. \quad (2.16)$$

This is the form of the constitutive equation for quasi-linear viscoelasticity (*Fung*, 1981).

2.3 Analytical Approach

2.3.1 Formulation

The contact problem of a spherical membrane enclosing an incompressible fluid (the weight of the enclosed fluid is neglected) and squeezed between two rigid smooth parallel plates as shown in Figure 2.1 is investigated. The undeformed membrane

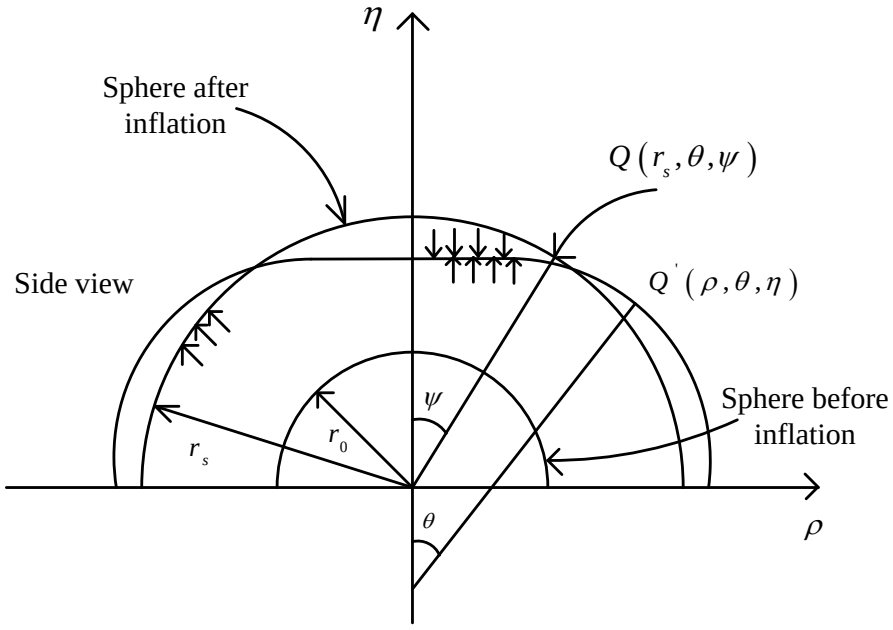

Figure 2.1: Geometry of contact problem of an inflated spherical membrane between two flat, rigid, parallel plates. The spherical coordinates are used for the inflated membrane before contact, the cylindrical coordinates are used for the inflated membrane after contact: $\rho = \rho(\psi, t), \eta = \eta(\psi, t)$.

has a uniform thickness h_0 and a radius r_0, with $\frac{h_0}{r_0} \ll 1$. It is inflated slightly to radius r_s before being compressed between the two rigid, smooth, and parallel plates. The two plates stay parallel and compress the membrane by a displacement along their common perpendicular axis. Either the height of the membrane $H_1(t)$ or the contact force $F(t)$ is specified at each $t \geq 0$. This deforms the membrane into an axisymmetric closed shape with two time-dependent regions: contact and non-contact. At each time $t \geq 0$, the former has a flat geometry, while the latter has an unknown geometry. The usual membrane approximations are assumed to hold: variations through the membrane thickness can be neglected and all physical quantities can be regarded as evaluated at the mid-surface.

The inflated spherical membrane before contact can be described using spherical coordinates while cylindrical coordinates are used for the membrane during contact. Let (r_0, ϕ, ψ) be the spherical coordinates of a particle of the membrane midsurface in the reference configuration. After contact, the coordinates of the particle (ρ, ϕ, η) are with respect to a cylindrical coordinate system. The deformation is described as

$$\rho = \rho(\psi, t), \eta = \eta(\psi, t). \tag{2.17}$$

Because of axial symmetry, the principal directions of stress and stretch are known in advance to be in the meridianal direction (1), circumferential direction (2), and normal direction (3) at each time t in the deformed membrane. The principal stresses and stretches in these directions are denoted respectively by $(\sigma_1, \lambda_1), (\sigma_2, \lambda_2), (\sigma_3, \lambda_3)$. The governing equations then are derived separately for the two regions. All physical quantities depend on the angle ψ and time t. For the purpose of notational simplicity, explicit indication of dependence on ψ will be suppressed. Because of the history dependence of the membrane material, dependence on the time variable t or s will be made explicit as needed.

2.3.1.1 Kinematics and Field Equations

The principal stretch ratios are given by

$$\begin{aligned} \lambda_1 &= \frac{1}{r_0}\sqrt{\rho'^2+\eta'^2}, \\ \lambda_2 &= \frac{\rho}{r_0 sin\psi}, \\ \lambda_3 &= \frac{1}{\lambda_1\lambda_2}, \end{aligned} \tag{2.18}$$

where the notation $()' = \frac{\partial}{\partial\psi}()$ has been introduced. The last equation arises from the incompressibility constraint. The deformation gradient and right Cauchy-Green tensor histories are given by

$$\mathbf{F}(s) = \begin{pmatrix} \lambda_1(s) & 0 & 0 \\ 0 & \lambda_2(s) & 0 \\ 0 & 0 & \lambda_3(s) \end{pmatrix}, \mathbf{C}(s) = \begin{pmatrix} \lambda_1^2(s) & 0 & 0 \\ 0 & \lambda_2^2(s) & 0 \\ 0 & 0 & \lambda_3^2(s) \end{pmatrix}, 0 \le s \le t. \tag{2.19}$$

The stretch invariants are given by

$$\begin{aligned} \mathrm{I}_1 &= \lambda_1^2+\lambda_2^2+\lambda_3^2, \\ \mathrm{I}_2 &= \lambda_1^2\lambda_2^2+\lambda_2^2\lambda_3^2+\lambda_3^2\lambda_1^2, \\ \mathrm{I}_3 &= \lambda_1^2\lambda_2^2\lambda_3^2 = 1. \end{aligned} \tag{2.20}$$

2.3.1.2 Constitutive Equation

According to the membrane approximation, $\sigma_3(t) \ll \sigma_1(t), \sigma_2(t)$. Thus,

$$\begin{aligned} \sigma_1(t) &\simeq \sigma_1(t)-\sigma_3(t), \\ \sigma_2(t) &\simeq \sigma_2(t)-\sigma_3(t). \end{aligned} \tag{2.21}$$

Therefore, by (2.1), (2.2), (2.19), and (2.20),

$$\sigma_1(t) = g_1[\underline{\lambda}(t)] + \int_0^t G_1[\underline{\lambda}(t), \underline{\lambda}(s), t-s]ds,$$
$$\sigma_2(t) = g_2[\underline{\lambda}(t)] + \int_0^t G_2[\underline{\lambda}(t), \underline{\lambda}(s), t-s]ds, \tag{2.22}$$

in which $\underline{\lambda}$ denotes the set of stretch ratios (λ_1, λ_2) and

$$\begin{aligned} g_\alpha[\underline{\lambda}(t)] &= g_\alpha[\lambda_1(t), \lambda_2(t)] \\ &= \alpha_0[\underline{\lambda}(t), 0]\left[\lambda_\alpha^2(t) - \frac{1}{\lambda_1^2(t)\lambda_2^2(t)}\right] + \alpha_1[\underline{\lambda}(t), 0]\left[\lambda_\alpha^4(t) - \frac{1}{\lambda_1^4(t)\lambda_2^4(t)}\right] \\ &\quad + \alpha_2[\underline{\lambda}(t), 0]\left[\lambda_\alpha^6(t) - \frac{1}{\lambda_1^6(t)\lambda_2^6(t)}\right], \end{aligned} \tag{2.23}$$

$$\begin{aligned} G_\alpha[\underline{\lambda}(t), \underline{\lambda}(s), t-s] &= G_\alpha[\lambda_1(t), \lambda_2(t), \lambda_1(s), \lambda_2(s), t-s] \\ &= \frac{\partial}{\partial(t-s)}\left\{\alpha_0[\underline{\lambda}(s), t-s]\left[\lambda_\alpha^2(t) - \frac{1}{\lambda_1^2(t)\lambda_2^2(t)}\right]\right. \\ &\quad + \alpha_1[\underline{\lambda}(s), t-s]\left[\lambda_\alpha^2(s)\lambda_\alpha^2(t) - \frac{1}{\lambda_1^2(s)\lambda_1^2(t)\lambda_2^2(s)\lambda_2^2(t)}\right] \\ &\quad \left. + \alpha_2[\underline{\lambda}(s), t-s]\left[\lambda_\alpha^4(s)\lambda_\alpha^2(t) - \frac{1}{\lambda_1^4(s)\lambda_1^2(t)\lambda_2^4(s)\lambda_2^2(t)}\right]\right\}, \end{aligned} \tag{2.24}$$

where $\alpha = 1, 2$. As the invariants are given by (2.20), the material properties α_i can now be regarded as functions of $\lambda_1(t), \lambda_2(t)$, and t.

2.3.1.3 Equations of Motion

Neglecting the effects of inertia, the equations of linear momentum reduce to force balance equations. The equation in the circumferential direction is automatically met owing to axisymetry. In the meridian and the normal directions of the deformed

membrane, and for $t \geq 0$, these are:

$$\frac{dT_1}{d\rho} + \frac{T_1 - T_2}{\rho} = 0, \tag{2.25}$$

$$K_1 T_1 + K_2 T_2 = p, \tag{2.26}$$

where T_1, T_2 are the stress resultants per unit length in the meridian and circumferential directions respectively,

$$T_1 = \sigma_1 \lambda_3 h_0, \qquad T_2 = \sigma_2 \lambda_3 h_0, \tag{2.27}$$

and p is a pressure normal to the membrane. Note that the right hand side of (2.25) is zero because the contacting plates are assumed to be smooth. K_1 and K_2 are principal curvatures in the deformed configuration determined as follows:

$$K_1 = \frac{d\theta}{ds}, \qquad K_2 = \frac{sin\theta}{\rho}, \tag{2.28}$$

where θ is the angle between the normal to the membrane and the centerline. This angle is related to the deformed configuration by:

$$cos\theta = \frac{d\rho}{ds}, \qquad sin\theta = -\frac{d\eta}{ds}. \tag{2.29}$$

Let the associated variable w be defined:

$$w = \frac{1}{r_0} \frac{\partial \rho}{\partial \psi}. \tag{2.30}$$

Note that w satisfies the compatibility condition obtained from the second equation of (2.18)

$$\frac{\partial \lambda_2}{\partial \psi} = \frac{w - \lambda_2 cos\psi}{sin\psi}. \tag{2.31}$$

The principal curvatures can be expressed in terms of $\lambda_1, \lambda_2, w, \psi$ by using (2.18), (2.28)-(2.30), and observing that $\eta' = -r_0\sqrt{\lambda_1^2 - w^2}$,

$$K_1 = \frac{w\lambda_1' - w'\lambda_1}{r_0\lambda_1^2(\lambda_1^2 - w^2)^{1/2}}, \qquad K_2 = \frac{\sqrt{\lambda_1^2 - w^2}}{r_0\lambda_1\lambda_2 sin\psi}. \tag{2.32}$$

Using (2.30) and (2.32), equations (2.25) and (2.26) can be written in terms of $T_1, T_2, \lambda_1, \lambda_2, w, \psi$ in the reference coordinates, for $t \geq 0$

$$\frac{\partial T_1}{\partial \psi} + \frac{T_1 - T_2}{\lambda_2 \sin\psi} w = 0, \tag{2.33}$$

$$\frac{w\lambda_1' - w'\lambda_1}{r_0\lambda_1^2(\lambda_1^2 - w^2)^{1/2}} T_1 + \frac{\sqrt{\lambda_1^2 - w^2}}{r_0\lambda_1\lambda_2 sin\psi} T_2 = p. \tag{2.34}$$

2.3.2 Boundary Value Problem

Let $\psi_c(t)$ denote the value of ψ corresponding to the boundary between the contact and non-contact regions at time t. In the contact region, $0 \leq \psi \leq \psi_c(t)$, the shape of the deformed membrane is flat, and the principal curvatures are known to be: $K_1 = K_2 = 0$. Therefore, the pressure between the membrane and the flat plate is balanced with the internal pressure between the fluid and the membrane, which is unknown. Equation (2.33) must be part of the system of equations to be solved. In the non-contact region, $\psi_c(t) \leq \psi \leq \pi/2$, the shape of the membrane and the curvatures are unknown, and there is only the pressure from fluid. Both equations (2.33) and (2.34) are part of the system of equations. Thus, different systems of equations are solved in the contact and non-contact regions, with matching conditions to be specified at $\psi_c(t)$. In the approach taken here, as in *Feng and Yang* (1973), the governing equations in each region are reduced to systems of first order equations for $(\lambda_1, \lambda_2, w)$.

2.3.2.1 Non-contact Region, $\psi_c(t) \leq \psi \leq \pi/2$

Let $T_1(t)$, $T_2(t)$ from (2.22) and (2.27) and K_1, K_2 from (2.32) be substituted into (2.33) and (2.34). The result, along with (2.31) is a system of three first order partial differential-Volterra integral equations for $(\lambda_1, \lambda_2, w)$.

$$\begin{aligned}
&\tfrac{\partial\lambda_1(t)}{\partial\psi}\left\{\mathrm{F}_1[\underline{\lambda}(t)] + \int_0^t \hat{\mathrm{F}}_1[\underline{\lambda}(t), \underline{\lambda}(s), t-s]ds\right\} \\
&\qquad + \int_0^t \tfrac{\partial\lambda_1(s)}{\partial\psi}\hat{\mathrm{F}}_2[\underline{\lambda}(t), \underline{\lambda}(s), t-s]ds \\
&= \mathrm{F}_2[\underline{\lambda}(t), w(t), \psi] + \int_0^t \hat{\mathrm{F}}_3[\underline{\lambda}(t), \underline{\lambda}(s), w(t), w(s), t-s, \psi]ds,
\end{aligned} \tag{2.35}$$

$$\frac{\partial\lambda_2(t)}{\partial\psi} = \frac{w(t) - \lambda_2(t)cos\psi}{sin\psi}, \tag{2.36}$$

$$\frac{\partial w(t)}{\partial\psi} = \frac{w(t)\lambda_1'(t)}{\lambda_1(t)} + \frac{\lambda_1^2(t)w^2(t)}{\lambda_2(t)sin\psi}\frac{\sigma_2(t)}{\sigma_1(t)} - \frac{pr_0}{2h_0}\frac{\sqrt{\lambda_1^2 - w^2}\lambda_1^2(t)\lambda_2(t)}{\sigma_1(t)}. \tag{2.37}$$

Expressions for $F_1, F_2, \hat{F}_1, \hat{F}_2, \hat{F}_3$ are given in the Appendix C.

2.3.2.2 Contact Region, $0 \leq \psi \leq \psi_c(t)$

The deformed membrane in the contact region is flat. Thus, $\eta' = 0$ and by the first of (2.18) and (2.30), $w = \lambda_1$. The principal curvatures are known to be $K_1 = K_2 = 0$. This known geometry of the contact region reduces the governing equations for the

contact region to the following,

$$\begin{aligned}
&\frac{\partial\lambda_1(t)}{\partial\psi}\left\{\mathrm{F}_1[\underline{\lambda}(t)]+\int_0^t \hat{\mathrm{F}}_1[\underline{\lambda}(t),\underline{\lambda}(s),t-s]ds\right\}\\
&\quad+\int_0^t \frac{\partial\lambda_1(s)}{\partial\psi}\hat{\mathrm{F}}_2[\underline{\lambda}(t),\underline{\lambda}(s),t-s]ds\\
&=\mathrm{F}_2[\underline{\lambda}(t),w(t),\psi]+\int_0^t \hat{\mathrm{F}}_3[\underline{\lambda}(t),\underline{\lambda}(s),w(t),w(s),t-s,\psi]ds, \qquad (2.38)
\end{aligned}$$

$$\frac{\partial\lambda_2(t)}{\partial\psi}=\frac{w(t)-\lambda_2(t)cos\psi}{sin\psi}. \qquad (2.39)$$

2.3.2.3 Boundary Conditions

At $\psi=0$: an analysis in *Green and Adkins* (1970) that considers the boundedness of the solution at $\psi=0$ implies:

$$\lambda_1(0,t)=\lambda_2(0,t)=\lambda_0(t), \quad w=\lambda_1, \qquad (2.40)$$

$$\frac{\partial\lambda_1}{\partial\psi}|_{\psi=0}=\frac{\partial\lambda_2}{\partial\psi}|_{\psi=0}=0. \qquad (2.41)$$

At $\psi=\psi_c(t)$: $\lambda_2(t)$, $w(t)$, $T_1(t)$ must be continuous. It is assumed by (2.22), (2.23), (2.24), and (2.27) that this is equivalent to requiring $\lambda_1(t),\lambda_2(t),w(t)$ to be continuous at $\psi=\psi_c(t)$. The same interface condition was used in *Feng and Yang* (1973) and *Nadler* (2010).

At $\psi=\pi/2$:

$$(\lambda_2 sin\psi)'=0. \qquad (2.42)$$

Displacement control:

This is specified by giving the displacement of the plate $D(t)=r_s-H_1(t), t\geq 0$, where $H_1(t)$ is the height of the membrane and $r_s=\lambda_s r_0$ is the radius of the slightly-inflated membrane. $H_1(t)$ is related to the deformation of the membrane by recalling

$\eta' = -r_0\sqrt{\lambda_1^2 - w^2}$, and observing that $\eta(0,t) = \eta(\psi_c(t), t)$,

$$H_1(t) = \eta(0,t) = \int_0^{\pi/2} r_0\sqrt{\lambda_1^2 - w^2}d\psi. \tag{2.43}$$

Force Control:

This is specified by giving the force applied to the plate, (or the contact force between the plate and the membrane) $F(t), t \geq 0$. Consideration of the equilibrium of the plate and the portion of the membrane $0 \leq \psi \leq \psi_c(t)$ gives the relation,

$$F(t) = \pi(sin^2\psi\rho^2)p|_{\psi_c}. \tag{2.44}$$

Since the fluid inside the membrane is incompressible, another constraint is that the volume maintains a constant. The volume before contact is

$$V_0 = \frac{4}{3}\pi r_0^3\lambda_s^3. \tag{2.45}$$

The volume after contact can be written in the from

$$V = 2\pi r_0 \int_0^{\pi/2} \rho^2\sqrt{\lambda_1^2 - w^2}d\psi. \tag{2.46}$$

Hence, the incompressibility of the contained fluid implies: $V = V_0$. Additionally, the viscosity of the fluid is also neglected so that the pressure throughout the fluid is uniform. Taking into account the condition that $K_1 = K_2 = 0$ in the contact region, (2.26) means that in the contact regions the pressure from the fluid and from the plates on the membrane balance each other.

2.3.3 Method of Solution

Let the following dimensionless quantities be introduced:

$$\begin{aligned}
&\bar{r} = \tfrac{r}{r_0}, \bar{\rho} = \tfrac{\rho}{r_0}, \bar{\eta} = \tfrac{\eta}{r_0}, \bar{h} = \tfrac{h}{h_0}, \bar{H}_1 = \tfrac{H_1}{r_0}, \\
&\bar{p} = \tfrac{p}{C_1}\tfrac{r_0}{h_0}, \bar{\sigma}_1 = \tfrac{\sigma_1}{C_1}, \bar{\sigma}_2 = \tfrac{\sigma_2}{C_1}, \bar{F} = \tfrac{F}{C_1 h_0 r_0},
\end{aligned} \tag{2.47}$$

where C_1 is a constant with the dimension of stress to be specified later. When λ_1, λ_2, w are expressed in terms of the dimensionless variables in (2.47), they are unchanged. All variables in (2.35)-(2.39) are now dimensionless, with p/h_0 in (2.37) replaced by $\bar{p}$. Henceforth, the upper bar notation is removed for notational simplicity. Let $t_i, i = 1, 2, \ldots, n$ be a discrete set of times at which the contact problem is to be solved. The time integrals in (2.35), (2.37), and (2.38) are approximated as finite sums using the trapezoidal rule,

$$\begin{aligned}
\int_{t_1}^{t_n} f\left[\underline{\lambda}(s), t_n - s\right] ds &= \tfrac{t_n - t_{n-1}}{2}\left[f\left(\underline{\lambda}(t_n), 0\right) + f\left(\underline{\lambda}(t_{n-1}), t_n - t_{n-1}\right)\right] \\
&\quad + \textstyle\sum_{k=1}^{n-2} \tfrac{t_{k+1} - t_k}{2}\left[f\left(\underline{\lambda}(t_{k+1}), t_n - t_{k+1}\right) + f\left(\underline{\lambda}(t_k), t_n - t_k\right)\right].
\end{aligned} \tag{2.48}$$

At each time t_n, the terms involving $\lambda_1(\psi, t_n), \lambda_2(\psi, t_n), w(\psi, t_n)$ can be separated out from the other terms. Equations (2.38), (2.39) in the contact region and (2.35)-(2.37) in the non-contact region can then be written as systems of ordinary differential equations of the form,

$$\frac{\partial}{\partial \psi}\underset{\sim}{\Lambda}(\psi, t_n) = \underline{\mathcal{F}}\left[\underset{\sim}{\Lambda}(\psi, t_n); \underset{\sim}{\Lambda}(\psi, t_i)|_{i=1}^{n-1}\right], \tag{2.49}$$

where $\underset{\sim}{\Lambda} = (\lambda_1, \lambda_2)$ in the contact region and $\underset{\sim}{\Lambda} = (\lambda_1, \lambda_2, w)$ in the non-contact region. Suppose the contact problem has been solved at times $t_1, \ldots, t_{n-1}$. The notation

$\underset{\sim}{\Lambda}(\psi, t_i)|_{i=1}^{n-1}$ indicates that $\underline{\mathcal{F}}$ depends on the independent variable ψ by means of the dependence on ψ of the solutions determined at times $t_1, \ldots, t_{n-1}$.

Let values be assumed for $\lambda_0(t_n)$ in (2.40), the angle of the contact region $\psi_c(t_n)$, and the pressure $p(t_n)$. With (2.40) and (2.41) as boundary conditions, the system (2.49) for the contact region is integrated using the 4th order Runge-Kutta procedure for $0 \leq \psi \leq \psi_c(t_n)$. The values $\lambda_1(\psi_c(t_n), t_n), \lambda_2(\psi_c(t_n), t_n), w(\psi_c(t_n), t_n)$ are then used as boundary conditions for the integration of system (2.49) for the non-contact region, Newton's iteration is used to determine $\lambda_0(t_n)$, $\psi_c(t_n)$, and $p(t_n)$ so that (2.42), $V = V_0$ and either (2.43) or (2.44) are satisfied. This method is repeated for each time t_i, with the final values for $\lambda_0(t_i)$, $\psi_c(t_i)$, and $p(t_i)$ used as the initial estimates of the values at time t_{i+1}.

2.4 FE Approach

2.4.1 Implementation of a NLV Model in ABAQUS

In order to extend the investigation to general cases of loading, the problem was also studied using a FE approach with the commercial code ABAQUS 6.10-1. This FE software allows the implementation of the NLV model through the material subroutine UMAT (*ABAQUS-v6.10*, 2010).

For an incompressible, NLV Pipkin-Roger model, with the use of a penalty approach, the Kirchhoff stress for a 3D solid element is written as follows:

$$\boldsymbol{\tau}(t) = \boldsymbol{F}(t) \left\{ \boldsymbol{R}[\boldsymbol{C}(t), 0] + \int_0^t \frac{\partial}{\partial(t-s)} \mathbf{R}[\mathbf{C}(s), t-s] ds \right\} \boldsymbol{F}^T(t) + KJ(J-1) \quad (2.50)$$

Here: $KJ(J-1)$ is the penalty term, coefficient K is chosen large enough to impose incompressiblity. It is somewhat similar to the bulk modulus.

The stresses are updated at each time t_i. This updating process includes two

aspects: the time dependence of stresses, and the nonlinearity in the constitutive model. The first aspect is performed in a similar way with that discussed in the method of solution (section 2.3.3) of the analytical approach. The nonlinearity of the constitutive model requires an appropriate implementation of the material Jacobian (DDSDDE). The following procedure (*Simo and Hughes*, 1998; *Bažant and Cedolin*, 2003; *ABAQUS-v6.10*, 2010; *Ji et al.*, 2013) has been employed in the derivation of the UMAT subroutine.

At each time $t = t_n$, 2^{nd} Piola-Kirchhoff stress $\mathbf{S} = J\mathbf{F}^{-1}\sigma\mathbf{F}^{-T}$ has the following form:

$$\begin{aligned}
\boldsymbol{S}(t) &= \boldsymbol{R}[\boldsymbol{C}(t), 0] + \int_0^t \frac{\partial}{\partial(t-s)}\mathbf{R}[\mathbf{C}(s), t-s]ds + KJ(J-1)\mathbf{C}^{-1} \\
&= \boldsymbol{R}[\boldsymbol{C}(t_n), 0] + \frac{t_n - t_{n-1}}{2}\frac{\partial}{\partial(t-s)}\mathbf{R}[\mathbf{C}(s), t-s]|_{t_n} + KJ(J-1)\mathbf{C}^{-1} \\
&\quad + \int_0^{t_{n-1}} \frac{\partial}{\partial(t-s)}\mathbf{R}[\mathbf{C}(s), t-s]ds
\end{aligned} \tag{2.51}$$

Let: $E = \frac{1}{2}(\mathbf{C} - \mathbf{I})$, material tangent denoted by $\mathcal{C}$ or $\mathcal{L}$ is computed as

$$\mathcal{C} = \mathcal{L} = \frac{\partial \mathbf{S}}{\partial \mathbf{E}} = 2\frac{\partial \mathbf{S}}{\partial \mathbf{C}}. \tag{2.52}$$

Note that here: $\mathbf{C} = \mathbf{C}(t_n)$, hence the derivative of $\int_0^{t_{n-1}} \frac{\partial}{\partial(t-s)}\mathbf{R}[\mathbf{C}(s), t-s]ds$ in (2.51) with respect to $\mathbf{C}(t_n)$ vanishes.

Using a push-forward step, the material tangent $\mathcal{L}_{ijkl}$ becomes $\mathbf{F}_{ip}\mathbf{F}_{jq}\mathbf{F}_{kr}\mathbf{F}_{ls}\mathcal{L}_{pqrs}$, and the final formula for material Jacobian (DDSDDE) used in UMAT subroutine for commercial code ABAQUS is as follows

$$\mathcal{L}^J_{ijkl} = \frac{1}{J}\mathbf{F}_{ip}\mathbf{F}_{jq}\mathbf{F}_{kr}\mathbf{F}_{ls}\mathcal{L}_{pqrs} + \frac{1}{2}(\delta_{ik}\sigma_{jl} + \delta_{jl}\sigma_{ik} + \sigma_{il}\delta_{jk} + \sigma_{jk}\delta_{il})$$

Prior to applying the UMAT subroutine to complicated cases like the forward problem considered in this chapter, the solutions obtained by using UMAT subroutine for simple cases (uniaxial, biaxial, simple shear of a block) are compared with the exact analytical solutions for verification. The detailed derivation of a UMAT subroutine for 3D solid elements with the above described procedure for an incompressible NLV single integral Pipkin-Rogers model and verifications are included in the Appendix D.

A UMAT subroutine for membrane elements was also developed and was used in the modeling of a contact problem of a fluid-filled membrane between two rigid, flat, parallel plates.

2.4.2 FE Modeling of the Contact Problem of a Fluid-Filled Membrane

The boundary value problem as shown in Figure 2.2 for the compression of a NLV fluid-filled spherical membrane between two flat, rigid, parallel plates is simulated and solved using the commercial code ABAQUS with the UMAT subroutine discussed in section 2.4.1. In the FE simulation, the spherical membrane is modeled using mem-

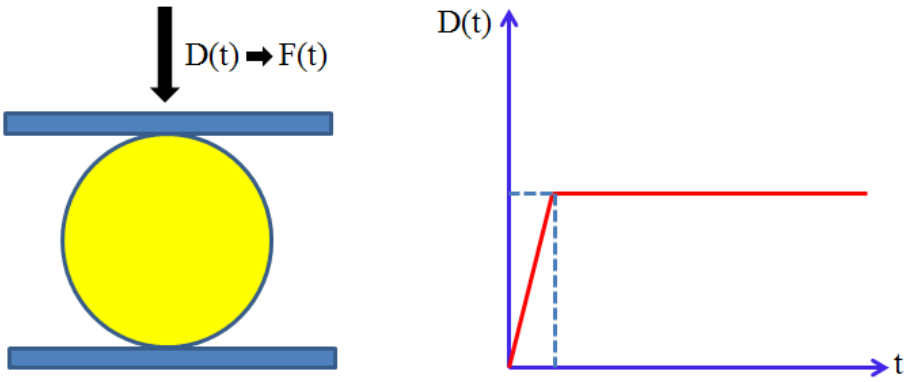

Figure 2.2: Boundary value problem for FE modeling of the contact problem of a fluid-filled membrane between two flat, rigid, parallel plates.

brane element M3D4 while the incompressible fluid inside the membrane is described by hydrostatic fluid elements F3D4 (*ABAQUS-v6.10*, 2010). The two rigid plates are modeled using the rigid planar shell R3D4. The problem includes two steps: the

slight inflation process and the step displacement. For step 1, the inflation process before contact is specified by imposing a pressure to the reference node of the cavity of the incompressible fluid. For step 2, a relaxation type of loading is performed by ramping the displacements of the two plates to a certain value, then holding it constant.

2.5 Numerical Results

For the purpose of illustrating the features associated with non-linear viscoelasticity during contact, specific choices are made for the scalar coefficients $\alpha_i, i = 0, 1, 2$ in (2.2). The choice of these properties was guided by two criteria: 1) The membrane responds as a Mooney-Rivlin material at $t = 0$ and $t \to \infty$; 2) Condition (2.11) is satisfied.

These two criteria are met by the following choices:

$$\begin{aligned} \alpha_0 - I_2\alpha_2 &= 2\left[G_1(t) + I_1 G_2(t)\right], \\ \alpha_1 + I_1\alpha_2 &= -2G_2(t), \\ \alpha_2 &= -2\Phi(I_1, I_2)\left[G_1(t) + 2G_2(t)\right], \end{aligned} \tag{2.53}$$

in which

$$\Phi(I_1, I_2) = e^{-a(I_1-3)}, \tag{2.54}$$

where a is a constant such that Φ and α_2 decrease to zero as the deformation gets large. $G_1(t)$, and $G_2(t)$ have the properties of stress relaxation functions. Then (2.11)

is satisfied with $K = 0$ and:

$$\begin{aligned}
\alpha_0 &= 2G_1(t)\left[1 - I_2\Phi(I_1, I_2)\right] + 2G_2(t)\left[I_1 - 2I_2\Phi(I_1, I_2)\right], \\
\alpha_1 &= 2G_1(t)I_1\Phi(I_1, I_2) + 2G_2(t)\left[2I_1\Phi(I_1, I_2) - 1\right], \\
\alpha_2 &= -2\Phi(I_1, I_2)\left[G_1(t) + 2G_2(t)\right].
\end{aligned} \tag{2.55}$$

With (2.53), (2.1) with (2.2) reduce to (2.3) and (2.4). These are the forms of the constitutive equations for a Mooney-Rivlin material at $t = 0$, and $t \to \infty$. Note that $\gamma_0 = G_2(0)/G_1(0)$ and $\gamma_\infty = G_2(\infty)/G_1(\infty)$ are the Mooney-Rivlin parameters, respectively, at $t = 0$, and $t \to \infty$. In the special case where $G_2(t) = \beta G_1(t)$, β being a constant, the material parameters in (2.55) have the form in (2.3) and the model reduces to quasi-linear viscoelasticity.

As particular choices for $G_1(t)$ and $G_2(t)$, let

$$\begin{aligned}
G_\alpha(t) &= G_{\alpha\infty} + (G_{\alpha 0} - G_{\alpha\infty})\, e^{-t/\tau_\alpha} \\
&= G_{\alpha 0}\left[g_\alpha + (1 - g_\alpha)\, e^{-t/\tau_\alpha}\right], \alpha = 1, 2.
\end{aligned} \tag{2.56}$$

Then, $G_{\alpha 0} = G_\alpha(0), G_{\alpha\infty} = G_\alpha(\infty)$, and τ_α are relaxation times. The parameters $g_1 = G_{1\infty}/G_{10}$ and $g_2 = G_{2\infty}/G_{20}$ represent the amount of decrease of $G_1(t)$ and $G_2(t)$. The parameters $\gamma_0 = G_{20}/G_{10}$ and $\gamma_\infty = G_{2\infty}/G_{1\infty}$ characterize the Mooney-Rivlin material at $t = 0$ and $t \to \infty$. They are related by

$$\gamma_\infty = \frac{g_2}{g_1}\gamma_0. \tag{2.57}$$

In the list of dimensionless parameters introduced in (2.47), let $C_1 = G_1(0)$. In addition, the dimensionless time t_0 is defined as $t_0 = t/\tau_1$. Thus, equations in (2.56)

become:

$$G_1(t) = G_{10}\left[g_1 + (1-g_1)e^{-t/\tau_1}\right] = C_1\left[g_1 + (1-g_1)e^{-t_0}\right],$$
$$G_2(t) = G_{20}\left[g_2 + (1-g_2)e^{-t/\tau_2}\right] = \gamma_0 C_1\left[g_2 + (1-g_2)e^{-ct_0}\right],$$

where $c = \tau_1/\tau_2$.

2.5.1 Analytical Formulation Solution

The numerical results to follow are presented in two groups so to illustrate: (a) The influence of the parameters in (2.56) on the elastic solution at $t = 0$ and $t \to \infty$, and (b) The evolution of the solution between these limits. Calculations were carried out for a dimensionless radius of the slightly inflated membrane $r_s = 1.03$. Figure 2.3 shows membrane profiles for different displacements for NLE response at $t = 0$ or $t \to \infty$, with the Mooney-Rivlin parameter $\gamma = 0.1$. The large dot indicates the transition between the contact and non-contact regions. Figure 2.4 shows contact force vs. contact displacement for several values of the Mooney-Rivlin parameter. The response becomes stiffer as γ increases. A comparison of force vs. displacement curves for elastic response and for viscoelastic response at different displacement rates is shown in Figure 2.5. Calculations were carried out with $G_1(t) = G_2(t)$. The force corresponding to a given displacement is less than in the elastic case and decreases as displacement rate decreases. When $D = 2t$, the deformation increases rapidly before significant stress relaxation occurs and the difference in contact force from the elastic case is small. When $D = t/2$ the deformation increases slowly, there is time for significant stress relaxation to occur and the difference in contact force from the elastic case is larger. Similar results are obtained when $G_1(t) \neq G_2(t)$. These results show that plot of force versus displacement is not a unique property, but depends on the time dependence of the viscoelastic material.

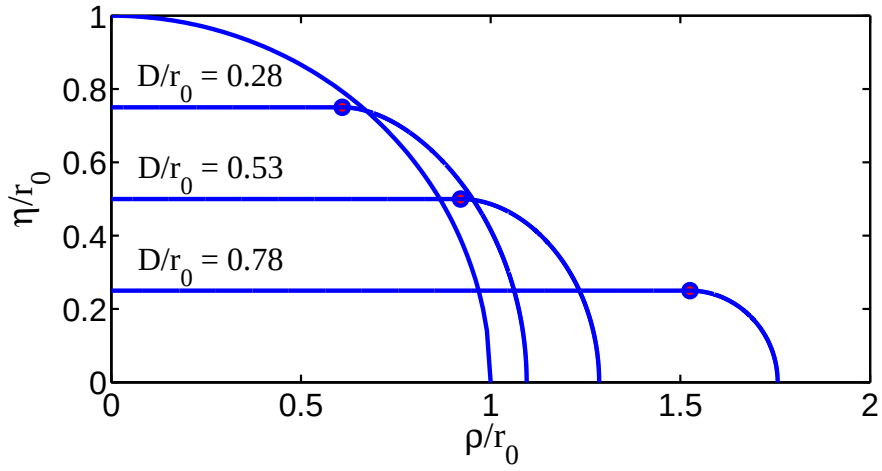

Figure 2.3: Profiles for a NLE membrane at different levels of displacement, with $\gamma = 0.1$. The heavy dot indicates the boundary of contact and non-contact regions.

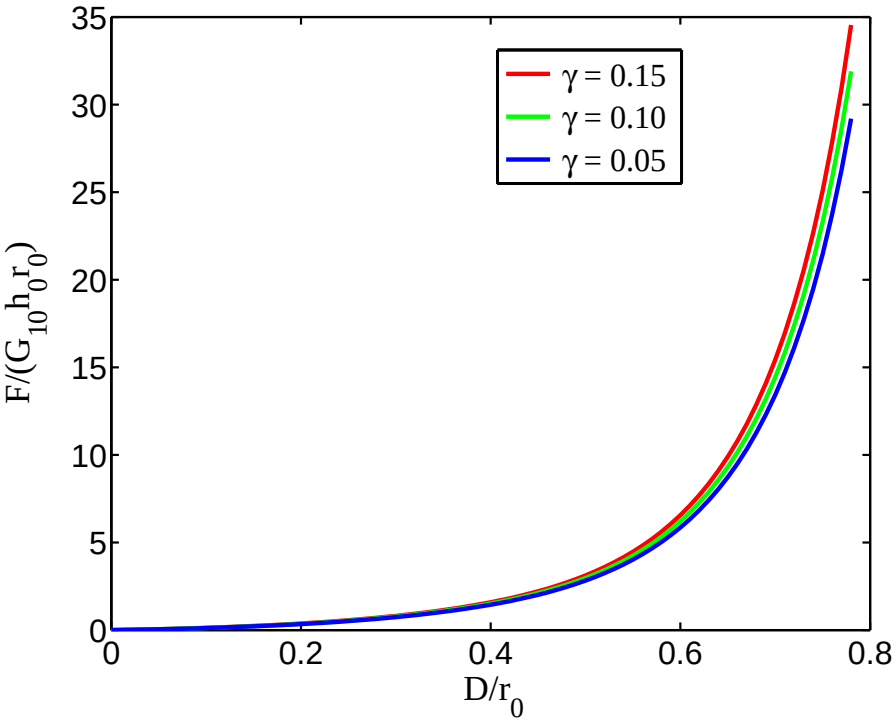

Figure 2.4: Force vs. displacement for a NLE membrane showing the influence of the Mooney-Rivlin parameter γ.

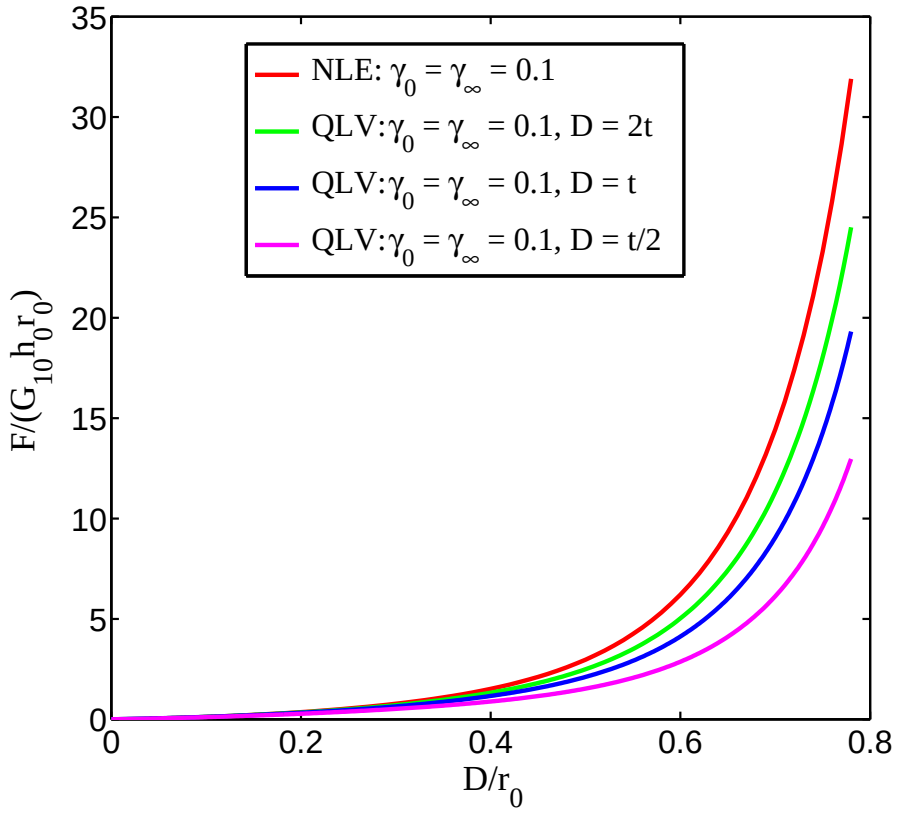

Figure 2.5: Comparison of force vs. indentation plots for a NLE membrane and a quasi-linear viscoelastic (QLV) membrane at various constant displacement rates.

The next set of figures explore the time-dependent response when each plate is subjected to a step displacement history, $D = D_0, t \geq 0$, where D_0 is a constant. Figure 2.6 shows the influence of the amount of displacement on the contact force relaxation when $G_2(t) = \beta G_1(t)$ (QLV) and when $G_2(t) \neq G_1(t)$ (NLV). The parameters are $g_1 = g_2 = 0.2, c = 1$ and $\gamma_0 = \gamma_\infty = 0.1$ for QLV and $g_1 = 0.2, g_3 = 0.3, c = 1/2$ and $\gamma_0 = 0.1, \gamma_\infty = 0.15$ for NLV. Results are shown for displacements of $D/r_0 = 0.53(H_1/r_0 = 0.5)$ and $D/r_0 = 0.78(H_1/r_0 = 0.25)$. When $D/r_0 = 0.53(H_1/r_0 = 0.5)$, there is very little difference between force relaxation for QLV and NLV. When $D/r_0 = 0.78(H_1/r_0 = 0.25)$, the force relaxation for QLV is slightly faster than that for NLV. When the displacement increases from $D/r_0 = 0.53$

to $D/r_0 = 0.78$, the force increases by a factor of 10, showing a significant stiffening of response. Figure 2.7 shows the influence of the ratio $c = \tau_1/\tau_2$ on the contact force relaxation at the displacement $D/r_0 = 0.78$. Calculations were carried out with $g_1 = g_2 = 0.2, \gamma_0 = 0.1$ and for $c = 1, 0.5, 2$. The response is QLV when $c = 1$. Stress relaxation for NLV is slightly faster or slower than that for QLV accordingly as $c = 2$ and $c = 0.5$. The dependence of contact force relaxation on the decrease of $G_2(t)$ relative to $G_1(t)$ is shown in Figure 2.8. When $D/r_0 = 0.78$, calculations were carried out with $\gamma_0 = 0.1$ and $c = 1$. QLV corresponds to $g_1 = g_2 = 0.2$. When $g_1 = 0.2$ and $g_2 = 0.1$, $G_2(t)$ decreases more than $G_1(t)$ and the contact force relaxes faster than for QLV. When $g_1 = 0.2$ and $g_2 = 0.3$, $G_2(t)$ decreases less than $G_1(t)$ and the contact force relaxes slower than for QLV.

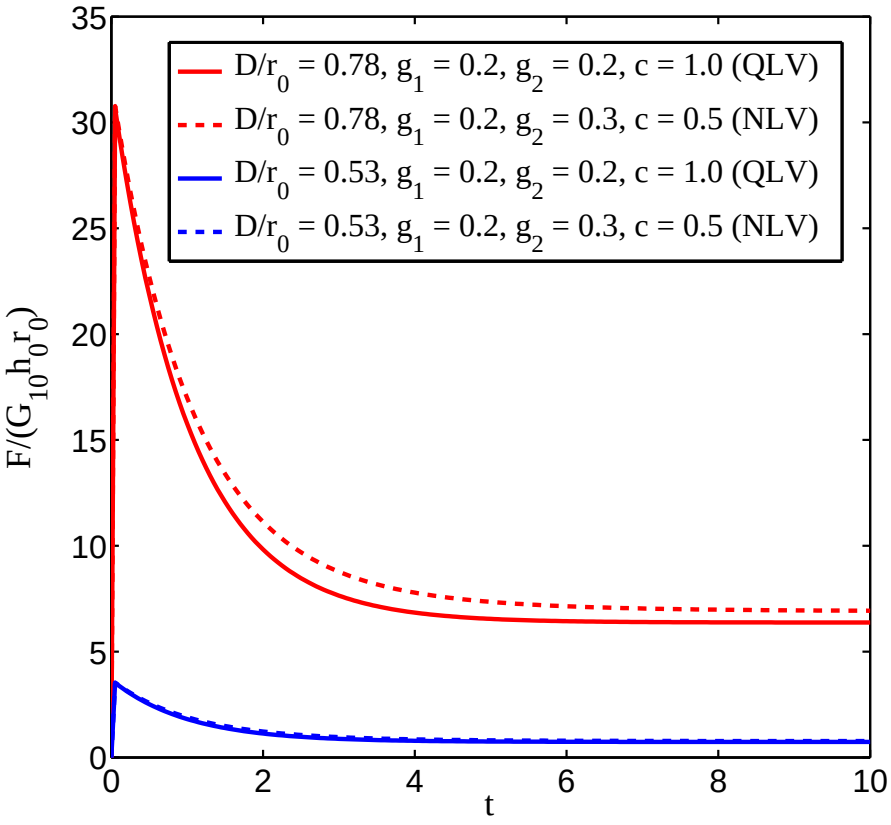

Figure 2.6: Contact force relaxation at two displacements for both the QLV and NLV cases.

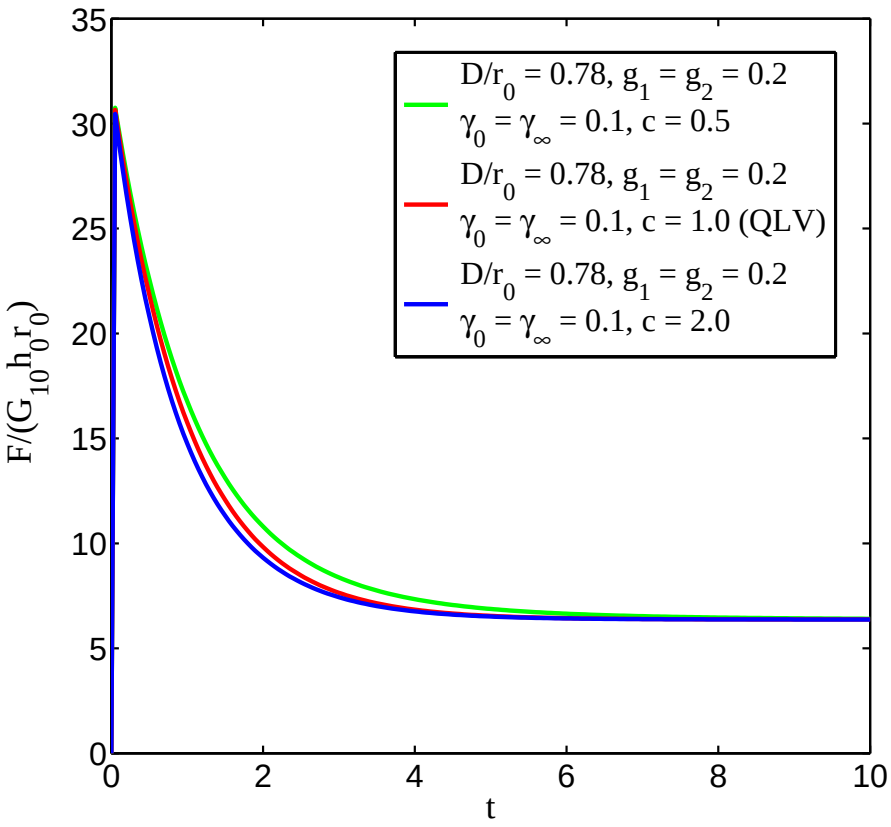

Figure 2.7: Contact force relaxation at displacement $D/r_0 = 0.78$ for both the QLV and NLV cases. $G_1(t)$ and $G_2(t)$ have different relaxation times for the case of NLV.

Figure 2.4 shows the non-dimensional force-displacement curve for a Mooney-Rivlin membrane for several values of the Mooney-Rivlin parameter γ. The instantaneous force $F(0)$ for $t = 0$ and the asymptotic force $F(\infty)$ for $t \to \infty$ correspond to Mooney-Rivlin parameters γ_0 and γ_∞, respectively. $F(0)$ and $F(\infty)$ can be determined from the non-dimensional force-displacement curve in Figure 2.4 by a discussion similar to that given in section 7 of *Nguyen et al.* (2013b). For a specified displacement D/r_0, let the curves corresponding to γ_0 and γ_∞ give the values $F/(C_1 h_0 r_0)|_{\gamma_0} = F_0^*$ and $F/(C_1 h_0 r_0)|_{\gamma_\infty} = F_\infty^*$. Then, $F(0) = G_{10} h_0 r_0 F_0^*$ and $F(\infty) = G_{1\infty} h_0 r_0 F_\infty^*$.

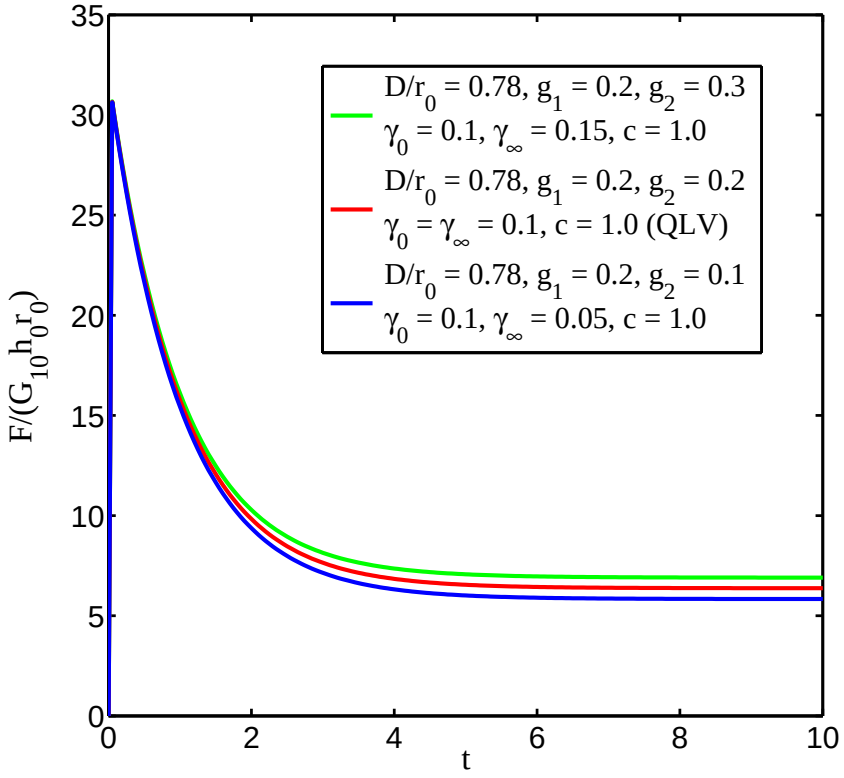

Figure 2.8: Contact force relaxation at displacement $D/r_0 = 0.78$ for both the QLV and NLV cases. $G_1(t)$ and $G_2(t)$ have different amounts of relaxation for the case of NLV.

The variation of contact position ψ_c with time is illustrated in Figure 2.9 for the case when $D/r_0 = 0.78$. The manner in which it varies has a complicated dependence on the material properties that can be accounted for by the following considerations. The instantaneous response at $t = 0$ is the same for all choices of material properties shown and corresponds to the Mooney-Rivlin parameter $\gamma_0 = 0.1$. The equilibrium state in the limit as $t \to \infty$ depends on γ_∞ which by (2.57) is determined by the ratio g_2/g_1. Figure 2.4 shows that the force-displacement response curves for the equilibrium states at $t = 0$ and as $t \to \infty$ depend on the Mooney-Rivlin parameter. Thus, even though the displacement may be fixed, force relaxation in combination with the change in this parameter leads to different states at $t = 0$ and as $t \to \infty$. For QLV, the states at $t = 0$ and as $t \to \infty$ are the same with $\gamma_0 = \gamma_\infty = 0.1$. It is

found that ψ_c does not vary with time. This is consistent with the result established in *Nguyen et al.* (2013b) that when the plates undergo a step displacement, then the deformation of the membrane does not vary with time. The states at $t = 0$ and as $t \to \infty$ are the same with $\gamma_0 = \gamma_\infty = 0.1$. On the other hand, when $g_1 = 0.2$ and $g_2 = 0.1$, then $\gamma_\infty = 0.05$ and when $g_1 = 0.2$ and $g_2 = 0.3$ then $\gamma_\infty = 0.15$. In these two cases, ψ_c, respectively, increases or decreases monotonically from its value in the instantaneous configuration at $t = 0$ to its value in the large time configuration as $t \to \infty$. Figure 2.9 also shows the case with $g_1 = g_2 = 0.2$, but $G_1(t) \neq G_2(t)$ because of different relaxation times. The states at $t = 0$ and as $t \to \infty$ are the same with $\gamma_0 = \gamma_\infty$. When $c = \tau_1/\tau_2 = 1/2$, ψ_c initially decreases with time because of the different relaxation processes and then increases to its original value. When $c = \tau_1/\tau_2 = 2$ the opposite behavior occurs.

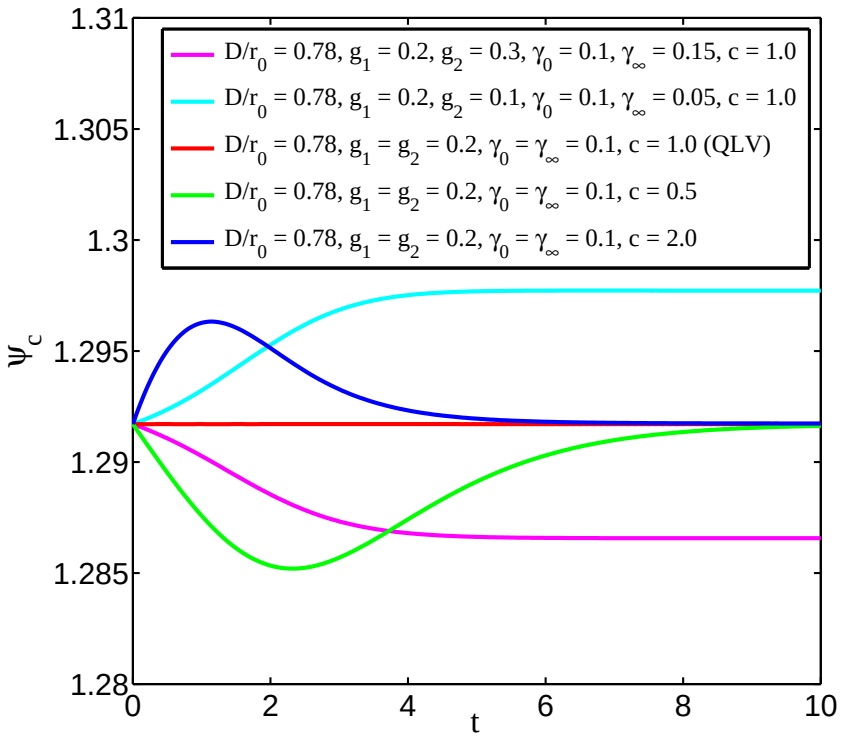

Figure 2.9: Variation of the contact position over time.

At a location inside the contact region $\psi = 0.25$, the behaviors of stresses and stretches of the spherical membrane at the step displacement $D/r_0 = 0.78$ are shown in Figure 2.10- 2.12. The influence of the ratio $c = \tau_1/\tau_2$ on the stretch ratio histories is shown in Figure 2.10. Calculations were carried out with $g_1 = g_2 = 0.2$, $\gamma_0 = \gamma_\infty = 0.1$ and for $c = 1, 0.5, 2$. When $c = 1$ the model reduces to QLV. The stretch ratios do not vary with time. When $c = 1/2$ both stretch ratios λ_1 and λ_2 increase then decrease to approach the long time value of QLV model. This behavior is reversed when $c = 2$.

Changing the amount of relaxation g_1 and g_2 also affects the behaviors of the stretch ratios $\lambda_1(t)$ and $\lambda_2(t)$ at $\psi = 0.25$ as shown in Figure 2.11. The stretch ratios increase and approach an asymptotic value when $g_1 < g_2$. On the other hand, when $g_1 > g_2$, they both decrease and approach smaller values. Figure 2.12 shows the principal stretches and stresses versus angle ψ at $t = 10$ for the displacement $D/r_0 = 0.78$ and material properties $g_1 = 0.2, g_2 = 0.3, c = 1$ and $\gamma_0 = 0.1$ (corresponding to $\gamma_\infty = 0.15$). As seen from Figure 2.11, these are essentially the distributions in the equilibrium state as $t \to \infty$. The distributions show substantial non-homogeneity, with λ_2 varying from about 1.1551 at the crown to 1.7564 at the edge. The big dot indicates the transition between the contact and non-contact regions. *Nadler* (2010) showed similar plots for a Neo-Hookean material. Here, calculations for the case of Neo-Hookean material ($\gamma = 0$) at a smaller displacement $D/r_0 = 0.309$ (not shown) agree with those in *Nadler* (2010). Both sets of calculations show that $\lambda_2 > \lambda_1$ and $\sigma_2 > \sigma_1$ for all ψ. Consider the radial line from the origin to the material particle at the transition point between the contact and non-contact regions. Its angle in the reference configuration is $\psi = \psi_c \simeq 73.7°$. In the current configuration at $t = 10$ it makes an angle of about 80.6°.

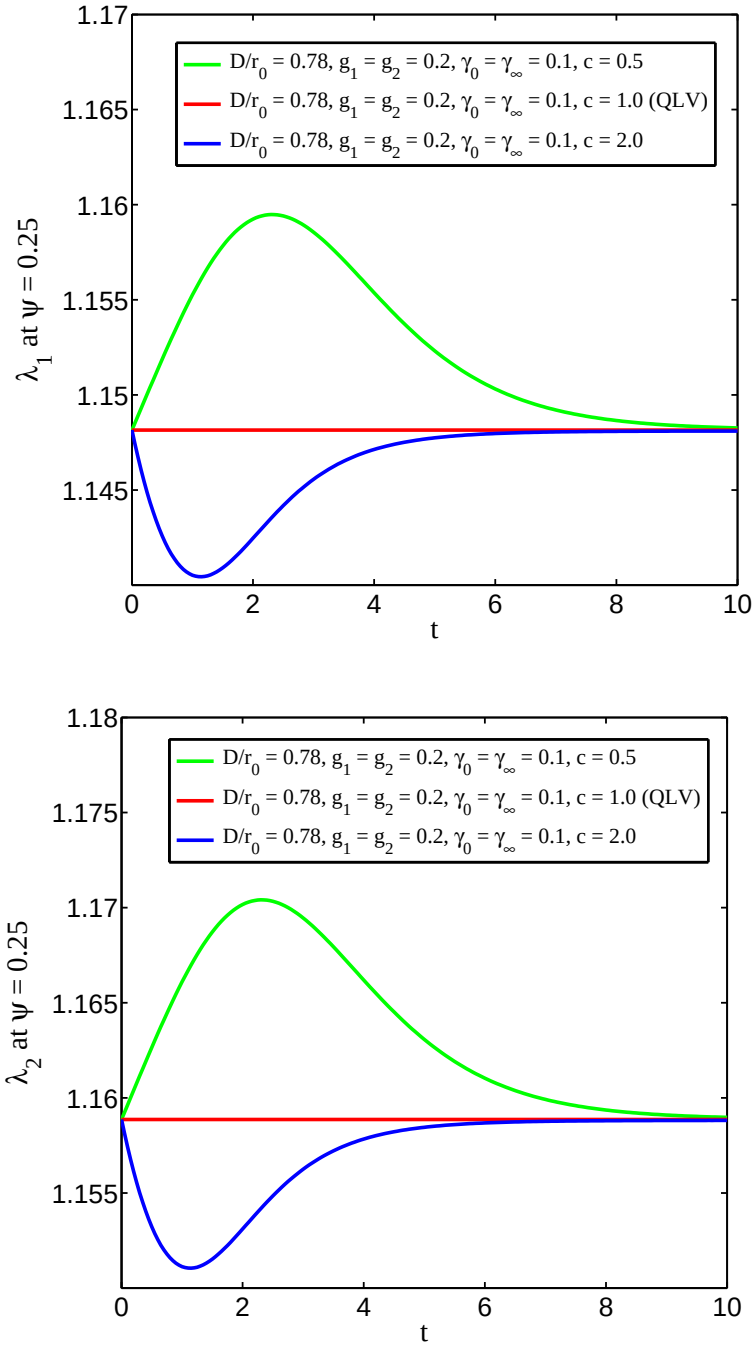

Figure 2.10: Influence of the relative relaxation times of $G_1(t)$ and $G_2(t)$ on the histories at $\psi = 0.25$ of stretches λ_1 and λ_2. This location is inside the contact region ($\psi_c = 1.2917$ for the case of QLV).

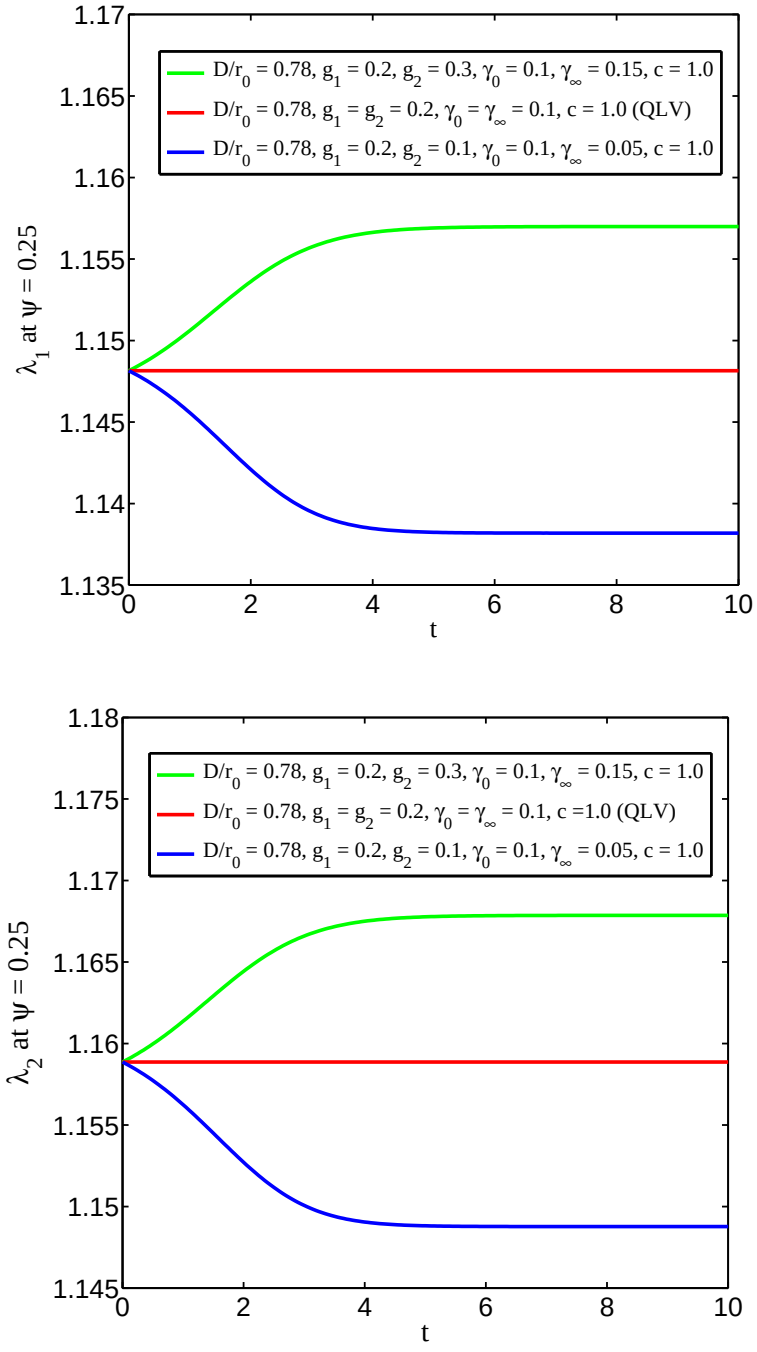

Figure 2.11: Influence of the amounts of relaxation of $G_1(t)$ and $G_2(t)$ on the histories at $\psi = 0.25$ of stretches λ_1 and λ_2. This location is inside the contact region ($\psi_c = 1.2917$ for the case of QLV).

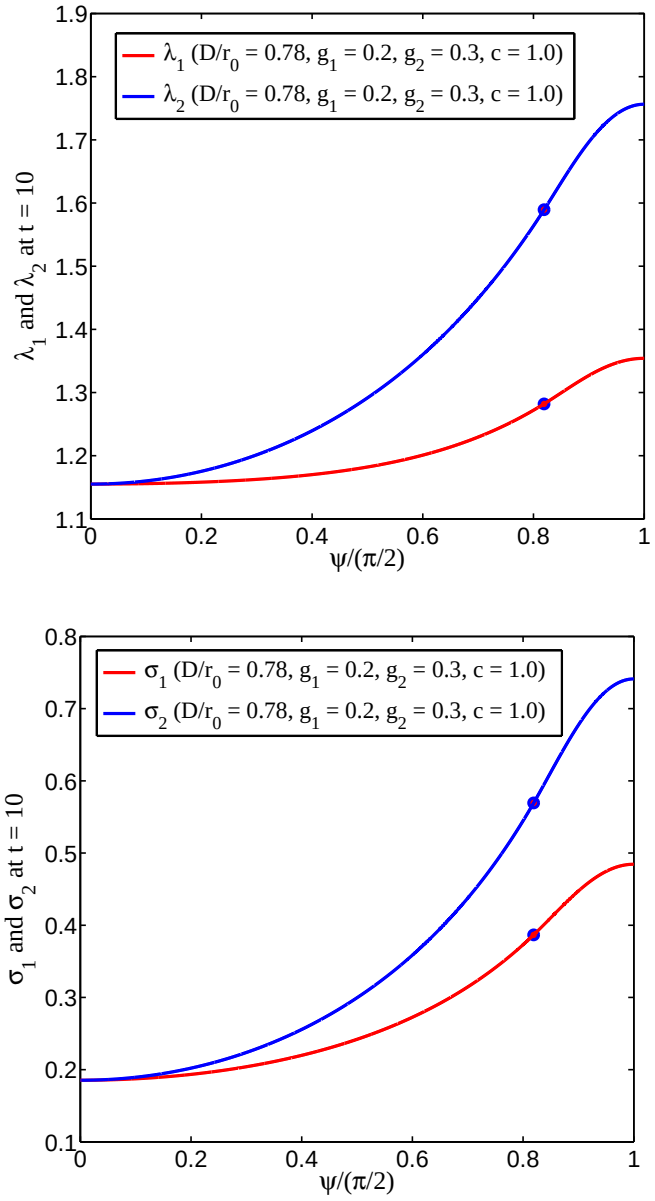

Figure 2.12: Stresses and stretches versus angle ψ in the reference configuration at time $t = 10$. Top figure: stretches λ_1, λ_2; bottom figure: stresses σ_1, σ_2. The heavy dot corresponds to the angle ψ_c at the boundary between the contact and non-contact regions.

In indentation experiments, piece-wise histories, loading and unloading, are normally performed. The initial unloading slope is usually related to the elastic properties using the Oliver-Pharr approach (*Olivera and Pharr*, 1992). Figure 2.13 and 2.14 present responses to tests with constant loading and unloading rates. The loading rate

is the same in all tests, $s_l = \dot{D}/r_0 = 1$. The maximum displacement is $D/r_0 = 0.28$ in Figure 2.13 and $D/r_0 = 0.78$ in Figure 2.14 (with the corresponding material properties $g_1 = 0.2, g_2 = 0.6, c = 1, \gamma_0 = 0.1, \gamma_\infty = 0.3$). Both figures show results for two different unloading rates: $s_u = \dot{D}/r_0 = 1$ and $s_u = \dot{D}/r_0 = 1/5$. These rates and the initial unloading slopes of the force displacement plots are listed in Table 2.1. For clarity, only results for the cases of non-linear elasticity and non-linear viscoelasticity are plotted, however, the initial slope of the QLV response is also included in Table 1 for comparison. As can be seen, the initial unloading slope shows a lot of variation depending on the rate of unloading as well as amount of deformation. The variation is due to the effect of both viscoelasticity and nonlinearity of the material properties. Hence, it is misleading to relate this initial unloading slope to elastic behavior.

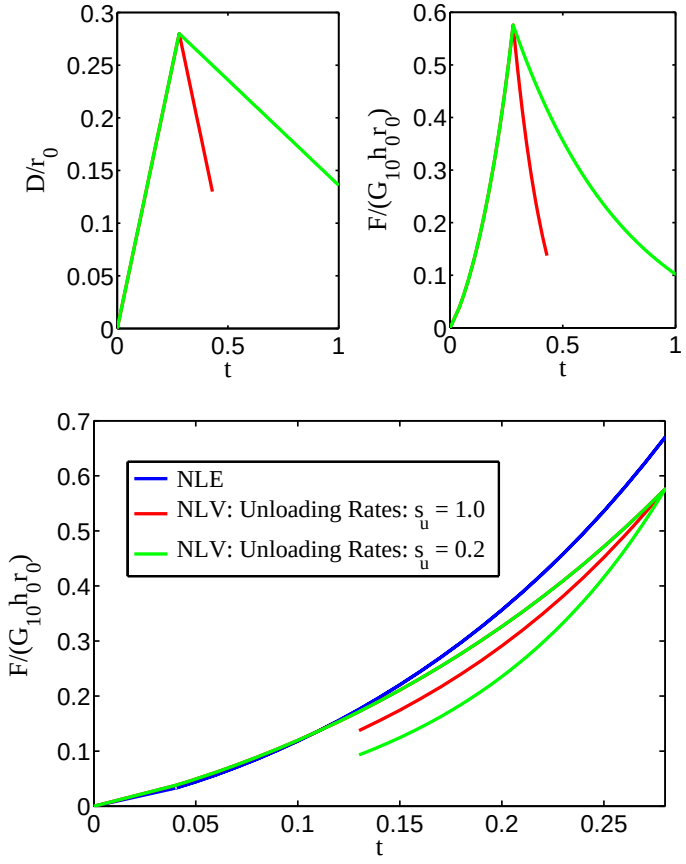

Figure 2.13: Loading and unloading behaviors for NLE and NLV membranes with $D/r_0 = 0.28, g_1 = 0.2, g_2 = 0.6, c = 1/2, \gamma_0 = 0.1, \gamma_\infty = 0.3$.

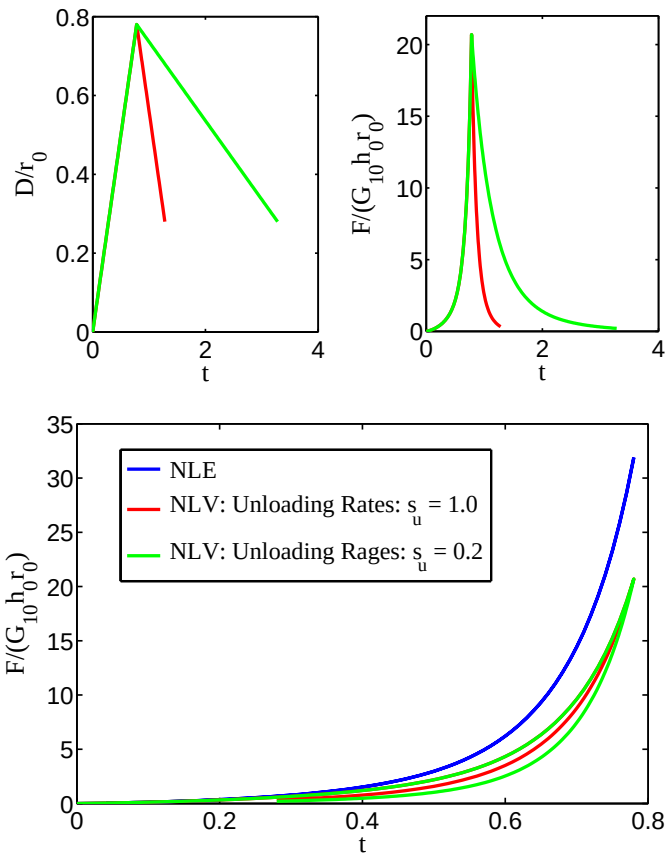

Figure 2.14: Loading and unloading behaviors for NLE and NLV membranes with $D/r_0 = 0.78, g_1 = 0.2, g_2 = 0.6, c = 1/2, \gamma_0 = 0.1, \gamma_\infty = 0.3$.

D/r_0	Unloading rate	Initial unloading slope for NLE	Initial unloading slope for QLV	Initial unloading slope for NLV
$D/r_0 = 0.28$	$s_u = \dot{D}/r_0 = 1$	4.7	4.6	4.5
	$s_u = \dot{D}/r_0 = 1/5$		6	6
$D/r_0 = 0.78$	$s_u = \dot{D}/r_0 = 1$	324.5	257	241
	$s_u = \dot{D}/r_0 = 1/5$		297	287.5

Table 2.1: Comparisons of the initial unloading slopes for different amounts of displacements and unloading rates for three cases: NLE, QLV, and NLV

2.5.2 FE Formulation Solution

Comparisons between FE models and the analytical formulation were also carried out. Figure 2.15 shows profile and perspective views of the deformed spherical

membrane at time $t = 10$ at two displacements, left figure: $D/r_0 = 0.28$, right figure $D/r_0 = 0.53$ with the corresponding material properties $g_1 = g_2 = 0.2, c = 1, \gamma_0 = \gamma_\infty = 0.1$. At a fixed time, the maximum principal stress is lowest at the crown and largest at the edge (around the biggest horizontal circumference of the membrane). These results are consistent with those of *Nadler* (2010) in the case of an elastic membrane. He showed that the principal stresses at the crown are very small and could become negative, indicating wrinkling. This is avoided by the small initial inflation from r_0 to r_s.

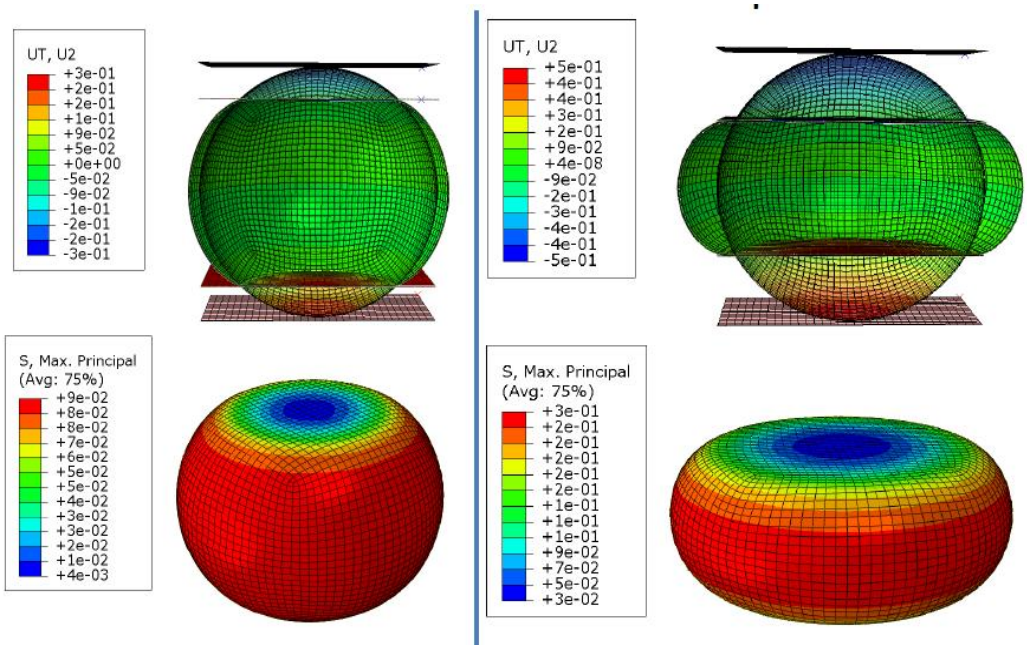

Figure 2.15: Profile and perspective views of the deformed membrane at two displacements from the FE model. Left figure: $D/r_0 = 0.28$, right figure: $D/r_0 = 0.53$ with the corresponding material properties: $g_1 = g_2 = 0.2, c = 1, \gamma_0 = \gamma_\infty = 0.1$ at time $t = 10$.

Figure 2.16 shows the relaxation of the stresses at the crown and the edge with $D/r_0 = 0.28, g_1 = g_2 = 0.2, c = 1, \gamma_0 = \gamma_\infty = 0.1$. The stresses remain positive for all times thereby showing that the membrane will not wrinkle. Figure 2.16 also compares σ_2 versus t as determined from the analytical formulation and from the FE formulation using ABAQUS. The comparison shows good agreement with the

analytical approach which is also based on membrane theory (the maximum difference $\frac{|\sigma_{FE}-\sigma_{Analytical}|}{(\sigma_{FE}+\sigma_{Analytical})/2} < 0.2\%$ at each time instant).

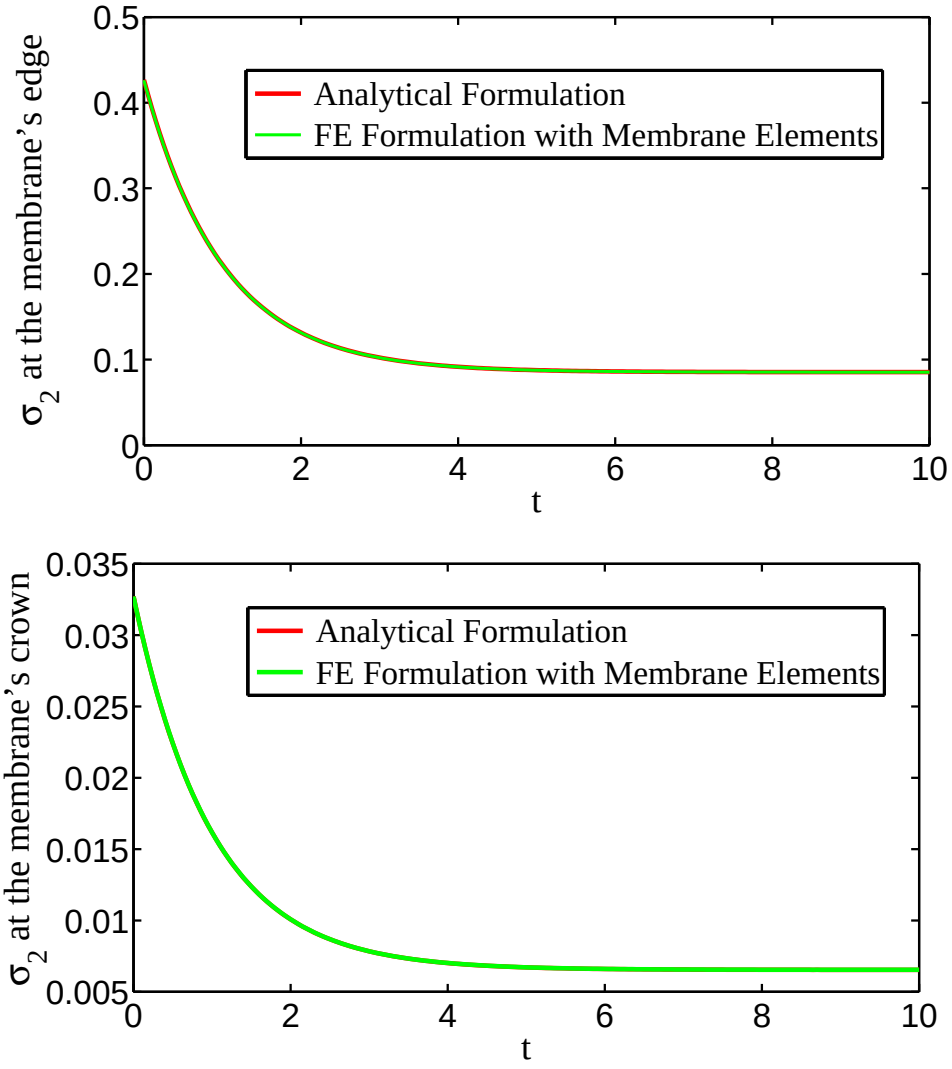

Figure 2.16: Comparison of the principal stresses versus time t at the crown and the edge of the spherical membrane, $D/r_0 = 0.28, g_1 = g_2 = 0.2, c = 1, \gamma_0 = \gamma_\infty = 0.1$.

2.6 Concluding Comments

This chapter considered the mechanics of a NLV closed membrane that contains a fluid and is squeezed between two rigid, smooth, parallel plates. The membrane

material is modeled by the Pipkin-Rogers single integral constitutive equation for non-linear viscoelasticity. This choice was made for several reasons. It incorporates many essential features of non-linear viscoelasticity, and is a straightforward extension of non-linear elasticity. Additionally, it includes QLV (*Fung*, 1981) as a special case.

The governing equations are solved by reducing the system of equations to a three-point boundary value problem with a contact region and a non-contact region separated by a time-dependent boundary. A system of non-linear partial differential Volterra integral equations associated with each region was studied. A numerical method is presented that marches forward in time. At each time, the boundary value problem reduces to one equivalent for a NLE material. A FE model of the problem using membrane elements is also included. Material properties are chosen such that the problem reduces to one for Mooney-Rivlin materials at $t = 0$ and in the limit as $t \to \infty$. Two plate displacement histories are investigated: constant rate and step loading histories. Force-displacement plots demonstrate the importance of the characteristic time for displacement relative to the characteristic relaxation time of the material. The results for step displacements show the effects of different elastic responses at $t = 0$ and in the limit as $t \to \infty$, as well as the time-dependent transition. Results for the elastic responses at $t = 0$ and in the limit as $t \to \infty$ are in qualitative agreement with corresponding results obtained in other work for a neo-Hookean nonlinearly elastic spherical membrane enclosing a fluid. The time-dependent transition is studied for different step plate displacements, as well as the influence of different material properties. A particular choice of material properties shows response in the special case of QLV. When the material is modeled by QLV, the results show that the deformation does not vary with time. Thus, in an experiment, time dependence of the deformation indicates that the material should not be modeled using QLV. A good agreement between the results obtained by direct numerical solution of the system of partial differential Volterra integral equations and the use of the commer-

cial code ABAQUS with membrane elements leads to a promising approach to tackle asymmetric contact problems.

The constitutive theory used here is fully characterized when the scalar coefficients $\alpha_1, \alpha_2, \alpha_3$ are known. For the numerical examples presented here, these are expressed in terms of the relaxation properties $G_1(t), G_2(t)$ and Φ as defined in (2.54). The simplest form for the relaxation properties corresponds to the three parameter solid shown in (2.56). Thus, seven scalar parameters are required to specify the constitutive equation used here, namely, $G_{10}, G_{1\infty}, \tau_1, G_{20}, G_{2\infty}, \tau_2$ and α. If, as experimental data suggests, the material can be modeled as QLV, then the number of scalar parameters reduces to four. The identification of these parameters using AFM is still a formidable problem. It appears likely that data from a single experimental configuration may not be sufficient to determine all the scalar parameters. A more extensive experimental program that includes tests conducted at different rates of loading and different applied forces may be necessary. In order to extract the scalar parameters from this extensive experimental configuration, one approache is to use an inverse analysis to fit the experimental data. However, the standard inverse analysis, which utilizing the sequential iteration process, is inefficient, due to expensive evaluations of the errors between the experimental data and simulations. Hence, an inverse technique that can overcome this limitation is necessary for the extraction of material properties. Surrogate modeling is a valuable tool for developing such a technique, as will be the focus of the next chapter.

CHAPTER III

Surrogate Model Based on Kriging and Inverse Problem

3.1 Iterative Inverse Analysis

The study of forward problems, as discussed in Chapter II, is a precursor to a harder and more challenging task, which is solving inverse problems for determining the NLV properties. Figure 3.1 shows the inverse scheme that is usually employed for extracting the optimized set of material parameters from the experimental data. The scheme involves the selection of an appropriate experimental setup to probe the mechanical properties. For polymeric synthetic capsules and biological cells, several techniques can be employed, as mentioned in Chapter I. The force-displacement-time response of a displacement control test is often utilized in the characterization process. The test process is then modeled using the FE method, in which the force-displacement-time response associated with an assumed set of NLV parameters is predicted. A cost function is constructed by computing the root mean square error (RMSE) between the experimental data and the FE prediction. The cost function at the assumed set of material parameters is compared with a tolerance value. If the cost function value is less than the tolerance, the assumed set is considered to be the optimized set. If this criterion is not met, the FE model and the cost function are

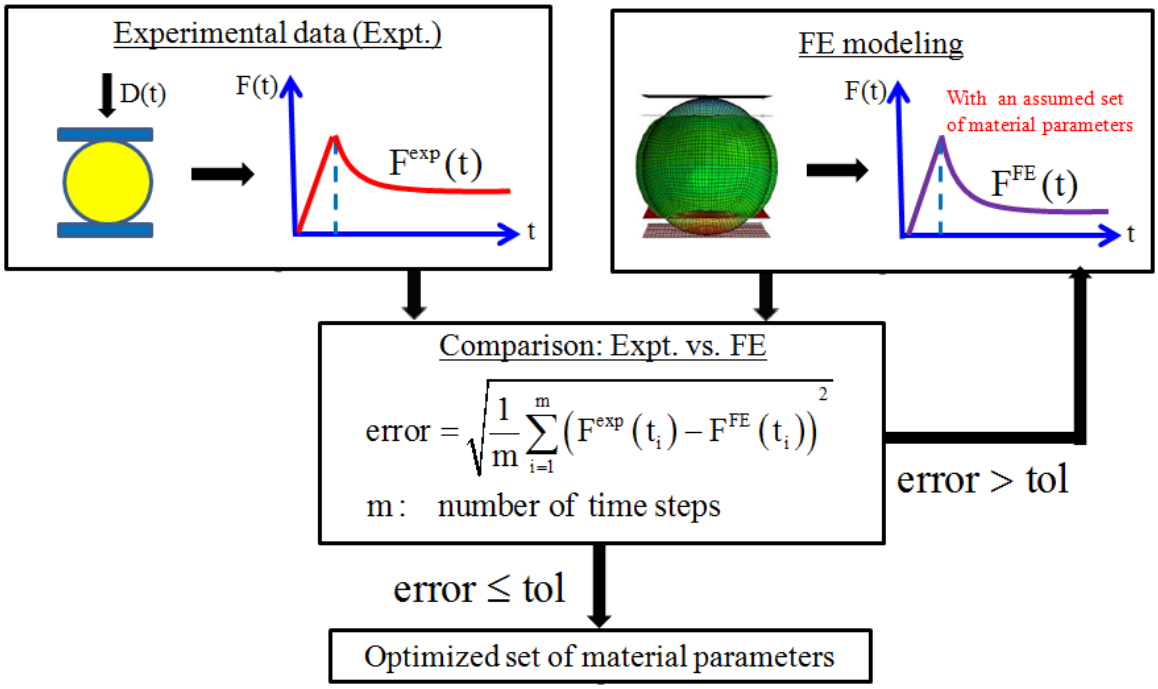

Figure 3.1: Iterative inverse technique for solving inverse problem.

re-evaluated at a different set of material parameters. This iterative inverse technique was employed in the literature (*Bernick et al.*, 2011; *Prevost et al.*, 2011). For example, an iteration number of about 500 was reported in the work by *Prevost et al.* (2011). However, this repeated process of FE simulations and cost function evaluations is associated with a computational cost issue (*Ladjal et al.*, 2009), which makes it difficult to analyze large amounts of experimental data and to use a complex FE model. In addition, the number of unknown material parameters needed to identify the experimental responses increases the difficulty of the problem. To overcome these issues, an inverse analysis approach based on establishing a meta model and a Kriging estimator (*Sacks et al.*, 1989; *Jones et al.*, 1998; *Lophaven et al.*, 2002; *Queipo et al.*, 2005; *Forrester et al.*, 2008; *Gustafson and Waas*, 2009; *Heinrich and Waas*, 2009) is utilized. The purpose is to replace the FE simulation by a functional relationship that can be evaluated quickly. An overview of this approach is presented in the following section.

3.2 Overview of Meta Model and Kriging Estimator

Figure 3.2 describes the inverse technique based on a surrogate model with a Kriging predictor.

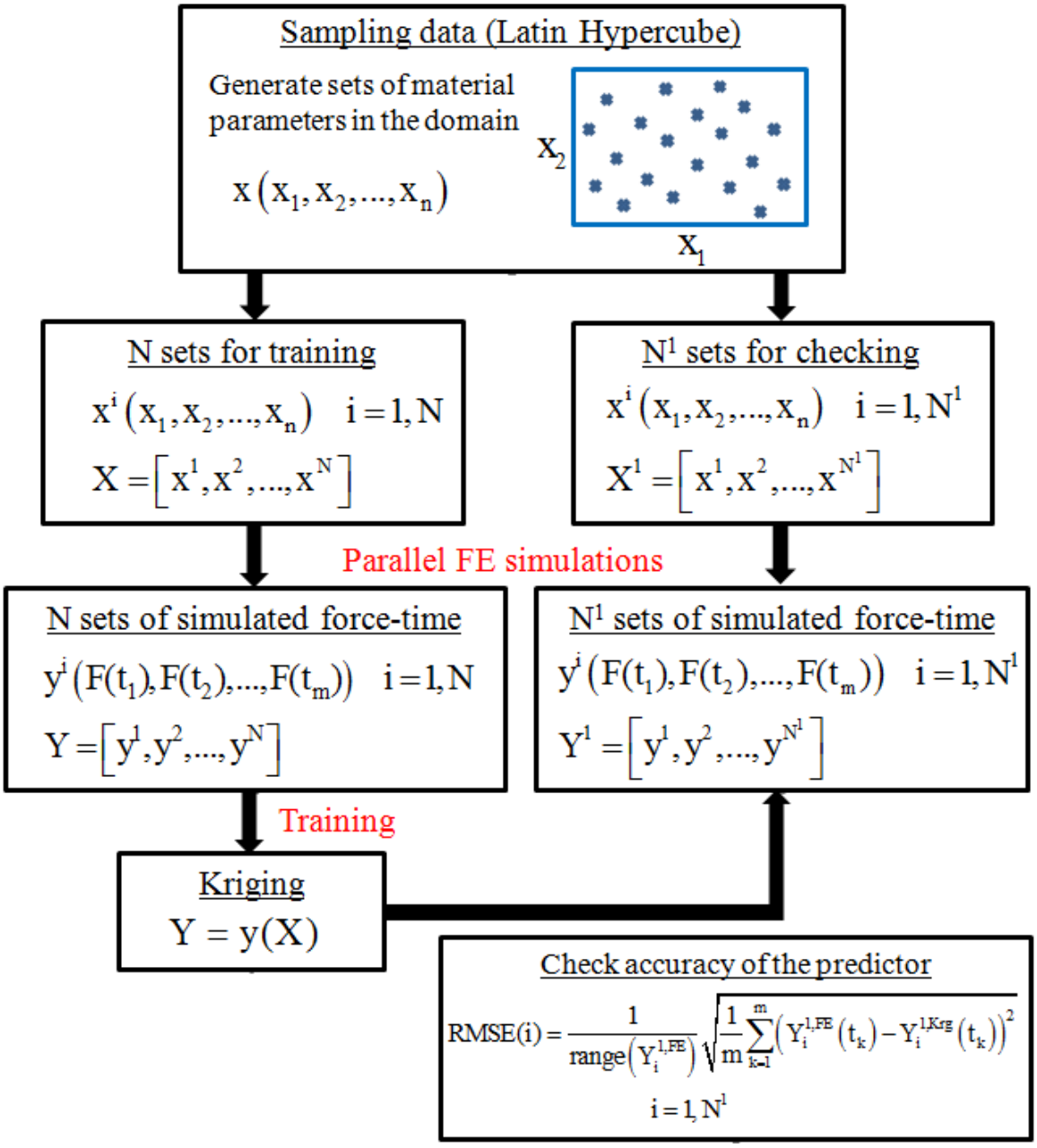

Figure 3.2: Surrogate model based on Kriging technique for solving an inverse problem.

A meta model is built by evaluating computationally intensive FE simulations at sets of selected training points and at sets of selected checking points. Here, a set of training points or a set of checking points is a combination of material parameters generated based on an appropriate sampling technique. Though this step might be costly initially, the FE evaluations can be done in parallel to reduce the total computation time. Additionally, the optimization process utilizing this meta model is much faster than the one performed on the actual model. The selected training points and checking points are obtained by the Latin Hypercube sampling algorithm. Optimal Latin Hypercube sampling algorithm can also be used owing to its capability to create a more uniformly distributed grid over the domain of the material parameters (*Queipo et al.*, 2005; *Forrester et al.*, 2008). This inverse approach has been used successfully in prior studies (*Gustafson and Waas*, 2009; *Heinrich and Waas*, 2009). The process is summarized as follows:

Let N denote the number of sets of training points. $X = [x^1, ..., x^N]$ represents the design site over the design domain, D: $x^i \in D \subset \mathbb{R}^n$, $i = \overline{1, N}$ where n is the number of material parameters in each set, $\mathbb{R}^n$ is a real space of n dimensions, and the design domain D is a subset of this n-dimension space. $Y = [y^1, ..., y^N]$ represents the corresponding responses from FE simulations: $y^i \in \mathbb{R}^m$, $i = \overline{1, N}$ where m is the number of time steps in each force-time response and $\mathbb{R}^m$ is a real space of m dimensions. A meta model is composed of X and Y.

A separate N^1 sets of checking points are also generated to check the accuracy of the technique. Let $X^1 = [x^1, ..., x^{N^1}]$ denote the generated sets over the design domain, D: $x^i \in D \subset \mathbb{R}^n$, $i = \overline{1, N^1}$ and $Y^1 = [y^1, ..., y^{N^1}]$ are the corresponding responses from FE simulations: $y^i \in \mathbb{R}^m$, $i = \overline{1, N^1}$.

Once a meta model is constructed, surrogate modeling based on a Kriging estimator is applied to predict a functional relationship between the design site X and the response site Y, as illustrated in Figure 3.3. This relationship is used to capture the

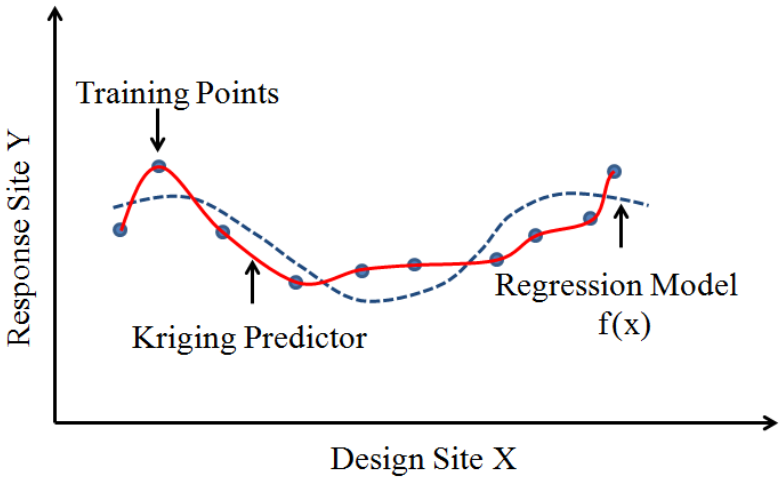

Figure 3.3: Kriging Predictor.

underlying FE simulations at the untried points in the design domain D. To serve this purpose, a fundamental assumption is employed in Kriging, which assumes that errors are correlated (*Sacks et al.*, 1989; *Jones et al.*, 1998; *Lophaven et al.*, 2002; *Forrester et al.*, 2008). In other words, the errors of two "close points" are "close". This assumption is reasonable when the problem involves no sources of random errors. Thus, in the case of deterministic computer simulations as are considered here, it is appropriate to assume that error terms are correlated. With this assumption, Kriging constructs a mapping y(x) from the design site X to the response site Y using the following form:

$$y(x) = f(\beta, x) + Z(x), \tag{3.1}$$

where $x \in D \subset \mathbb{R}^n$ is an n-dimensional input in the domain D of the design site. The first function $f(\beta, x)$ is a regression model represented as a linear combination of p chosen functions $f_i : \mathbb{R}^n \to \mathbb{R}^m$, $i = \overline{1, p}$ as follows:

$$f(\beta, x) = \beta_1 f_1(x) + ... + \beta_p f_p(x) = f(x)^T \beta, \tag{3.2}$$

where β is a vector of regression coefficients. The second function $Z(x)$ is a stochastic

(random) process. Its mean is assumed to be zero, and its variance is denoted as σ^2. The representation in (3.1) can be interpreted as the combination of a global approximation for $y(x)$ through the use of the regression model $f(\beta, x)$ and local deviations captured by the stochastic process $Z(x)$. The covariance of this stochastic process is related to the correlation between two points:

$$Cov[Z(x^{(i)}), Z(x^{(j)})] = \sigma^2 R_{krg}(\theta, x^{(i)}, x^{(j)}), \tag{3.3}$$

where R_{krg} is a correlation function and θ are correlation parameters.

The algorithm for the Kriging predictor has been implemented in the MATLAB DACE toolbox (*Lophaven et al.*, 2002) and is employed in this study. This toolbox contains several options for the regression model $f(\beta, x)$ in the forms of polynomial functions of orders 0, 1, 2. It also provides several choices for correlation models. With a selected polynomial regression function and a correlation model, the regression coefficients β and the correlation parameters θ for constructing the Kriging predictor are determined using the training group (X,Y). Prior to applying this predictor to predict the response at untrained points, its accuracy is verified using the checking group (X^1,Y^1). Recall that X^1 has N^1 sets of checking points generated independently of the sets of training points in X, which are used to construct a meta model and a Kriging predictor, whereas Y^1 has N^1 corresponding force-time responses obtained from actual FE simulations. The accuracy of the predictor is determined by comparing these actual FE responses with the responses predicted using the constructed Kriging predictor. In this thesis, the RMSE values will be computed and used to evaluate the performance of the Kriging estimator in capturing the FE simulations. If the errors are small enough, this Kriging predictor will be employed to replace the costly FE simulations in the inverse scheme. With a sufficiently large number of training points to start with, one-shot Kriging predictors (shown in following chapters) are

sufficient to predict the responses in FE simulations within the material domain, for the examples studied in this thesis.

3.3 Application to Inverse Problem

The inverse problem for extracting the NLV properties from experimental data using various testing scenarios can be solved automatically and efficiently with the presented inverse analysis methodology. This method can be combined with many constitutive models and overcomes the issues resulting from the sequential inverse approach (section 3.1), which is lengthy and impractical, requiring iterative evaluations of costly FE modeling. It also allows for efficient analysis of large amounts of data, which is necessary in testing samples with large variations, such as biological cells. Two inverse problems are selected to illustrate the efficiency of the method. The first focuses on analyzing experimental data from the compression of a fluid-filled capsule. The second studies the AFM indentation problem on biological cells. Details of the experimental setups, FE models, and inverse processes are presented in Chapter IV and Chapter V.

In addition to the above application in solving inverse problems, which is the focus of this thesis, the following additional aspects of surrogate modeling and Kriging predictor are also worth to be noted.

- As discussed in the work by *Gustafson and Waas* (2009), Kriging predictor can be used to investigate the sensitivity of input parameters. Specifically, the regression coefficients β were employed to analyze and compare how sensitive each input variable is with respect to the model output. Such a study can also be incorporated in order to examine the role of each NLV parameter considered in this thesis. The sensitivity of each material parameter is expected to be useful for narrowing and lowering the range and the dimension of the design domain. This can further reduce the computational cost of the inverse process.

- Additionally, in this thesis, the domain was chosen sufficiently large to encompass the sets of material parameters that correspond to the experimental responses. A Kriging predictor is constructed within this design domain and is applied to predict the response at an arbitrary set of material parameters, which also lies within this domain. Such a prediction is considered as an interpolation. A question remains is the effectiveness of the constructed Kriging predictor in predicting the responses at sets of material parameters that lie outside this domain. It might be interesting to investigate this extrapolation capacity of the constructed Kriging predictor. One approach is to generate checking groups that contains sets of checking points lying outside the design domain. Comparisons between the actual FE simulations and Kriging predictions for these checking sets then can be utilized to determine whether or to which extent the Kriging predictor is effective for extrapolating purposes. Understanding this aspect might provide insight to address the cases when the selected design domain does not include the sets of material parameters that yield the responses measured in experiments.

- Another question is related to the determination of the range of the design domain. In this thesis, the upper and lower bounds (range) of the design domain were still selected mainly based on trial and guessing. Specifically, the inverse problem was solved with an assumed design domain, which might be small initially. Based on the obtained sets of material parameters and comparisons of their corresponding FE responses with the experimental data, the domain was then manually adjusted and expanded until it was sufficiently large to encompass the sets of material parameters that correspond to the experimental responses. This manual process might be enhanced by incorporating the sensitivity study and the knowledge of extrapolation capacity of the Kriging predictor.

- For the two problems discussed in Chapter IV and Chapter V, the options in the MATLAB Dace toolbox for the polynomial regression function of either second (reg-

poly2) or first order (regpoly1) and the general exponential (correxpg) correlation model were utilized. These options were chosen as the RMSE values evaluated for the checking sets corresponding to the use of these options were sufficiently small.

CHAPTER IV

Compression of Fluid-Filled Polymeric Capsules and Inverse Analysis to Determine Non-Linear Viscoelastic Properties

4.1 Introduction

This chapter considers an experiment in which commercially available soft gel capsules filled with a fluid are compressed between two flat, relatively rigid, parallel plates. The bottom plate is stationary while the displacement of the top plate is controlled. The bottom plate is a transparent prism through which the contact area can be monitored by means of an optical arrangement. The reaction force on the capsule is recorded and the force-displacement-time data is used in an inverse analysis to determine the capsule wall material properties. This inverse analysis uses a surrogate model based on a Kriging estimator (*Sacks et al.*, 1989; *Lophaven et al.*, 2002). It is based upon optimizing the error between simulated force-displacement-time responses obtained from a FE model of the experiment and the experimental data. Since the capsule is subjected to large relative displacement of the top plate with respect to the stationary plate, material and geometric nonlinearity are incorporated into the FE model. Furthermore, as observed from experiments, the capsule material exhibits time-dependent characteristics. Therefore, in this study, a NLV constitutive relation

for modeling the capsule material is used. The enclosed fluid is assumed to be incompressible, nonviscous, and in a steady state. Combining FE modeling and a Kriging estimator will allow for automatic identification of the NLV properties of a capsule wall from a general 3D compression test.

The remainder of this chapter is composed of three sections. Section 4.2 includes details of the compression experiment and the optical arrangement for obtaining the reaction force-displacement-time as well as contact area outputs. The FE model and measurements of the geometrical dimensions and wall thickness are described in section 4.3. The constitutive relation for the capsule material is also discussed in this section. An inverse technique utilizing a surrogate model with a Kriging predictor is applied to the measured data and the results are shown in section 4.4. The use of contact area measurements is also presented together with a discussion of many phenomena such as the buckling of the capsule wall. The conclusions and suggestions for further studies are included in this section as well.

4.2 Details of Experiment

Commercially available polymeric capsules (Brand name: Natural Vitamin D3 400 IU 100 Softgels), which are fish liver oil, soft gel capsules made of bovine gelatin and enclosing a fluid, were compressed between two flat, rigid, parallel plates using an Instron testing machine. Displacement control tests were conducted by specifying the displacement of the top plate while the bottom one remained stationary. Two types of input were used: ramp-hold (RH) or relaxation, and ramp-reverse (RR) or hysteresis, each consisting of two steps. For the RH (relaxation) test, the top plate moved down at a rate of 5 mm/s to a specified value. After reaching that value, the applied displacement of the top plate was held constant to study the relaxation behavior of the polymeric capsules. For the RR (hysteresis) test, the plate moved down at a slower rate of 0.2 mm/s to acquire the loading path. Upon reaching a specified

value, the plate moved upward at the same rate; this corresponded to the unloading stage. The time variation of the capsule's reaction force during the loading, holding, and unloading stages was measured through a load cell attached to the top plate. A clear cube beam splitter (Edmund Optics) was used as the bottom plate in order to record the contact area between the capsule and the bottom plate. This beam splitter reflects the horizontal contact area onto a vertical, planar image. Contact area images (after reflection through the beam splitter) while the capsule is in RH (relaxation) as well as RR (hysteresis) tests are captured through an optical arrangement using a high speed camera (Grasshopper camera with 15 frames/second). The specified value for the displacement is chosen such that the capsule undergoes large deformation. The values employed in this study are $d = 1.0\ mm$ and $d = 1.5\ mm$. Significant changes in the contact curvature were observed, which gives rise to the nonlinearity in the geometry of the problem. A typical experimental setup is shown in Figure 4.1. The left figure shows an undeformed capsule, while the right is an illustration of the deformed state and exhibits a change in curvature within the contact region.

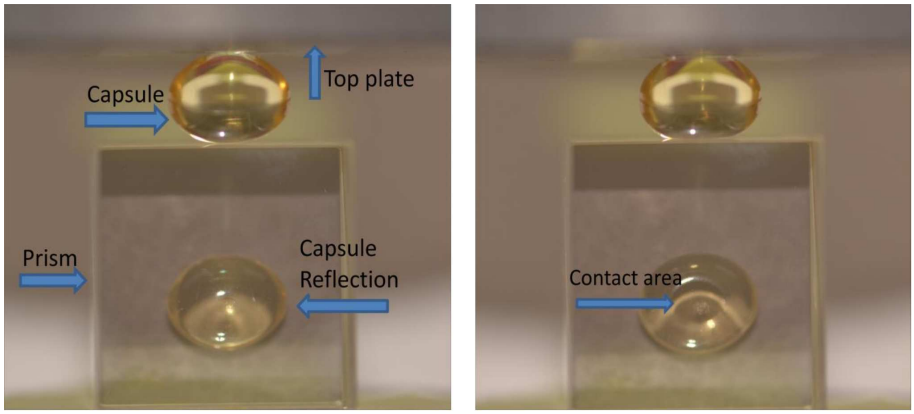

Figure 1a: An undeformed state of the capsule

Figure 1b: A deformed state of the capsule with contact area image

Figure 4.1: Compression experiment setup

Using this setup and the optical arrangement, contact area and force-time data are acquired simultaneously. The applied displacement input, typical contact area image, and force-time data for four compression inputs are shown in the following four

figures. Figure 4.2 contains the data for the RH (relaxation) tests with a specified displacement of $d = 1.5\ mm$, while the data for RR (hysteresis) tests with the same specified displacement input is shown in Figure 4.3. The data for RH (relaxation) and RR (hysteresis) tests with a specified displacement of $d = 1.0\ mm$ are presented in Figure 4.4 and Figure 4.5, respectively. Comparisons between these tests allow the investigation of the effect of the amount of deformation as well as that of the rate of loading.

The contact area edge is observed to be close to an elliptical shape and increases with increasing deformation during the loading part. The force-time data shows the typical relaxation behavior of the polymeric capsule. General consistency was obeyed when comparing the experimental data from these four tests. At a higher value of the displacement, the maximum reaction force is higher. At the same value of displacement, the peak value of the RR (hysteresis) test is smaller than the corresponding value of the RH (relaxation) test, since the former's (RR) rate of loading is much slower, hence the material has more time to relax.

4.3 FE Modeling

The compression experiment with RR (hysteresis) and RH (relaxation) inputs is simulated by FE analysis using the commercial software ABAQUS-6.10 (*ABAQUS-v6.10*, 2010). To obtain information about the geometry, each capsule is sliced into two halves. Each half is put on the prism such that the planar, horizontal image of the cross section is reflected onto a vertical plane and is captured by the Grasshopper camera. Figure 4.6 shows typical images of two cross sections: one is along the longitudinal axis of the capsule and the other is along the shorter axis. Using the averaged dimensions and thicknesses of 20 samples, the polymeric capsule is modeled as a deformable ellipsoidal shell with a major axis dimension of $2a = 9.96\ mm$ and a minor axis dimension of $2b = 2c = 6.51\ mm$. The variations in the capsule shell

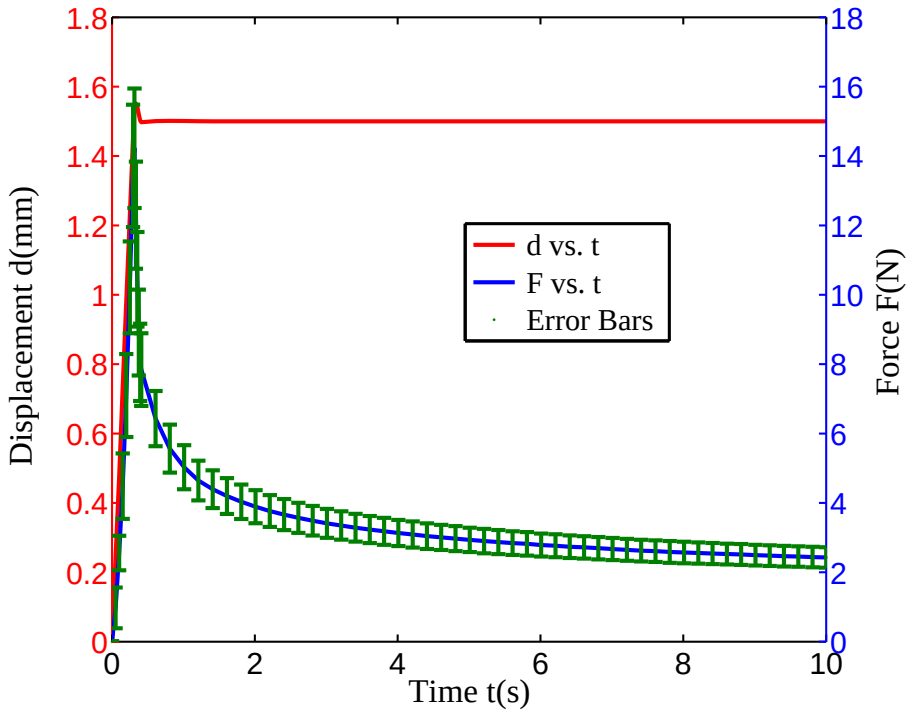

(a)

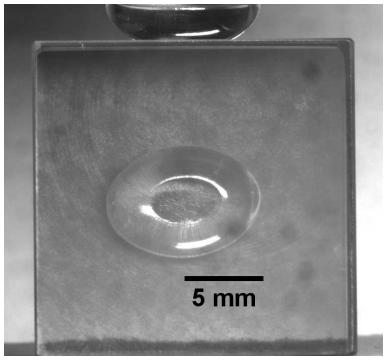

(b)

Figure 4.2: Experimental data for RH (relaxation) tests at the specified displacement of $d = 1.5\ mm$ ($n = 9$) with loading rate of 5 mm/s and 10s hold time (a) Force-displacement-time (b) Contact area at time t>0.4s

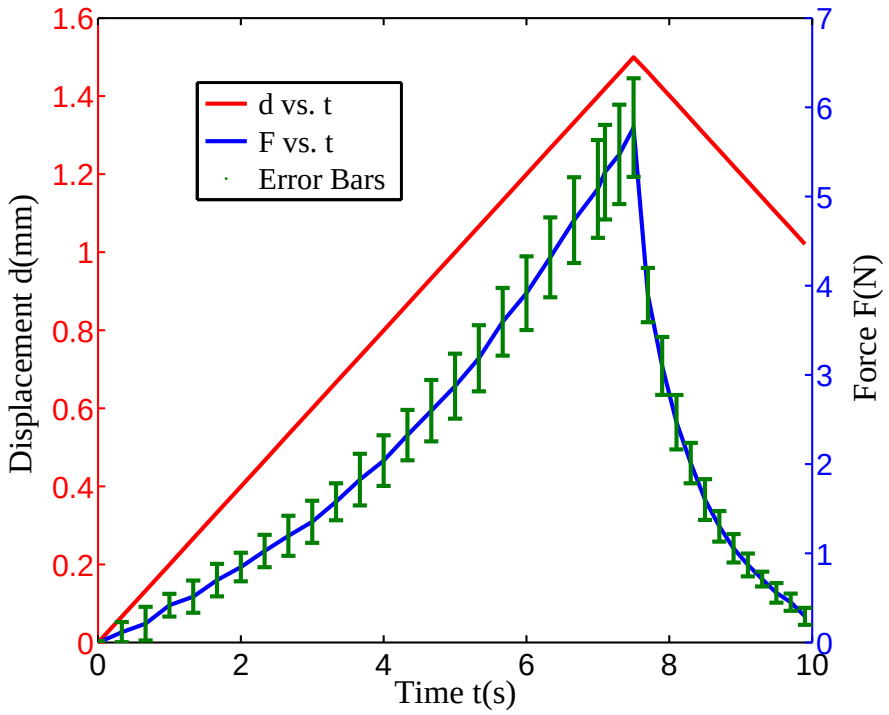

(a)

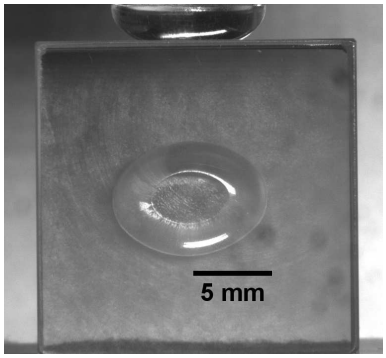

(b)

Figure 4.3: Experimental data for RR (hysteresis) tests at the specified displacement of $d = 1.5\ mm$ ($n = 9$) with loading and unloading rates of 0.2 mm/s (a) Force-displacement-time (b) Contact area at time t=7.5s

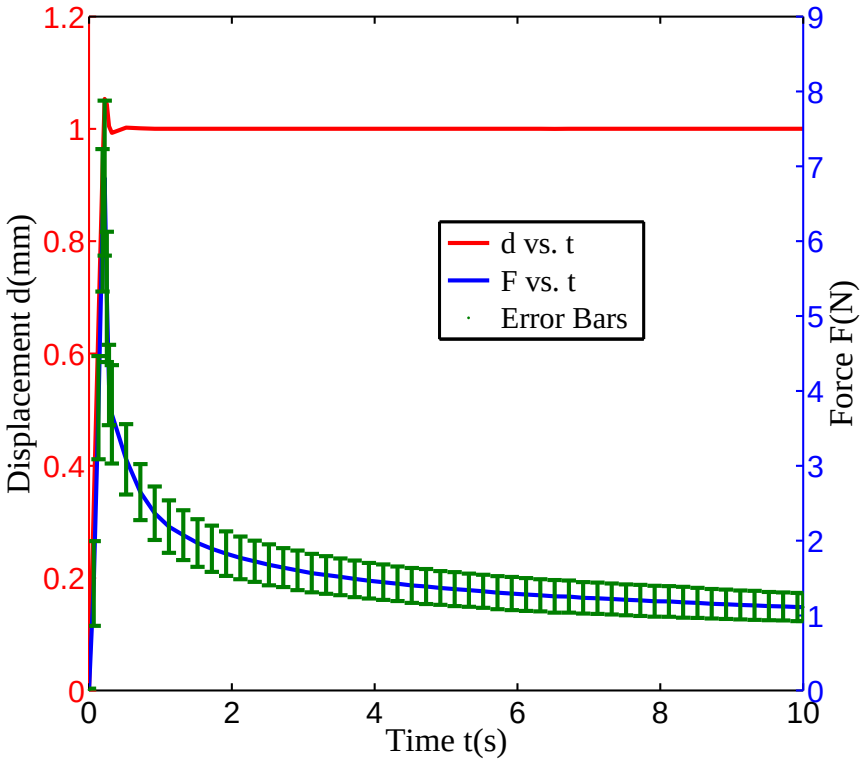

(a)

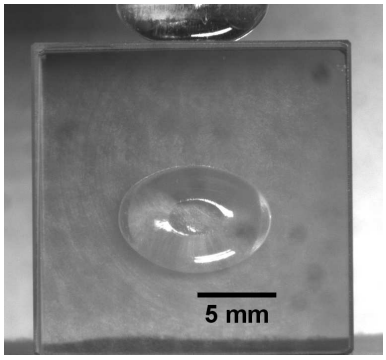

(b)

Figure 4.4: Experimental data for RH (relaxation) tests at the specified displacement of $d = 1.0\ mm$ ($n = 9$) with loading rate of 5 mm/s and 10s hold time (a) Force-displacement-time (b) Contact area at time t>0.3s

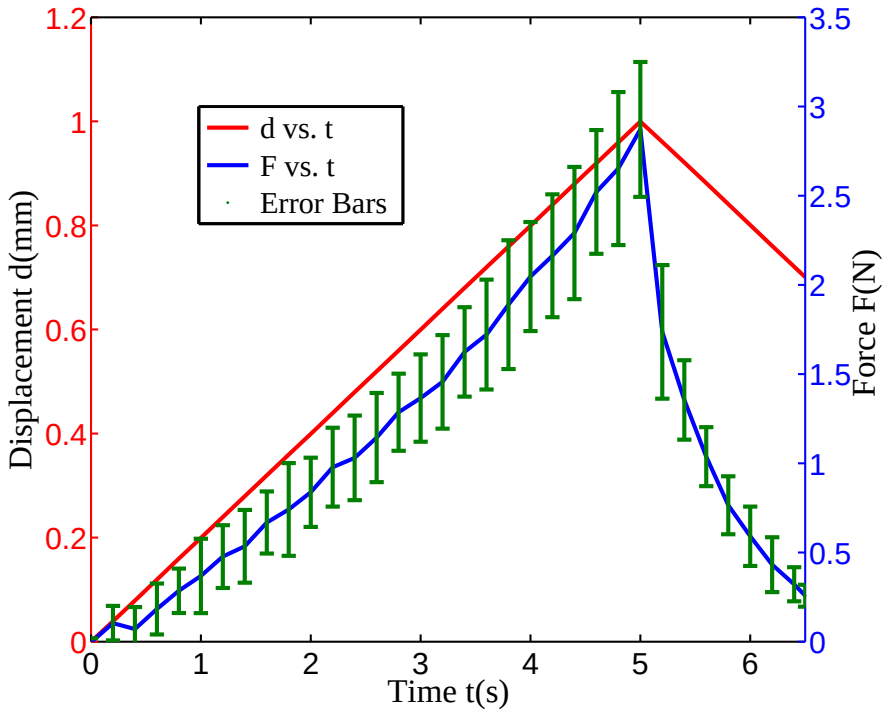

(a)

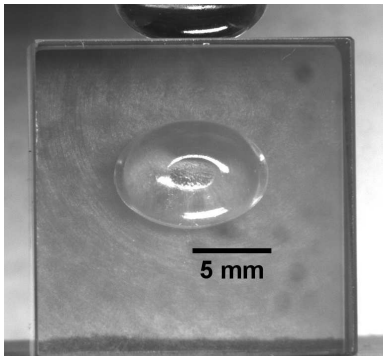

(b)

Figure 4.5: Experimental data for RR (hysteresis) tests at the specified displacement of $d = 1.0\ mm$ ($n = 7$) with loading and unloading rates of 0.2 mm/s (a) Force-displacement-time (b) Contact area at time t=5.0s

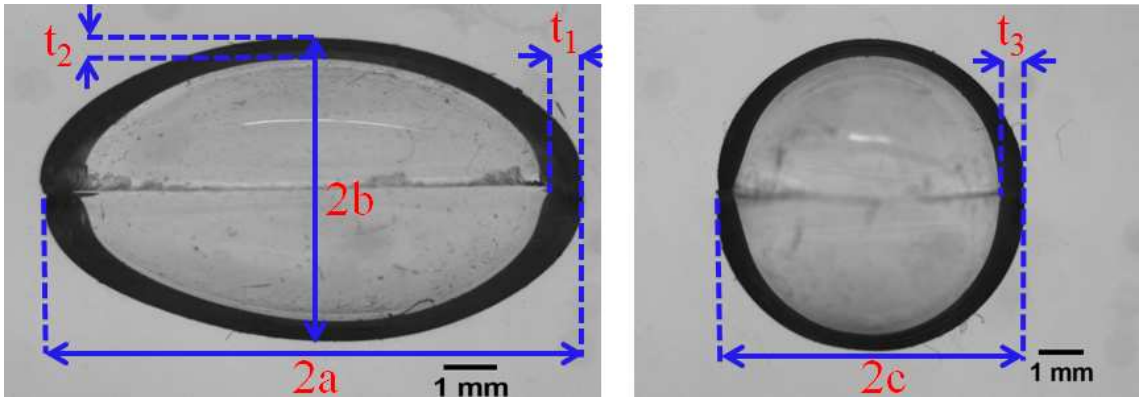

Figure 4.6: Dimensions and thickness measurements

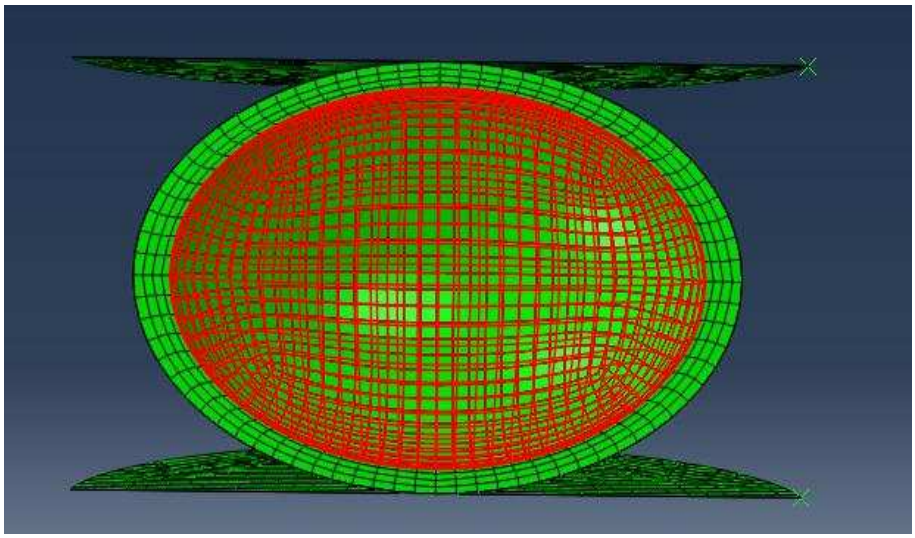

Figure 4.7: FE model for fluid-filled capsules

are accounted for by using non-uniform wall thicknesses incorporating the values of $t_1 = 0.62\,mm$ and $t_2 = t_3 = 0.4\,mm$. The shell wall is modeled with the use of 3D solid elements C3D8R. The enclosed fluid is assumed to be incompressible and modeled by F3D4 fluid elements. The nodes of these fluid elements coincide with the nodes of the inner surface of the shell wall and are arranged in a counter clockwise order such that the positive normal directions of the elements point toward the center of the capsule. The two contact plates are modeled as rigid bodies using R3D3 and R3D4 elements. A convergence study was also performed to optimize the mesh size. In this study, a mesh size of 12662 elements with four elements along the capsule thickness is utilized for obtaining the force-time response, while a more refined mesh, especially in the contact region, of 101132 elements having four elements along the capsule thickness is employed for extracting contact-area information. An illustration of FE model is shown in Figure 4.7. The tangential contact behavior between the plates and the capsule is assumed to be frictionless, while the vertical contact behavior is modeled using the hard contact feature for pressure-overclosure relationship in ABAQUS. In this contact feature, the option that allows separation after contact is applied to investigate whether there is any loss of contact during the compression test.

The actual displacement-time history of the top plate from the experiment is used to specify the input for FE simulations. For the case of RH (relaxation) tests, this actual history is essential for capturing the effect of the overshoot in the input data due to the very fast ramp rate (as shown in Figure 4.2 and Figure 4.4). Reaction force and contact area are extracted from FE simulations and compared with the experimental data. For the contact area, since there might be a gap between the capsule and the plates in the contact region, the history output CAREA (an option in ABAQUS allows the extraction of contact area) was not used. The profiles of the contact pressure were utilized instead to determine the boundary of the contact region and compute the area. Different NLV constitutive models for the capsule's material

can be employed with the approach considered here. For convenience, the ABAQUS 6-10 NLV model is chosen owing to its built-in option in the software.

ABAQUS built-in NLV model

As presented in section 4.8-2 of ABAQUS Theory Manual version 6-10 (*ABAQUS-v6.10*, 2010), the finite-strain viscoelasticity model employed in ABAQUS has the following hereditary integral form:

$$\begin{aligned}
\tau^D(t) &= \tau_0^D(t) + dev\left[\int_0^t \frac{\dot{G}(s)}{G_0}\bar{F}_t^{-1}(t-s)\tau_0^D(t-s)\bar{F}_t^{-T}(t-s)ds\right], \\
\tau^H(t) &= \tau_o^H(t) + \int_o^t \frac{\dot{K}(s)}{K_0}\tau_0^H(t-s)ds,
\end{aligned}$$

where τ^D and τ^H are the deviatoric and volumetric parts respectively. $G(s)$ is the shear relaxation function while $K(s)$ is the bulk relaxation function. This form is a non-linear single integral model based on a generalization of the linear viscoelastic model considering a transformation of the stress state at time $(t-s)$ to the one at time t through the relative deformation gradient $F_t(t-s)$ defined as follows:

$$F_{t-s}(t) = \frac{\partial x(t)}{\partial x(t-s)}.$$

Note that this can be rewritten as:

$$\begin{aligned}
F_{t-s}(t) &= \mathbf{F}(t)\mathbf{F}^{-1}(t-s), \\
\bar{F}_{t-s}(t) &= \bar{\mathbf{F}}(t)\bar{\mathbf{F}}^{-1}(t-s),
\end{aligned}$$

where $\mathbf{F}$ is the deformation gradient and $\bar{\mathbf{F}} = det(\mathbf{F})^{-1/3}\mathbf{F}$. Therefore, the deviatoric part can also be represented as:

$$\tau^D(t) = \tau_0^D(t) + dev\left\{\bar{\mathbf{F}}(t)\left[\int_0^t \frac{\dot{G}(s)}{G_0}\bar{\mathbf{F}}^{-1}(t-s)\tau_0^D(t-s)\bar{\mathbf{F}}^{-T}(t-s)ds\right]\bar{\mathbf{F}}^{\mathbf{T}}(t)\right\}.$$

With the assumption of incompressible shell wall material, the material properties that need to be determined in this model belong to two parts of the model. For the elastic part, an incompressible, Mooney-Rivlin relation is used which requires two parameters $C_1, C_2 = \alpha C_1$:

$$\tau_0 = -p\mathbf{I} + 2(C_1 + I_1 C_2)\mathbf{B} - 2C_2\mathbf{B^2}, \tag{4.1}$$

where p is the indeterminate pressure arising from the incompressibility constraint. $\mathbf{B}$ is the left Cauchy-Green tensor. The incompressibility is taken cared by ABAQUS using a high bulk modulus value.

For the viscoelastic part, the relaxation function expressed in terms of an n term Prony series (g_k, τ_k) is employed.

$$G(s) = G_\infty + \sum_{k=1}^{n} G_k e^{-s/\tau_k} = G_0\left[g_\infty + \sum_{k=1}^{k=n} g_k e^{-s/\tau_k}\right], \tag{4.2}$$

where

$$g_\infty = 1 - \sum_{k=1}^{k=n} g_k > 0. \tag{4.3}$$

4.4 Results and Discussions

4.4.1 Implementation of Inverse Process

The ABAQUS built-in NLV material model with incompressibility was used to model the capsule shell wall. Six unknown material properties need to be determined.

Two Mooney-Rivlin parameters C_1, $C_2 = \alpha C_1$ are utilized for describing the NLE part. A two term Prony series (g_k, τ_k), $k = \overline{1,2}$ are to capture the relaxation behavior. Therefore, the material domain is a sixth dimensional space of $x(C_1, \alpha, g_1, \tau_1, g_2, \tau_2)$. To illustrate the application of the above inverse process, consider the mean data of the RH (relaxation) test with the specified displacement of $d = 1.5\ mm$. The lower bound and upper bound for material parameters are in Table 4.1.

	C_1(MPa)	α	g_1	τ_1(s)	g_2	τ_2(s)
Lower bound	5	0	0.5	0.03	0	1
Upper bound	50	0.5	1	0.3	0.5	5

Table 4.1: Boundary of the material domain used in the process of determining the NLV properties of the tested polymeric fluid-filled capsules

The process is divided into five steps following the description in Chapter III.

Step 1: Generate sets of material properties to build a meta model and testing cases

In the sixth dimensional space, select N sets of $x(C_1, \alpha, g_1, \tau_1, g_2, \tau_2)$ for training points and M sets for testing the Kriging estimator. The selection technique is based on the Latin Hypercube sampling (using MATLAB function "lhsdesign" (*MATLAB R2010a*, 2010)) and satisfies the constraint $g_1 + g_2 < 1$. For the problem here, $N = 492$ and $M = 92$ correspond to $X(6, 492)$ and $X^1(6, 92)$.

Step 2: Evaluation of FE simulations

The time period of the RH (relaxation) test is divided into 1200 time steps $t_i, i = \overline{1, 1200}$. For each set in $X(6, 492)$ and $X^1(6, 92)$, FE simulation is used to extract the force-time response $(t_i,\ y_i(t_i))$, $i = \overline{1, 1200}$. These evaluations of FE simulations were done in parallel to reduce the computational time. The corresponding force values are saved in $Y(1200, 492)$ and $Y^1(1200, 92)$. The combination of $X(6, 492)$ and $Y(1200, 492)$ constructs a meta model for the problem, while the combination of $X^1(6, 92)$ and $Y^1(1200, 92)$ is used for testing the accuracy of the predictor.

Step 3: Apply a Kriging Predictor

Once a meta model is generated, a non-linear relationship between the material in-

puts and force responses is derived based on a Kriging predictor as described in Chapter III. This step utilizes the DACE toolbox implemented in MATLAB (*Lophaven et al.*, 2002).

Step 4: Checking the accuracy of the Kriging Predictor

The accuracy of the predictor is evaluated by applying it to the testing sets $X^1(6, 92), Y^1(1200, 92)$. Here, each set $x(C_1, \alpha, g_1, \tau_1, g_2, \tau_2)$ in $X^1(6, 92)$ is composed of six material parameters and was not used for training the Kriging Predictor in step 3. Each set $y(t_i), i = \overline{1, 1200}$ in $Y^1(6, 92)$ is the corresponding FE force time response. Figure 4.8 shows representative comparisons of the actual FE responses in testing cases Y^1 and the corresponding predictions from Kriging.

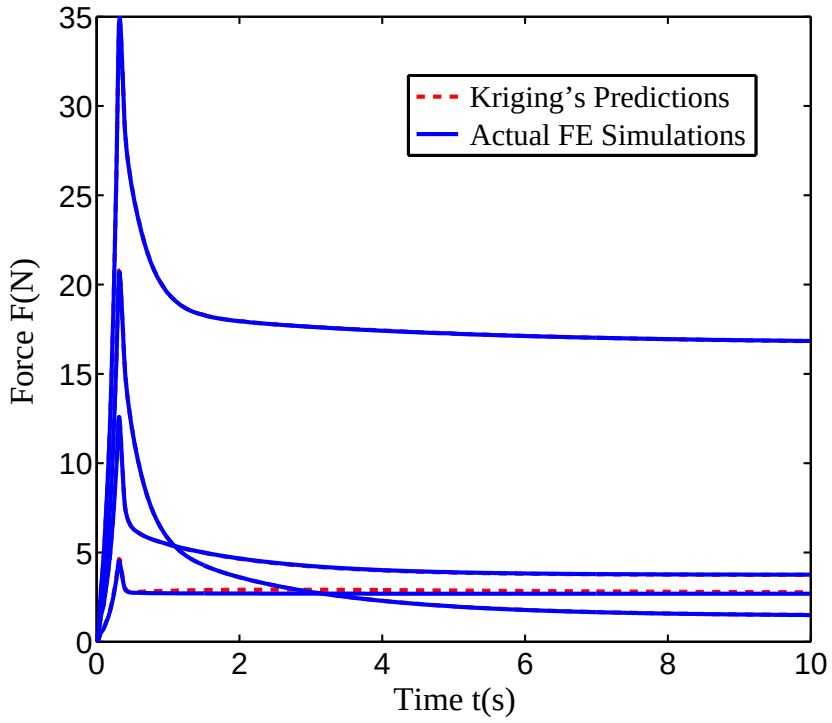

Figure 4.8: Representative comparisons of force-time responses between the actual FE simulations and Kriging predictions of the test cases for the RH (relaxation) input at $d = 1.5\ mm$

As observed in the figure, many of Kriging predictions overlayed with the actual FE responses. This indicates that the difference between the actual FE response and

the corresponding Kriging prediction is small. Particularly, the RMSE values are

$$RMSE(i) = \frac{1}{range(y^i_{FE})}\sqrt{\frac{1}{1200}\sum_{k=1}^{1200}(y^i_{FE(k)} - y^i_{Krg(k)})^2}, \tag{4.4}$$

is evaluated for each test case $i = \overline{1, 92}$. For the 92 test cases considered here, the RMSE values range from 0.05% to 4%. The accuracy of the predictor can also be improved by adding more training points to the meta model. Since the basis of the inverse technique is the same, so for this problem, we only consider one shot Kriging and the above error is considered to be reasonable, *Forrester et al.* (2008).

Step 5: Optimization on the Kriging Predictor

The Kriging predictor now is used to interpolate the force-time response at the untrained material sets. This evaluation is much faster than FE simulations, therefore, an optimization can be performed to quickly extract the optimized sets of material parameters that can fit the experimental data. The function $fmincon$ in MATLAB with multiple start points optimization technique is utilized. This option also takes into account the constraint $g_1 + g_2 < 1$. The optimized set obtained after this step for the problem considered here is,

$C_1 = 21.2546$ MPa, $\alpha = 0.3720$, $g_1 = 0.7674$, $\tau_1 = 0.0623$s, $g_2 = 0.1546$, $\tau_2 = 1.3936$s. Since the Kriging predictor gives only an approximation, the response of this optimized set is re-checked by using an actual FE simulation. A comparison between FE simulation at this optimized set with the mean experimental data for RH (relaxation) test at $d = 1.5\ mm$ is shown in Figure 4.9. A prediction of the RH (relaxation) response at $d = 1.0\ mm$ using this obtained material parameter set is also included. The RMSE values for the fitting and for the prediction are 0.0147 and 0.0224, respectively, indicating quite good agreement with experimental data.

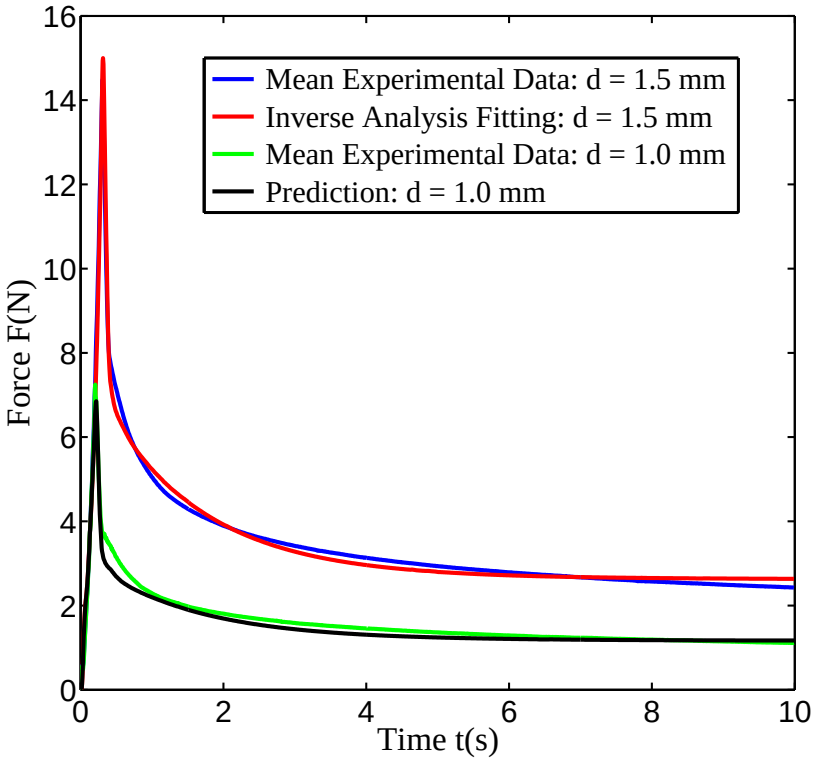

Figure 4.9: Comparisons between experimental data with FE predictions using the optimized material set from inverse analysis for the mean RH (relaxation) data at $d = 1.5\ mm$

4.4.2 Fitting Experimental Data

The above approach is also applied to other displacement inputs: RH (relaxation) at $d = 1.0\ mm$, RR (hysteresis) at $d = 1.5\ mm$ and $d = 1.0\ mm$ by constructing their corresponding meta models and Kriging predictors. Representative comparisons between actual FE force-time responses and Kriging predictions for the testing cases X_1 (untrained sets of material parameters), and Y_1 (corresponding FE force-time responses) in the case of RR (hysteresis) tests at $d = 1.5\ mm$ are shown in Figure 4.10. Very small differences between actual FE responses and corresponding Kriging predictions indicate that Kriging can be used to predict the responses from FE simulations of RR (hysteresis) tests.

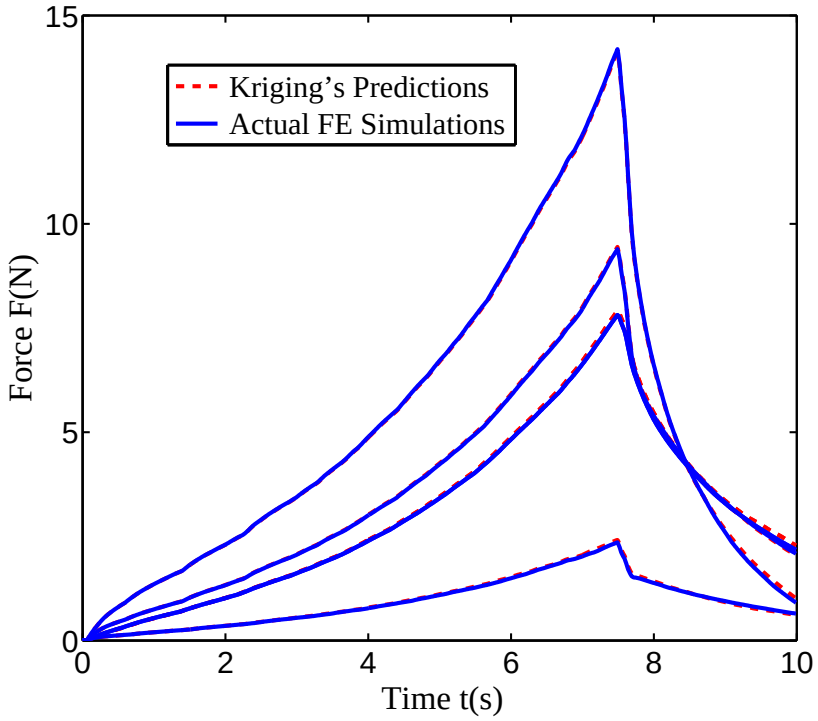

Figure 4.10: Representative comparisons of force-time responses between the actual FE simulations and Kriging predictions of the test cases for the RR (hysteresis) input at $d = 1.5\ mm$

Inverse analysis can be done on these meta models and Kriging predictors simultaneously to extract better predictions for the material parameter set. Specifically, simultaneously fitting the two RH (relaxation) tests were performed to improve the predictions for both RH (relaxation) data as shown in Figure 4.11. The RMSE values are 0.0166 and 0.019 for responses at $d = 1.5\ mm$ and at $d = 1.0\ mm$, respectively, with the following optimized parameter set:

$C_1 = 24.6162$ MPa, $\alpha = 0.0818$, $g_1 = 0.7281$, $\tau_1 = 0.0693$s, $g_2 = 0.1812$, $\tau_2 = 1.4148$s.

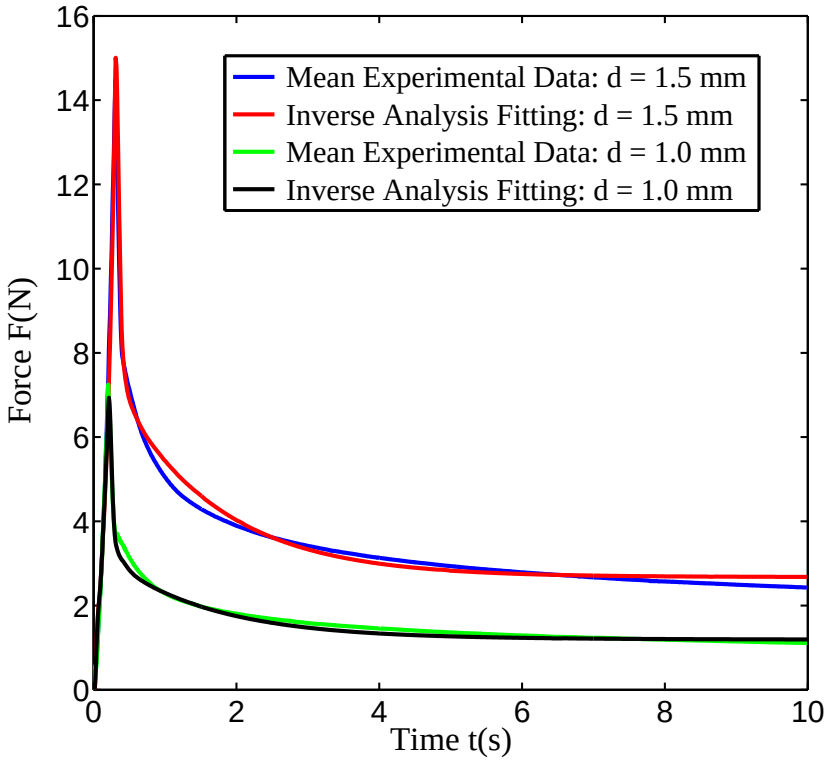

Figure 4.11: Comparisons between experimental data with FE predictions using the optimized material set from inverse analysis for both RH (relaxation) experimental data at $d = 1.5\ mm$ and $d = 1.0\ mm$

By the use of Kriging predictors and also verification with actual FE simulations, several different combinations of Mooney-Rivlin parameters C_1, C_2 with the same $(C_1 + C_2)$ or instantaneous shear modulus were found to give very close force-time results. This suggests that optimization based on force-time curve might not be sensitive enough to extract a unique set of C_1 and $C_2 = \alpha C_1$.

Similar observations were also found for RR (hysteresis) loading. One optimized set extracted from the mean experimental data of the RR (hysteresis) test at $d = 1.5\ mm$ is

$C_1 = 28.8179$ MPa, $\alpha = 0$, $g_1 = 0.7652$, $\tau_1 = 0.1608$s, $g_2 = 0.2183$, $\tau_2 = 5$s.

The fitting for this test and the prediction for the response at $d = 1.0\ mm$ are presented in Figure 4.12. The RMSE values are 0.0188 and 0.0444 respectively. Similarly,

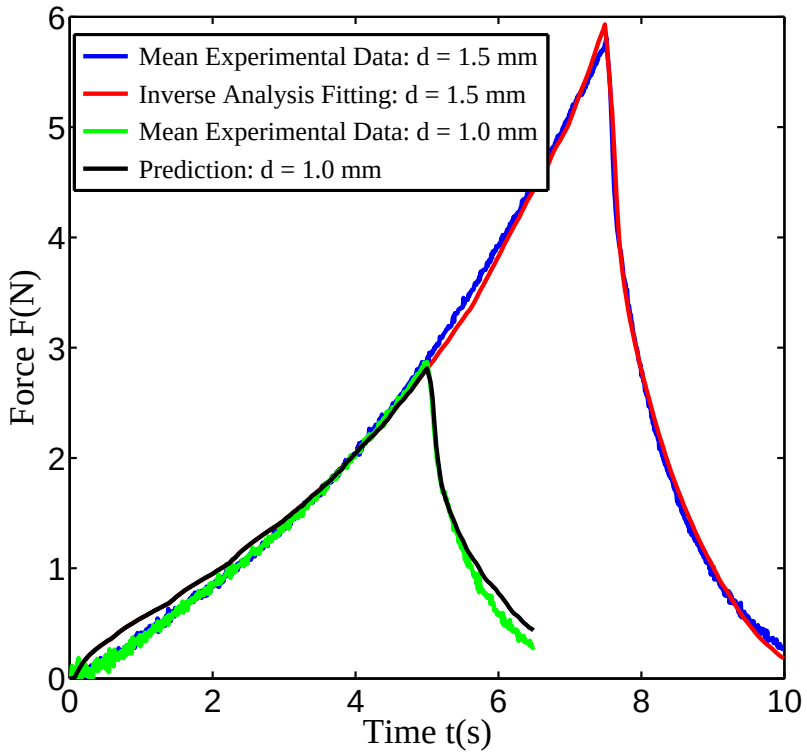

Figure 4.12: Comparisons between experimental data with FE predictions using the optimized material set from inverse analysis for the mean RR (hysteresis) data at $d = 1.5\ mm$

fittings by simultaneously optimizing these two RR (hysteresis) tests can also be done (results are not shown here). The RMSE value is 0.0212 for response at $d = 1.5\ mm$ and 0.0391 for response at $d = 1.0\ mm$ with the following set of material parameters $C_1 = 21.3007$ MPa, $\alpha = 0.0134$, $g_1 = 0.6860$, $\tau_1 = 0.2365$s, $g_2 = 0.2885$, $\tau_2 = 4.8279$s. It is also noted that optimizing the data from RR (hysteresis) inputs might yield several optimized sets which result in close force-time responses, hence similar RMSE values when compared to the experimental data. One way to observe this is in the optimization step on the Kriging predictor for RR (hysteresis) test at $d = 1.5\ mm$ using the $fmincon$ function in MATLAB. If the domain is narrowed down by changing the upper bound of $g_1 + g_2$ (which is related to the long term response), different sets of material parameters can be obtained. For example, consider two material sets

obtained by varying the upper bound of $g_1 + g_2$ from 0.999 to 0.85:

Material Set 1:

$C_1 = 28.8179$ MPa, $\alpha = 0$, $g_1 = 0.7652$, $\tau_1 = 0.1608$s, $g_2 = 0.2183$, $\tau_2 = 5$s, where $g_1 + g_2 = 0.9835$.

Material Set 2:

$C_1 = 21.9096$ MPa, $\alpha = 0$, $g_1 = 0.5036$, $\tau_1 = 0.2018$s, $g_2 = 0.3464$, $\tau_2 = 1.1285$s, where $g_1 + g_2 = 0.85$.

As shown in Figure 4.13, verifications by actual FE simulations show that the RR (hysteresis) responses of these two material sets are almost the same (the differences are very small to be seen in the figure) while the RH (relaxation) responses exhibit more variations. This implies that the RR (hysteresis) test data might not be sensitive to extract the long term response of the relaxation behavior.

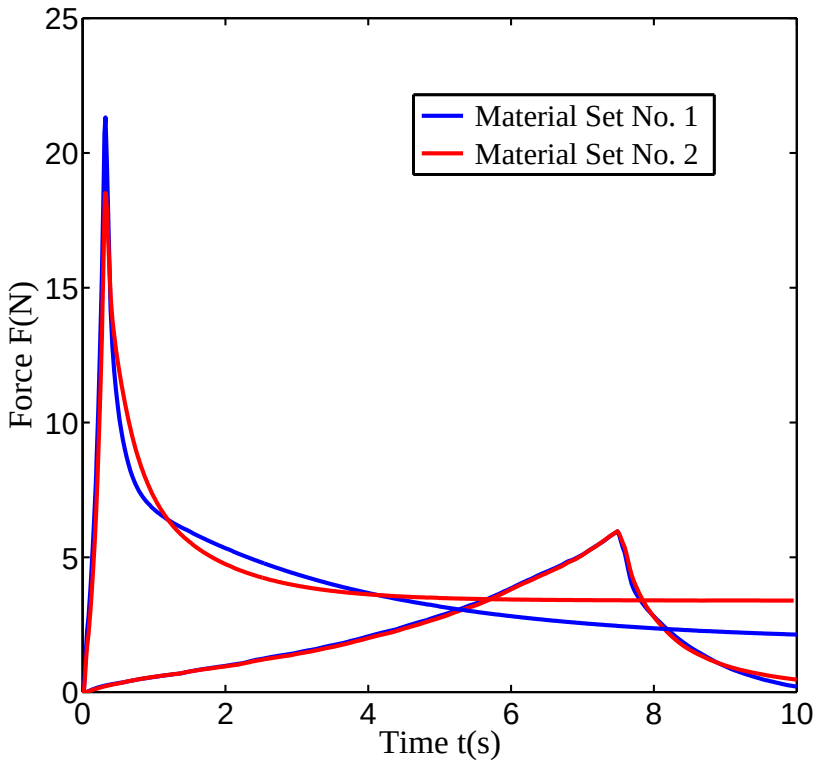

Figure 4.13: Comparisons of FE predictions with two material parameter sets for RH (relaxation) and RR (hysteresis) tests at $d = 1.5$ mm

Within one group of loading, the inverse analysis is able to yield the optimized set of material parameters that can also capture the experimental response at another amount of displacement quite reasonably. Using one group to predict the other has higher error. Specifically, Figure 4.14 and Figure 4.15 show the fits for RH (relaxation) and RR (hysteresis) experimental data at two applied displacement $d = 1.0\ mm$ and $d = 1.5\ mm$ using the optimized set obtained from inverse analysis for three cases:

(a) Using a combination of two mean RH (relaxation) tests at $d = 1.0\ mm$ and $d = 1.5\ mm$

(b) Using a combination of two mean RR (hysteresis) tests at $d = 1.0\ mm$ and $d = 1.5\ mm$

(c) Using a combination of the mean RH (relaxation) and RR (hysteresis) tests at $d = 1.5\ mm$.

As can be seen in Figure 4.14, using two RH (relaxation) tests results in the best fit while using the two RR (hysteresis) tests has the poorest fit for the ramp and hold type of loading. On the contrary, for the ramp and reverse type of loading in Figure 4.15, the best fit is resulted from the use of two RR (hysteresis) tests while the poorest fit is resulted from the use of two RH (relaxation) tests. Combining two groups: RH (relaxation) and RR (hysteresis) such as in case (c) can improve the predictions for both types of loading as shown in these two figures.

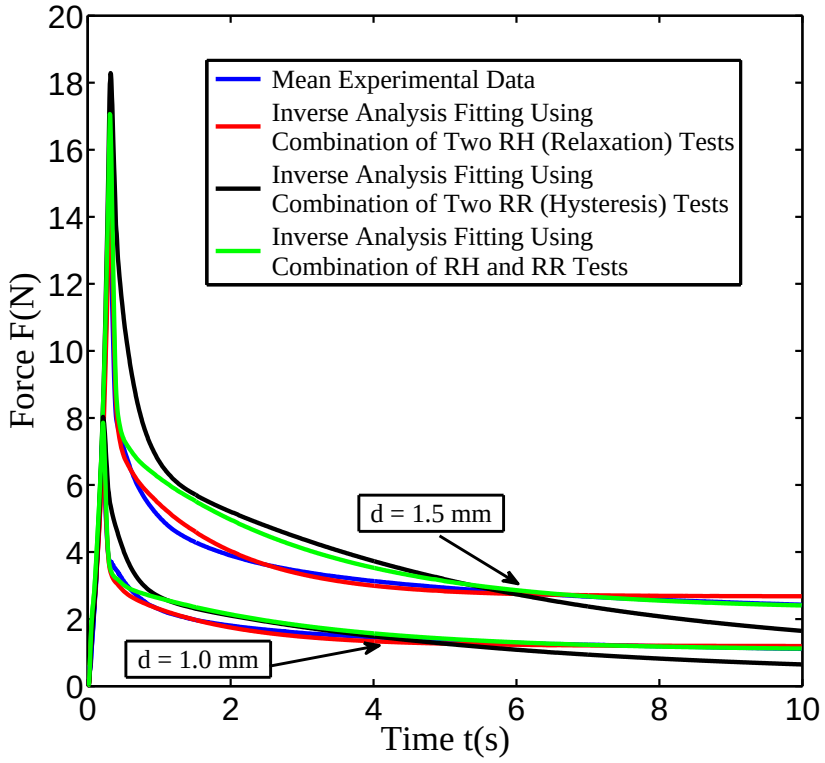

Figure 4.14: Fitting RH (relaxation) data at two applied displacements $d = 1.0\ mm$ and $d = 1.5\ mm$ with the optimized parameter sets obtained from inverse analysis for three combinations: (a) Using a combination of two mean RH (relaxation) tests (red), (b) Using a combination of two mean RR (hysteresis) tests (black), (c) Using a combination of the mean RH (relaxation) and RR (hysteresis) tests (green)

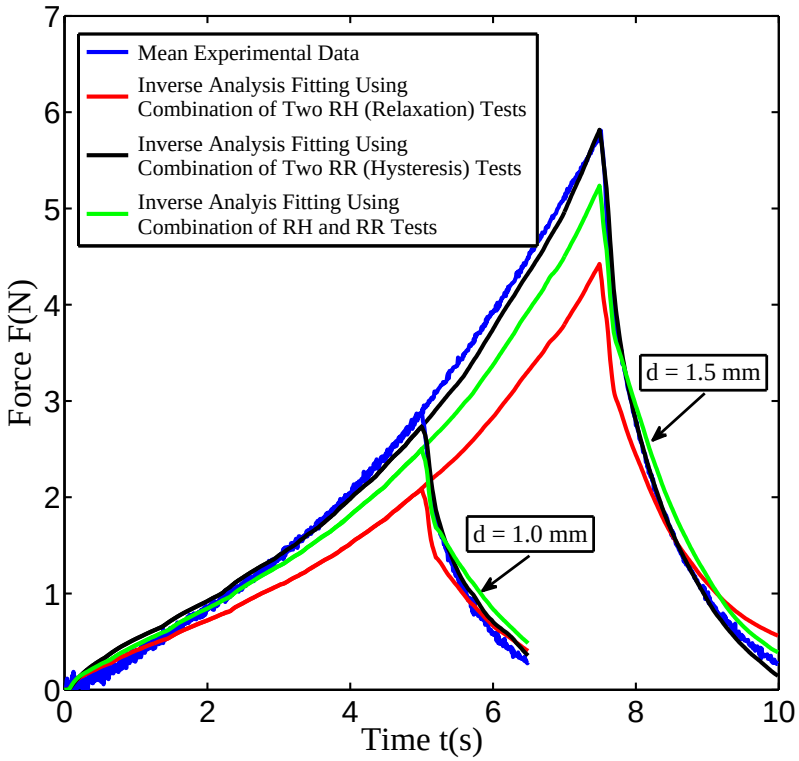

Figure 4.15: Fitting RR (hysteresis) data at two applied displacements $d = 1.0\ mm$ and $d = 1.5\ mm$ with the optimized parameter sets obtained from inverse analysis for three combinations: (a) Using a combination of two mean RH (relaxation) tests (red), (b) Using a combination of two mean RR (hysteresis) tests (black), (c) Using a combination of the mean RH (relaxation) and RR (hysteresis) tests (green)

The differences in these predictions which correspond to different combinations of the material parameters that were obtained above might be attributed to the differences in the type of loading: RH (relaxation) versus RR (hysteresis); the loading rates: fast 5 mm/s versus slow 0.2 mm/s; and the behavior of the enclosed fluid under these loading rates that the model might not be able to capture perfectly. Another source of the difference is the variation between samples including the capsule thickness and dimensions. Since the main purpose here is to present an inverse approach for fitting experimental data based on a 3D NLV, FE model and a Kriging predictor, a detailed study of these differences and a discussion of constitutive model

selection are not included in the scope of this work. These can be investigated further by performing tests at different loading rates to examine the range of the loading that can be captured well by the model. More samples can be tested to quantify the variations between them. In addition, utilizing a mixture of RR (hysteresis) and RH (relaxation) tests will be a good combination to enhance the prediction of the model and justify the best set of NLV material properties for various responses. It is also observed that the experimental results also depend on many factors such as humidity or temperature, hence further study might be needed to investigate these influences.

4.4.3 Contact Area

To extract contact area from FE simulations, a finer mesh is required, especially in the contact region. Due to this very fine mesh which leads to a much more expensive computational cost of FE modeling, the study here did not consider the dependence of contact area on the six material parameters using an inverse analysis. Instead, another approach is employed which is to compare the experimental contact area with the predicted value from FE model using the optimized material set obtained from the above inverse analysis process on force-time data. The process is as follows: after getting the optimized material set for the force-time response, a very fine mesh FE simulation with this material input is evaluated. As observed in the experiment, there is a possibility of the contact loss between the capsule and the plates. Therefore, to determine the contact area, two contact pressure paths were used. One path is along the longitudinal axis while the other is along the shorter axis. Contact pressure at various times shows the existence of zero contact pressure between the plate and the capsule as in Figure 4.16 which presents typical pressure profiles along the longitudinal axis for the RH (relaxation) test at $d = 1.5\ mm$. In this figure, the zero-distance is at the center of the contact region. Similar results (not shown here) were also found for pressure along the shorter axis of the capsule. This indicates a loss of contact between

the capsule and the plates (buckling) at certain time steps such as at $t = 0.21$s. The contact region is approximated as an ellipse, and hence the area can be calculated using the two contact pressure paths.

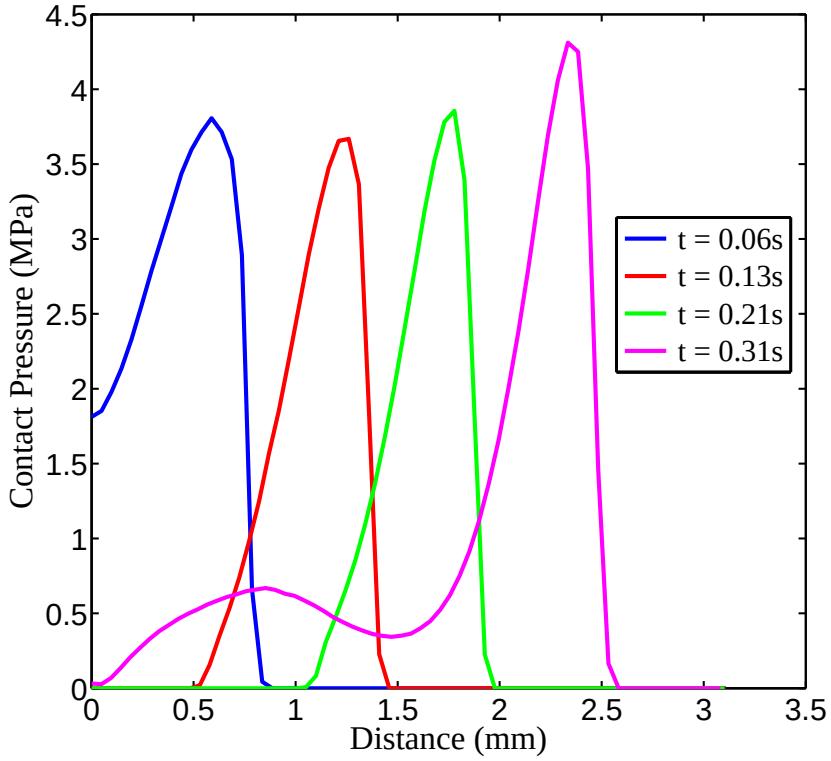

Figure 4.16: Typical contact pressure along the longitudinal profile for the case of a RH (relaxation) test at $d = 1.5\ mm$

For experimental contact area measurement, image processing software (ImageJ) is utilized to extract the magnitude of the contact area. A comparison between the mean experimental data and the FE prediction of the contact area is presented in Figure 4.17. The set of material parameters $C_1 = 21.2546$ MPa, $\alpha = 0.3720$, $g_1 = 0.7674$, $\tau_1 = 0.0623$s, $g_2 = 0.1546$, $\tau_2 = 1.3936$s obtained from the inverse analysis using the mean RH (relaxation) data at $d = 1.5\ mm$ was used for the FE simulation. Similarly, a comparison between the RR (hysteresis) mean contact measurement at $d = 1.5\ mm$ with FE prediction is in Figure 4.18. In this figure,

the optimized set from inverse analysis for this RR (hysteresis) test: $C_1 = 28.8179$ MPa, $\alpha = 0$, $g_1 = 0.7652$, $\tau_1 = 0.1608$s, $g_2 = 0.2183$, $\tau_2 = 5$s was utilized. For each test, these comparisons imply that using the optimized set obtained from each corresponding inverse analysis can yield a reasonable contact area value as measured in experiments. This shows the effectiveness of the inverse analysis in capturing both force-time response and contact area of each individual test. In Figure 4.17, due to the overshooting in the applied displacement, the FE model predicts an overshoot in the contact area as well. However, this overshoot is not clear in the experimental data which might be due to the image resolution as well as the slight changes of the amount of overshooting between different tests. Hence, when averaging the contact area, the artifacts lead to a mean data with a not very visible overshoot behavior.

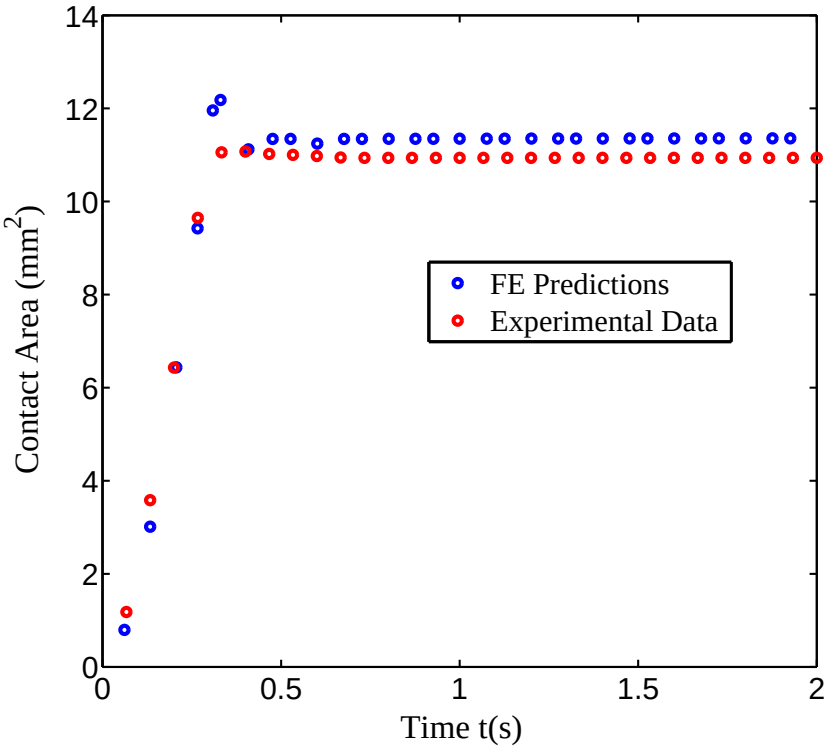

Figure 4.17: Comparison of contact areas between FE modeling and mean experimental measurement for the RH (relaxation) test at $d = 1.5$ mm

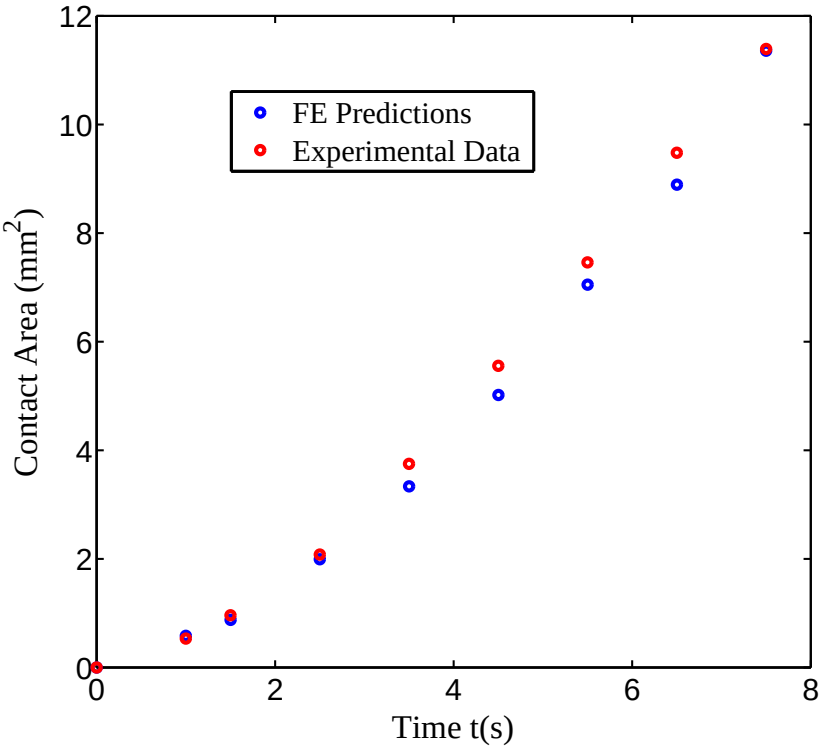

Figure 4.18: Comparison of contact areas between FE modeling and mean experimental measurement for the RR (hysteresis) test at $d = 1.5\ mm$

As the current optical arrangement does not have enough resolution to verify if and when any buckling phenomenon happens during the compression process, it might be useful to couple this setup with other approaches such as using a compression pad for pressure measurement between the plate and the capsule. This can be an interesting aspect for future studies in order to gain more insight in the contact feature in these types of problems.

4.4.4 Concluding Comments

An inverse analysis methodology has been presented that uses experimental data from compression of a fluid-filled capsule and a corresponding 3D FE model based on surrogate modeling with a Kriging predictor. It is shown to have the capability to automatically and efficiently extract the NLV properties from various testing scenar-

ios. This method can be combined with many constitutive models and overcomes the lengthy, impractical issue of the sequential inverse approach which requires iterative evaluations of costly FE simulations. Furthermore, the Kriging predictor can also be utilized to study the sensitivity of the material parameters with respect to the test responses. For example, the use of Kriging predictor indicates that with the NLV constitutive model considered in this study, the RR (hysteresis) test seems to be less sensitive in extracting the long term response of the relaxation behavior. Hence, a combination of both RH (relaxation) and RR (hysteresis) data should be used in order to obtain better predictions. This aspect will be further investigated for evaluations of the effectiveness of various models in capturing behavior observed in experiments.

CHAPTER V

AFM Indentation for Non-Linear Viscoelastic Identification of Breast Cancer Cells

5.1 Introduction

In this chapter, the methodology presented in the previous Chapters (II, III, IV) is applied to investigate a more complicated problem associated with the mechanics of single cells and its potential use for cancer detection. Specifically, a combination of AFM indentation experiments, FE modeling, and an inverse process based on surrogate modeling and a Kriging predictor is employed to characterize the NLV properties of single breast cancer cells. Additionally, comparison studies are also included to determine the differences between breast cancer cell lines in terms of their NLV behaviors.

Details of the AFM experiments are discussed in section 5.2. They are conducted to examine the correlation between changes in the NLV responses of the cells and the induced alterations in their cytoskeletal structures in two cases. The first aims to study this link when the alteration is due to the transformation between different states of cancer. For this goal, non-malignant (MCF-10A) and malignant (MCF-7) cells are indented by 5 μm spherical probes. Many complex aspects, such as large deformations, loading rate dependencies, and relaxation phenomena, are combined

to address several limitations in many current studies, which were discussed in detail in Chapter I. Thus, a series of loading "programs" is employed. It is composed of applying a small force to initiate the contact between the probe and the cell surface followed by a sequence of ramp-reverse (RR) and ramp-hold (RH) piezo movements. In the second case, the same indentation procedure was applied to investigate the effect of the induced cytoskeletal structure on the cells' NLV characteristics due to a drug treatment.

The AFM indentation test results are then modeled using the FE method. A widely used model, in which the cell is described as an isotropic, homogenized, axisymmetric body with an oblate-shape and a circular base, is employed (*Ladjal et al.*, 2009). The cell material constitutive relationship, however, is a large strain viscoelastic model. The non-linear elastic part of the material is captured by a hyper-elastic model while the viscoelastic part composes of a two term Prony series to describe the time-dependent relaxation. In order to simulate the actual operation in the AFM, the FE model also includes the AFM cantilever in the modeling by using a spring with the same stiffness. One end of the spring is attached to the spherical indenter; the other is loaded with the prescribed input. Details of this modeling part are presented in section 5.3.

Once a FE model is constructed, an inverse analysis is needed to optimize the error between the experimental data and FE predictions. The iterative inverse approach is computationally expensive, as also noted in *Ladjal et al.* (2009). Therefore, an inverse technique based on a surrogate model with the use of a Kriging estimator (*Sacks et al.*, 1989; *Lophaven et al.*, 2002; *Queipo et al.*, 2005; *Forrester et al.*, 2008; *Gustafson and Waas*, 2009; *Heinrich and Waas*, 2009) is employed to address this issue. Its implementation and application to the analysis of the obtained AFM experimental data are included in section 5.4. This procedure allows an automatic and efficient extraction of the NLV parameters. The variations of the shear relaxation

modulus over time for each tested cell is, therefore, also obtained. Next, statistical comparisons using the shear relaxation modulus and the amount of relaxation for the two cases (MCF-10A versus MCF-7, and untreated versus treated MCF-10A) were also conducted to investigate differences in terms of these mechanical properties. Results are presented along with a discussion on the use of the cell's relaxation responses as potential cell markers for cancer detection. The section concludes with a summary of limitations and concluding comments.

5.2 Details of AFM Indentation Experiment

5.2.1 Cell Culture and Sample Preparation

Human mammary epithelial cells (MCF-10A) were cultured in mammary epithelial growth medium (MEGM, Lonza) with the GA-1000 replaced by 100 ng/ml cholera toxin (Sigma). Human breast cancer cell line (MCF-7) was maintained in Dulbecco's modified eagle medium (DMEM, Life Technologies) supplemented with 10% fetal bovine serum (FBS, Life Technologies), 1% penicillin/streptomycin (P/S, Life Technologies), 1% fungizone (Life Technologies), and 5 g/ml gentamycin (Life Technologies). For preparing samples for AFM tests, cells were resuspended and seeded onto glass coverslips at density of 40,000 - 80,000 cells per coverslip. Cells were cultured under 37^0C and 5% CO_2 for at least overnight before any test was performed. For pharmacological treatment assays, MCF-10A cells were incubated with 500 μM cytochalasin D (Life Technologies) for 2 hours and then tested by indentation. More details are provided by *Shao* (2014) from whom this section has been taken.

5.2.2 AFM Indentation Setup

The working principle of an AFM Bruker Dimension Icon instrument (*Veeco Instruments Inc.*, 2010) is illustrated in Figure 5.1. The sample is fixed to a rigid

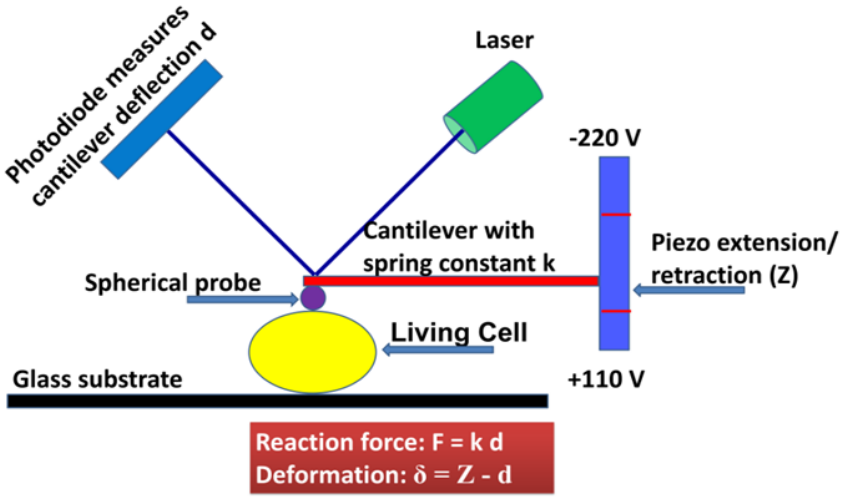

Figure 5.1: Illustration of working principle of AFM indentation test on cells.

substrate and compressed by a probe attached to one end of an AFM cantilever (for indenting cells, a spherical probe is often used to reduce damage during the tests). The other end of the cantilever is connected to a piezo. As this piezo extends, the probe moves downward and comes into contact with the sample. On the other hand, as the piezo retracts, the probe moves upward.

Upon contact, the sample's reaction force F causes the cantilever to bend leading to a shift of the laser beam on the photodiode. The amount of shifting is related to the deflection d of the cantilever, which is in turn related to the reaction force by a linear relation $F = kd$. Here, k is the spring constant of the cantilever normally calibrated using the built-in thermal tune function in the AFM instrument (*Matei et al.*, 2006). The deformation δ of the sample is the difference between the piezo distance Z and the cantilever deflection d: $\delta = Z - d$. With this working principle, the sample's deformation δ, therefore, cannot be controlled. In other words, in the AFM, the control modes can only be either controlling the piezo movement Z or using a feedback loop to control the deflection d, which is correlated to the force F. The first control mode, in which the indentation is performed by ramping and reversing the piezo movement Z, is frequently employed. However, this leads to variations

in the loading inputs upon changing samples and setups. In addition, variations in cell heights and properties also contribute to this issue. Therefore, in order to get almost the same input and also to combine many aspects into the loading process, including loading rate dependencies, hysteresis and relaxation behaviors, the following procedure was employed.

Indentation experiments were performed in a cell culture medium at room temperature using the contact mode in fluid of an AFM Bruker Dimension Icon system (Electron Microbeam Analysis Laboratory, University of Michigan). Cantilevers adhered with 5 μm diameter spherical borosilicate particles (Novascan Technologies, Inc.) were employed. Their nominal manufactured spring constant value is k = 0.06 N/m. Before indentation on cells, the deflection sensitivity (DS) to convert the photodiode (or laser) signal of the cantilever deflection from Voltage to *nm* was calibrated by obtaining force curves on a clean glass slide and measuring their slope values. Once the DS value was attained, the thermal tune option (*Matei et al.*, 2006) was used to measure the cantilever spring constant. The values used in this work were found to be 0.120 N/m, 0.083 N/m, and 0.080 N/m. The clean glass slide was then replaced by a glass coverslip with the cells seeded on the top. When replacing the coverslip, the laser sum signal was maintained the same to minimize the change in DS value (*Taatjes and Mossman*, 2005). Next, the spherical indenter was positioned at the center region of each selected cell, and indentation tests were conducted using the script mode, that included two steps as follows:

Step 1: Ramping the setpoint (force) to engage the probe on the cell's surface with a small force value (ramp velocity: 1 nm/s, δd = 4 nm, and the applied force value was about 0.3 - 0.5 nN). This step was to initiate the contact between the probe with the sample's surface. A small value of force was utilized to reduce its effects on the subsequent step, in which the piezo movement (Z) was controlled.

Step 2: A sequence of RR (hysteresis) and RH (relaxation) loading processes, as

shown in Figure 5.2, was applied to the piezo. It was employed to study the hysteresis as well as relaxation responses of the cells. This loading series consisted of one load-unload cycle at rate 10 μm/s, one load-unload cycle at rate 5 μm/s, and one load-unload cycle at rate 1 μm/s followed by a fast ramp at rate 10 μm/s and a hold period of 50s. In the first RR cycle, the piezo moved down by an amount of 2 μm, then retracted by an amount of 1 μm. These positions of loading were repeated in the following cycles. These values were chosen to examine a relative large deformation, and also to reduce the negative range of the force-time responses in the unloading paths due to the characteristics of viscoelasticity under displacement control of the AFM piezo.

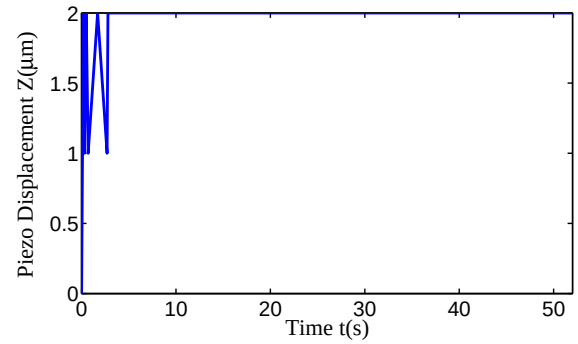

(a)

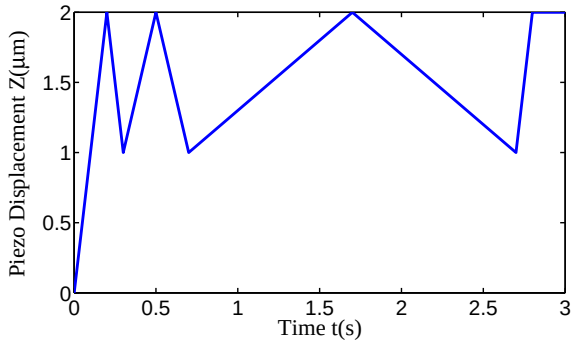

(b)

Figure 5.2: Applied input Z for controlling the AFM piezo movement: (a) The entire step (b) Zoom-in view of the RR (ramp-reverse) cycles.

For each cell, offset option is also utilized to move the probe to the nearby locations to acquire force-time data at these neighboring positions (2 - 4 locations per cell

were used). In this work, data for each individual cell is the average of these local measurements.

A similar process was employed in a recent work by *Bernick et al.* (2011) to study the biomechanics of neurons, however, no comparison studies were included. To the extent of the author's knowledge, this work is the first to study the experimental data obtained from this type of experimental setup for distinguishing different cell lines.

5.2.3 Experimental Data

For the purpose of investigating the roles of viscoelastic properties in establishing biomarkers for cancer detection purpose, two approaches were studied with the described indentation procedure. In the first, experiments were conducted on two groups of benign (MCF-10A) and malignant (MCF-7) cells to study the changes of viscoelastic parameters at different states of breast cancer. In the second approach, the drug cytochalasin D, which can disrupt the cytoskeleton structure, is used to treat MCF-10A cells. The hypothesis here is that alteration in the cytoskeleton structure, either by cancer transformation (*Li et al.*, 2008, 2009) or by drug treatment (*Moreno-Flores et al.*, 2010; *Lam et al.*, 2012), is correlated with the change in viscoelastic behavior.

Data obtained from three setups is presented in this chapter to validate this hypothesis. Table 5.1 is a summary of the number of cells tested as well as the value of the calibrated spring constant of the cantilever used in each setup.

Cell Groups	Expt.#1	Expt.#2	Expt.#3
MCF-10A (Benign)	n=23	n=24	
MCF-7 (Malignant)	n=23	n=24	
MCF-10A (Untreated)			n=17
MCF-10A (Treated)			n=17
k (N/m)	0.120	0.083	0.080
Probe No.	1	2	3

Table 5.1: Number of breast cancer cells tested in three AFM indentation setups

Mean and standard deviations for MCF-10A and MCF-7 groups from the first

setup are shown in Figure 5.3. The top figure shows the force-time responses for both RR (hysteresis) and RH (relaxation) loading types. The bottom one is a zoom-in view of the force-time behavior in RR (hysteresis) cycles. Similarly, Figure 5.4 presents the mean and standard deviations for MCF-10A and MCF-7 groups acquired from the second setup. Data obtained from the drug treatment approach is presented in Figure 5.5 which includes the mean and standard deviations for the untreated MCF-10A cells as compared to the treated cells. Due to the nature of biological cells, large variations were observed. Additionally, the magnitudes of the peak forces are significantly influenced by the loading rates. As shown in Figures 5.3 - 5.5, in all three setups, the peak force value drops as the loading rate decreases. This suggests a relaxing behavior of the cell, which also corresponds to the relaxation parts during the ramp-hold (RH) periods.

For a preliminary, qualitative comparison, each force-time curve is normalized by the value of its maximum peak force. The corresponding normalization data from these setups are plotted in Figures 5.6 - 5.8. As observed in Figure 5.6, the force-time responses of MCF-7 cells exhibited more relaxation than the ones obtained from MCF-10A cells. Specifically, at the end of the loading range, the mean force-time of the MCF-10A group dropped by about 57.72%, while an amount of about 76.86% was seen in the MCF-7 group. This trend was also observed in Figure 5.7. Here, the mean force-time of the MCF-10A group decreased by about 50.62% as compared to about 77.19% drop in MCF-7 group. Similarly, the treated MCF-10A group also experienced more relaxation than the untreated MCF-10A group. Data presented in Figure 5.8 showed that, at the end of the loading range, the decreases in the force-time responses for the untreated and treated groups were about 53.13% and 87.23%, respectively. These may imply that changes in the cytoskeleton, either due to disease states or a drug treatment, can be correlated with the viscoelastic (history-dependent) properties, especially the relaxation characteristics.

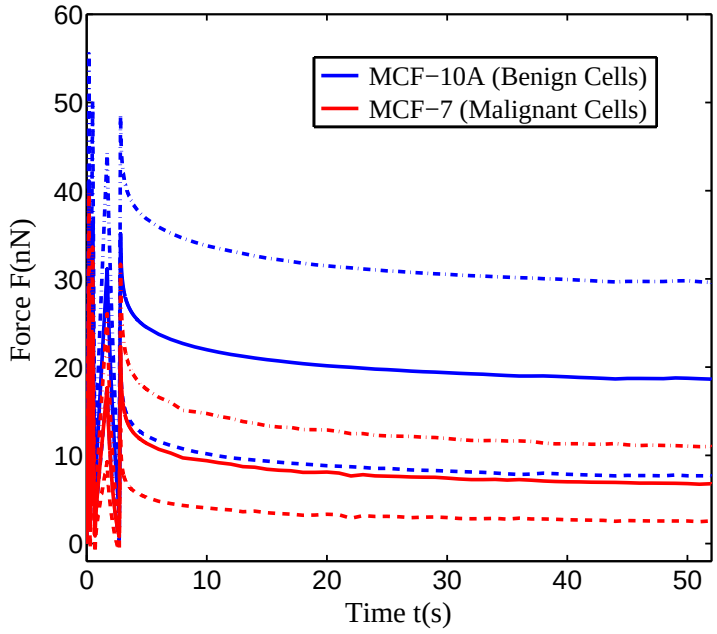

(a)

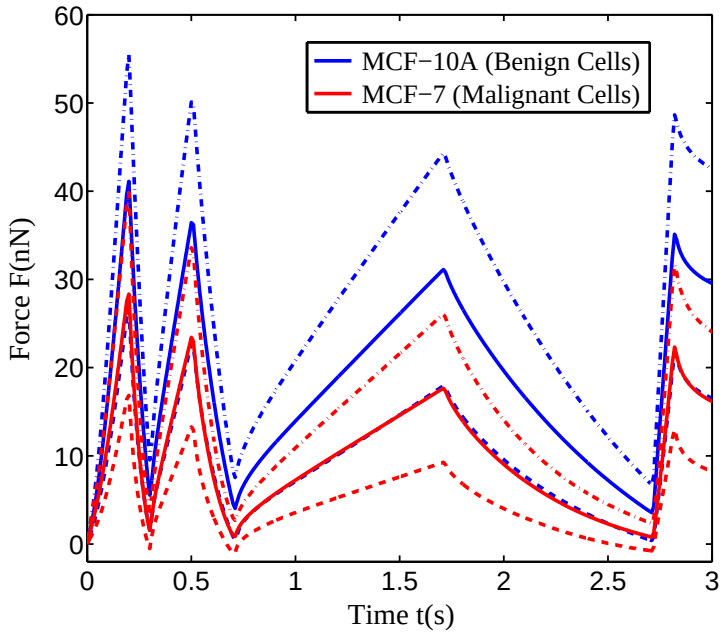

(b)

Figure 5.3: AFM experimental data (mean and standard deviations) for MCF-10A and MCF-7 cells obtained in the first setup: (a) Both RR (ramp-reverse) and RH (ramp-hold) responses (b) Zoom-in view of the RR (ramp-reverse) responses.

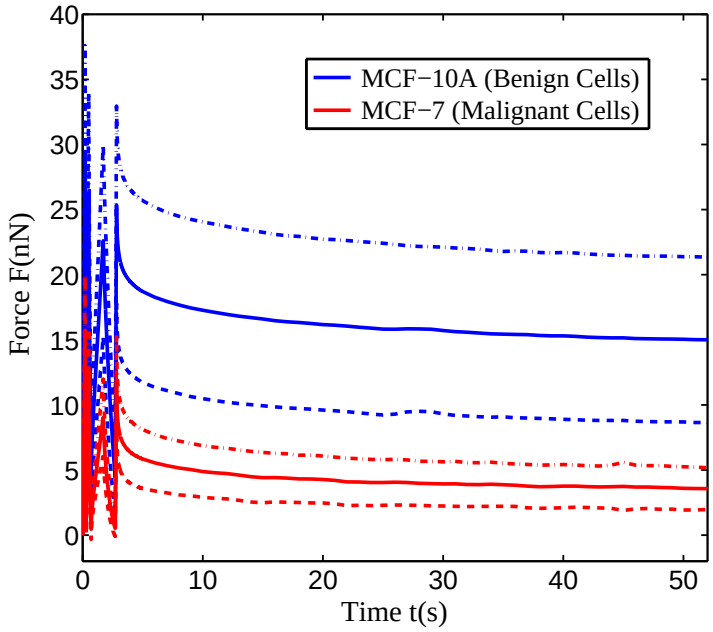

(a)

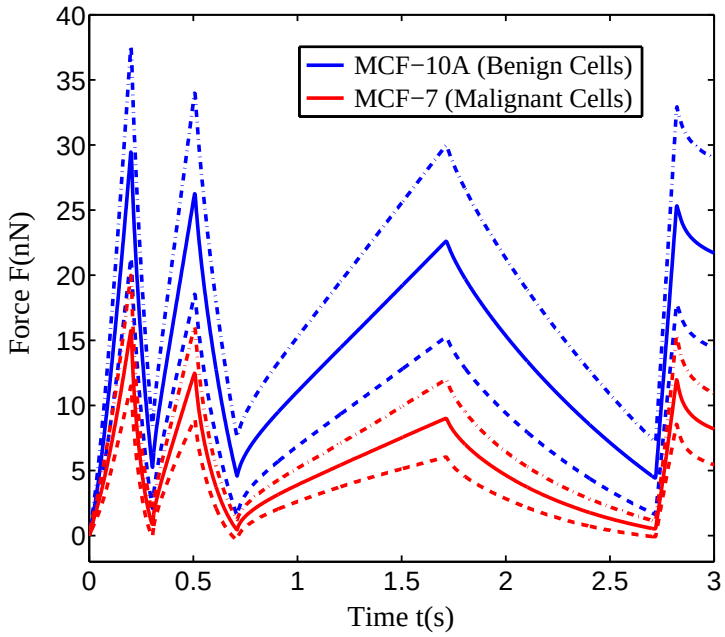

(b)

Figure 5.4: AFM experimental data (mean and standard deviations) for MCF-10A and MCF-7 cells obtained in the second setup: (a) Both RR (ramp-reverse) and RH (ramp-hold) responses (b) Zoom-in view of the RR (ramp-reverse) responses.

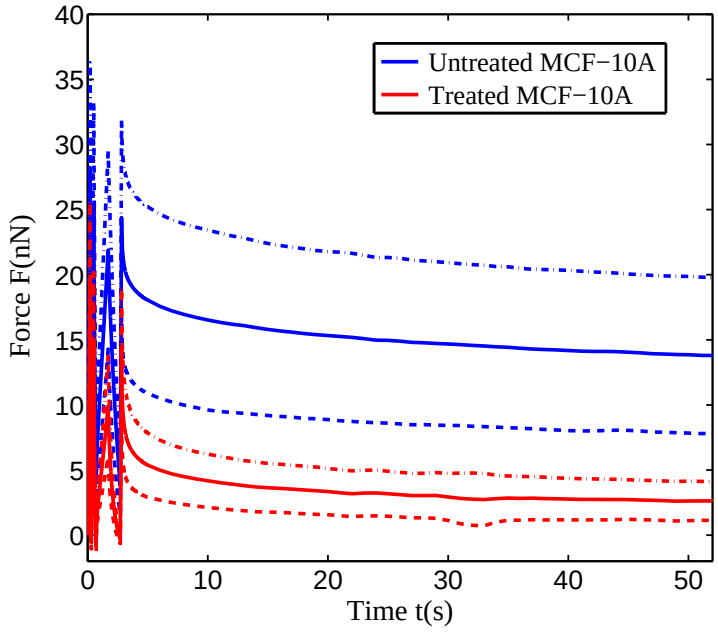

(a)

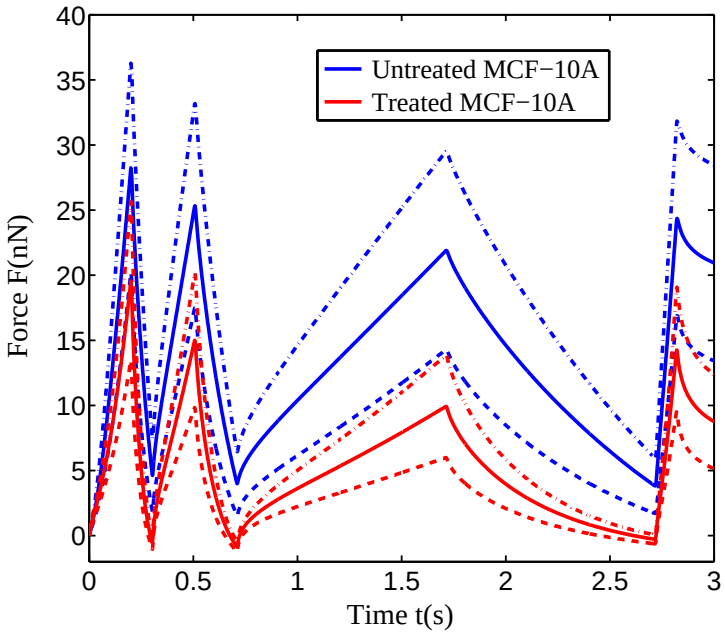

(b)

Figure 5.5: AFM experimental data (mean and standard deviations) for MCF-10A cells, untreated and treated with the drug cytochalasin D, obtained in the third setup: (a) Both RR (ramp-reverse) and RH (ramp-hold) responses (b) Zoom-in view of the RR (ramp-reverse) responses.

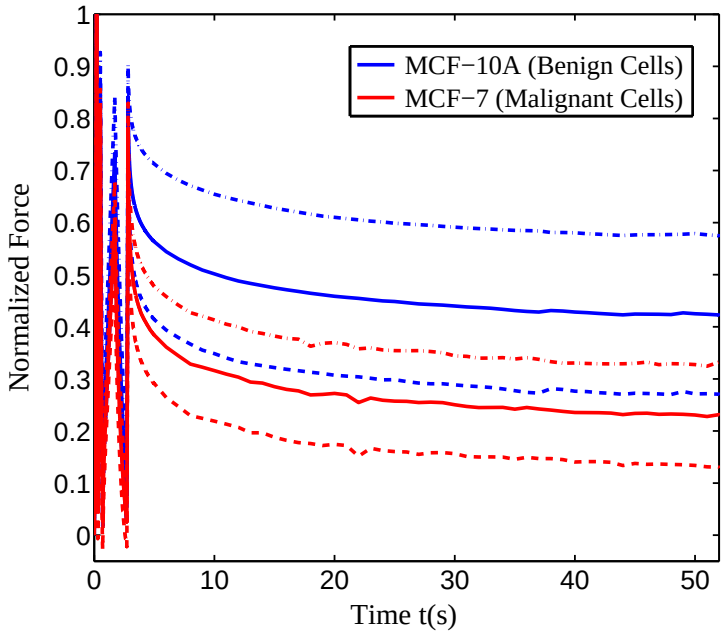

Figure 5.6: Normalization by the peak force for MCF-10A and MCF-7 cells (first setup).

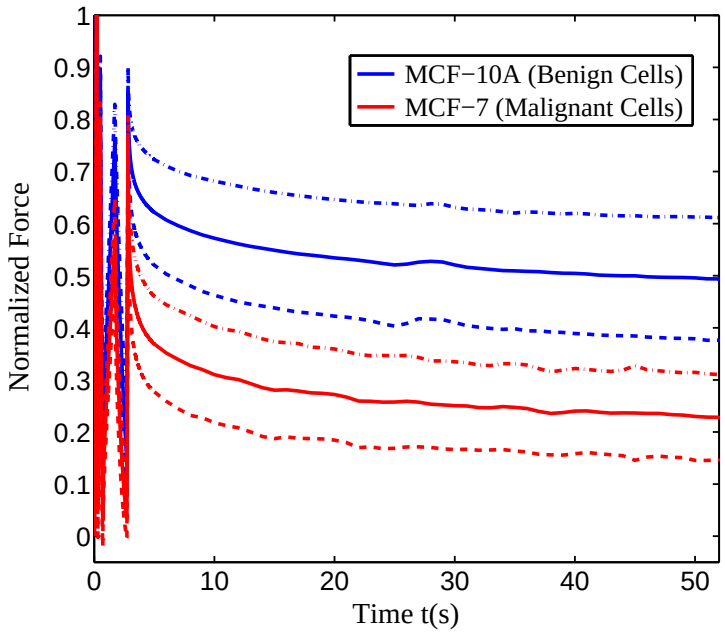

Figure 5.7: Normalization by the peak force for MCF-10A and MCF-7 cells (second setup).

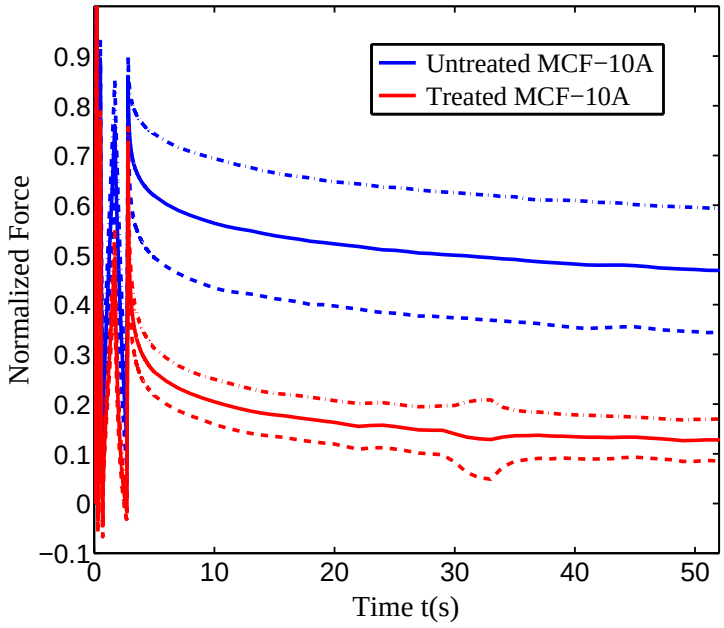

Figure 5.8: Normalization by the peak force for MCF-10A cells and MCF-10A cells treated with the drug cytochalasin D (third setup).

5.3 FE Modeling

The FE method with the commercial code ABAQUS (*ABAQUS-v6.10*, 2010) was employed to model the two-step indentation process described in section 5.2.2. The seeded cell was assumed to be an isotropic, homogenized, axisymmetric body having an oblate-shape with a circular base (*Ladjal et al.*, 2009). For each tested cell, the diameter of the base was estimated as the square root of the product of two representative distances taken from its optical images (*Bernick et al.*, 2011). A typical image for a tested cell is shown in Figure 5.9. The cell height was estimated using the contact points of force-curves on the cell body and on the nearby glass surface (*Bernick et al.*, 2011). For this purpose, after the measurements using the above two-step indentation process were conducted, the typical indentation procedure, in which the AFM ramp mode was used to ramp the piezo movement in a ramp-reverse loading, were also performed to acquire the force curves on specified locations of the

cell body and the glass coverslip's surface. A trigger value of 50 nm was selected to limit the amount of the maximum cantilever deflection, which corresponded to a limit value of about 4 - 6 nN for the maximum applied force. A typical comparison between force curves on the cell body and on the glass substrate is shown in Figure 5.10. The difference between the two contact points gives an estimation for the cell height.

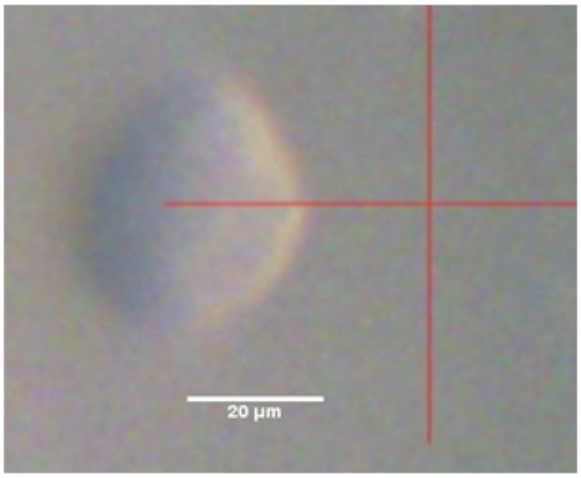

Figure 5.9: An optical image of a single breast cancer cell on a glass substrate captured by the optical microscopy in an AFM Bruker Dimension Icon.

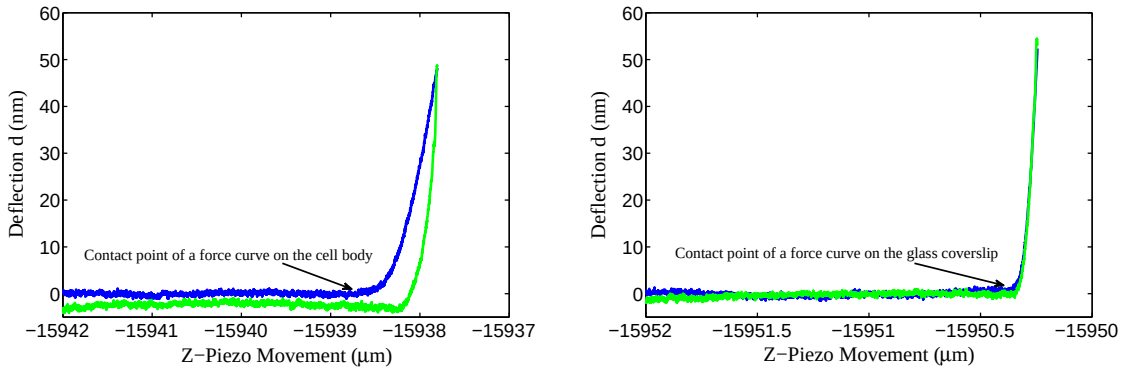

(a) (b)

Figure 5.10: Cantilever deflection vs. the piezo movement curves (with the reference corresponds to the highest location of the scanner): (a) On a breast cancer cell body (b) On the glass surface. The difference between the two contact points gives an estimation of the cell height

.

Mean and standard deviations of the estimated diameters and heights for the

tested cell groups are shown in Table 5.2.

	Expt.#1		
	MCF-10A	MCF-7	Combine
Height H(μm)	9.91 ± 2.47	14.64 ± 5.21	12.22 ± 4.66
Diameter D(μm)	28.31 ± 6.07	29.52 ± 4.32	28.88 ± 5.28
	Expt.#2		
	MCF-10A	MCF-7	Combine
Height H(μm)	10.16 ± 2.94	13.78 ± 4.90	11.96 ± 4.40
Diameter D(μm)	31.66 ± 6.15	30.07 ± 5.06	31.00 ± 5.60
	Expt.#3		
	MCF-10A (Untreated)	MCF-10A (Treated)	Combine
Height H(μm)	8.54 ± 2.00	9.15 ± 2.36	8.84 ± 2.17
Diameter D(μm)	27.30 ± 5.15	27.96 ± 4.50	27.63 ± 4.77

Table 5.2: Mean and standard deviations for cell's diameter and height estimated from three setups

For the first setup, an axisymmetric FE model for a representative cell, using the mean height and diameter values of $H = 12.22$ μm and $D = 28.88$ μm, was used to simulate the indentation process. The cantilever with the spherical probe was modeled as a spring connected to a rigid sphere of diameter 5 μm. The spring stiffness was set equal to the calibrated value obtained from the AFM experiments, which was 0.12 N/m in this case. The spherical probe was modeled as a rigid body. Its contact with the cell was assumed to be frictionless, and the normal behavior was modeled by the hard contact option in ABAQUS. The entire procedure of the two-step indentation as described in section 5.2.2 was simulated, in which the input was applied to the free end of the spring. The cell deformation was extracted as the displacement of the other end of the spring. The difference between the displacements of these two ends of the spring is how much the cantilever bends during the indentation process, and is related to the reaction force by the linear relation: $F = kd$. The boundary conditions of the problem were imposed by fixing the bottom surface with the assumption that the cells attach firmly to the coverslip. This approach was also used to model the indentation processes in the other two setups. Specifically, for the second setup, the dimensions

of the representative cell were $H = 11.96$ μm and $D = 31.00$ μm, and the spring constant stiffness was 0.083 N/m. For the third setup, these values were $H = 8.84$ μm, $D = 27.63$ μm, and k = 0.080 N/m. Convergence studies were also performed by varying the mesh size of each model. Illustrated in Figure 5.11 are three cases of meshing used for the first setup, in which the numbers of total elements were (a) 1192, (b) 4213, and (c) 16582. The force-time responses from the last two mesh sizes were converged, and were only slightly different from the response obtained from the first mesh. In this work, the middle mesh size was used to simulate the indentation for the first setup. The same process was applied to determine the optimum mesh size in modeling the second and the third setups. FE models using the mean geometric values for individual groups in each setup were also constructed. Their use will be discussed in detail in the next section.

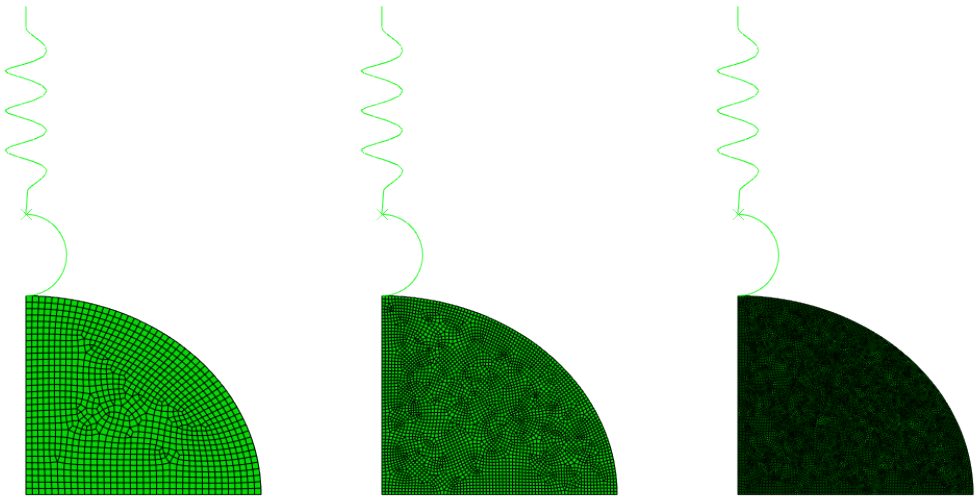

(a) (b) (c)

Figure 5.11: FE model for an AFM indentation test on breast cancer cells with three cases of meshing: (a) 1192 elements, (b) 4213 elements, and (c) 16582 elements

5.4 Results and Discussions

5.4.1 Implementation of the Inverse Analysis

At a relatively large imposed displacement (Figure 5.2), the cell behavior is better captured using a non-linear constitutive relation. Here, the built-in NLV model in ABAQUS (*ABAQUS-v6.10*, 2010) presented in section 4.3 was also employed to describe the time-dependent behavior of the cells. For simplicity, a neo-Hookean type model for the NLE part was utilized. With the incompressibility assumption, for each tested cell, five unknown material parameters need to be characterized, and its shear relaxation modulus as a function of time is constructed as follows:

$$G(s) = G_\infty + \sum_{k=1}^{2} G_k e^{-s/\tau_k} = G_0 \left[g_\infty + \sum_{k=1}^{k=2} g_k e^{-s/\tau_k} \right], \tag{5.1}$$

where $G_0 = G(0)$ is the instantaneous shear modulus, which also has the meaning of the neo-Hookean parameter C_1, is used to capture the NLE part. The coefficients g_1, τ_1, g_2, τ_2,in which $g_1 + g_2 < 1$, are from the two term Prony series (g_k, τ_k), $k = \overline{1,2}$ utilized to capture the relaxation behavior.

The inverse analysis based on surrogate modeling with a Kriging estimator, as discussed in Chapters III and IV (*Sacks et al.*, 1989; *Lophaven et al.*, 2002; *Queipo et al.*, 2005; *Forrester et al.*, 2008; *Gustafson and Waas*, 2009; *Heinrich and Waas*, 2009), was employed to extract these five NLV properties for each tested cell from its AFM indentation data. In this work, the material properties for all tested cells were searched within the material domain given in Table 5.3.

	C_1(kPa)	g_1	τ_1(s)	g_2	τ_2(s)
Lower bound	0.08	0.01	0.01	0.01	2
Upper bound	4	1	2	1	40

Table 5.3: Boundary of the material domain used in the process of determining the NLV properties of the tested breast cancer cells in three setups

For each FE model discussed in section 5.3, within the given material domain, the MATLAB's function "*lhsdesign*", in which the Latin Hypercube sampling technique was implemented, was applied to generate N and N^1 sets of material properties for a training group and a checking group, respectively. With the condition that $g_1 + g_2 < 1$, a training group composed of $N = 970$ sets of $x^i(G_0, g_1, \tau_1, g_2, \tau_2)$, $i = \overline{1, N}$ was used in this work. A checking group composed $N^1 = 354$ sets of $x^i(G_0, g_1, \tau_1, g_2, \tau_2)$, $i = \overline{1, N^1}$, which are different from the sets in the training group, was also generated. Since these sets of material parameters are independent, FE simulations were evaluated and the corresponding force-time responses were extracted in parallel. In this work, each force-time response was represented by $m = 5095$ discrete times, which were used to discretize the total loading time in the ramp-reverse and ramp-hold cycles. Specifically, $N = 970$ sets of $(t_j, F(t_j))$, $j = \overline{1, m}$ and $N^1 = 354$ sets of $(t_j, F^1(t_j))$, $j = \overline{1, m}$ were obtained for the training and checking groups, respectively. In other words, the training group has $N = 970$ sets of material parameters $x^i(G_0, g_1, \tau_1, g_2, \tau_2)$, $i = \overline{1, N}$, which correspond to $N = 970$ sets of force values $y^i(F(t_j))$, $i = \overline{1, N}, j = \overline{1, m}$. Similarly, the checking group contains $N^1 = 354$ sets of material parameters $x^i(G_0, g_1, \tau_1, g_2, \tau_2)$, $i = \overline{1, N^1}$, which correspond to $N^1 = 970$ sets of force values $y^i(F^1(t_j))$, $i = \overline{1, N^1}, j = \overline{1, m}$. The MATLAB's Dace Toolbox (*Lophaven et al.*, 2002) is, therefore, applied to the training group to construct a non-linear functional relationship between $X(5, 970)$ and $Y(5095, 970)$. Its accuracy is checked through the checking group $X^1(5, 354)$ and $Y^1(5095, 354)$. For the specific problem considered here, since no experimental force-time curve obtained in the three setups has a peak force value smaller than 4 nN, an extra criterion is utilized to remove the force responses which violate this observation in both training and checking groups. This extra criterion is used to help the construction of the surrogate model easier and reduce the need of adding more training points. Typically, with this criterion, about 4-10 cases were removed from the training group, and about 2-5 were

removed from the checking group. The specific numbers depend on the FE model used in generating the surrogate model. For brevity, this section only discusses the surrogate model and the Kriging predictor constructed using one particular FE model from the first setup. Surrogate models and Kriging predictor for other FE models, as discussed in section 5.3, were also constructed using this described procedure.

In particular, a surrogate model with a Kriging predictor was constructed, using the FE model for a representative cell of $H = 12.22$ μm and $D = 28.88$ μm (first setup). It is a non-linear relationship between sets of material properties $X(5, 962)$ and sets of the corresponding force responses $Y(5095, 962)$. The accuracy of this Kriging predictor was verified through the checking group, which is composed of $X^1(5, 349)$ and $Y^1(5095, 349)$. For these 349 cases, the RMSE values were evaluated as follows:

$$RMSE(i) = \frac{1}{range(y^i_{FE})} \sqrt{\frac{1}{5095} \sum_{k=1}^{5095} (y^i_{FE(k)} - y^i_{Krg(k)})^2}. \tag{5.2}$$

These values range from 0.03 % to 8 %. Representative comparisons between the actual FE responses and the predictions obtained by Kriging predictor are shown in Figure 5.12. As shown in this figure, many predictions from Kriging overlayed with the actual FE responses, and the differences between the two corresponding curves (red and blue) are not visible in this plot. The property extraction process is then implemented by optimizing the error between the obtained experimental data with predictions from this Kriging predictor using the MATLAB's function *fmincon*. FE simulations were also evaluated at these extracted sets of material properties, and then were compared with the experimental data. Representative comparisons between the experimental data and FE evaluations using the optimized sets of material properties from this inverse procedure are presented in Figure 5.13.

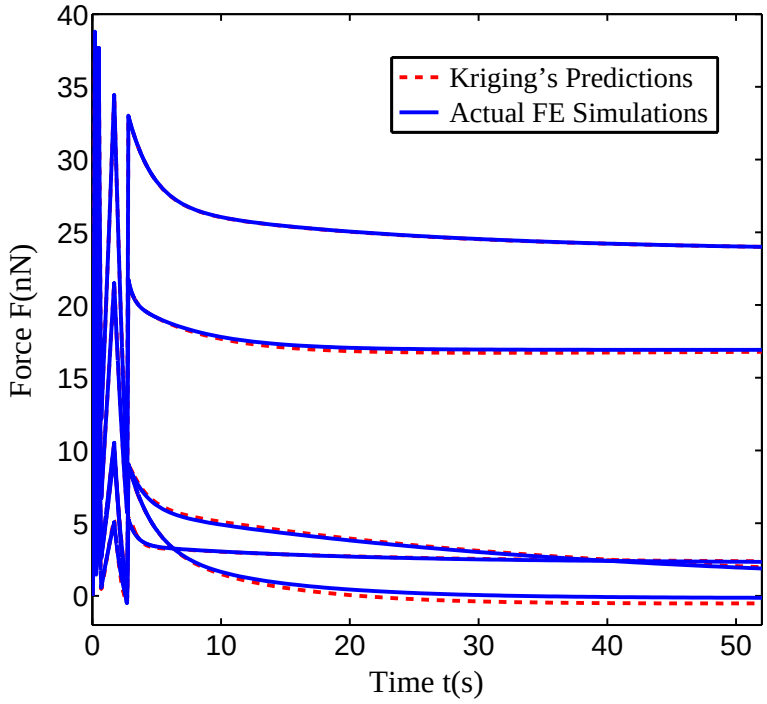

(a)

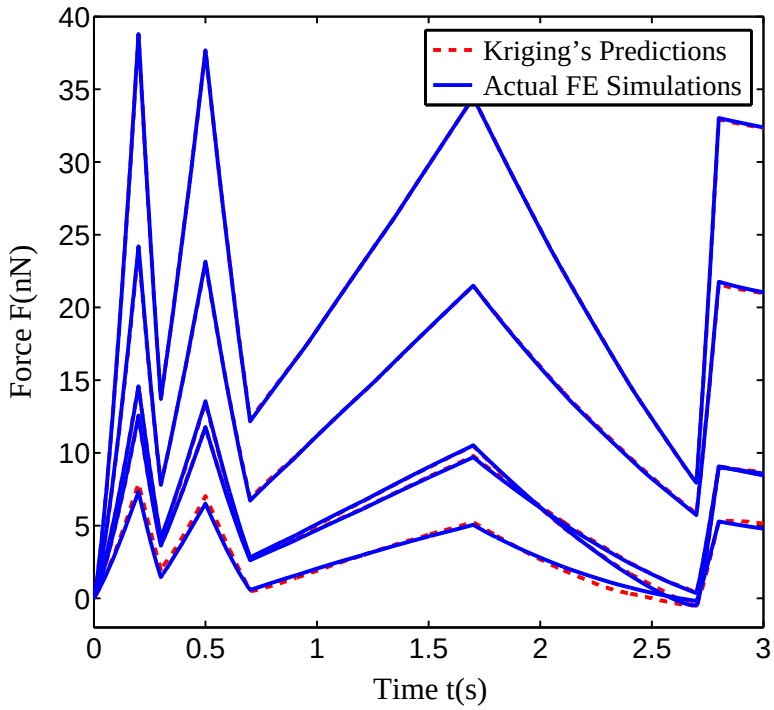

(b)

Figure 5.12: Representative comparisons between FE and Kriging predictions: (a) Both RR (ramp-reverse) and RH (ramp-hold) loadings (b) Zoom-in view of RR (ramp-reverse) cycles

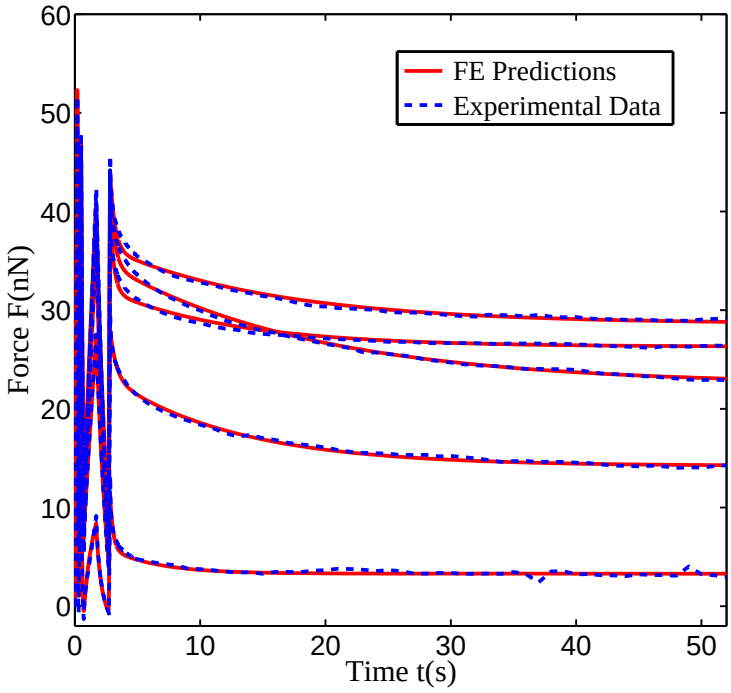

(a)

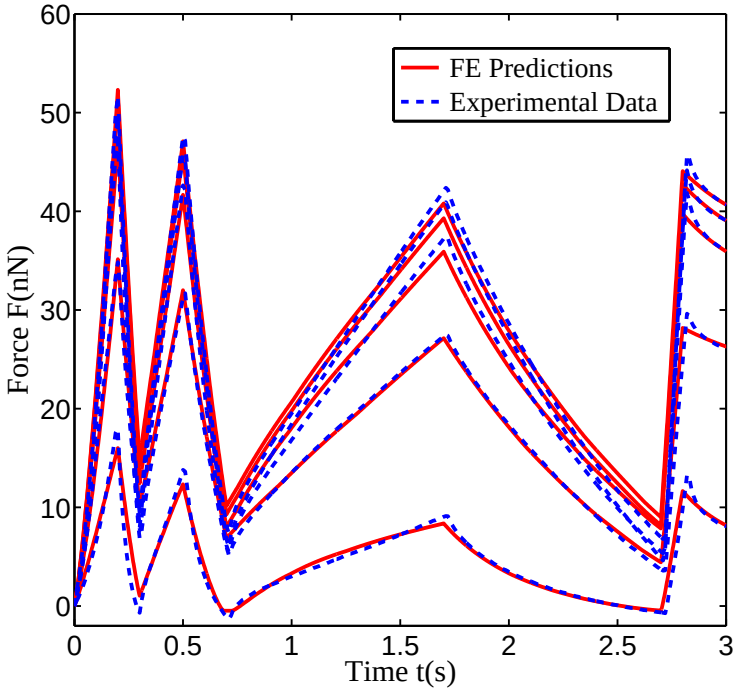

(b)

Figure 5.13: Representative comparisons between experimental data and FE predictions at the corresponding extracted sets of material parameters: (a) Both RR (ramp-reverse) and RH (ramp-hold) loadings (b) Zoom-in view of RR cycles.

As shown in this Figure, predictions from FE captured quite well the complicated responses of the experimental data from five individual MCF-10A cells in the first setup. The RMSE values for these fittings were evaluated as follows:

$$RMSE(i) = \frac{1}{range(y^i_{exp})}\sqrt{\frac{1}{5095}\sum_{k=1}^{5095}(y^i_{FE(k))} - y^i_{exp(k)})^2}. \tag{5.3}$$

Such values for fitting the data obtained from $n = 23$ MCF-10A and $n = 23$ MCF-7 cells of the first setup lie between 2 % to 8 %, with a mean value of about 4 % which indicate reasonable agreement between FE predictions and experimental data from all tested cells. With the same approach, NLV properties were also extracted from the experimental data from the other two setups.

At this step, an optimal set of five NLV parameters $(G_0, g_1, \tau_1, g_2, \tau_2)$ was extracted for each tested cell. For comparison purpose, the shear relaxation moduli were constructed using equation (5.1). Comparisons utilizing this shear relaxation modulus is expected to be more reasonable and consistent than using individual material parameters. Results are discussed in detail in the next section.

5.4.2 Discussion, Limitations, and Concluding Comments

Shear relaxation moduli for MCF-10A and MCF-7 cells measured in the first setup are shown in Figure 5.14(a). Here, the instantaneous shear modulus values for MCF-10A cells are $G(0) = 2.94 \pm 1.35$ kPa as compared to $G(0) = 1.94 \pm 1.02$ kPa obtained for MCF-7 cells. The mean results of the instantaneous shear modulus indicate that MCF-10A cells are about 1.5 times stiffer than MCF-7 cells at the instantaneous response. At the long term response, such as at the end of the loading, $t = 52s$, the shear modulus values for MCF-10A and MCF-7 cells obtained in this setup are $G(52) = 1.00 \pm 0.64$ kPa and $G(52) = 0.36 \pm 0.21$ kPa, respectively. The mean results of this long-term shear modulus indicate a larger difference of 2.8 times as

compared to the corresponding instantaneous values. To further determine whether the observed differences here are significant or not, statistical comparisons using the Wilcoxon rank sum test in MATLAB are used. Figure 5.14(b) shows that the two groups exhibit significant differences in terms of the shear relaxation modulus. The difference becomes more significant at the long term response. Such results indicate that combining the history-dependent characteristics into the calculations of the shear relaxation modulus might help to rule out larger difference between these two cell groups.

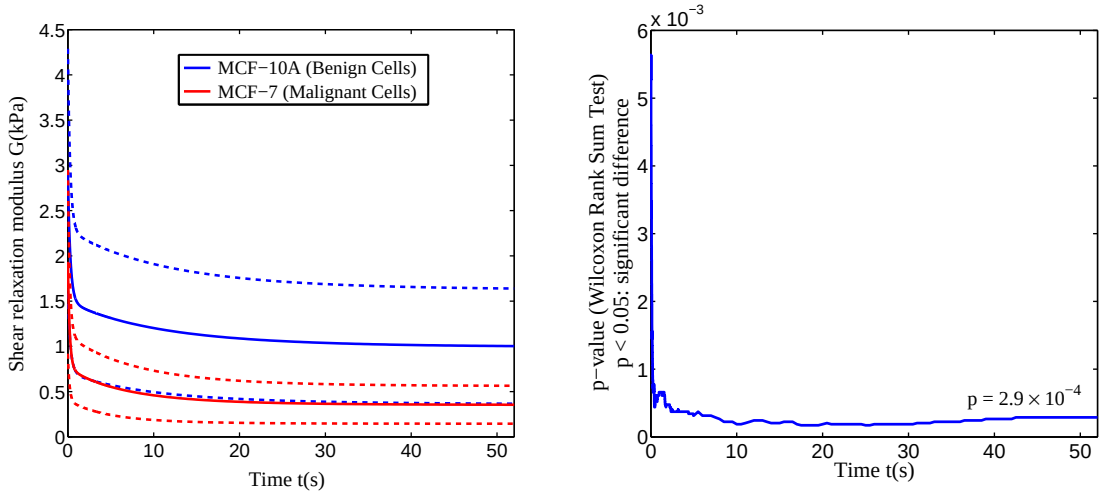

(a) (b)

Figure 5.14: Comparisons between MCF-10A and MCF-7 cells (in the first setup): (a) Mean and standard deviations of the shear relaxation modulus for $n = 23$ MCF-10A (blue) and $n = 23$ MCF-7 (red) cells (b) Statistical comparison: $p < 0.05$ indicates significant difference.

In addition to the shear relaxation modulus, the amount of relaxation $G(t)/G(0)$ can also be compared between two groups. Figure 5.15 shows the mean and standard deviation of the normalized shear relaxation modulus for both groups. In this case, the mean amount of relaxation for the MCF-10A group is about 67 %, while an amount of about 81 % was found for the MCF-7 group. At the end of the loading, statistical analysis using the MATLAB Wilcoxon rank sum test also indicates a significant

difference in the amount of relaxation between the two groups ($p = 1.2 \times 10^{-4}$).

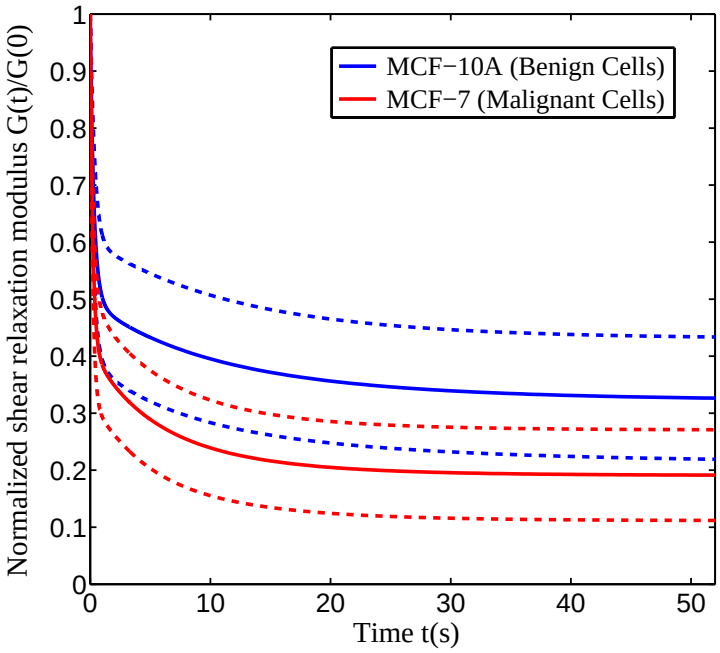

Figure 5.15: Mean and standard deviations of the normalized shear relaxation modulus $G(t)/G(0)$ for MCF-10A and MCF-7 cells (in the first setup)

Similar observations were also obtained when analyzing the data taken from the second setup. As shown in Figure 5.16(a), at each time, the shear relaxation modulus of the MCF-10A group exhibits a higher value than the modulus of the MCF-7 group. The statistical analysis also results in a significantly small p-value for the comparisons using the shear moduli of both groups. Again, the p-value becomes smaller at the long term response, as this might be due to the incorporation of viscoelasticity in the calculation of the shear relaxation modulus function. MCF-7 group also exhibits a larger amount of relaxation as compared to the MCF-10A group as presented in Figure 5.17. Specifically, the mean shear relaxation modulus for the MCF-7 group drops by 78 %, while the shear modulus for the MCF-10A group decreases by 57 % at the end of the loading. The p-value for this case is $p = 9.7 \times 10^{-7}$, which means the difference in terms of the amount of relaxation is significant as well.

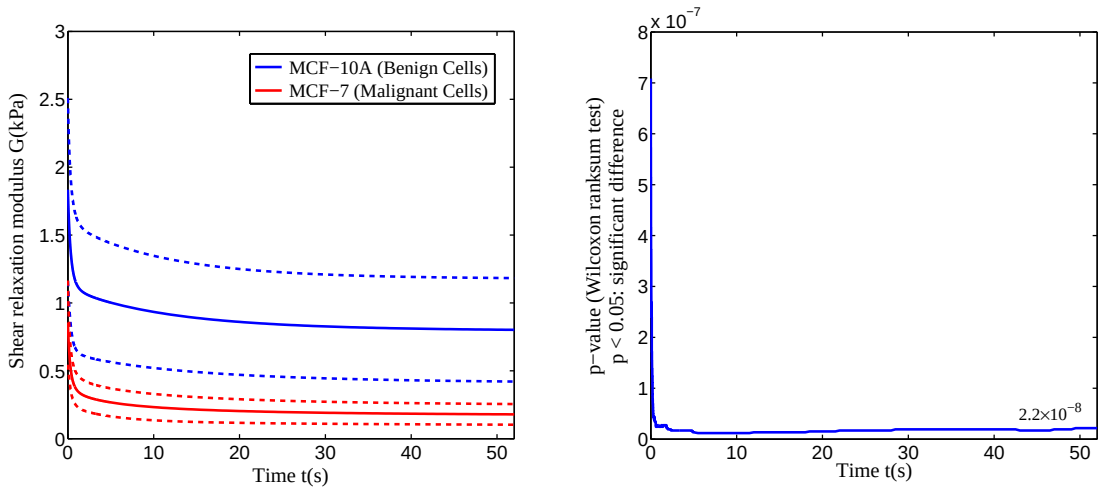

(a) (b)

Figure 5.16: Comparisons between MCF-10A and MCF-7 cells (in the second setup): (a) Mean and standard deviations of the shear relaxation modulus for $n = 24$ MCF-10A (blue) and $n = 24$ MCF-7 (red) cells (b) Statistical comparison: $p < 0.05$ indicates significant difference.

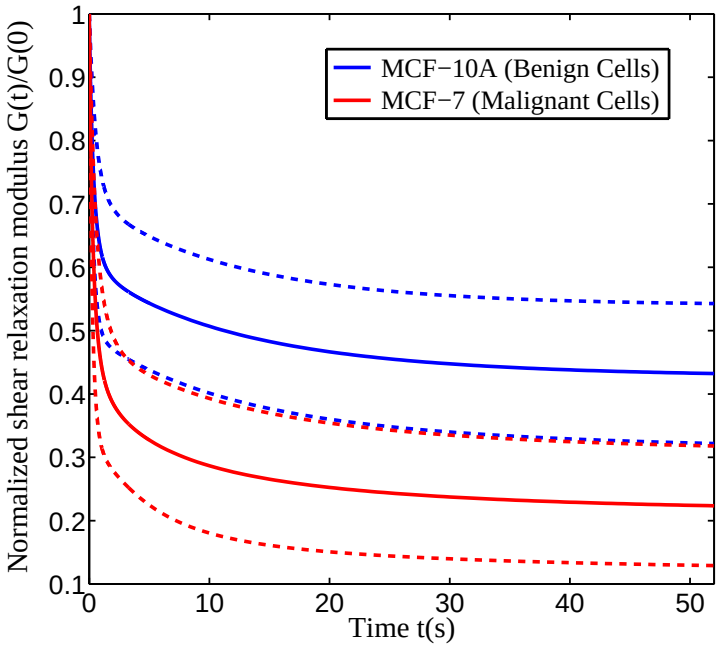

Figure 5.17: Mean and standard deviations of the normalized shear relaxation modulus $G(t)/G(0)$ for MCF-10A and MCF-7 cells (in the second setup).

So far, the results obtained for MCF-10A and MCF-7 cells from both setups

exhibit a similar trend for the relative difference between these two cell groups. The benign cells (MCF-10A) are stiffer and exhibit less relaxation than the malignant (MCF-7) cells. By considering viscoelasticity in the characterization of the shear modulus, the relative difference between them are also exhibited in terms of the long-term shear modulus. The data exhibited a larger difference in the long term response as compared to the corresponding difference in the instantaneous one.

Next, the data obtained for the untreated and treated MCF-10A cells using the drug cytochalasin D are also compared. Figure 5.18(a) shows the difference of the shear relaxation modulus between the two groups. Treating MCF-10A cells by the drug cytochalasin D does lead to a decrease in the stiffness. The difference is amplified in the long term response. As shown in Figure 5.18(b), the p-value drops drastically from the instantaneous to long term responses. Here, the plot was presented only up to a time $t = 3s$ for clarity. This agrees with the large difference in terms of the amount of relaxation obtained from these two cell groups. Specifically, at the end of the loading, the mean shear modulus of the untreated group decreases by about 60 %, while the mean value of the treated group drops by about 89 % (Figure 5.19). The p-value for this difference is $p = 1.2 \times 10^{-6}$.

Notice that the above comparisons in each setup were based on the NLV properties for both cell groups extracted using a FE model with a representative cell having the mean geometric dimensions. It is still challenging to take into account the dimension of each individual cell and construct separate FE models and surrogate modelings. Here, an alternative approach to investigate the effect of geometry on the relative difference between two group of cells is taken. For brevity, only results from the first setup are considered here. In particular, two separate FE models were used to model two cell groups. The first uses the mean height and diameter estimated for MCF-10A ($H = 9.90$ μm, $D = 28.30$ μm) group while the second uses the mean height and diameter ($H = 14.64$ μm, $D = 29.52$ μm) estimated for MCF-7 group.

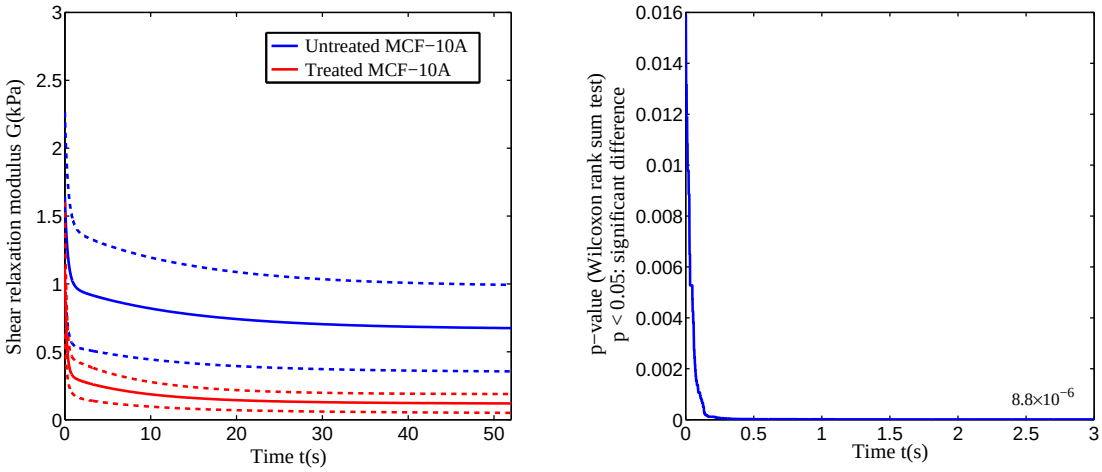

(a) (b)

Figure 5.18: Comparisons between the untreated MCF-10A cells and MCF-10A cells treated with the drug cytochalasin D (in the third setup): (a) Mean and standard deviations of the shear relaxation modulus for $n = 17$ untreated MCF-10A (blue) and $n = 17$ treated MCF-10A (red) cells (b) Statistical comparison: $p < 0.05$ indicates significant difference.

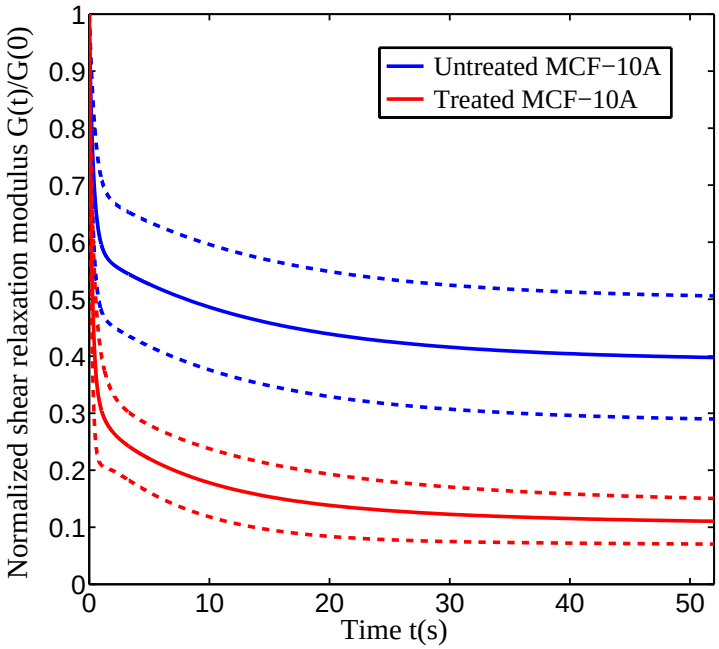

Figure 5.19: Mean and standard deviations of the normalized shear relaxation modulus $G(t)/G(0)$ for untreated and treated MCF-10A cells (in the third setup).

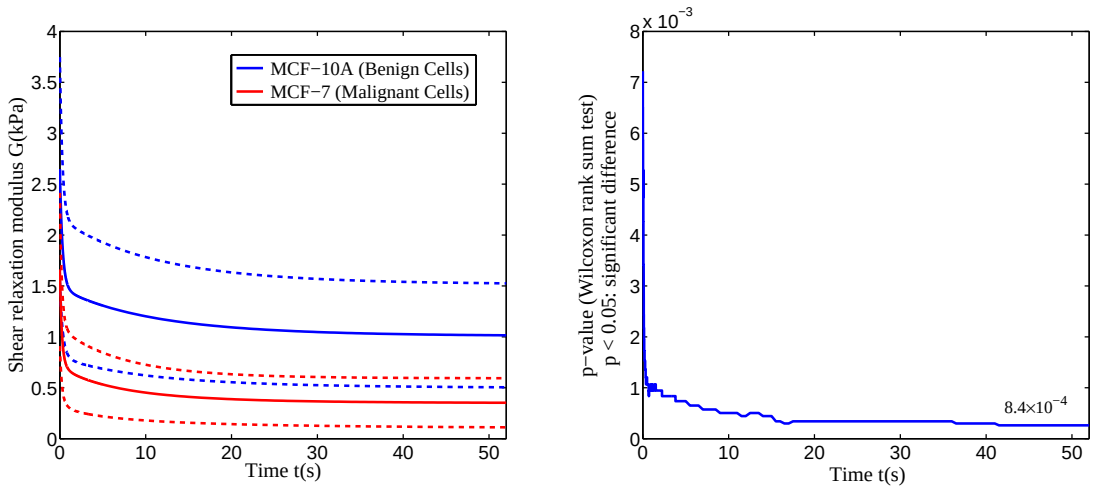

(a) (b)

Figure 5.20: Comparisons between MCF-10A cells and MCF-7 cells (in the first setup) using the data extracted based on two separate FE models: (a) Mean and standard deviations of the shear relaxation modulus for $n = 23$ MCF-10A and $n = 23$ MCF-7 cells (b) Statistical comparison: $p < 0.05$ indicates significant difference.

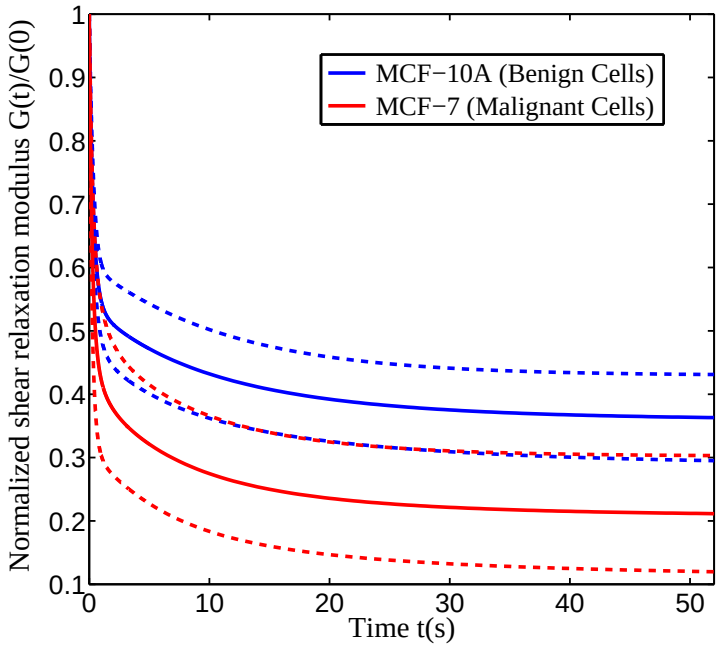

Figure 5.21: Mean and standard deviations of the normalized shear relaxation modulus $G(t)/G(0)$ for MCF-10A cells and MCF-7 cells (in the first setup) using the data extracted based on two separate FE models.

Interestingly, similar observations were still found for the relative difference between the two MCF-10A and MCF-7 groups as shown in Figure 5.20 and Figure 5.21.

The above analysis focuses only on the relative differences between two cell groups within one setup. The benign cells (MCF-10A) exhibit higher shear relaxation modulus statistically, as compared to the malignant cells (MCF-7). The amount of relaxation is also useful to distinguish these two groups of cells. Transformation into the malignant state might contribute to more relaxation in the response of the malignant cells. Disrupting the cytoskeleton of the MCF-10A cells also causes a drop in both shear relaxation modulus and an increase in the amount of relaxation. These relative differences were found to be consistent from setup to setup, which means that under the same experimental condition, including viscoelastic characteristics into the determination of the material properties proves helpful in providing more insight to differentiate different cell groups for disease detection purpose. Though the absolute values are not reliable (*Harouaka et al.*, 2013), the values for the shear relaxation modulus for MCF-10A and MCF-7 cells found in this work are within the range reported in the literature. For example, *Li et al.* (2008, 2009) reported the range for Young's modulus of MCF-7 cells to be 0.3-0.6 kPa, and the modulus of MCF-10A to be 1.4-1.8 times stiffer; *Leporatti et al.* (2009) reported the values in the range 15-30 kPa for MCF-7 cells; and the value in the work of *Moreno-Flores et al.* (2010) for MCF-7 cells is 4.7 ± 0.4 kPa. In this work, a combination of three setups provides a prediction of the instantaneous modulus of $E(0) = 3G(0) = 6.5 \pm 3.3$ kPa and $E(0) = 3G(0) = 4.2 \pm 2.7$ kPa for $n = 64$ MCF-10A and $n = 47$ MCF-7 cells, respectively. The predictions for the long term modulus, at $t = 52$s, are $E(52) = 3G(52) = 2.5 \pm 1.5$ kPa and $E(52) = 3G(52) = 0.8 \pm 0.5$ kPa for $n = 64$ MCF-10A and $n = 47$ MCF-7 cells, respectively.

The following limitations and sources of errors are noted in order to further investigate NLV aspects of living cells and evaluate whether the above differences could be

adopted for clinical use. Among these limitations, several are related to experimental issues, including the uncertainty in determining the contact points between cell body and the cantilever, cell geometric determination, and errors in the AFM calibrations. For example, an error of about 10-20% could be associated with the calibration of deflection sensitivity and spring constant (*Cumpson et al.*, 2004; *Dokukin et al.*, 2013). The optical resolution in the AFM Dimension Icon system used for all the tests in this thesis was limited, so it is advisable to enhance this feature for better estimations of the cell dimensions and shapes. Having a higher optical resolution also aids the selections of the cells for indentation purposes. This might help to reduce scatter due to geometry effects in the measured data. This issue could be addressed using an AFM system that has an inverted optical microscopy. Such a system is the MFP 3D, manufactured by Asylum Research. Other sources, such as the resolution and backlash in the Z-stepper motor intrinsic mechanical design (Appendix B, (*Titushkin*, 2013)), might cause error in cell height determination. Unintended delay can happen in running a script with high loading rates, such as in the first ramp-reverse cycle at the rate of 10μm/s. This contributes to an artifact in the acquisition of the force responses. For instance, instead of having a sharp peak force between the loading and unloading paths, a delay of the piezo might occur and cause unintended relaxation in the force-time response. A possible reason for this issue is the clogging up of the messaging in the computer operation (*Shaw*, 2013). Additionally, as a cell is dynamic and heterogeneous, the model considered here is still a very simple model. Though the NLV constitutive model with Prony series terms was able to capture various aspect of the responses, such as loading rate dependencies and relaxation characteristics, further refinement is necessary. For instance, the response associated with high rate loading and transition between various loading rates, if improved, is expected to lead to better agreement with the experimental data. Furthermore, improvements can be made to enhance the accuracy of the current surrogate modeling and Kriging

predictor, including adding more training points in the design site.

In summary, this chapter presents a methodology to study the NLV properties of breast cancer cells. Experimental data was acquired at a large strain regime incorporating many aspects, such as non-linear mechanics, rate dependency, and history-dependent characteristics. The data was analyzed using FE models and inverse modeling in connection with surrogate modeling and a Kriging predictor to resolve the computational cost issue. Comparisons were made based on the extracted shear relaxation modulus and results indicated significant differences in terms of the NLV responses between MCF-10A and MCF-7 cells as well as between untreated and treated MCF-10A cells.

CHAPTER VI

Conclusions and Future Work

6.1 Summary

A study of polymeric capsules and biological cells from a mechanics perspective is presented in this thesis. One objective is to develop an efficient methodology to determine history-dependent (viscoelastic) properties of these structures with a consideration of non-linear, large deformation theory and a combination of experiments, FE modeling, and a material property identification process. Another objective is to correlate the changes in these extracted properties with alterations in cell internal structure. Such a correlation may potentially lead to a useful disease detection method.

First, a constitutive relationship that can capture history-dependent behaviors (viscoelasticity) was discussed in Chapter II. Here, various aspects of a model based on a single integral NLV Pipkin-Rogers framework were studied by formulating and solving a boundary value problem. The formulation and solution methods incorporate important features in testing scenarios used for material identification. A problem of interest was compression of a liquid-filled, polymeric membrane by contact between two flat, rigid, and parallel plates. Under a displacement control assumption, the compression process was simulated and information, such as the relaxation force-time response, stretch distribution, and stretch history for the NLV membrane,

was obtained through both analytical and FE formulation approaches. Results provided insight into how viscoelastic parameters, including the relaxation time and the amount of relaxation, affect the deformation process. The presented procedure and the understanding obtained in this chapter served as a basis for the modeling process needed in solving the inverse problem to extract the NLV properties.

The next focus of this thesis was determining the NLV parameters using a simple and efficient inverse procedure to optimize the error between experimental data and FE predictions. For this purpose, a surrogate model and a Kriging predictor were applied. The goal was to construct a non-linear functional relationship that can be evaluated quickly to replace the need for repeating evaluations of costly and time-consuming FE simulations. In particular, the following steps are included in the inverse process.

- Within the material domain, sets of material parameters are generated for a training group and a checking group using a Latin Hypercube technique.
- FE simulations are evaluated and the corresponding force-time responses are extracted in parallel to allow a reduction in the total time cost of the inverse procedure.
- A Kriging predictor is constructed by training the relationship between the sets of material properties and their corresponding force-time responses using the MATLAB Dace toolbox. The predictor's accuracy is then checked through the use of the sets of material parameters and force-time responses in the checking group. When the error is small enough, the predictor is used to replace actual FE simulations.
- An optimization technique is implemented on the predictor to yield the optimized set of material parameters that can predict the force-time data observed in experiments.

The efficiency of the above inverse technique was examined by considering two specific inverse problems. In the first problem, experimental force versus time responses of liquid-filled polymeric capsules subjected to specified ramp-reverse and ramp-hold displacement control inputs in compression tests were used as the targets for the

fitting process. Results showed good agreement between the experimental data and predictions from the inverse process. The fitting procedure was more efficient than the traditional sequential inverse analysis, which would require repetitive evaluations of the 3D FE model used in this problem to simulate the compression process. Further studies in Chapter IV also suggest that using a combination of ramp-reverse and ramp-hold inputs leads to better predictions of the optimized NLV parameters.

The second problem dealt with a more challenging setup which was AFM indentation on biological cells. Breast cancer cells were tested to examine how the cell's NLV properties change as the cell's cytoskeleton structure was altered. Two cases were considered in Chapter V. The first studied two groups corresponding to the benign (MCF-10A) and malignant (MCF-7) states. The second examined two groups of MCF-10A cells, untreated and treated with the drug cytochalasin D. Force-time data for both cases were acquired following the experimental setup described in this chapter. It includes a two-step indentation input and combines both ramp-reverse and ramp-hold loading types with loading rates spanning between 1 μm/s to 10 μm/s. With the use of the same inverse technique (surrogate modeling and a Kriging Predictor), the relaxation properties of all the tested cells were extracted. The shear relaxation modulus for each tested cell was then determined as a function of time and used for quantitative comparisons to evaluate how statistically significant the relative differences between the two cell groups are. Results indicated that the shear relaxation modulus values for the two groups (MCF-10A and MCF-7 cells in the first case, and untreated and treated MCF-10A cells in the second case) were statistically different. Under an identical testing setup, the mean shear relaxation modulus of the benign (MCF-10A) is higher as compared to the mean value of the malignant (MCF-7) cells. Similarly, the untreated group also exhibits a higher value of the mean shear relaxation modulus as compared to the mean value of the treated one. The obtained results also suggested that significant differences might be associated with the long

term shear modulus. Additionally, the amount of relaxation was also observed to exhibit a statistically significant difference between the groups in each case. The benign group exhibits less relaxation as compared to the malignant group. Treating with the drug cytochalasin D to disrupt the cytoskeleton also leads to a drop in the amount of relaxation in the cell's response. These results may imply that considering viscoelastic aspects, such as the amount of relaxation and history effects, into the calculations of material parameters might provide potential criteria for comparison purposes. Together with preliminary work, which mostly uses analytical approaches to examine the differences in the stiffness (*Li et al.*, 2008, 2009), the approach and results obtained here serve as additional attempts for formulating effective bio-markers for breast cancer detection. The presented methodology in this thesis is, to the best knowledge of the author, the first that studies the differences between breast cancer cell lines by considering many features obtained using AFM experimental data (large strain regime, hysteresis responses with various loading rates, and relaxation behavior), utilizing the FE method for modeling purpose, and applying an automatic and efficient inverse process for material property identification.

6.2 Future Work

Various aspects of this thesis can be extended to further explore the methodology needed for understanding and determining the mechanical properties of polymeric capsules and biological cells. Suggestions for future research are presented next.

6.2.1 Experiments

6.2.1.1 Compression Test

As observed in compression tests, a buckling (loss of contact between specimen and indentor) phenomenon could occur at a large enough applied displacement. Studying

this event when taking into account viscoelastic effects, such as loading rates and loading types (RR-Hysteresis and RH-Relaxation), can provide more precise understanding of the mechanical features for the tested structures, especially at the large deformation regime. The knowledge might also be applied to the analysis of mechanical responses obtained from other testing setups, such as an AFM indentation test on micro-capsules using a tipless cantilever. Hence, it would be useful to improve the resolution of the optical arrangement used in this thesis to capture this time-dependent buckling phenomenon.

6.2.1.2 AFM Indentation

In this thesis, AFM indentation tests on breast cancer cells were conducted at room temperature. It is recommended to repeat the presented testing procedure at 37^0C to keep the cells at their physiological temperature and to study the effects of testing temperature on cells' viscoelastic properties. This purpose can be implemented by using an AFM system with a temperature control function. Such a system is the MFP 3D instrument, manufactured by Asylum Research.

Another feature that was not considered in this thesis is the effect of the probe's size on the measured force-time data. It might be useful to investigate such an effect by employing AFM cantilevers attached to spherical probes of various diameters.

Additionally, the effectiveness of the presented methodology for comparison and diagnosing purposes can also be further studied by conducting the following additional AFM indentation measurements:

- It is necessary to extend the current drug treatment approach to include the effects of the drug concentration on the cell's viscoelastic responses. A suggestion is to treat MCF-10A and MCF-7 cells with different amounts of drugs and investigate the changes in relaxation properties. It might also be interesting to examine whether the alterations in terms of these properties are cell-type dependent. If this is the case,

the drug treatment method followed by measuring viscoelastic features may be useful for differentiating different cell types.

- Cell's preparation using a patterning technique is another useful approach (*Shao*, 2014). The technique enables the control of the cell's size and shape through confining it into a specific area. Due to the differences in the confinement area, the cytoskeletal structure can be altered differently. Therefore, characterizing the viscoelastic properties for the patterned cells will allow a further study of the correlation between the alteration in the cell's cytoskeleton and the viscoelastic properties.

- As this thesis's main focus is from a mechanics perspective, it did not examine specific changes and alterations in the cytoskeleton structure. Future studies should combine both mechanical measurements and observations of cytoskeletal structure to investigate the correlation between them. An AFM system that can be used to obtain this goal is the MFP-3D, Asylum Research system. The instrument allows simultaneous AFM and fluorescence measurements. Hence it is able to capture the changes, such as actin filament's orientation, while measuring the mechanical responses (*Li et al.*, 2008).

In addition, the presented procedure is also applicable to the study of viscoelastic features of other soft materials, such as biological tissues.

6.2.1.3 Other Experimental Setups

As the presented procedure uses a FE method, it is expected to be useful for the analysis of experimental data obtained from other experimental setups. For example, the aspiration process in a micropipette experiment can be captured by a FE model that includes contact features, history-dependent characteristics, and variations in the applied pressure (*Dong and Skalak*, 1992). Hence, an extension of this thesis is to employ other experimentations for testing purposes and to analyze the obtained data by a combination of FE modeling and an inverse process based on a surrogate

model and a Kriging predictor. Outcomes are expected to contribute to the current methods for data interpretation from these mechanical testing platforms.

6.2.2 Modeling

A cell is a complex and dynamic structure. In this work, it is simplified as a homogeneous, axisymmetric, and solid body. Therefore, in future work, many complicated features should be added to this model. One possibility is to model the cell as a 3D capsule filled with a fluid (cytoplasm). Another is utilizing the application of tensegrity concepts (*Mofrad and Kamm*, 2006) to include various components, such as actin and intermediate filaments, into the cell model.

APPENDICES

APPENDIX A

AFM Indentation of Prostate Cancer Cells

This Appendix contains a study of mechanical properties of two prostate cancer (PC-3) cell lines, provided by *Elbez* (2013). Specifically, epithelial (PC-3E) and mesenchymal (PC-3M) cells (*Roca et al.*, 2013) were indented using AFM indentation technique. The following is a summary of experiments, data analysis, discussions, and suggestions for further work.

A.1 Experiments and FE Model

A.1.1 Materials

Prostate cancer cells (PC-3E and PC-3M) were cultured in RPMI-1640 supplemented with 10% Foetal Bovine Serum (FBS), and 1% Anti-Anti (anti-miccotic, anti-microbial) in a cell incubator at 37^0C, with humidity control and 5% CO_2. Cells were plated on tissue culture dishes until reaching a confluency of 80%. Cells were then washed using Phosphate Buffer Saline (PBS), and were put back in 8 mL cell culture media before being detached using a cell scrapper. Glass coverslips were drawn in cell culture media and placed in cell culture dishes, before adding cells at a confluency of around 10%, and let to adhere and divide for 24 hours.

To keep cells healthy before experiments, they were kept in a smaller incubator at 37^0C. The growth media with HEPES at 25 mM to avoid pH changes in the absence of CO_2 were supplemented. CO_2 independent media was regularly changed in between experiments. More details are provided by *Elbez* (2013) from whom this section has been taken.

A.1.2 AFM Indentation Tests

With the experimental setup described in Chapter V, PC-3E and PC-3M cells were indented in the CO_2 independent medium using the following loading input, which is composed of two steps.

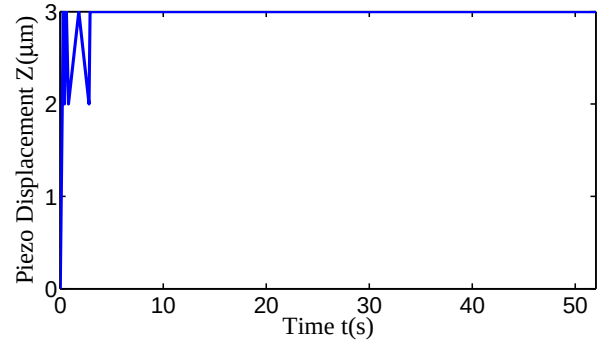

(a)

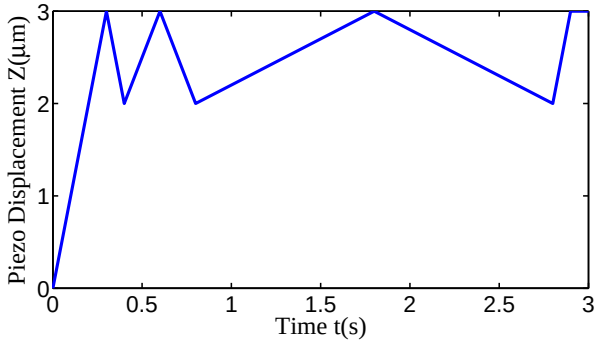

(b)

Figure A.1: Applied input Z for controlling the AFM piezo movement: (a) The entire step (b) Zoom-in view of the RR (ramp-reverse) cycles.

Step 1: Ramping the setpoint (force) to engage the probe on the cell's surface with a small force value (ramp velocity: 1 nm/s, $\delta d = 5$ nm, and the applied force value

was about 0.2 - 0.4 nN, depending on the spring constant value of each cantilever). A hold period of 15s was utilized in these experiments.

Step 2: A sequence of RR (hysteresis) and RH (relaxation) loading processes, as shown in Figure A.1, was applied to the piezo. In the first RR cycle, the piezo moved down by an amount of 3 μm, then retracted by an amount of 1 μm. These positions of loading were repeated in the following cycles (Figure A.1).

A.1.3 Experimental Data

Table A.1 presents the number of cells tested in four setups and the value of the calibrated spring constant of the cantilever used in each setup.

Cell Groups	Expt.#1	Expt.#2	Expt.#3	Expt.#4
PC-3M (Mesenchymal)	n=9	n=20	n=7	n=11
PC-3E (Epithelial)	n=27	n=14	n=8	n=13
k (N/m)	0.072	0.072	0.054	0.072
Probe No.	1	1	2	3

Table A.1: Number of prostate cancer cells tested in four AFM indentation setups

Mean and standard deviations for PC-3M and PC-3E groups from these four setups are shown in Figures A.2 - A.5, respectively. Data suggested significant viscoelastic features, including the dependence of the peak forces on the loading rates and the relaxation behavior in the ramp-hold loading. Each force-time curve is also normalized by the value of its maximum peak force. The corresponding normalized data are plotted in Figures A.6 - A.9. At the end of the loading, the mean amount of relaxation of the PC-3E group is slightly higher than the mean value of the PC-3M group. Specifically, the relaxation amounts of the PC-3E group are 68 %, 70 %, 82 %, and 63 % as compared to 61 %, 61 %, 74 %, and 56 % drops observed in PC-3M group for the four setups, respectively. The difference between the two groups, however, was not significant.

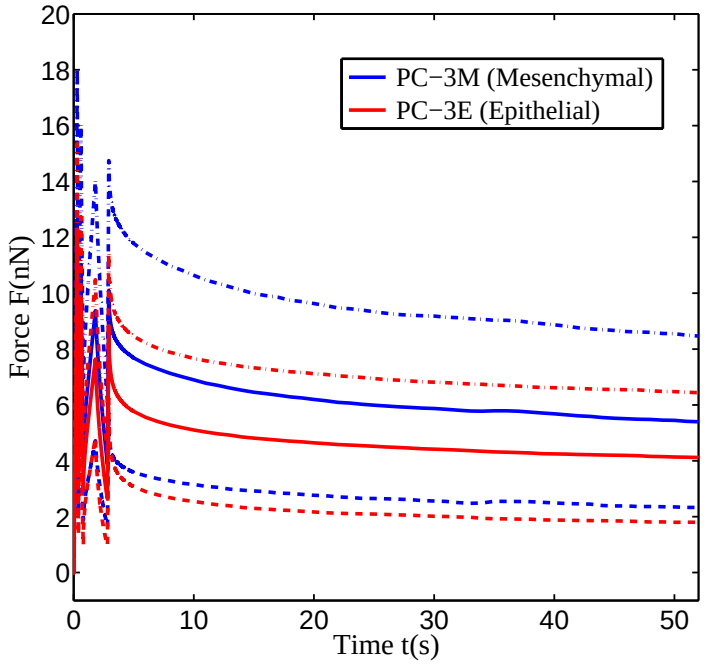

(a)

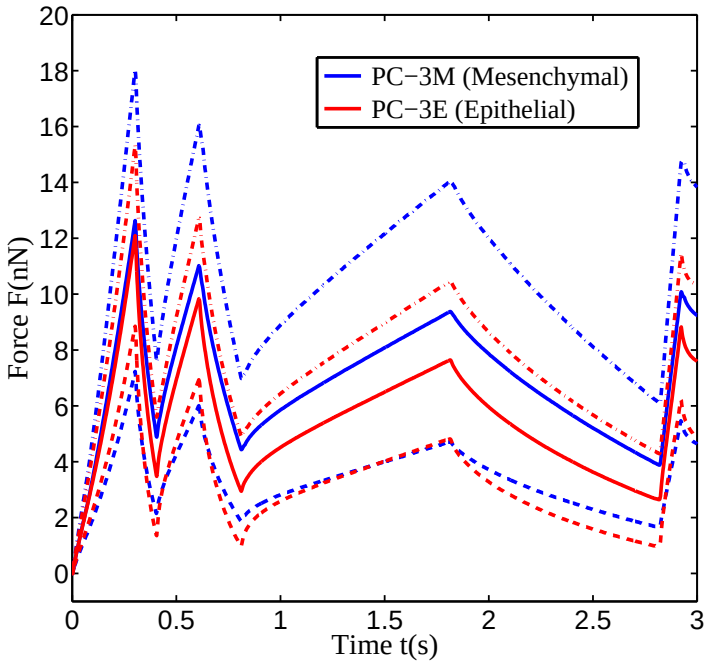

(b)

Figure A.2: AFM experimental data (mean and standard deviations) for PC-3M and PC-3E cells obtained in the first setup: (a) Both RR (ramp-reverse) and RH (ramp-hold) responses (b) Zoom-in view of the RR (ramp-reverse) responses.

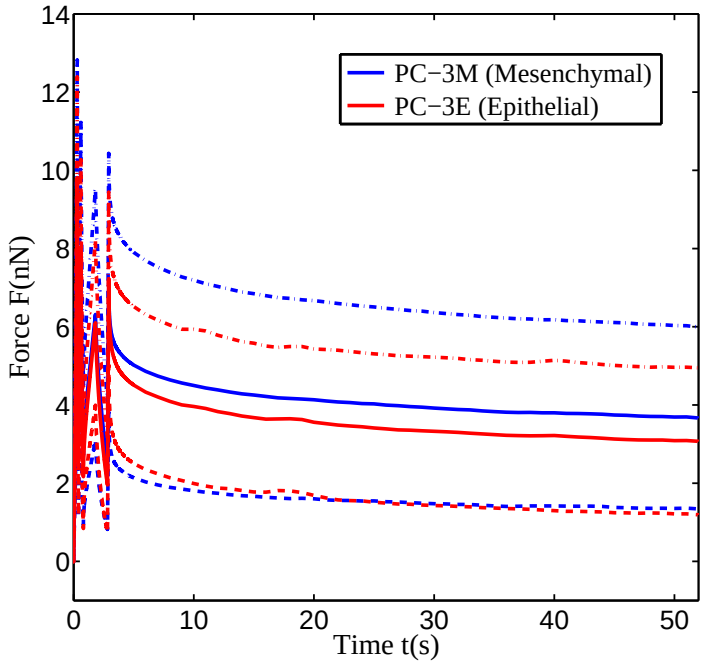

(a)

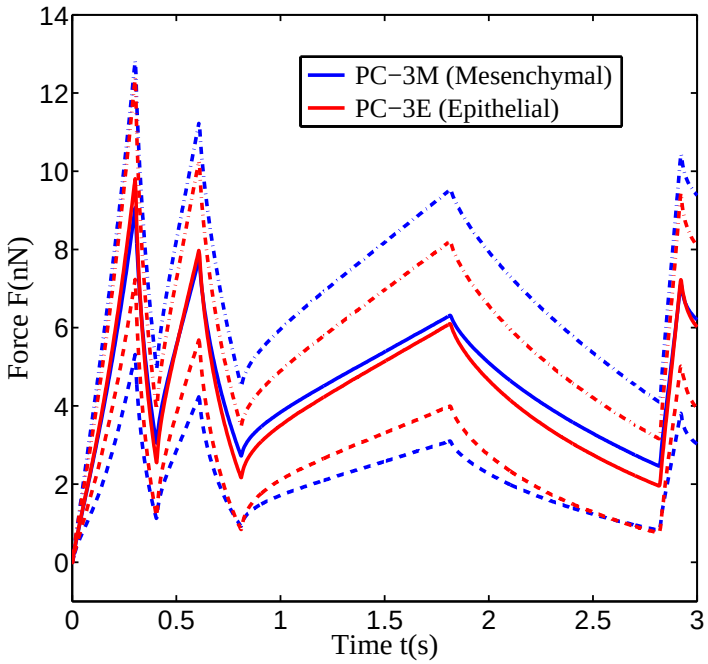

(b)

Figure A.3: AFM experimental data (mean and standard deviations) for PC-3M and PC-3E cells obtained in the second setup: (a) Both RR (ramp-reverse) and RH (ramp-hold) responses (b) Zoom-in view of the RR (ramp-reverse) responses.

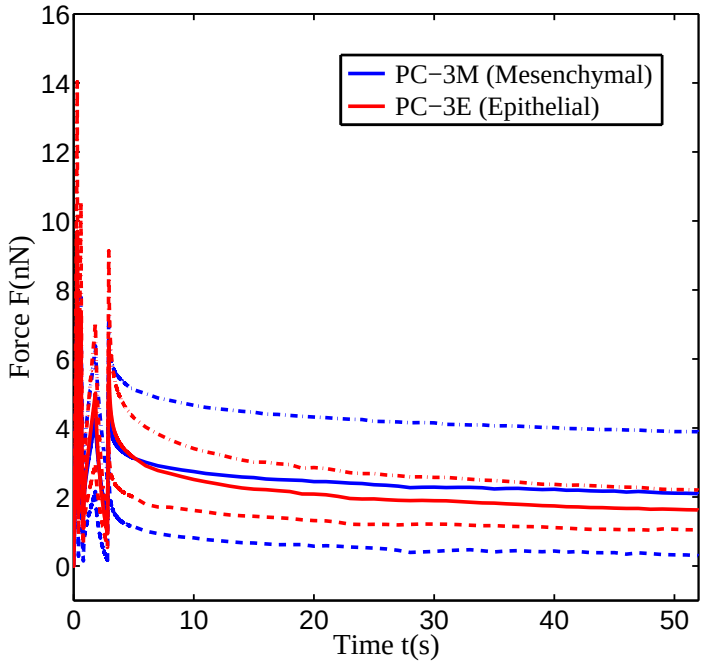

(a)

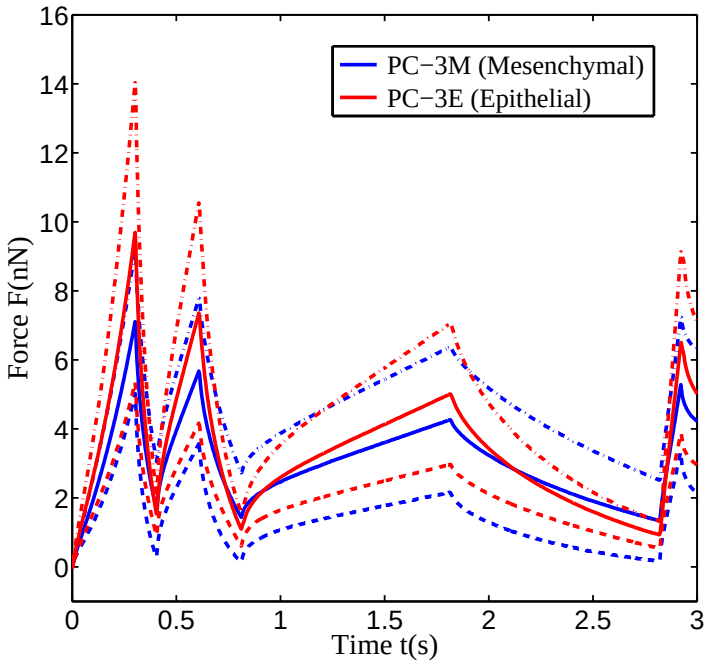

(b)

Figure A.4: AFM experimental data (mean and standard deviations) for PC-3M and PC-3E cells obtained in the third setup: (a) Both RR (ramp-reverse) and RH (ramp-hold) responses (b) Zoom-in view of the RR (ramp-reverse) responses.

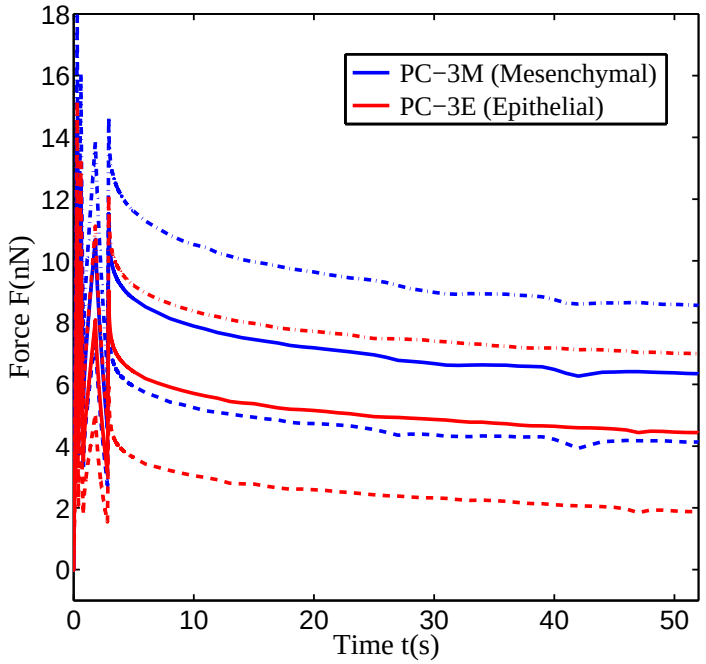

(a)

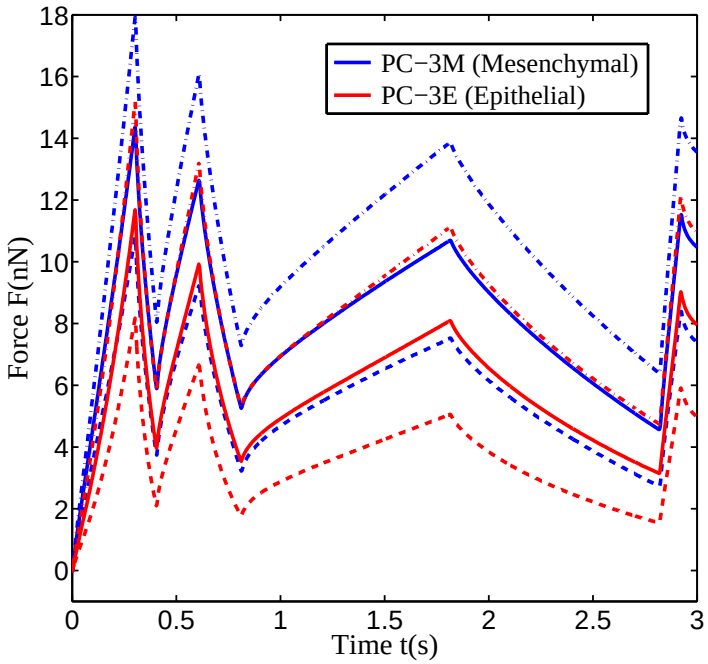

(b)

Figure A.5: AFM experimental data (mean and standard deviations) for PC-3M and PC-3E cells obtained in the fourth setup: (a) Both (ramp-reverse) and RH (ramp-hold) responses (b) Zoom-in view of the RR (ramp-reverse) responses.

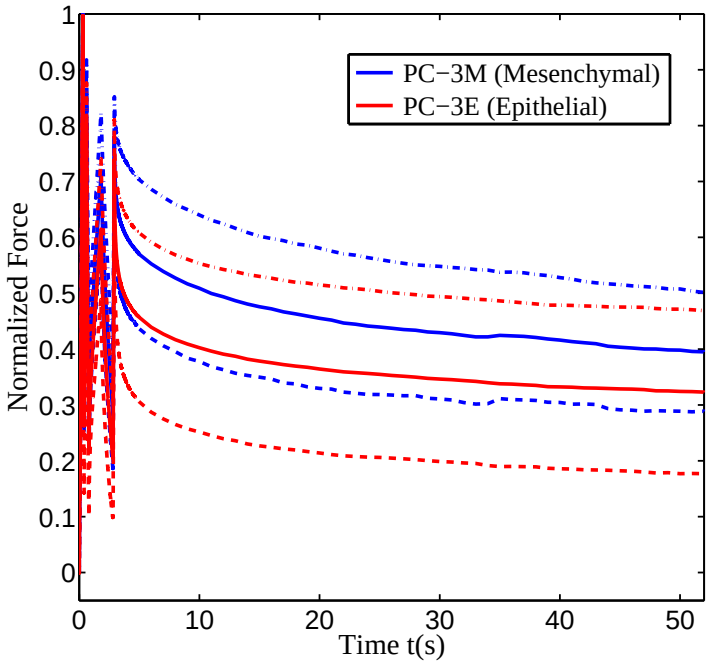

Figure A.6: Normalization by the peak force for PC-3M and PC-3E cells (first setup).

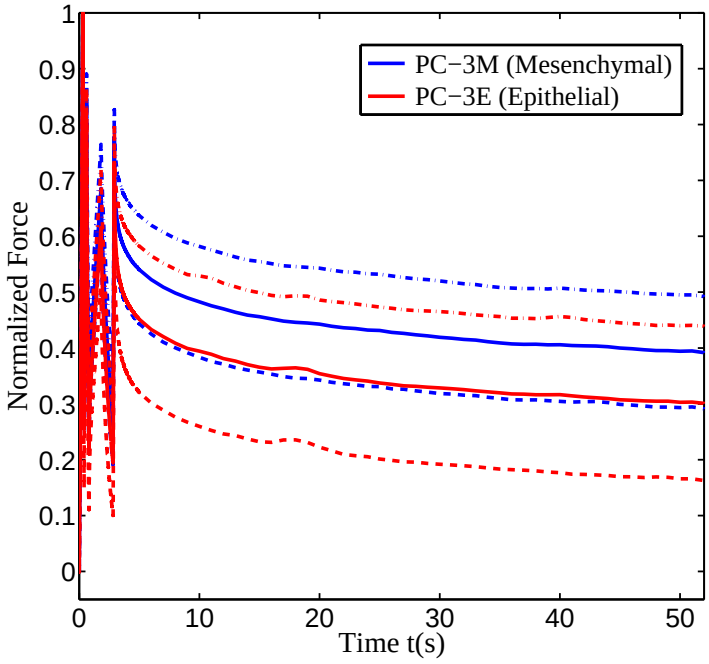

Figure A.7: Normalization by the peak force for PC-3M and PC-3E cells (second setup).

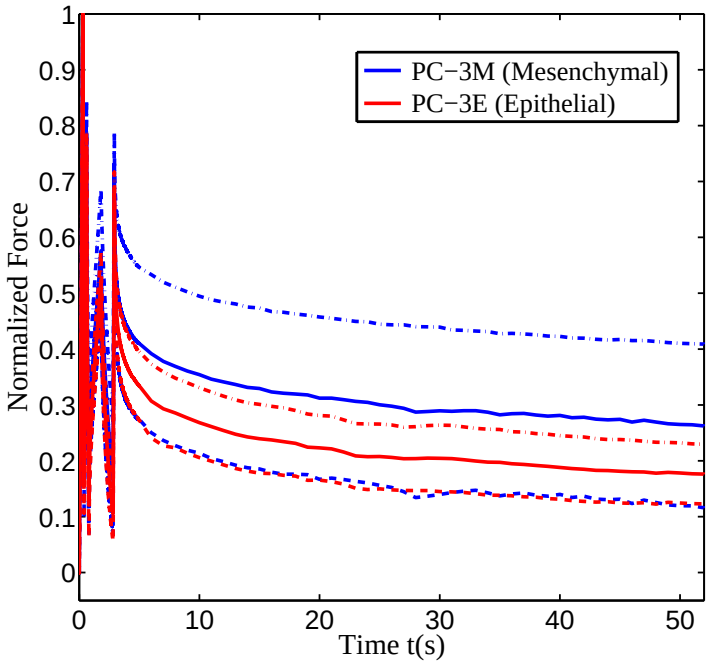

Figure A.8: Normalization by the peak force for PC-3M and PC-3E cells (third setup).

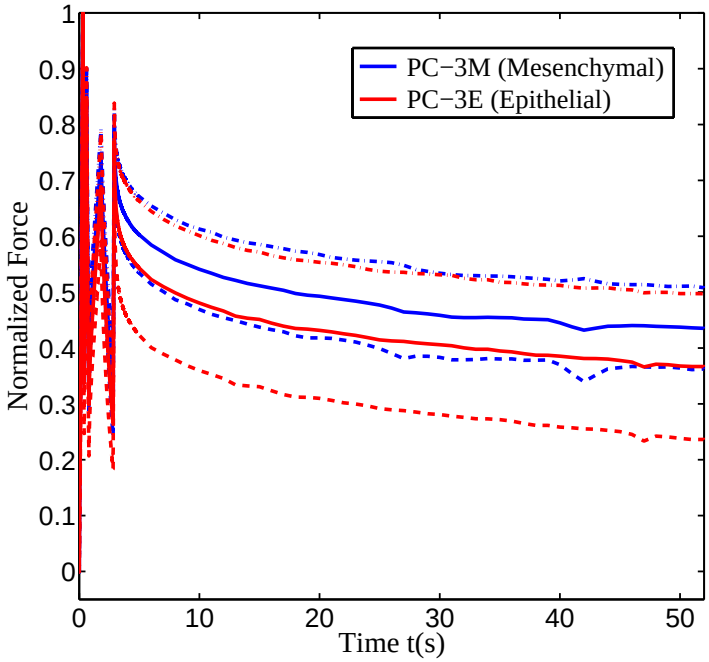

Figure A.9: Normalization by the peak force for PC-3M and PC-3E cells (fourth setup).

No definitive conclusion is made at this point. More experiments, in which more cells are tested, are necessary to determine whether these two cell groups have different mechanical characteristics or not. In addition, better understanding of their physiology and the transition between them might be needed in order to progress and achieve a strong conclusion about these two cell lines. Therefore, more well-characterized cell lines were studied for comparison purpose. The study was presented in Chapter V. In this appendix, results obtained from PC-3M and PC-3E cells are used to investigate the effectiveness of the inverse process and to determine whether the extracted properties are in the range reported in the literature for prostate cancer cells. Therefore, in the following sections, a FE model, using a representative cell having the mean diameter and height of $n = 109$ cells tested in four setups, is employed in modeling the indentation process.

A.1.4 FE Model

Specifically, with the methods described in Chapter V for estimating a cell's geometric dimensions, the height and the diameter of the cell base are approximated to be $H = 18.84 \pm 3.97$ μm and $D = 21.84 \pm 2.52$ μm, respectively. Figure A.10 shows a typical optical image of a single prostate cancer cell for cell base's diameter estimation. Prostate cancer cell height determination is illustrated in Figure A.11.

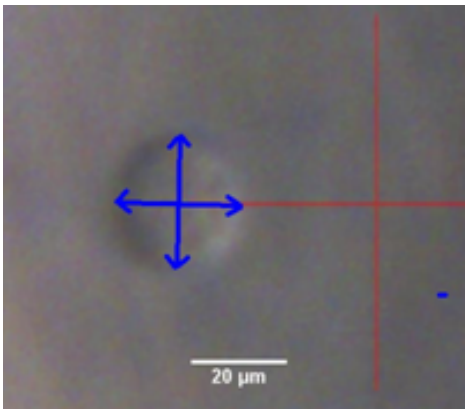

Figure A.10: An optical image of a single prostate cancer cell on a glass substrate in AFM Bruker Dimension Icon.

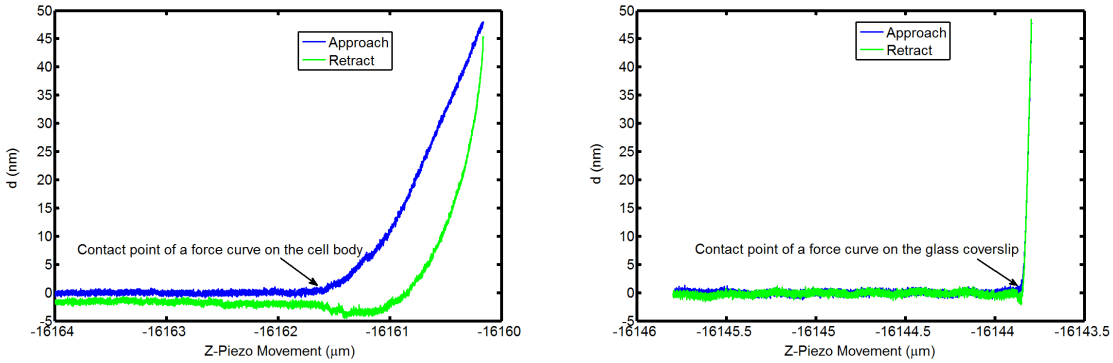

Figure A.11: Cantilever deflection vs. the piezo movement curves (with the reference corresponds to the highest location of the scanner): (a) On a prostate cancer cell body (b) On the glass surface. The difference between the two contact points gives an estimation of the cell height.

An axisymmetric FE model of the cell, using the mean diameter of $D = 21.84$ μm for the circular base and the mean cell height of $H = 18.84$ μm, is utilized to simulate the indentation process for all tested cells. The same approach as discussed in Chapter V is applied to the modeling. Illustrated in Figure A.12 is the utilized FE model, which has a converged, and refined mesh at the contact region (1021 elements).

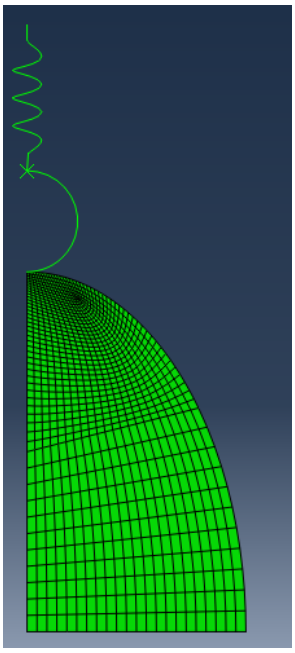

Figure A.12: FE model for AFM indentation tests on PC-3 cells.

Based on the calibration values in Table A.1, two cases of the above FE modeling were constructed. In the first, the spring has a stiffness of k=0.072 N/m, and a force of $5 \times 0.072 = 0.36$ nN is applied in the first step. In the second one, the spring has a stiffness of k=0.054 N/m, and a force of $5 \times 0.054 = 0.27$ nN is applied in the first step. The first model is used to construct a surrogate model and a Kriging predictor for inverse analysis of experimental data from experiments (#1,#2,#4) while the second model is used for inverse analysis of experimental data from experiment (#3).

A.2 Inverse Analysis and Fitting Experimental Data

For each case of FE modelling, a surrogate model with a Kriging predictor (*Sacks et al.*, 1989; *Lophaven et al.*, 2002; *Queipo et al.*, 2005; *Forrester et al.*, 2008; *Gustafson and Waas*, 2009; *Heinrich and Waas*, 2009) is constructed for the inverse process. The material domain is a fifth dimensional space of $x(C_1, g_1, \tau_1, g_2, \tau_2)$ with the bounds as shown in Table A.2 with the constraint $g_1 + g_2 < 1$.

	C_1(Pa)	g_1	τ_1(s)	g_2	τ_2(s)
Lower bound	20	0.01	0.01	0.01	2
Upper bound	1000	1	2	1	40

Table A.2: Boundary of the material domain used in the process of determining the NLV properties of the tested prostate cancer cells in four setups

In this study, for each case of FE modeling, a meta model was constructed using $N = 717$ sets of training points $X(5, 717)$ which result in $Y(5095, 717)$ corresponding force responses. $N^1 = 241$ sets of checking points were also used to generate $X^1(5, 241), Y^1(5095, 241)$ for checking the accuracy of the Kriging predictor. Here, the time period of the loading is divided into 5095 discrete time steps. All the training points and checking points were generated using the Latin Hypercube technique (*lhsdesign* function in MATLAB) with the consideration of the constraint $g_1 + g_2 < 0.99$. It is noted that the extreme cases of the material parameter selections

might lead to difficulty in predicting the non-linear relationship between X and Y. Hence, to improve the prediction of the surrogate model and Kriging predictor, two criteria were applied in this study for removing these extreme cases from the sets of training and checking points:

(1) For $t > 0$, the force response is in the repulsive range,

(2) The maximum peak force is larger than $3nN$.

The first criterion was based on the observation that with the applied piezo displacement, all the force-time data obtained in this work remains in the repulsive range. The second criterion is based on the minimum value of the maximum peak force of $n = 109$ obtained force-time data. This criterion can be relaxed by adding more training points. The cases that violate at least one criterion were removed form the meta model and checking sets. With this consideration, this study uses a training group composed of $(X(5, 656), Y(5095, 656))$ and a checking group composed of $(X^1(5, 210), Y^1(5095, 210))$ for the first FE model. The second case has $(X(5, 658), Y(5095, 658))$ for training and $(X^1(5, 211), Y^1(5095, 211))$ for checking groups, respectively.

Typical comparisons between the Kriging's predictions and actual FE results for the checking cases are shown in Figure A.13 and Figure A.14 for the first FE and the second FE modeling, respectively. The comparisons show good agreements between the two predictions. The maximum RMSE values for these two cases are 4.38 % and 5.29 %, respectively.

Next, optimization with *fmincon* option in MATLAB is applied to the Kriging predictors in order to minimize the error between the experimental data and predictions of Kriging. For each cell's data, this process yields an optimized set of five parameters, which in turn are used to construct a shear relaxation modulus.

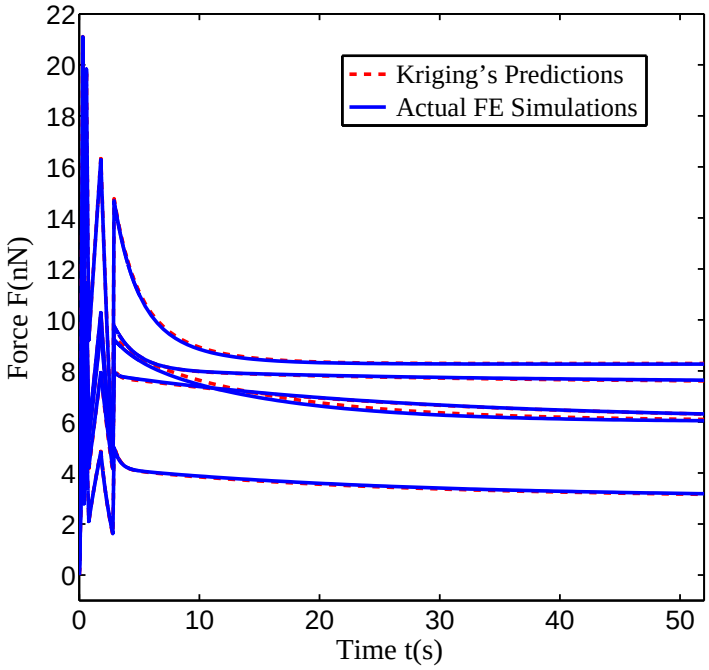

Figure A.13: Representative comparisons between FE and Kriging predictions using the first FE model.

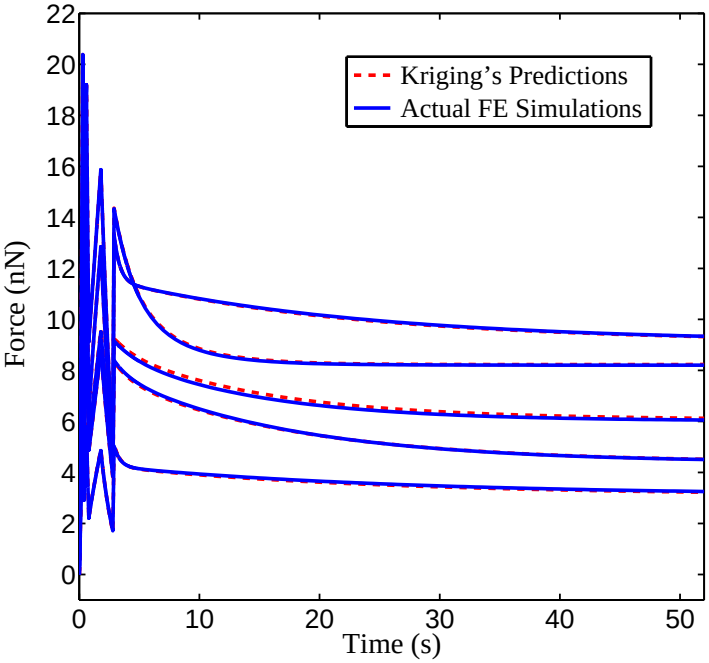

Figure A.14: Representative comparisons between FE and Kriging predictions using the second FE model.

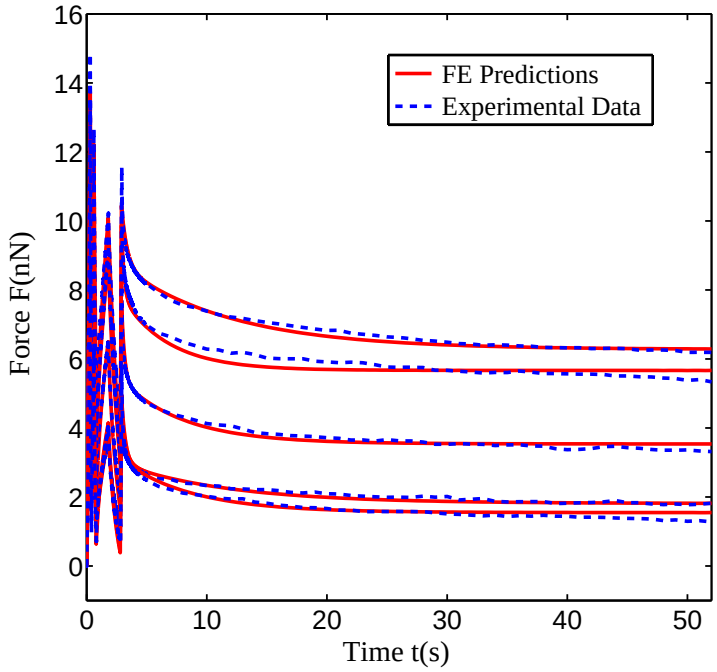

(a)

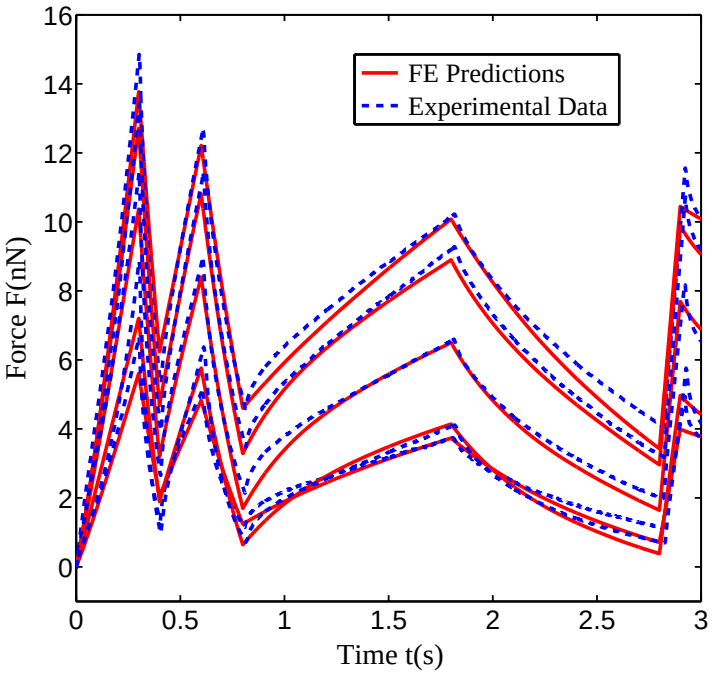

(b)

Figure A.15: Representative comparisons between experimental data and FE predictions at the corresponding extracted sets of material parameters: (a) Both RR (ramp-reverse) and RH (ramp-hold) loadings (b) Zoom-in view of RR (ramp-reverse) cycles.

Figure A.15 shows representative comparisons between the experimental data and actual FE solutions evaluated at these optimized sets, which indicate the effectiveness of the inverse modeling in connection with surrogate modeling in extracting the optimal set of material parameters that can predict the behavior observed in experiments. Here, the inverse method was able to analyze data from all ($n = 109$) tested cells. The mean and standard deviations of the extracted shear relaxation moduli for these $n = 109$ cells are plotted in Figure A.16. Specifically, the instantaneous value is $E(0) = 3G(0) = 1.32 \pm 0.54$ kPa, while the long term value, at $t = 52$s, is $E(52) = 3G(52) = 0.45 \pm 0.26$ kPa. In the literature, *Faria et al.* (2008) reported a value of 1.4 ± 0.16 kPa for Young's modulus of the PC-3 cell lines. In their work, a pyramid probe was used for indenting the cells at only one rate of 5.7 μm/s, and the data was interpreted by the Hertz contact model. In another work, *Lekka et al.* (2012) obtained the value of 1.95 ± 0.47 kPa for the Young's modulus of the PC-3 cell line. Thus, though a direct comparison can not be made due to the differences in these studies, the modulus obtained using the approach presented in this thesis lies within a reasonable range.

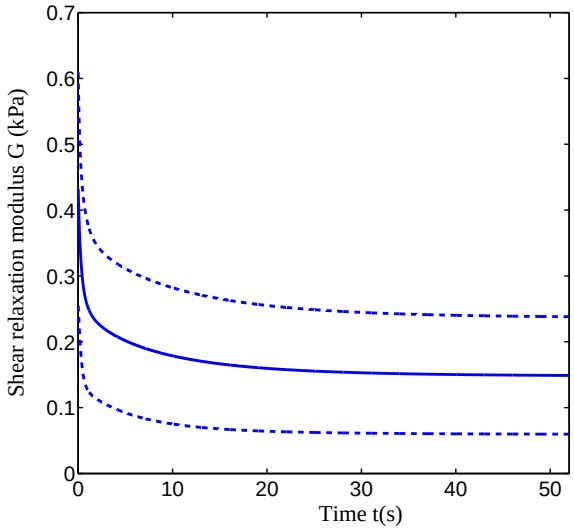

Figure A.16: Mean and standard deviations of the shear relaxation modulus for $n = 109$ prostate cancer cells.

As mentioned earlier, in this study, a definitive conclusion about the differences in terms of the NLV properties for the two groups PC-3E and PC-3M haven't been made. Understanding the physiological/biological aspects of these two cell lines is needed to provide insight into the mechanical aspects of these two cell lines. To progress next, it is suggested to utilize more well-characterized cell lines for comparison purpose, such as the benign and malignant prostate cancer cells as studied in *Faria et al.* (2008). Chapter V provides details of such a study, focusing on the differences between benign and malignant breast cancer cell lines in terms of their viscoelastic characteristics. It would be useful to extend it to investigate the differences between benign and malignant prostate cancer cells.

APPENDIX B

AFM Indentation Experiment

Bruker Dimension Icon system (*Veeco Instruments Inc.*, 2010) as shown in Figure B.1 was employed in this work. Figure B.2 shows the Dimension Icon Head (scanner), which is an important part of the system. Its working principle is illustrated in Figure B.3 (*Veeco Instruments Inc.*, 2010).

Figure B.1: Dimension Icon system (*Veeco Instruments Inc.*, 2010)

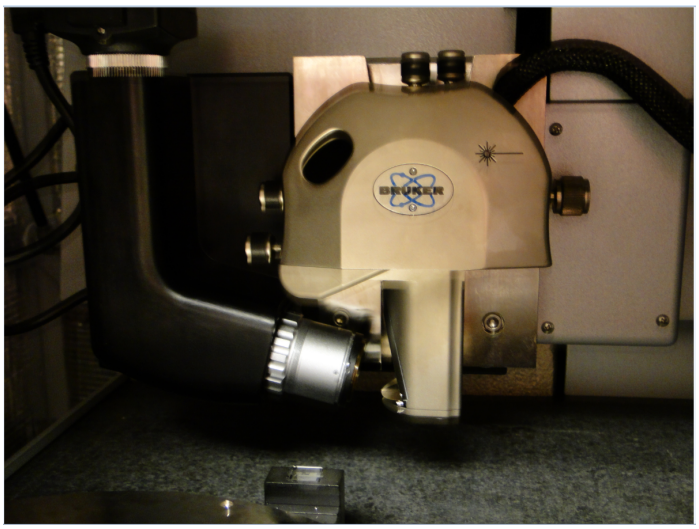

Figure B.2: AFM Dimension Icon head

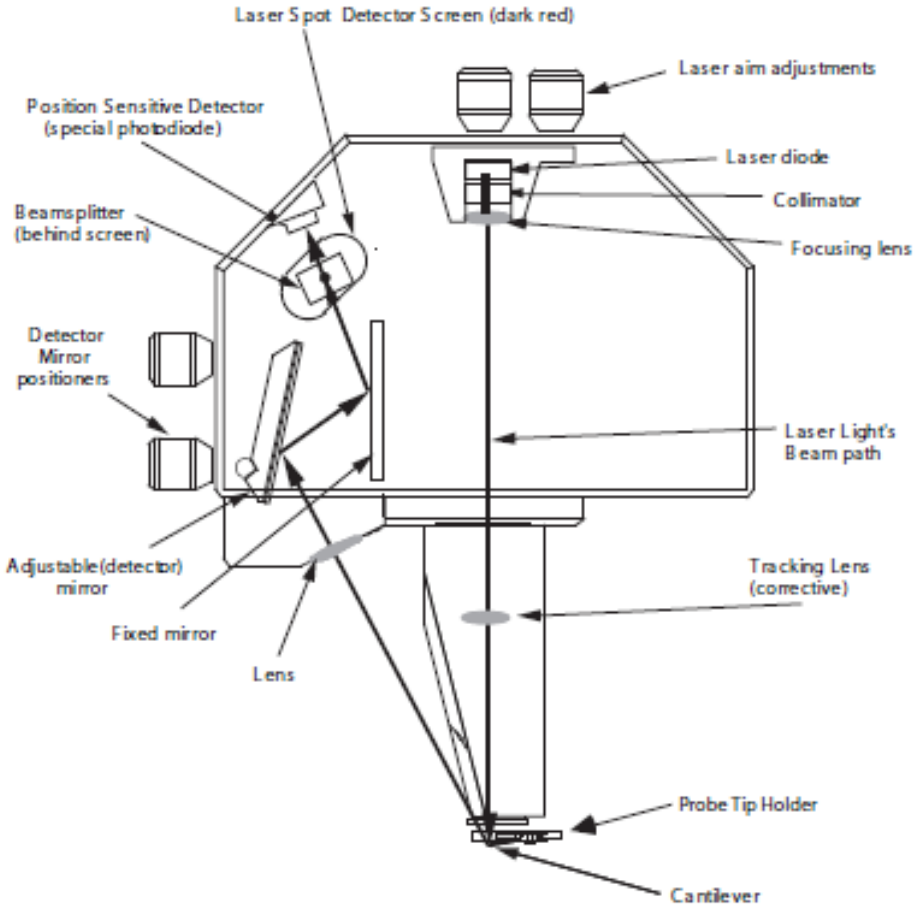

Figure B.3: Working principle within the AFM head (*Veeco Instruments Inc.*, 2010)

This appendix provides additional details associated with the procedure that was followed in Chapter V and Appendix A to setup indentation tests in fluid environment using the contact mode of this AFM system. The mechanism related to the ramp mode in this AFM for acquiring force curve and determining the sample's height is also discussed in more detail in section B.2 of this appendix.

B.1 Procedure for Setting Up AFM Indentation Tests

Step 1: Preliminary Setup

AFM cantilever is inserted into a fluid cell holder, which is then mount into the AFM scanner as depicted in Figure B.4. A protective, plastic skirt is used to cover the fluid cell holder to prevent fluid from the electronic parts of the scanner.

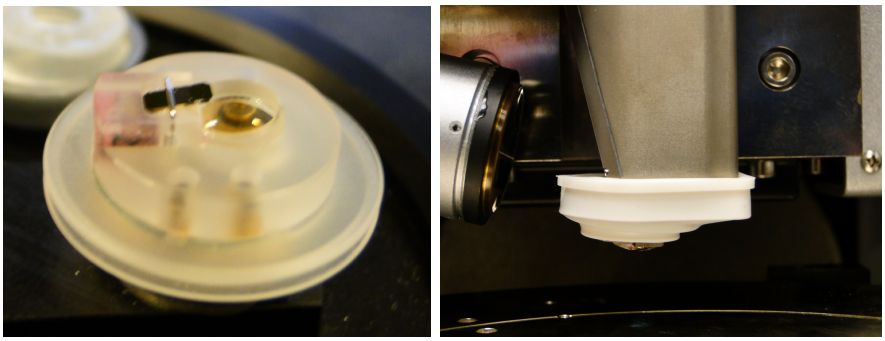

(a) (b)

Figure B.4: AFM scanner with a fluid cell holder and a protective, plastic skirt: (a) Fluid cell holder with a cantilever (b) Fluid cell holder mounted on the scanner. The white, plastic skirt is used for protective purpose

Step 2: Align and Optimize Laser Signal in Air

Aligning the laser is the trickiest step in the procedure. It requires manual adjustments of the two top laser knobs (shown in Figure B.3) to align the laser on the free end of the cantilever. First, this step is performed in air by manually adjusting these knobs until a maximum laser sum signal is achieved. Next, the two side knobs (detector mirror positioners in Figure B.3) are adjusted to center the reflected laser

in the photodiode (which means both vertical (d) and horizonal cantilever deflections are zero), and false engagement is performed to check the quality of the laser position. In this case, since the probe is not prevented by any sample, moving the piezo up and down (Z) should not result in any change in the cantilever deflection. In other word, in false engagement, d is equal to zero. However, in AFM, due to laser interference, tilt in the force curve (d versus Z) might occur. The amount of tilt is significantly affected by the laser position as shown in Figure B.5. In this figure, both laser positions provide significant laser sum signal, however, the amounts of tilt are different. Therefore, extra effort was used in each setup to manually optimize the laser position in order to minimize this tilt artifact (*Taatjes and Mossman*, 2005).

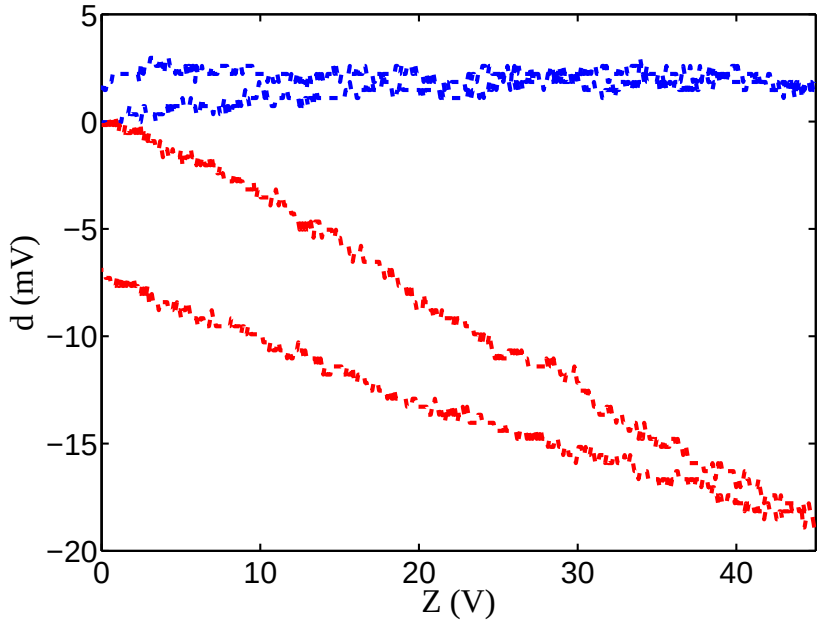

Figure B.5: Cantilever deflection (d) versus piezo movement (Z) in false engagement

Step 3: Add Fluid, Realign and Optimize Laser Signal

Once the laser is optimized in air, a drop of fluid (culture medium) is added to cover the cantilever and the probe as illustrated in Figure B.4(b). The laser sum signal drops significantly due to the effect of the added fluid. To gain back the laser signal, the right top laser knob is adjusted counter clockwise to move the laser back

to the free end of the cantilever. False engagement is performed and the laser position is slightly adjusted until the tilt in the force curve is minimized.

Step 4: Calibration

- A clean glass slide with a drop of fluid is loaded onto the sample stage. The scanner is lowered until the two fluid drops merge and form a meniscus (Figure B.6). The laser sum signal is rechecked to make sure that there is still a high laser sum signal.

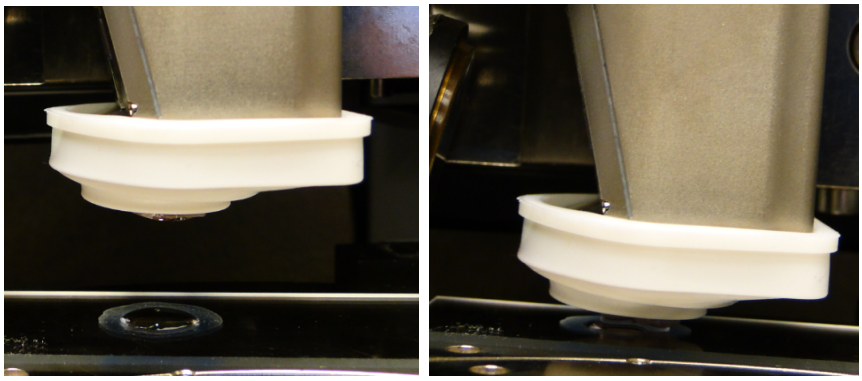

(a) (b)

Figure B.6: AFM setup for calibration purpose using a clean glass slide

Next, focusing is performed to manually bring the cantilever closer to the glass substrate. The side knobs are then adjusted to set the vertical deflection of the cantilever around -1V while the horizontal signal is set to be zero. At this point, engagement are conducted to engage the probe on the glass surface. A force curve is then acquired in the ramp mode. If the baseline of the acquired force curve is tilted, it is necessary to withdraw the probe out of contact with the glass surface and slightly re-adjust the top two knobs, re-engage, and acquire a new force curve. The procedure is repeated until a force curve with a flat base line is achieved. Normally, at this step it should not be difficult to get this optimized laser position owing to the previous steps with alignment and false engagement performed in air and in the drop of fluid. Slightly adjustment is recommended at this step. Once the optimized laser

position is achieved, the top two knobs are fixed, and no longer adjusted for the rest of the setup. The DS value is then calibrated using the slope of the acquired force curve. In this work, the DS calibrated value is the average of multiple measurements.

- The spring constant of the cantilever is then calibrated using thermal tune option in the AFM. A typical image for the built-in thermal tune acquisition option in this AFM system is shown in Figure B.7. The principle of this calibration method was explained in the literature (*Matei et al.*, 2006) as well as in the instrument software. In this work, simple harmonic oscillator option is used to fit the resonant peak obtained from free thermal vibration of the cantilever.

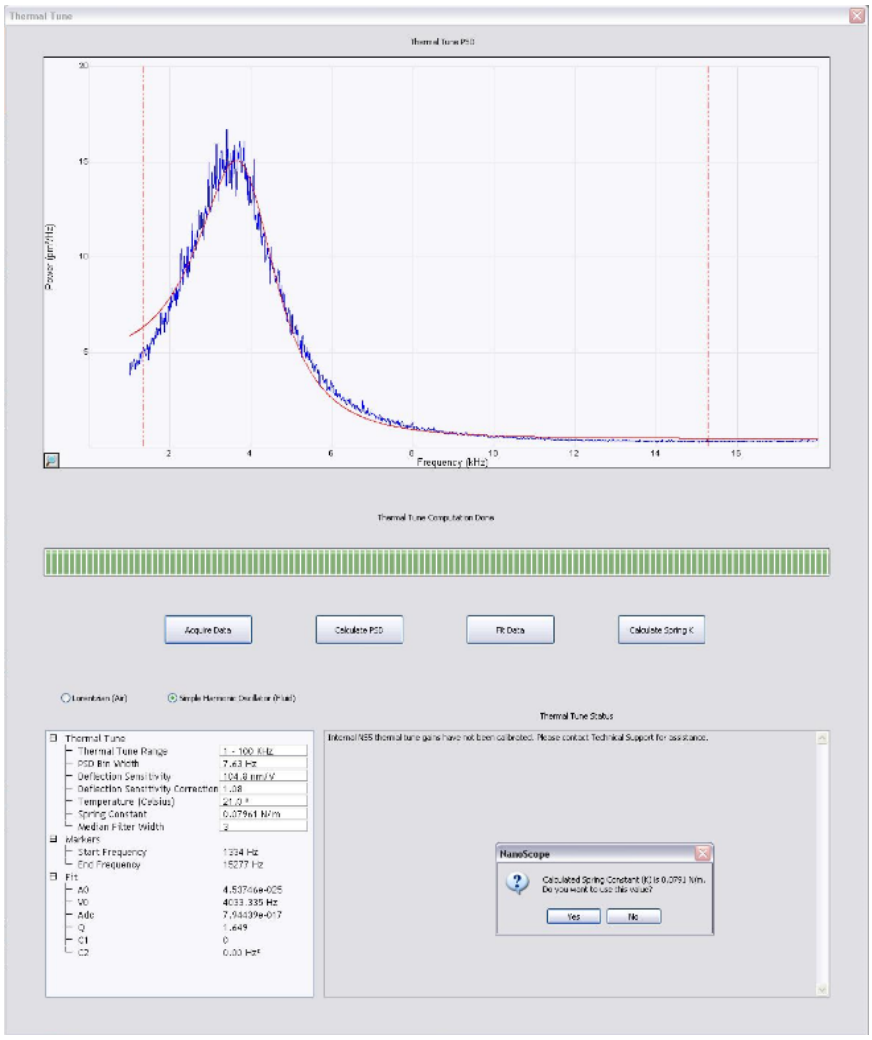

Figure B.7: Thermal tune for calibrating the cantilever spring constant

Step 5: Indentation on Samples

After the calibration step, the clean glass slide is replaced by a coverslip with cells seeded on the top and covered by fluid (culture medium) as shown in Figure B.8(a). Indentations on cells are performed within a meniscus illustrated in Figure B.8(b). When changing the coverslips, it is important to not adjust the two knobs at the top of the scanner, since this will affect the laser position and the calibration values.

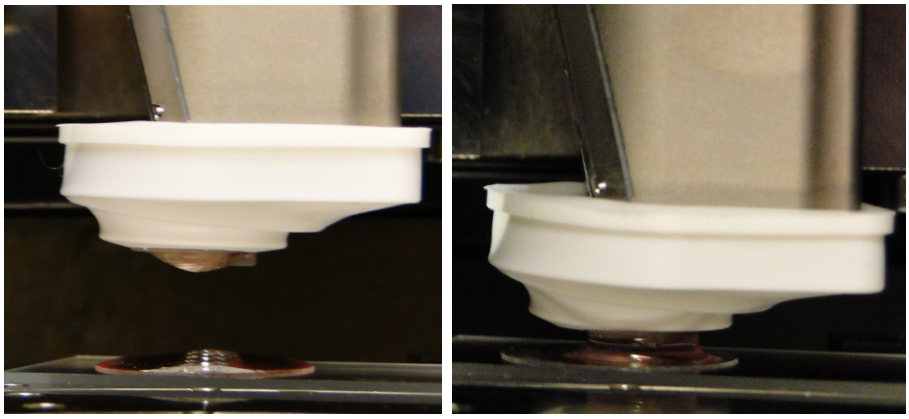

(a) (b)

Figure B.8: AFM setup for indentation on cell

For indentation on cells, script mode was used to combine two control modes: force control and piezo movement control. A typical script is shown in Figure B.9

B.2 AFM Ramp Mode Mechanism

In AFM Dimension Icon, estimating the cell height requires understanding of both piezo movements and the mechanism of the Z-stepper motor in moving the scanner up and down. Figure B.10 shows the working principle of a piezo. Illustration of the piezo in connection with Z-stepper motor in a ramp mode is shown in Figure B.11 (*Veeco Instruments Inc.*, 2010; *Titushkin*, 2013). Here, the Z-stepper motor position (or $Z[Scanner]$) is measured downward. Its reference point is at the highest position of the scanner.

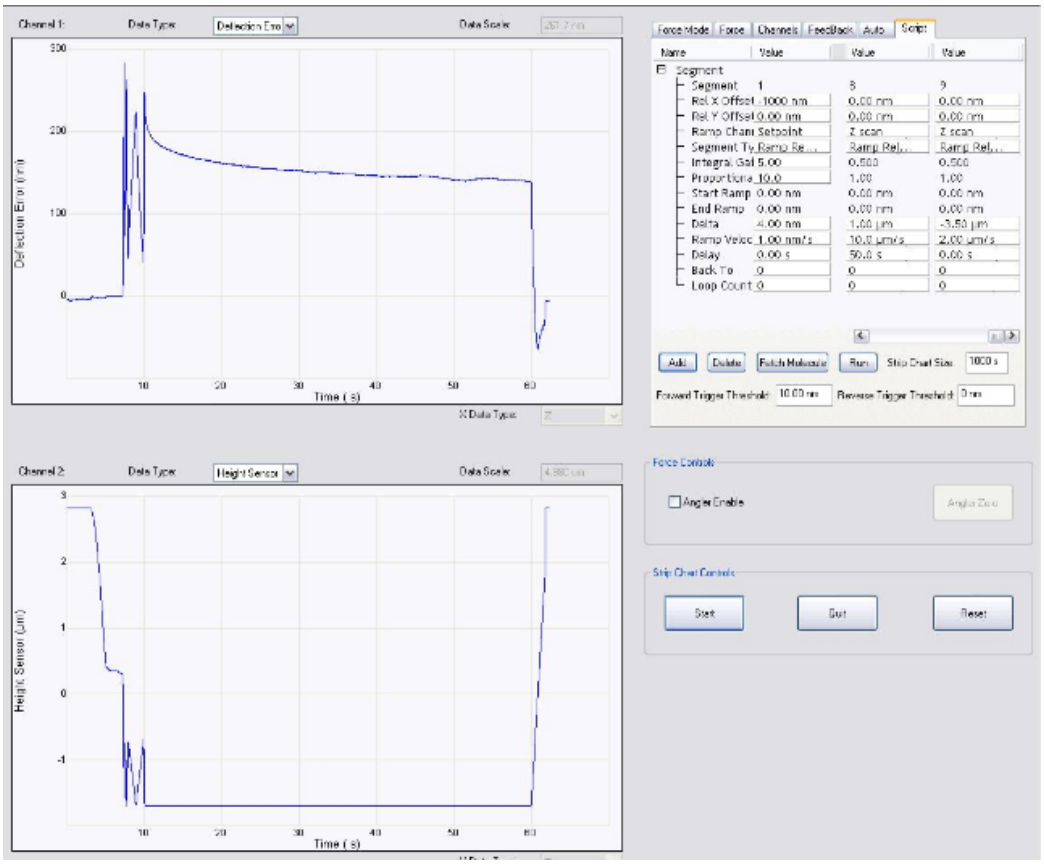

Figure B.9: Script used in AFM indentation tests

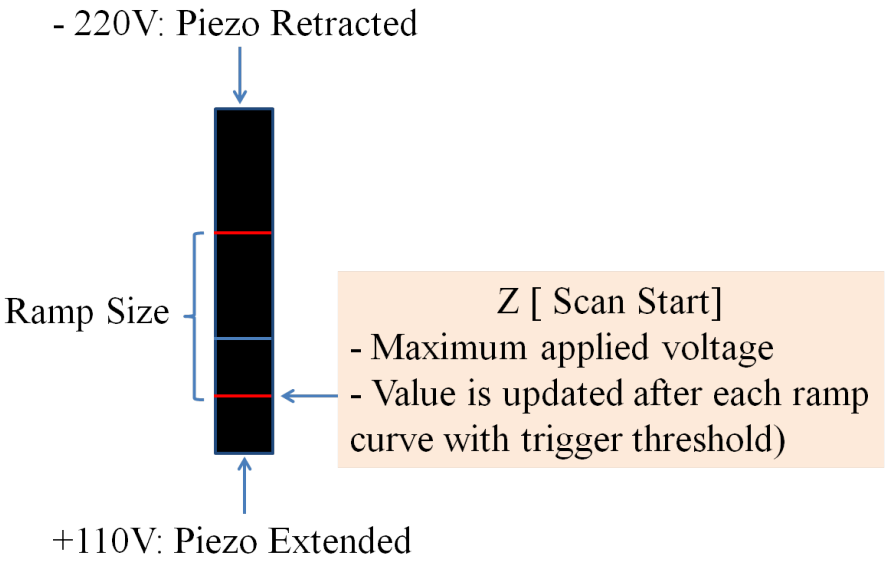

Figure B.10: Schematic illustration of the piezo in AFM Dimension Icon system

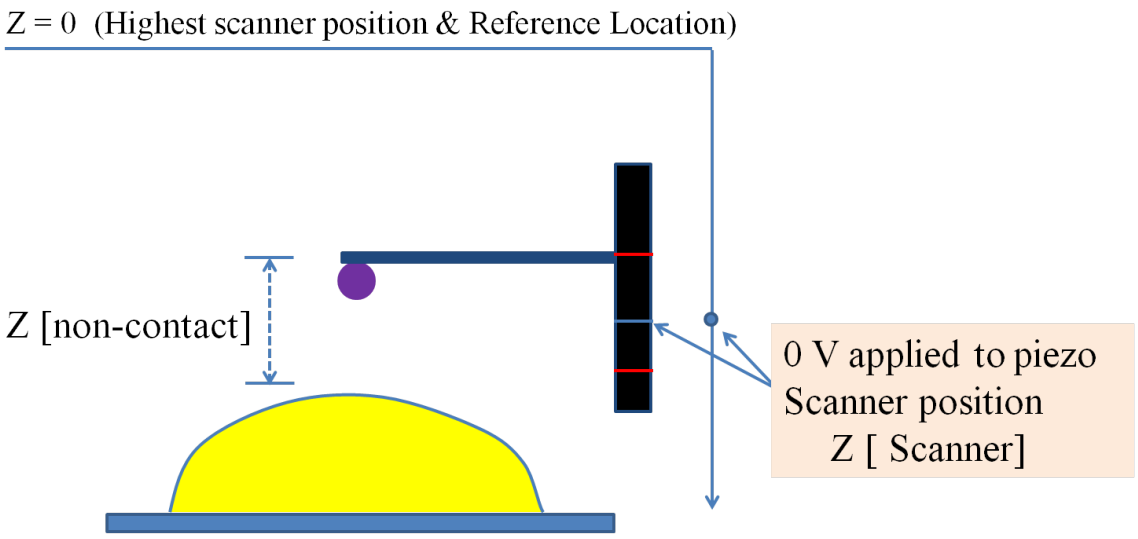

Figure B.11: Schematic illustration of AFM ramp mode

This value of the scanner position corresponds to the piezo position when no voltage is applied. The voltage applied to the piezo at the beginning of each force curve is computed through the maximum applied voltage ($Z[ScanStart]$) and the ramp size. When trigger mode is on, the piezo extends downward until the cantilever deflection (d) reaches the trigger value. This position is updated as the $Z[ScanStart]$ value. The piezo is then retracted by an amount of one ramp size. Therefore, the position of the contact point with the sample is calculated using a force curve (d versus Z) as follows:

$$Z[surface] = Z[scanner] - Z[scanstart] + [rampsize] - Z[non-contact]. \quad \text{(B.1)}$$

Here, $Z[non-contact]$ is the distance in the non-contact part of the force curve. With this method, the difference between the $Z[surface]$ values obtained from a force curve on sample and on glass substrate provides an estimate for the sample height.

APPENDIX C

Governing Equations

This Appendix contains expressions that were used in establishing the partial differential-Volterra integral governing equations in Chapter II.

$$
\begin{aligned}
F_1[\underline{\lambda}(t)] &= -\frac{1}{\lambda_1(t)^2\lambda_2(t)} g_1[\underline{\lambda}(t)] \\
&\quad + \frac{1}{\lambda_1(t)\lambda_2(t)} \frac{\partial g_1[\underline{\lambda}(t)]}{\partial \lambda_1(t)}, \\
F_2[\underline{\lambda}(t), \eta(t)] &= -\frac{g_1[\lambda(t)]}{\lambda_1(t)\lambda_2(t)} \\
&\quad - \frac{\eta(t) - \lambda_2(t)}{\lambda_1(t)\lambda_2(t)} \frac{\partial g_1[\underline{\lambda}(t)]}{\partial \lambda_2(t)} + \frac{\eta(t) g_2[\underline{\lambda}(t)]}{\lambda_1(t)\lambda_2(t)^2}, \\
H_1[\underline{\lambda}(t), \underline{\lambda}(s), t-s] &= -\frac{G_1[\underline{\lambda}(t), \underline{\lambda}(s), t-s]}{\lambda_1(t)^2\lambda_2(t)}, \\
&\quad + \frac{1}{\lambda_1(t)\lambda_2(t)} \frac{\partial G_1[\underline{\lambda}(t), \underline{\lambda}(s), t-s]}{\partial \lambda_1(s)} \\
H_2[\underline{\lambda}(t), \underline{\lambda}(s), t-s] &= \frac{1}{\lambda_1(t)\lambda_2(t)} \frac{\partial G_1[\underline{\lambda}(t), \underline{\lambda}(s), t-s]}{\partial \lambda_1(s)}, \\
H_3[\underline{\lambda}(t), \underline{\lambda}(s), \eta(t), \eta(s), t-s] &= -\frac{1}{\lambda_1(t)\lambda_2(t)} G_1[\underline{\lambda}(t), \underline{\lambda}(s), t-s] \\
&\quad + \frac{\eta(t)}{\lambda_1(t)\lambda_2(t)^2} G_2[\underline{\lambda}(t), \underline{\lambda}(s), t-s], \\
&\quad - \frac{\eta(t) - \lambda_2(t)}{\lambda_1(t)\lambda_2(t)} \frac{\partial G_1[\underline{\lambda}(t), \underline{\lambda}(s), t-s]}{\partial \lambda_2(t)}, \\
&\quad - \frac{\eta(s) - \lambda_2(s)}{\lambda_1(t)\lambda_2(t)} \frac{\partial G_1[\underline{\lambda}(t), \underline{\lambda}(s), t-s]}{\partial \lambda_2(s)}.
\end{aligned}
$$

APPENDIX D

Derivations for Material Subroutine (UMAT)

This Appendix presents the derivation of a user subroutine (UMAT) for a NLV single integral Pipkin-Rogers model discussed in Chapter II.

D.1 Constitutive Model

The Kirchhoff stress $\boldsymbol{\tau} = J\boldsymbol{\sigma}$ for an incompressible, NLV, single integral Pipkin-Rogers model is represented as follows:

$$\begin{aligned}
\boldsymbol{\tau}(t) &= -p\boldsymbol{I} + \boldsymbol{F}(t)\left\{\boldsymbol{R}[\boldsymbol{C}(t),0] + \int_0^t \frac{\partial}{\partial(t-s)}\mathbf{R}[\mathbf{C}(s),t-s]ds\right\}\boldsymbol{F}^T(t), \\
\boldsymbol{R}[\boldsymbol{C}(t),s] &= \alpha_0\boldsymbol{I} + \alpha_1\boldsymbol{C}(t) + \alpha_2\boldsymbol{C^2}(t), \\
\alpha_i &= \alpha_i(\boldsymbol{I_1}(t),\boldsymbol{I_2}(t),s). \qquad \text{(D.1)}
\end{aligned}$$

Here, the coefficients $\alpha_i(\boldsymbol{I_1}(t),\boldsymbol{I_2}(t),s)$ have the following forms:

$$\begin{aligned}
\alpha_0 &= G_1(s)[1-\boldsymbol{I_2}\Phi(\boldsymbol{I_1},\boldsymbol{I_2})] + G_2(s)[\boldsymbol{I_1} - 2\boldsymbol{I_2}\Phi(\boldsymbol{I_1},\boldsymbol{I_2})], \\
\alpha_1 &= G_1(s)\boldsymbol{I_1}\Phi(\boldsymbol{I_1},\boldsymbol{I_2}) + G_2(s)[2\boldsymbol{I_1}\Phi(\boldsymbol{I_1},\boldsymbol{I_2}) - 1], \\
\alpha_2 &= -\Phi(\boldsymbol{I_1},\boldsymbol{I_2})[G_1(s) + 2G_2(s)], \qquad \text{(D.2)}
\end{aligned}$$

where $\Phi(\boldsymbol{I_1}, \boldsymbol{I_2}) = e^{-a(\boldsymbol{I_1}-3)}$.

Particular choices of G_1 and G_2 are in terms of Prony series:

$$\begin{aligned} G_1(s) &= G_{1\infty} + \sum_{k=1}^{n} G_{1k} e^{-s/\tau_{1k}} \\ &= G_{10}\left[g_{1\infty} + \sum_{k=1}^{n} g_{1k} e^{-s/\tau_{1k}} \right], \end{aligned} \tag{D.3}$$

with the condition: $g_{1\infty} + \sum_{k=1}^{n} g_{1k} = 1$.

$$\begin{aligned} G_2(s) &= G_{2\infty} + \sum_{k=1}^{m} G_{2k} e^{-s/\tau_{2k}} \\ &= G_{20}\left[g_{2\infty} + \sum_{k=1}^{m} g_{2k} e^{-s/\tau_{2k}} \right], \end{aligned} \tag{D.4}$$

with the condition: $g_{2\infty} + \sum_{k=1}^{m} g_{2k} = 1$.

D.2 User Subroutine (UMAT)

In the case of incompressibility, using a penalty approach, the Kirchhoff stress is rewritten as follows:

$$\boldsymbol{\tau}(t) = \boldsymbol{F}(t)\left\{ \boldsymbol{R}[\boldsymbol{C}(t), 0] + \int_0^t \frac{\partial}{\partial(t-s)} \mathbf{R}[\mathbf{C}(s), t-s] ds \right\} \boldsymbol{F}^T(t) + KJ(J-1), \tag{D.5}$$

where $KJ(J-1)$ is the penalty term, and coefficient K is chosen large enough to impose incompressibility. The material subroutine requires the update of both the true stress and the material Jacobian (DDSDDE).

D.2.1 Update the True Stress in UMAT

This section presents two main steps used for updating the true stress: $\boldsymbol{\sigma} = \frac{1}{J}\boldsymbol{\tau}$.

Step 1: Calculate $\boldsymbol{R}[\boldsymbol{C}(t), 0]$:

Let: $G_{20} = dG_{10}$, the formulae used for calculations of $\boldsymbol{R}[\boldsymbol{C}(t), 0]$ become:

$$\begin{aligned}
\alpha_0 &= G_{10}[1 + d\boldsymbol{I_1}] - G_{10}\Phi\boldsymbol{I_2}(1+2d), \\
\alpha_1 &= -dG_{10} + G_{10}\Phi\boldsymbol{I_1}(1+2d), \\
\alpha_2 &= -G_{10}\Phi(1+2d), \\
\boldsymbol{R}[\boldsymbol{C}(t), 0] &= \alpha_0\boldsymbol{I} + \alpha_1\boldsymbol{C} + \alpha_2\boldsymbol{C^2}.
\end{aligned} \tag{D.6}$$

Step 2: Calculate the time integration $\int_0^t \frac{\partial}{\partial(t-s)}\mathbf{R}[\mathbf{C}(s), t-s]ds$

$$\frac{\partial}{\partial(t-s)}\mathbf{R}[\mathbf{C}(s), t-s] = \alpha_0'\mathbf{I} + \alpha_1'\mathbf{C}(s) + \alpha_2'\mathbf{C^2(s)} \tag{D.7}$$

Here: $\alpha_i' = \frac{\partial}{\partial(t-s)}\alpha_i(\mathbf{I_1}(s), \mathbf{I_2}(s), t-s)$. For brevity, let: $\underline{\mathbf{I}} = (\mathbf{I_1}, \mathbf{I_2})$. The integration is calculated by discretizing the time domain as follows:

$$\begin{aligned}
\int_{t_1}^{t_{n1}} \mathbf{R}\left[\underline{\mathbf{I}}(s), t_{n1} - s\right] ds &= \tfrac{t_{n1}-t_{n1-1}}{2}\left[\mathbf{R}\left(\underline{\mathbf{I}}(t_{n1}), t_{n1} - t_{n1}\right) + \mathbf{R}\left(\underline{\mathbf{I}}(t_{n1-1}), t_{n1} - t_{n1-1}\right)\right] \\
&+ \textstyle\sum_{k=1}^{n1-2} \tfrac{t_{k+1}-t_k}{2}\left[\mathbf{R}\left(\underline{\mathbf{I}}(t_{k+1}), t_{n1} - t_{k+1}\right) + \mathbf{R}\left(\underline{\mathbf{I}}(t_k), t_{n1} - t_k\right)\right].
\end{aligned}$$

Detailed calculation of this integration uses "STATEV" variables for storing and updating purposes.

D.2.2 Update the Material Jacobian: DDSDDE

2^{nd} Piola-Kirchhoff stress: $\mathbf{S} = J\mathbf{F}^{-1}\sigma\mathbf{F}^{-T}$, at $t = t_{n1}$

$$\begin{aligned}
\boldsymbol{S}(t) &= \boldsymbol{R}[\boldsymbol{C}(t), 0] + \int_0^t \frac{\partial}{\partial(t-s)}\mathbf{R}[\mathbf{C}(s), t-s]ds + KJ(J-1)\mathbf{C}^{-1} \\
&= \boldsymbol{R}[\boldsymbol{C}(t_{n1}), 0] + \frac{t_{n1} - t_{n1-1}}{2}\frac{\partial}{\partial(t-s)}\mathbf{R}[\mathbf{C}(s), t-s]|_{t_{n1}} + KJ(J-1)\mathbf{C}^{-1} \\
&\quad + \int_0^{t_{n-1}} \frac{\partial}{\partial(t-s)}\mathbf{R}[\mathbf{C}(s), t-s]ds
\end{aligned} \tag{D.8}$$

Using Cayley-Hamilton's principle

$$\boldsymbol{C^2} = \boldsymbol{I_1 C} - \boldsymbol{I_2 I} + \boldsymbol{I_3 C^{-1}},$$

2^{nd} Piola-Kirchhoff stress becomes:

$$\begin{aligned} \mathbf{S} &= (P + Q\mathbf{I_1})\mathbf{I} - Q\mathbf{C} + R\boldsymbol{I_3}\Phi\mathbf{C^{-1}} + KJ(J-1)\mathbf{C^{-1}} \\ &\quad + \int_0^{t_{n-1}} \frac{\partial}{\partial(t-s)}\mathbf{R}[\mathbf{C}(s), t-s]ds, \end{aligned} \tag{D.9}$$

P, Q, R are calculated as follows:

$$\begin{aligned} A &= \sum_{k=1}^{n}\left(\frac{g_{1k}}{\tau_{1k}}\right) \\ B &= \sum_{k=1}^{m}\left(\frac{g_{2k}}{\tau_{2k}}\right) \\ \triangle t &= t_{n1} - t_{n1-1} \\ P &= \left[1 - \frac{\triangle t}{2}A\right] G_{10} \\ Q &= \left[d - \frac{\triangle t}{2}dB\right] G_{10} \\ R &= \left\{-[1+2d] + \left[\frac{\triangle t}{2}(A + 2dB)\right]\right\} G_{10} \end{aligned}$$

Denote $E = \frac{1}{2}(\mathbf{C} - \mathbf{I})$ and $\mathcal{C}$ (or $\mathcal{L}$) as the material tangent, which is related to 2^{nd} Piola-Kirchhoff stress as follows:

$$\mathcal{C} = \mathcal{L} = \frac{\partial \mathbf{S}}{\partial \mathbf{E}} = 2\frac{\partial \mathbf{S}}{\partial \mathbf{C}}$$

Note that here: $\mathbf{C} = \mathbf{C}(t_n)$, hence the derivative of $\int_0^{t_{n-1}} \frac{\partial}{\partial(t-s)}\mathbf{R}[\mathbf{C}(s), t-s]ds$ in equa-

tion (D.9) with respect to $\mathbf{C}$ vanishes. Therefore,by recalling the following derivatives,

$$\begin{aligned}
\frac{\partial \mathbf{I_1}}{\partial \mathbf{C}} &= \mathbf{I}, \\
\frac{\partial \mathbf{I_3}}{\partial \mathbf{C}} &= \mathbf{I_3}\mathbf{C^{-1}}, \\
\frac{\partial J}{\partial \mathbf{C}} &= \frac{J}{2}\mathbf{C^{-1}}, \\
\frac{\partial \Phi}{\partial \mathbf{C}} &= -a\Phi\mathbf{I},
\end{aligned}$$

and using index notation, the material tangent $\mathcal{L}$ becomes:

$$\begin{aligned}
\mathcal{L}_{pqrs} &= 2Q\delta_{pq}\delta_{rs} - Q(\delta_{pr}\delta_{qs} + \delta_{ps}\delta_{qr}) \\
&\quad +2R\Phi\mathbf{I_3}\mathbf{C^{-1}}_{pq}\mathbf{C^{-1}}_{rs} - aR\Phi\mathbf{I_3}(\delta_{pq}\mathbf{C^{-1}}_{rs} + \mathbf{C^{-1}}_{pq}\delta_{rs}) \\
&\quad -R\mathbf{I_3}\Phi(\mathbf{C^{-1}}_{pr}\mathbf{C^{-1}}_{qs} + \mathbf{C^{-1}}_{qs}\mathbf{C^{-1}}_{qr}) \\
&\quad -KJ(J-1)(\mathbf{C^{-1}}_{pr}\mathbf{C^{-1}}_{qs} + \mathbf{C^{-1}}_{qs}\mathbf{C^{-1}}_{qr}) \\
&\quad +K(2J-1)J\mathbf{C^{-1}}_{pq}\mathbf{C^{-1}}_{rs}. \qquad \text{(D.10)}
\end{aligned}$$

To obtain the final material Jacobian (DDSDDE) used in UMAT subroutine, $\mathcal{L}$ is pushed-forward:

$$\begin{aligned}
\frac{1}{J}\mathbf{F}_{ip}\mathbf{F}_{jq}\mathbf{F}_{kr}\mathbf{F}_{ls}\mathcal{L}_{pqrs} &= \frac{1}{J}\{2Q\mathbf{B}_{ij}\mathbf{B}_{kl} - Q(\mathbf{B}_{ik}\mathbf{B}_{jl} + \mathbf{B}_{il}\mathbf{B}_{jk}) \\
&\quad +2R\Phi\mathbf{I_3}\delta_{ij}\delta_{kl} - aR\Phi\mathbf{I_3}(\mathbf{B}_{ij}\delta_{kl} + \delta_{ij}\mathbf{B}_{kl}) \\
&\quad -R\mathbf{I_3}\Phi(\delta_{ik}\delta_{jl} + \delta_{il}\delta_{jk})\} \\
&\quad -K(J-1)(\delta_{ik}\delta_{jl} + \delta_{il}\delta_{jk}). \\
&\quad +K(2J-1)\delta_{ij}\delta_{kl} \qquad \text{(D.11)}
\end{aligned}$$

Final formula for DDSDDE

$$\mathcal{L}^J_{ijkl} = \frac{1}{J}\mathbf{F}_{ip}\mathbf{F}_{jq}\mathbf{F}_{kr}\mathbf{F}_{ls}\mathcal{L}_{pqrs} + \frac{1}{2}(\delta_{ik}\sigma_{jl} + \delta_{jl}\sigma_{ik} + \sigma_{il}\delta_{jk} + \sigma_{jk}\delta_{il}). \qquad \text{(D.12)}$$

D.3 Verification by Comparing with Analytical Solutions

FE solutions for three simple testing scenarios (uniaxial, biaxial, and simple shear of a cubic block) were compared with the corresponding analytical solutions to verify the use of UMAT subroutine. Such a comparison is presented in Figure D.1. Here, a uniaxial test on a cubic block by applying a stretch λ in the x direction with the stretch history described as follows:

$$\begin{aligned} \lambda &= 1+t, 0 \leq t \leq 0.01, \\ \lambda &= 2, 0.01 \leq t \leq 0.15. \end{aligned}$$

In this example, the following set material properties was used: $g_1 = g_2 = 0.99$, $\tau_1 = \tau_2 = 0.01$, $G_{10} = 100, a = 0, d = 1$.

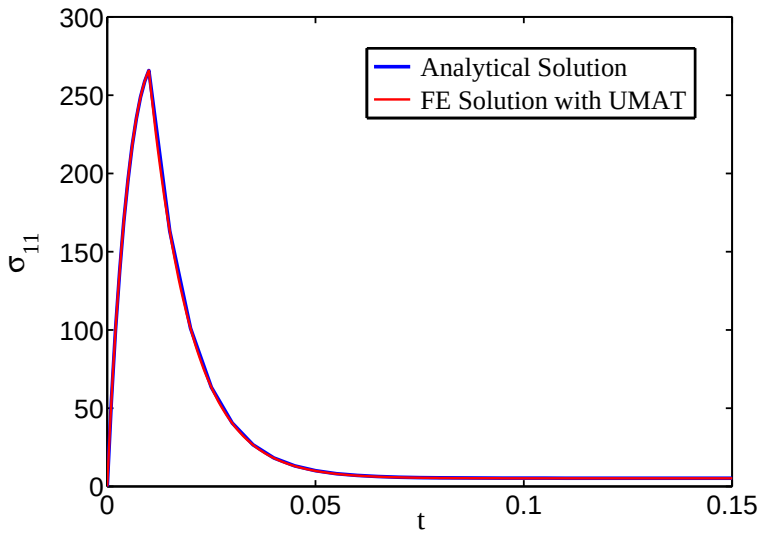

Figure D.1: Comparisons between analytical and FE solutions in the case of uniaxial deformation

Similar results were also obtained for the other two test cases. However, a convergence issue occurs when the applied stretch ratio is too large. For example, in the case of uniaxial testing consider here, the FE code aborted if $\lambda = 3$.

APPENDIX E

User Subroutine (UMAT) for ABAQUS

E.1 UMAT User Subroutine for an Incompressible, NLV Single Integral Pipkin-Rogers Model for 3D Solid Elements

```
C**********************************************************************
C  UMAT describing 3D, NLV single integreal Pipkin_Rogers Model
C  Two relaxation functions: G1(t), G2(t)
C  Relaxation functions are described by n terms Prony Series
C**********************************************************************
      SUBROUTINE UMAT(STRESS,STATEV,DDSDDE,SSE,SPD,SCD,RPL,DDSDDT,
     1 DRPLDE,DRPLDT,STRAN,DSTRAN,TIME,DTIME,TEMP,DTEMP,PREDEF,DPRED,
     2 CMNAME,NDI,NSHR,NTENS,NSTATV,PROPS,NPROPS,COORDS,DROT,PNEWDT,
     3 CELENT,DFGRD0,DFGRD1,NOEL,NPT,LAYER,KSPT,KSTEP,KINC)

      INCLUDE 'ABA_PARAM.INC'

      CHARACTER*80 CMNAME
    DIMENSION STRESS(NTENS),STATEV(NSTATV),DDSDDE(NTENS,NTENS),
    1 DDSDDT(NTENS),DRPLDE(NTENS),STRAN(NTENS),DSTRAN(NTENS),TIME(2),
    2 PREDEF(1),DPRED(1),PROPS(NPROPS),COORDS(3),DROT(3,3),
    3 DFGRD0(3,3),DFGRD1(3,3),TSIG(3,3),TFP(3,3),TDP(3,3),TDTSTP(3,3),
    4 TDTFE(3,3),TDTFP(3,3),TDTSIG(3,3),TDTDP(3,3)
```

```
      DIMENSION STRESST(3,3),B(3,3),BB(3,3),C(3,3),CC(3,3),CNM1(3,3),
     1CCNM1(3,3),AR0(3,3),ARNM11(3,3),ARNM12(3,3)
     2,ARSTOREINT1(3,3),ARSTOREINT2(3,3),ARUSET(3,3)
     3,ARSTORE1M(3,3),ARSTORE2M(3,3),ARSTOREM(3,3)
C NOTE: Sizes of Agc1-Atauc2 can be changed based on Prony series terms used
    DIMENSION ARSTORE1(9),ARSTORE2(9),ARUSE1(9),ARUSE2(9),ARUSE(9),
     #ARSTOREIN1(9),ARSTOREIN2(9),
     #Agc1(100),Agc2(100),Atauc1(100),Atauc2(100)
        COMMON/MECHPROP/EYONG,GNU,EN,CR
        COMMON/RATE/A,GAMDOT0,SS,H
        COMMON/TEMP11/TEMP0,BK,ALPHA
C*********************************************************************
C******** Variable Names:
C******** F=(J^(-1/3))*DFGRD, deformation gradient with eliminated volume change
C******** B: Left-Cauchy Tensor at time t(n): B, BB=B*B
C******** Right-Cauchy Tensor at time t(n): C, CC=C*C
C******** CNM1: Right-Cauchy Tensor at time t(n-1), CCNM1=CNM1*CNM1
C******** AR0: R[C(t(n)),0] inside the constitutive model
C******** ARNM11,ARNM12,ARSTOREINT,ARSTORE,STRESST: store the previous quantities
C******** Ac1: relaxtion time of G1(t), Ac=Ac2/Ac1
C*********************************************************************
C  MATERIAL PROPERTIES FROM THE INPUT DECK (SI UNITS)
C*********************************************************************

C Prony series terms of G1(t)
      An=Props(1)
C Prony series terms of G2(t)
      Am=Props(2)
C Relaxation properties of G1(t)
      Do I=1,An
      Agc1(I)=Props(2+I)
      Atauc1(I)=Props(2+An+I)
      enddo
C Relaxation properties of G2(t)
      Do I=1,Am
      Agc2(I)=Props(2+2*An+I)
      Atauc2(I)=Props(2+2*An+Am+I)
      enddo

C Initial Modulus of G1(t), G2(t): G20=d *G10
C Length of props: 2+2*An+2*Am+3
```

```
      AG10=Props(2+2*An+2*Am+1)
      Ad=Props(2+2*An+2*Am+2)
      Akz=Props(2+2*An+2*Am+3)

      Aa=0D0
      Do I=1,An
      Aa=Aa+Agc1(I)/Atauc1(I)
      enddo

      Ab=0D0
      Do I=1,Am
      Ab=Ab+Agc2(I)/Atauc2(I)
      enddo
C****** Time
      ATNM1=TIME(2)
      ATN=ATNM1+DTIME
C Large Bulk Modulus for enforcing Incompressibility

      Ag1=0D0
      Do I=1,An
      Ag1temp=1D0-STATEV(50+I)
      Ag1=Ag1+Agc1(I)*(1D0-Ag1temp*EXP(-DTIME/Atauc1(I)))
      STATEV(50+I)=1D0-Ag1temp*EXP(-DTIME/Atauc1(I))
      enddo
      Ag1=AG10*(1D0-Ag1)

      Ag2=0D0
      Do I=1,Am
      Ag2temp=1D0-STATEV(50+An+I)
      Ag2=Ag2+Agc2(I)*(1D0-Ag2temp*EXP(-DTIME/Atauc2(I)))
      STATEV(50+An+I)=1D0-Ag2temp*EXP(-DTIME/Atauc2(I))
      enddo
      Ag2=Ad*AG10*(1D0-Ag2)

      AK=1000D0*(Ag1+Ag2)
      AK2=0D0
C***** Deformation gradient DFGRD1(3,3), Jacobian
      AJ=DFGRD1(1,1)*(DFGRD1(2,2)*DFGRD1(3,3)-DFGRD1(2,3)*DFGRD1(3,2))
     #-DFGRD1(2,1)*(DFGRD1(1,2)*DFGRD1(3,3)-DFGRD1(1,3)*DFGRD1(3,2))
     #+DFGRD1(3,1)*(DFGRD1(1,2)*DFGRD1(2,3)-DFGRD1(1,3)*DFGRD1(2,2))
```

```
      AJM1=DFGRD0(1,1)*(DFGRD0(2,2)*DFGRD0(3,3)-DFGRD0(2,3)*DFGRD0(3,2))
     #-DFGRD0(2,1)*(DFGRD0(1,2)*DFGRD0(3,3)-DFGRD0(1,3)*DFGRD0(3,2))
     #+DFGRD0(3,1)*(DFGRD0(1,2)*DFGRD0(2,3)-DFGRD0(1,3)*DFGRD0(2,2))
C*******************************UPDATE STRESSES
C********** Calculate right cauchy tensor at time t(n)
      DO I=1,3
    DO J=1,3
      C(I,J) = 0D0
      CNM1(I,J)=0D0
      DO L=1,3
      C(I,J) = C(I,J)+DFGRD1(L,I)*DFGRD1(L,J)
      CNM1(I,J) = CNM1(I,J)+DFGRD0(L,I)*DFGRD0(L,J)
      ENDDO
      ENDDO
      ENDDO
C*********** Calculate CC=C*C at time t(n)
      DO I=1,3
    DO J=1,3
      CC(I,J) = 0D0
      CCNM1(I,J) = 0D0
      DO L=1,3
      CC(I,J) = CC(I,J) + C(I,L)*C(L,J)
      CCNM1(I,J) = CCNM1(I,J) + CNM1(I,L)*CNM1(L,J)
      ENDDO
      ENDDO
      ENDDO
C************ Calculate R[C(t),0]
      AI1=C(1,1)+C(2,2)+C(3,3)
      AI2=C(1,1)*C(2,2)+C(2,2)*C(3,3)+C(3,3)*C(1,1)-C(1,2)**2D0-
     #C(2,3)**2D0-C(1,3)**2D0

      Aphy=EXP(-Akz*(AI1-3D0))

      Alpha00=1D0+AI1*Ad-AI2*Aphy*(1D0+2D0*Ad)

      Alpha10=-Ad+AI1*Aphy*(1D0+2D0*Ad)

      Alpha20=-Aphy*(1D0+2D0*Ad)

      Do I=1,3
      Do J=1,3
```

```
      AR0(I,J)=0D0
      if (I.EQ.J) then
      AR0(I,J)=Alpha00+Alpha10*C(I,J)+Alpha20*CC(I,J)
      else
      AR0(I,J)=Alpha10*C(I,J)+Alpha20*CC(I,J)
      endif
      Enddo
      Enddo
C********** Update the integral R[C(s),t-s]
      AI1NM1=CNM1(1,1)+CNM1(2,2)+CNM1(3,3)
      AI2NM1=CNM1(1,1)*CNM1(2,2)+CNM1(2,2)*CNM1(3,3)+CNM1(3,3)
     #*CNM1(1,1)-CNM1(1,2)**2D0-CNM1(2,3)**2D0-CNM1(1,3)**2D0

      AphyNM1=EXP(-Akz*(AI1NM1-3D0))

C     For each term of G1(t)
      Do I=1,9
      ARUSE1(I)=0D0
      Enddo
      Do I1=1,An
C     At time: ATNM1
      Alpha0NM1p1=(-1D0+AphyNM1*AI2NM1)*Agc1(I1)/Atauc1(I1)
     #*EXP(-DTIME/Atauc1(I1))

      Alpha1NM1p1=-AphyNM1*AI1NM1*Agc1(I1)/Atauc1(I1)
     #*EXP(-DTIME/Atauc1(I1))

      Alpha2NM1p1=AphyNM1*Agc1(I1)/Atauc1(I1)
     #*EXP(-DTIME/Atauc1(I1))

      Do I=1,3
      Do J=1,3
      ARNM11(I,J)=0D0
      if (I.EQ.J) then
      ARNM11(I,J)=Alpha0NM1p1
     #+Alpha1NM1p1*CNM1(I,J)
     #+Alpha2NM1p1*CCNM1(I,J)
      else
      ARNM11(I,J)=
     #Alpha1NM1p1*CNM1(I,J)
     #+Alpha2NM1p1*CCNM1(I,J)
```

```
      endif
      Enddo
      Enddo

C     At time: ATN

      Alpha0p1=(-1D0+Aphy*AI2)*Agc1(I1)/Atauc1(I1)

      Alpha1p1=-Aphy*AI1*Agc1(I1)/Atauc1(I1)

      Alpha2p1=Aphy*Agc1(I1)/Atauc1(I1)

C     Call the saved values
      DO I=1,9
      ARSTORE1(I)=STATEV(I1*9-9+I)
      ENDDO

      DO I=1,3
      DO J=1,3
      ARSTOREINT1(I,J)=0D0
      if (I.EQ.J) then
      ARSTOREINT1(I,J)=0.5D0*DTIME*(Alpha0p1
     #+Alpha1p1*C(I,J)+Alpha2p1*CC(I,J)
     #+ARNM11(I,J))
      else
      ARSTOREINT1(I,J)=0.5D0*DTIME*(
     #Alpha1p1*C(I,J)+Alpha2p1*CC(I,J)
     #+ARNM11(I,J))
      endif
      ENDDO
      ENDDO

      CALL VOIGTV(ARSTOREINT1,ARSTOREIN1)

      DO I=1,9
      ARSTORE1(I)=ARSTORE1(I)*EXP(-DTIME/Atauc1(I1))+ARSTOREIN1(I)
      ARUSE1(I)=ARUSE1(I)+ARSTORE1(I)
      ENDDO

      Do I=1,9
      STATEV(9*I1-9+I)=ARUSE1(I)
```

```
       enddo


       enddo

C     For the each term of G2(t)
       Do I=1,9
       ARUSE2(I)=0D0
       Enddo

       Do I1=1,Am
C      At time: ATNM1
       Alpha0NM1p2=(-AI1NM1
     #+AphyNM1*AI2NM1*2D0)*Ad*Agc2(I1)/Atauc2(I1)
     #*EXP(-DTIME/Atauc2(I1))

       Alpha1NM1p2=(1D0-
     #AphyNM1*AI1NM1*2D0)*Ad*Agc2(I1)/Atauc2(I1)
     #*EXP(-DTIME/Atauc2(I1))

       Alpha2NM1p2=AphyNM1*2D0*Ad*Agc2(I1)/Atauc2(I1)
     #*EXP(-DTIME/Atauc2(I1))

       Do I=1,3
       Do J=1,3
       ARNM12(I,J)=0D0
       if (I.EQ.J) then
       ARNM12(I,J)=Alpha0NM1p2
     #+Alpha1NM1p2*CNM1(I,J)
     #+Alpha2NM1p2*CCNM1(I,J)
       else
       ARNM12(I,J)=
     #Alpha1NM1p2*CNM1(I,J)
     #+Alpha2NM1p2*CCNM1(I,J)
       endif
       Enddo
       Enddo

C     At time: ATN
        Alpha0p2=(-AI1
     #+Aphy*AI2*2D0)*Ad*Agc2(I1)/Atauc2(I1)
```

```
        Alpha1p2=(1D0-
     #Aphy*AI1*2D0)*Ad*Agc2(I1)/Atauc2(I1)

        Alpha2p2=Aphy*2D0*Ad*Agc2(I1)/Atauc2(I1)

C     Call saved values:
      DO I=1,9
      ARSTORE2(I)=STATEV(9*An+9*I1-9+I)
      ENDDO

      DO I=1,3
      DO J=1,3
      ARSTOREINT2(I,J)=0D0
      if (I.EQ.J) then
      ARSTOREINT2(I,J)=0.5D0*DTIME*(Alpha0p2
     #+Alpha1p2*C(I,J)+Alpha2p2*CC(I,J)
     #+ARNM12(I,J))
      else
      ARSTOREINT2(I,J)=0.5D0*DTIME*(
     #Alpha1p2*C(I,J)+Alpha2p2*CC(I,J)
     #+ARNM12(I,J))
      endif
      ENDDO
      ENDDO

      CALL VOIGTV(ARSTOREINT2,ARSTOREIN2)

      DO I=1,9
      ARSTORE2(I)=ARSTORE2(I)*EXP(-DTIME/Atauc2(I1))+ARSTOREIN2(I)
      ARUSE2(I)=ARUSE2(I)+ARSTORE2(I)
      ENDDO

      DO I=1,9
      STATEV(9*An+9*I1-9+I)=ARUSE2(I)
      ENDDO

      enddo

      DO I=1,9
      ARUSE(I)=ARUSE1(I)+ARUSE2(I)
      enddo
```

```
      CALL INVOIGTV(ARUSE,ARUSET)

      DO I=1,3
      DO J=1,3
      STRESST(I,J)=0D0
      IF (I.EQ.J) THEN
      DO M=1,3
      DO N=1,3
      STRESST(I,J)=STRESST(I,J)+AG10*DFGRD1(I,M)*
     #(AR0(M,N)+ARUSET(M,N))*DFGRD1(J,N)/AJ
      ENDDO
      ENDDO
      STRESST(I,J)=STRESST(I,J)+AK*(AJ-1D0)+AK2*log(AJ)/AJ
      ELSE
      DO M=1,3
      DO N=1,3
      STRESST(I,J)=STRESST(I,J)+AG10*DFGRD1(I,M)
     #*(AR0(M,N)+ARUSET(M,N))*DFGRD1(J,N)/AJ
      ENDDO
      ENDDO
      ENDIF
      ENDDO
      ENDDO

      DO I=1,3
      STRESS(I)=STRESST(I,I)
      ENDDO
      STRESS(4)=STRESST(1,2)
      STRESS(5)=STRESST(1,3)
      STRESS(6)=STRESST(2,3)
C**********************UPDATE MATERIAL JACOBIAN
C***** Left-Cauchy tensor: B
      Do I=1,3
      Do J=1,3
      B(I,J)=0D0
      Do M=1,3
      B(I,J)=B(I,J)+DFGRD1(I,M)*DFGRD1(J,M)
      Enddo
      Enddo
      Enddo
```

```
C**** Square of Left-Cauchy Tensor: B*B
      Do I=1,3
      Do J=1,3
      BB(I,J)=0D0
      Do M=1,3
      BB(I,J)=BB(I,J)+B(I,M)*B(M,J)
      Enddo
      Enddo
      Enddo
C***** Invariants of B, BB
      AP=(1D0-0.5D0*DTIME*Aa)*AG10/AJ
      AQ=(Ad-0.5D0*DTIME*Ad*Ab)*AG10/AJ
      AR=(-(1D0+2D0*Ad)+0.5D0*DTIME*(Aa
     #+2D0*Ad*Ab))*AG10
C*** Jacobian
       DDSDDE(1,1)=
     #-2D0*Akz*AR*AJ*Aphy*B(1,1)
     #-2D0*AK*(AJ-1D0)
     #+AK*(2D0*AJ-1D0)
     #+2D0*STRESST(1,1)
     #-2D0*AK2*log(AJ)/AJ
     #+AK2/AJ

      DDSDDE(2,2)=
     #-2D0*Akz*AR*AJ*Aphy*B(2,2)
     #-2D0*AK*(AJ-1D0)
     #+AK*(2D0*AJ-1D0)
     #+2D0*STRESST(2,2)
     #-2D0*AK2*log(AJ)/AJ
     #+AK2/AJ

      DDSDDE(3,3)=
     #-2D0*Akz*AR*AJ*Aphy*B(3,3)
     #-2D0*AK*(AJ-1D0)
     #+AK*(2D0*AJ-1D0)
     #+2D0*STRESST(3,3)
     #-2D0*AK2*log(AJ)/AJ
     #+AK2/AJ

      DDSDDE(1,2)=
     #2D0*AQ*B(1,1)*B(2,2)
```

```
#-2D0*AQ*B(1,2)*B(1,2)
#+2D0*AR*AJ*Aphy
#-Akz*AR*AJ*Aphy*(B(1,1)+B(2,2))
#+AK*(2D0*AJ-1D0)
#+AK2/AJ

 DDSDDE(1,2)=DDSDDE(1,2)
 DDSDDE(2,1)=DDSDDE(1,2)

 DDSDDE(2,3)=
#2D0*AQ*B(2,2)*B(3,3)
#-2D0*AQ*B(2,3)*B(2,3)
#+2D0*AR*AJ*Aphy
#-Akz*AR*AJ*Aphy*(B(2,2)+B(3,3))
#+AK*(2D0*AJ-1D0)
#+AK2/AJ

 DDSDDE(2,3)=DDSDDE(2,3)
 DDSDDE(3,2)=DDSDDE(2,3)

 DDSDDE(1,3)=
#2D0*AQ*B(1,1)*B(3,3)
#-2D0*AQ*B(1,3)*B(1,3)
#+2D0*AR*AJ*Aphy
#-Akz*AR*AJ*Aphy*(B(1,1)+B(3,3))
#+AK*(2D0*AJ-1D0)
#+AK2/AJ

 DDSDDE(1,3)=DDSDDE(1,3)
 DDSDDE(3,1)=DDSDDE(1,3)

 DDSDDE(1,4)=
#-Akz*AR*AJ*Aphy*B(1,2)
#+STRESST(1,2)

 DDSDDE(1,4)=DDSDDE(1,4)
 DDSDDE(4,1)=DDSDDE(1,4)

 DDSDDE(1,5)=
#-Akz*AR*AJ*Aphy*B(1,3)
#+STRESST(1,3)
```

```
 DDSDDE(1,5)=DDSDDE(1,5)
 DDSDDE(5,1)=DDSDDE(1,5)

 DDSDDE(1,6)=
#2D0*AQ*B(1,1)*B(2,3)
#-2D0*AQ*B(1,2)*B(1,3)
#-Akz*AR*AJ*Aphy*B(2,3)

 DDSDDE(1,6)=DDSDDE(1,6)
 DDSDDE(6,1)=DDSDDE(1,6)

 DDSDDE(2,4)=
#-Akz*AR*AJ*Aphy*B(1,2)
#+STRESST(1,2)

 DDSDDE(2,4)=DDSDDE(2,4)
 DDSDDE(4,2)=DDSDDE(2,4)

 DDSDDE(2,5)=
#2D0*AQ*B(2,2)*B(1,3)
#-2D0*AQ*B(1,2)*B(2,3)
#-Akz*AR*AJ*Aphy*B(1,3)

 DDSDDE(2,5)=DDSDDE(2,5)
 DDSDDE(5,2)=DDSDDE(2,5)

 DDSDDE(2,6)=
#-Akz*AR*AJ*Aphy*B(2,3)
#+STRESST(2,3)

 DDSDDE(2,6)=DDSDDE(2,6)
 DDSDDE(6,2)=DDSDDE(2,6)

 DDSDDE(3,4)=
#2D0*AQ*B(3,3)*B(1,2)
#-2D0*AQ*B(1,3)*B(2,3)
#-Akz*AR*AJ*Aphy*B(1,2)

 DDSDDE(3,4)=DDSDDE(3,4)
 DDSDDE(4,3)=DDSDDE(3,4)
```

```
 DDSDDE(3,5)=
#-Akz*AR*AJ*Aphy*B(1,3)
#+STRESST(1,3)

 DDSDDE(3,5)=DDSDDE(3,5)
 DDSDDE(5,3)=DDSDDE(3,5)

 DDSDDE(3,6)=
#-Akz*AR*AJ*Aphy*B(2,3)
#+STRESST(2,3)

 DDSDDE(3,6)=DDSDDE(3,6)
 DDSDDE(6,3)=DDSDDE(3,6)

 DDSDDE(4,4)=
#2D0*AQ*B(1,2)*B(1,2)
#-AQ*(B(1,1)*B(2,2)+B(1,2)*B(1,2))
#-AR*AJ*Aphy
#-AK*(AJ-1D0)
#+(STRESST(1,1)+STRESST(2,2))/2D0
#-AK2*log(AJ)/AJ

 DDSDDE(5,5)=
#2D0*AQ*B(1,3)*B(1,3)
#-AQ*(B(1,1)*B(3,3)+B(1,3)*B(1,3))
#-AR*AJ*Aphy
#-AK*(AJ-1D0)
#+(STRESST(1,1)+STRESST(3,3))/2D0
#-AK2*log(AJ)/AJ

 DDSDDE(6,6)=
#2D0*AQ*B(2,3)*B(2,3)
#-AQ*(B(2,2)*B(3,3)+B(2,3)*B(2,3))
#-AR*AJ*Aphy
#-AK*(AJ-1D0)
#+(STRESST(2,2)+STRESST(3,3))/2D0
#-AK2*log(AJ)/AJ

 DDSDDE(4,5)=
#2D0*AQ*B(1,2)*B(1,3)
```

```
     #-AQ*(B(1,1)*B(2,3)+B(1,3)*B(1,2))
     #+STRESST(2,3)/2D0

      DDSDDE(5,4)=DDSDDE(4,5)

      DDSDDE(4,6)=
     #2D0*AQ*B(1,2)*B(2,3)
     #-AQ*(B(2,2)*B(1,3)+B(1,2)*B(2,3))
     #+STRESST(1,3)/2D0

      DDSDDE(6,4)=DDSDDE(4,6)

      DDSDDE(5,6)=
     #2D0*AQ*B(1,3)*B(2,3)
     #-AQ*(B(3,3)*B(1,2)+B(1,3)*B(2,3))
     #+STRESST(1,2)/2D0

      DDSDDE(6,5)=DDSDDE(5,6)

C9987  format('','**************************')
C     ITERATION ENDS HERE
    RETURN
    END
C=============================
      SUBROUTINE VOIGTV(AA1,VOIGT1)
C      IMPLICIT REAL*8(A-H,O-Z)
    INCLUDE 'aba_param.inc'
C   REAL A,VOIGT1,VOIGT2

c---- converts a 2nd order tensor to column vector using chi2 mapping
c---- Note order : {11,22,33,12,13,23,21,31,32}

      DIMENSION AA1(3,*), VOIGT1(*)
       DO I=1,3
        VOIGT1(I) = AA1(I,I)
       ENDDO
        VOIGT1(4) = AA1(1,2)
        VOIGT1(5) = AA1(1,3)
        VOIGT1(6) = AA1(2,3)
        VOIGT1(7) = AA1(2,1)
        VOIGT1(8) = AA1(3,1)
```

```
        VOIGT1(9) = AA1(3,2)
      RETURN
    END
C=======================
      SUBROUTINE INVOIGTV(VOIGT,AB1)
C     IMPLICIT REAL*8(A-H,O-Z)
    INCLUDE 'aba_param.inc'
C     REAL A,VOIGT1,VOIGT2

c---- obtains a 2nd order tensor from column vector using inverse chi2 mapping
c---- Note order : {11,22,33,12,13,23,21,31,32}

      DIMENSION AB1(3,*), VOIGT(*)
       DO I=1,3
         AB1(I,I) = VOIGT(I)
       ENDDO
         AB1(1,2) = VOIGT(4)
         AB1(1,3) = VOIGT(5)
         AB1(2,3) = VOIGT(6)
         AB1(2,1) = VOIGT(7)
         AB1(3,1) = VOIGT(8)
         AB1(3,2) = VOIGT(9)
       RETURN
       END
```

E.2 UMAT User Subroutine for an Incompressible, NLV Single Integral Pipkin-Rogers Model for Membrane Elements

```
C**********************************************************************
C  UMAT: membrane elements, NLV single integral Pipkin-Rogers Model
C**********************************************************************
      SUBROUTINE UMAT(STRESS,STATEV,DDSDDE,SSE,SPD,SCD,RPL,DDSDDT,
    1 DRPLDE,DRPLDT,STRAN,DSTRAN,TIME,DTIME,TEMP,DTEMP,PREDEF,DPRED,
     2 CMNAME,NDI,NSHR,NTENS,NSTATV,PROPS,NPROPS,COORDS,DROT,PNEWDT,
     3 CELENT,DFGRD0,DFGRD1,NOEL,NPT,LAYER,KSPT,KSTEP,KINC)
```

```
      INCLUDE 'ABA_PARAM.INC'

      CHARACTER*80 CMNAME
     DIMENSION STRESS(NTENS),STATEV(NSTATV),DDSDDE(NTENS,NTENS),
     1 DDSDDT(NTENS),DRPLDE(NTENS),STRAN(NTENS),DSTRAN(NTENS),TIME(2),
     2 PREDEF(1),DPRED(1),PROPS(NPROPS),COORDS(3),DROT(3,3),
     3 DFGRD0(3,3),DFGRD1(3,3),TSIG(3,3),TFP(3,3),TDP(3,3),TDTSTP(3,3),
     4 TDTFE(3,3),TDTFP(3,3),TDTSIG(3,3),TDTDP(3,3)
      DIMENSION STRESST(3,3),B(3,3),BB(3,3),C(3,3),CC(3,3),CNM1(3,3),
     1CCNM1(3,3),AR0(3,3),ARNM11(3,3),ARNM12(3,3)
     2,ARSTOREINT1(3,3),ARSTOREINT2(3,3),ARUSET(3,3),STRESST1(3,3)
     3,ARSTORE1M(3,3),ARSTORE2M(3,3),ARSTOREM(3,3)
     DIMENSION ARSTORE1(9),ARSTORE2(9),ARUSE(9),ARSTOREIN1(9),ARSTOREIN2(9)
        COMMON/MECHPROP/EYONG,GNU,EN,CR
        COMMON/RATE/A,GAMDOT0,SS,H
        COMMON/TEMP11/TEMP0,BK,ALPHA
C*************************************************************
C******** F=(J^(-1/3))*DFGRD, deformation gradient with eliminated volume change
C******** B: Left-Cauchy Tensor: B, BB=B*B
C******** C: Right-Cauchy Tesor at time t(n): C, CC=C*C
C******** CNM1: Right-Cauchy Tensor at time t(n-1), CCNM1=CNM1*CNM1
C******** AR0: R[C(t(n)),0] inside the constitutive model the constitutive model
C******** ARNM11,ARNM12,ARSTOREINT,ARSTORE,STRESST: to store the previous ↩
    quantities
C*************************************************************
C  MATERIAL PROPERTIES FROM THE INPUT DECK (SI UNITS)
C*************************************************************
      Aa=PROPS(1)
      Ab=PROPS(2)
      Ac=PROPS(3)
      Ad=PROPS(4)
      Akz=PROPS(5)
      AG10=PROPS(6)
      AK=PROPS(7)
C****** Time
      ATNM1=TIME(2)
      ATN=ATNM1+DTIME
C***** Deformation gradient DFGRD1(3,3), Jacobian
      AJ=DFGRD1(1,1)*(DFGRD1(2,2)*DFGRD1(3,3)-DFGRD1(2,3)*DFGRD1(3,2))
     1-DFGRD1(2,1)*(DFGRD1(1,2)*DFGRD1(3,3)-DFGRD1(1,3)*DFGRD1(3,2))
```

```
     2+DFGRD1(3,1)*(DFGRD1(1,2)*DFGRD1(2,3)-DFGRD1(1,3)*DFGRD1(2,2))

      AJM1=DFGRD0(1,1)*(DFGRD0(2,2)*DFGRD0(3,3)-DFGRD0(2,3)*DFGRD0(3,2))
     1-DFGRD0(2,1)*(DFGRD0(1,2)*DFGRD0(3,3)-DFGRD0(1,3)*DFGRD0(3,2))
     2+DFGRD0(3,1)*(DFGRD0(1,2)*DFGRD0(2,3)-DFGRD0(1,3)*DFGRD0(2,2))

      AJ1=AJ**(-2D0/3D0)

      AJ1M1=AJM1**(-2D0/3D0)
C****** UPDATE STRESSES
C********** Calculate right cauchy tensor CE at time t(n)
      DO I=1,3
      DO J=1,3
      C(I,J) = 0D0
      CNM1(I,J)=0D0
      DO L=1,3
      C(I,J) = C(I,J) +AJ1*DFGRD1(L,I)*DFGRD1(L,J)
      CNM1(I,J) = CNM1(I,J) +AJ1M1*DFGRD0(L,I)*DFGRD0(L,J)
      ENDDO
      ENDDO
      ENDDO
C*********** Calculate CEE=CE*CE at time t
      DO I=1,3
    DO J=1,3
      CC(I,J) = 0D0
      CCNM1(I,J) = 0D0
      DO L=1,3
      CC(I,J) = CC(I,J) + C(I,L)*C(L,J)
      CCNM1(I,J) = CCNM1(I,J) + CNM1(I,L)*CNM1(L,J)
      ENDDO
      ENDDO
      ENDDO
C************ Calculate R[C(t),0]
      AI1=C(1,1)+C(2,2)+C(3,3)
      AI2=C(1,1)*C(2,2)+C(2,2)*C(3,3)+C(3,3)*C(1,1)-C(1,2)**2-
     1C(2,3)**2-C(1,3)**2

      Alpha00=1D0+AI1*Ad-AI2*EXP(-Akz*(AI1-3D0))*(1D0+2D0*Ad)

      Alpha10=-Ad+AI1*EXP(-Akz*(AI1-3D0))*(1D0+2D0*Ad)
```

```
      Alpha20=EXP(-Akz*(AI1-3D0))*(1D0+2D0*Ad)



      Do I=1,3
      Do J=1,3
      AR0(I,J)=0D0
      if (I.EQ.J) then
      AR0(I,J)=Alpha00+Alpha10*C(I,J)+Alpha20*CC(I,J)
      else
      AR0(I,J)=Alpha10*C(I,J)+Alpha20*CC(I,J)
      endif
      End do
      End do
C********** Update the integral R[C(s),t-s]
      AI1NM1=CNM1(1,1)+CNM1(2,2)+CNM1(3,3)
      AI2NM1=CNM1(1,1)*CNM1(2,2)+CNM1(2,2)*CNM1(3,3)+CNM1(3,3)
     1*CNM1(1,1)-CNM1(1,2)**2-CNM1(2,3)**2-CNM1(1,3)**2

      AphyNM1=EXP(-Akz*(AI1NM1-3D0))

      Alpha0NM1p1=(-1D0+AphyNM1*AI2NM1)*(1-Aa)*EXP(ATNM1)

      Alpha0NM1p2=(-AI1NM1
     1+AphyNM1*AI2NM1*2D0)*Ad*Ac*(1-Ab)*EXP(Ac*ATNM1)

      Alpha1NM1p1=-AphyNM1*AI1NM1*(1-Aa)*EXP(ATNM1)

      Alpha1NM1p2=(1D0-
     1AphyNM1*AI1NM1*2D0)*Ad*Ac*(1-Ab)*EXP(Ac*ATNM1)

      Alpha2NM1p1=AphyNM1*(1-Aa)*EXP(ATNM1)

      Alpha2NM1p2=AphyNM1*2D0*Ad*Ac*(1-Ab)*EXP(Ac*ATNM1)

      Do I=1,3
      Do J=1,3
      ARNM11(I,J)=0D0
      ARNM12(I,J)=0D0
      if (I.EQ.J) then
      ARNM11(I,J)=Alpha0NM1p1
     1+Alpha1NM1p1*CNM1(I,J)
```

```
     2+Alpha2NM1p1*CCNM1(I,J)

      ARNM12(I,J)=Alpha0NM1p2
     1+Alpha1NM1p2*CNM1(I,J)
     2+Alpha2NM1p2*CCNM1(I,J)
      else
      ARNM11(I,J)=
     1Alpha1NM1p1*CNM1(I,J)
     2+Alpha2NM1p1*CCNM1(I,J)

      ARNM12(I,J)=
     1Alpha1NM1p2*CNM1(I,J)
     2+Alpha2NM1p2*CCNM1(I,J)
      endif
      End do
      End do

      Aphy=EXP(-Akz*(AI1-3D0))

      Alpha0p1=(-1D0+Aphy*AI2)*(1-Aa)*EXP(ATN)

      Alpha0p2=(-AI1
     1+Aphy*AI2*2D0)*Ad*Ac*(1-Ab)*EXP(Ac*ATN)

      Alpha1p1=-Aphy*AI1*(1-Aa)*EXP(ATN)

      Alpha1p2=(1D0-
     1Aphy*AI1*2D0)*Ad*Ac*(1-Ab)*EXP(Ac*ATN)

      Alpha2p1=Aphy*(1D0-Aa)*EXP(ATN)

      Alpha2p2=Aphy*2D0*Ad*Ac*(1-Ab)*EXP(Ac*ATN)

      DO I=1,9
      ARSTORE1(I)=STATEV(I)
      ARSTORE2(I)=STATEV(I+9)
      ENDDO

      DO I=1,3
      DO J=1,3
      ARSTOREINT1(I,J)=0D0
```

```
 ARSTOREINT2(I,J)=0D0
 if (I.EQ.J) then
 ARSTOREINT1(I,J)=0.5D0*DTIME*(Alpha0p1
1+Alpha1p1*C(I,J)+Alpha2p1*CC(I,J)
2+ARNM11(I,J))

 ARSTOREINT2(I,J)=0.5D0*DTIME*(Alpha0p2
1+Alpha1p2*C(I,J)+Alpha2p2*CC(I,J)
2+ARNM12(I,J))
 else
 ARSTOREINT1(I,J)=0.5D0*DTIME*(
1Alpha1p1*C(I,J)+Alpha2p1*CC(I,J)
2+ARNM11(I,J))

 ARSTOREINT2(I,J)=0.5D0*DTIME*(
1Alpha1p2*C(I,J)+Alpha2p2*CC(I,J)
2+ARNM12(I,J))
 endif
 ENDDO
 ENDDO

 CALL VOIGTV(ARSTOREINT1,ARSTOREIN1)
 CALL VOIGTV(ARSTOREINT2,ARSTOREIN2)

 CALL INVOIGTV(ARSTORE1,ARSTORE1M)
 CALL INVOIGTV(ARSTORE2,ARSTORE2M)

 DO I=1,9
 ARSTORE1(I)=ARSTORE1(I)+ARSTOREIN1(I)
 ARSTORE2(I)=ARSTORE2(I)+ARSTOREIN2(I)
 ARUSE(I)=ARSTORE1(I)*EXP(-ATN)+ARSTORE2(I)*EXP(-Ac*ATN)
 ENDDO

 CALL INVOIGTV(ARUSE,ARUSET)

 Do I=1,3
 Do J=1,3
 ARSTOREM(I,J)=ARSTORE1M(I,J)*EXP(-ATN)+ARSTORE2M(I,J)*EXP(-Ac*ATN)
1+0.5D0*DTIME*(ARNM11(I,J)*EXP(-ATN)+ARNM12(I,J)*EXP(-Ac*ATN))
 Enddo
 Enddo
```

```
      DO I=1,3
      DO J=1,3
      STRESST1(I,J)=0D0
      STRESST(I,J)=0D0
      IF (I.EQ.J) THEN
      DO M=1,3
      DO N=1,3
      STRESST(I,J)=STRESST(I,J)+AG10*AJ1*DFGRD1(I,M)*
     1(ARO(M,N)+ARUSET(M,N))*DFGRD1(J,N)/AJ
      STRESST1(I,J)=STRESST1(I,J)+AG10*AJ1*DFGRD1(I,M)*ARSTOREM(M,N)
     3*DFGRD1(J,N)
      ENDDO
      ENDDO
      STRESST(I,J)=STRESST(I,J)+AK*(AJ-1)
      ELSE
      DO M=1,3
      DO N=1,3
      STRESST(I,J)=STRESST(I,J)+AG10*AJ1*DFGRD1(I,M)
     1*(ARO(M,N)+ARUSET(M,N))*DFGRD1(J,N)/AJ
      STRESST1(I,J)=STRESST1(I,J)+AG10*AJ1*DFGRD1(I,M)*ARSTOREM(M,N)
     3*DFGRD1(J,N)
      ENDDO
      ENDDO
      ENDIF
      ENDDO
      ENDDO

      DO I=1,2
      STRESS(I)=STRESST(I,I)
      ENDDO
      STRESS(3)=STRESST(1,2)
      write(17,*) STRESST(3,3)
      write(18,*) AJ
      Do I=1,9
      STATEV(I)=ARSTORE1(I)
      STATEV(I+9)=ARSTORE2(I)
      Enddo
C***** UPDATE MATERIAL JACOBIAN
C***** Left-Cauchy tensor: B
      Do I=1,3
```

```
      Do J=1,3
      B(I,J)=0D0
      Do M=1,3
      B(I,J)=B(I,J)+DFGRD1(I,M)*DFGRD1(J,M)
      Enddo
      Enddo
      Enddo
C**** Square of Left-Cauchy Tensor: B*B
      Do I=1,3
      Do J=1,3
      BB(I,J)=0D0
      Do M=1,3
      BB(I,J)=BB(I,J)+B(I,M)*B(M,J)
      Enddo
      Enddo
      Enddo
C***** Invariants of B, BB
      AI1b=B(1,1)+B(2,2)+B(3,3)
      AI2b=B(1,1)*B(2,2)+B(2,2)*B(3,3)+B(3,3)*B(1,1)
     1-B(1,2)**2-B(2,3)**2-B(1,3)**2

      AP=(1D0-0.5D0*DTIME*(1D0-Aa))*AG10/AJ
      AQ=(Ad-0.5D0*DTIME*Ac*Ad*(1D0-Ab))*AG10/AJ
      AR=(-(1D0+2D0*Ad)+0.5D0*DTIME*(1D0-Aa+2D0*Ac*Ad*(1D0-Ab)))*AG10/AJ

      Aphy=EXP(-Akz*(AI1b-3D0))

      B11=B(1,1)
      B22=B(2,2)
      B33=B(3,3)
      B12=B(1,2)
      B21=B(2,1)
      B13=B(1,3)
      B31=B(3,1)
      B23=B(2,3)
      B32=B(3,2)
C*** Jacobian (Integrations inside the derivation were done by Maple)
       DDSDDE(1,1)=(2D0*B11*(AQ*B11 *(-B33 * (-2D0*(-AQ*B33+ AR * Akz *
     #Aphy) / B33 +(2D0*AR*Aphy + AK) * B22)/(2D0* AQ * B11+(2D0*A
     #P * B33 + AK-2D0* AR * Akz * Aphy * B33 +2D0* AR * Aphy) / B33 +
     #2D0*AQ* B22)+1D0)+AQ* (B11 + B22 + B33)+B33 * (AP + AQ * (B1
```

```
#1 + B22)) * (-2D0*(-AQ * B33 + AR * Akz * Aphy) / B33+(2D0 * AR *
#Aphy + AK) * B22)/(2D0*AQ * B11+(2D0 * AP * B33 + AK-2D0 * AR *
#Akz * Aphy * B33+2D0 * AR * Aphy) / B33+2D0*AQ * B22)-2D0 * AQ *
# B11 + AP - AQ * B33)+2D0*(AQ * B33 * B12 *(2D0* AR * Aphy + AK)
# /(2D0* AQ * B11+(2D0* AP * B33 + AK-2D0 * AR * Akz * Aphy * B33
#+2D0* AR * Aphy) / B33+2D0* AQ * B22) * B11 - AQ * B12 - (AP + AQ
# * (B11 + B22)) * B33 * B12*(2D0 * AR * Aphy + AK)/(2D0*AQ * B11
# + (2D0*AP* B33+ AK-2D0 * AR * Akz * Aphy * B33 +2D0 * AR * Aphy)
# / B33 +2D0 * AQ * B22)) * B12)+(STRESST1(1,1))*2D0/AJ

 DDSDDE(2,2)=(2D0*(-2D0*B12**2D0*B33**2D0*AQ*B11 *AR * Aphy+2D0 *
#B12**2D0*AQ* AR * Akz * Aphy * B33 + 2D0*B22 * AP * B11 * B33 *
#*2D0* AR * Aphy+2D0* B22 * AQ * B11 **2D0*B33 ** 2D0 * AR * Aphy -
# B12**2D0* B33**2D0* AQ * B11 * AK-4D0* B22 * B33 * AP * AR * A
#kz * Aphy + B22 * AP * AK+2D0 * B22 * AP**2D0 * B33 - B12**2D0 * A
#Q * AK + B22 * AP * B11 * B33 **2D0* AK + B22 * AQ * B11**2D0 * B3
#3 **2D0* AK +4D0* B22 * AQ * B11 * AP * B33+2D0 * B22 * AQ * B11 *
# AR * Aphy-2D0*B12**2D0* B33 **2D0* AP * AR * Aphy-4D0 * B22 *
#AQ * B11 * AR * Akz * Aphy * B33 -2D0* B12**2D0 * AQ * AR * Aphy -
# 2D0* B12**2D0* AQ**2D0 * B22 * B33 +2D0*B22 * AQ **2D0* B11 * B3
#3 **2D0+2D0* B22 * AQ * AP * B33 **2D0-2D0*B12**2D0 * AQ * AP * B
#33 + 2D0*AQ **2D0*B22**2D0*B11 * B33+2D0 * AQ * B22**2D0 * AP *
# B33 -2D0*B12 **2D0* AQ**2D0* B11 * B33+2D0 * B22 * AQ**2D0 * B1
#1 **2D0* B33 + 2D0* B22 * AP * AR * Aphy+ B22 * AQ * B11 * AK - B1
#2 ** 2D0*B33**2D0 * AP * AK) / (2D0* AQ * B11 * B33+2D0* AP * B33
#+ AK - 2D0*AR * Akz * Aphy * B33 + 2D0* AR * Aphy+2D0* AQ * B22 *
#B33))+STRESST1(2,2)*2D0/AJ

 DDSDDE(1,2)=(2D0*(2D0*B12**2*AQ* AR * Akz * Aphy * B33+2D0* B22 *
#AP * B11 * B33 ** 2 * AR * Aphy - 2D0*B22 * B33 * AP * AR * Akz *
#Aphy - B12 ** 2 * AQ * AK + AQ * B22 ** 2 * B11 * B33 ** 2 * AK -
#B12 ** 2 * AQ * B33 ** 2 * B22 * AK-2D0* B12 ** 2 * AQ * B33 ** 2
# * B22 * AR * Aphy-2D0* AQ * B22 ** 2 * AR * Akz * Aphy * B33+2D0
# * AQ * B22 ** 2 * B11 * B33 ** 2 * AR * Aphy+2D0 * B22 * AQ * AR
#* Akz * Aphy * B33 ** 2 + B22 * AP * B11 * B33 ** 2 * AK+2D0 * B22
# * AQ * B11 * AP * B33+2D0 * B22 * AQ * B11 * AR * Aphy-2D0 * B12
#** 2 * B33 ** 2 * AP * AR * Aphy - B22 * AQ * B33 * AK-2D0 * B22 *
# AQ * B11 * AR * Akz * Aphy * B33-2D0* B12 ** 2 * AQ * AR * Aphy
#-2D0* B12 ** 2 * AQ ** 2 * B22 * B33-2D0* B22 * AQ ** 2 * B11 * B
#33 ** 2 - 2D0* B12 ** 2 * AQ * AP * B33+2D0* AQ ** 2 * B22 ** 2 *
#B11 * B33 - 2D0*B12 ** 2 * AQ **2D0*B11 * B33+2D0 * B22 * AQ ** 2
```

```
# * B11 ** 2 * B33 + B22 * AQ * B11 * AK - B12 ** 2 * B33 ** 2 * AP
# * AK-2D0* B22 * AQ * B33 * AR * Aphy)/(2D0*AQ* B11 * B33 + 2D0
#* AP * B33 + AK -2D0*AR * Akz * Aphy * B33+2D0* AR *Aphy+2D0*
#AQ * B22 * B33))+(STRESST1(2,2)+STRESST1(1,1))/2D0/AJ

 DDSDDE(2,1)=(2D0*(-2D0*B12**2*B33** 2* AQ * B11 * AR * Aphy+2D0 *
#B12 ** 2 * AQ * AR * Akz * Aphy * B33 +2D0* B22 * AP * B11 * B33 *
#* 2 * AR * Aphy+2D0* B22 * AQ * B11 ** 2 * B33 ** 2 * AR * Aphy -
# B12 ** 2 * B33 ** 2 * AQ * B11 * AK-2D0 * B11 * AQ * B33 * AR * A
#phy - B12 ** 2 * AQ * AK-2D0*AQ * B11 ** 2 * AR * Akz * Aphy * B
#33-2D0* B11 * B33 * AP * AR * Akz * Aphy+2D0* B11 * AQ * AR * Ak
#z * Aphy * B33 ** 2 + B22 * AP * B11 * B33 ** 2 * AK + B22 * AQ *
#B11 ** 2 * B33 ** 2 * AK +2D0* B22 * AQ * B11 * AP * B33+2D0 * B22
# * AQ * B11 * AR * Aphy-2D0* B12 ** 2 * B33 ** 2 * AP * AR * Aphy
# -2D0* B22 * AQ * B11 * AR * Akz * Aphy * B33-2D0* B12 ** 2 * AQ
#* AR * Aphy-2D0*B12 ** 2 * AQ ** 2 * B22 * B33-2D0 * B22 * AQ **
# 2 * B11 * B33 ** 2-2D0* B12 ** 2 * AQ * AP * B33+2D0 * AQ ** 2 *
# B22 ** 2 * B11 * B33-2D0* B12 ** 2 * AQ ** 2 * B11 * B33+2D0 * B
#22 * AQ ** 2 * B11 ** 2 * B33 + B22 * AQ * B11 * AK - B11 * AQ * B
#33 * AK - B12 ** 2 * B33 ** 2 * AP * AK)/(2D0*AQ * B11 * B33 + 2D0
# * AP * B33 + AK-2D0*AR * Akz * Aphy * B33+2D0* AR * Aphy+2D0 *
# AQ * B22 * B33))+(STRESST1(2,2)+STRESST1(1,1))/2D0/AJ

 DDSDDE(1,3)=(B12 *(2D0*AP**2*B33 + AP * AK+2D0* AQ ** 2 * B22 * B3
#3 ** 2 - 2 * AQ ** 2 * B11 * B33 ** 2 + 2 * AQ * AP * B33 ** 2 - A
#Q * B33 * AK + 2 * AP * AR * Aphy - 4 * B33 * AQ * B22 * AR * Akz
#* Aphy - 6 * B33 * AP * AR * Akz * Aphy + 2 * AQ * AR * Akz * Aphy
# * B33 ** 2 + 2 * B22 * AQ * B33 * AP + 2 * B11 * AQ * B33 * AP -
#2 * AQ * B33 * AR * Aphy) / (2 * AQ * B11 * B33 + 2 * AP * B33 + A
#K - 2 * AR * Akz * Aphy * B33 + 2 * AR * Aphy + 2 * AQ * B22 * B33
#))+(STRESST1(1,2))/AJ

 DDSDDE(3,1)=(B12*(-AQ**2D0*B11 * B33 +2D0*AQ*B11 * AR * Akz * Aphy
# + AP**2D0+ AQ * B11 * AP + AQ * B22 * AP - AP * AR * Akz * Aphy
#+ AQ * B33 * AP + B33 * AQ**2D0 * B22 - AQ * B33 * AR * Akz * Aphy
#) / AJ / (AP + AQ * B11 + AQ * B22 - AR * Akz * Aphy))
#+(STRESST1(1,2))/AJ

 DDSDDE(2,3)=(B12 * (-B33 * AQ **2D0*B22+AQ*B22*AP-3D0 * AP * AR *
#Akz * Aphy-2D0 * AQ * B11 * AR * Akz * Aphy + AQ * B33 * AR * Akz
#* Aphy + AQ **2D0* B11 * B33 + AQ * B11 * AP + AQ * B33 * AP + AP
```

```
     #**2D0)/ AJ / (AP + AQ * B11 + AQ * B22 - AR * Akz * Aphy))
     #+(STRESST1(1,2))/AJ

      DDSDDE(3,2)=(B12*(-B33*AQ**2D0*B22+2D0*AQ * B22 * AR * Akz * Aphy
     # + AP **2D0+ AQ * B11 * AP + AQ * B22 * AP - AP * AR * Akz * Aphy
     #+ AQ * B33 * AP + AQ**2D0 * B11 * B33 - AQ * B33 * AR * Akz * Aphy
     #) / AJ / (AP + AQ * B11 + AQ * B22 - AR * Akz * Aphy))
     #+(STRESST1(1,2))/AJ

      DDSDDE(3,3)=(B12*(AQ*B12*(-B33 *(-2D0* (-AQ * B33 + AR * Akz * Aph
     #y) / B33+(2D0* AR * Aphy + AK) * B22)/(2D0* AQ * B11+(2D0 * AP *
     # B33 + AK-2D0* AR * Akz * Aphy * B33+2D0* AR * Aphy) / B33+2D0 *
     # AQ * B22)+1D0) - AQ * B12) + (AQ * B33 * B12 ** 2 *(2D0* AR * Aph
     #y + AK) / (2 * AQ * B11 + (2 * AP * B33 + AK - 2 * AR * Akz * Aphy
     # * B33 + 2 * AR * Aphy) / B33 + 2 * AQ * B22) + AP + AQ * (B11 + B
     #22 + B33) - AQ * (B11 + B22)) * B22 + (AQ * B33 * B12 ** 2 * (2 *
     #AR * Aphy + AK) / (2 * AQ * B11 + (2 * AP * B33 + AK - 2 * AR * Ak
     #z * Aphy * B33 + 2 * AR * Aphy) / B33 + 2 * AQ * B22) + AP + AQ *
     #(B11 + B22 + B33) - AQ * (B11 + B22)) * B11 + B12 * (AQ * B12 * (-
     #B33 * ((2 * AR * Aphy + AK) * B11 - 2 * (-AQ * B33 + AR * Akz * Ap
     #hy) / B33) / (2 * AQ * B11 + (2 * AP * B33 + AK - 2 * AR * Akz * A
     #phy * B33 + 2 * AR * Aphy) / B33 +2D0 * AQ * B22)+1D0)-AQ*B12))
     #+(STRESST1(2,2)+STRESST1(1,1))/2D0/AJ

C       CALCULATE INTEGRAL OF DMU/DR
C       write(100,9987)
C9987   format('','**************************')
C      ITERATION ENDS HERE
     RETURN
     END
C=================================
      SUBROUTINE VOIGTV(A,VOIGT1)
C       IMPLICIT REAL*8(A-H,O-Z)
     INCLUDE 'aba_param.inc'
C    REAL A,VOIGT1,VOIGT2

c----- converts a 2nd order tensor to column vector using chi2 mapping
c----- Note order : {11,22,33,12,23,31,21,32,13}

      DIMENSION A(3,*), VOIGT1(*)
       DO I=1,3
```

```
        VOIGT1(I) = A(I,I)
       ENDDO
        VOIGT1(4) = A(1,2)
        VOIGT1(5) = A(1,3)
        VOIGT1(6) = A(2,3)
        VOIGT1(7) = A(2,1)
        VOIGT1(8) = A(3,1)
        VOIGT1(9) = A(3,2)
      RETURN
    END
C=======================
      SUBROUTINE INVOIGTV(VOIGT1,A)
C    IMPLICIT REAL*8(A-H,O-Z)
    INCLUDE 'aba_param.inc'
C    REAL A,VOIGT1,VOIGT2

c---- obtains a 2nd order tensor from column vector using inverse chi2 mapping
c---- Note order : {11,22,33,12,23,31,21,32,13}

      DIMENSION A(3,*), VOIGT1(*)
       DO I=1,3
         A(I,I) = VOIGT1(I)
       ENDDO
         A(1,2) = VOIGT1(4)
         A(1,3) = VOIGT1(5)
         A(2,3) = VOIGT1(6)
         A(2,1) = VOIGT1(7)
         A(3,1) = VOIGT1(8)
         A(3,2) = VOIGT1(9)
       RETURN
       END
```

BIBLIOGRAPHY

BIBLIOGRAPHY

ABAQUS-v6.10 (2010), *ABAQUS User's Manual 6.10*, Dassault Systèmes Simulia Corp., Providence, RI, USA.

Bao, G., and S. Suresh (2003), Cell and molecular mechanics of biological materials, *Nature Materials*, *2*, 715–725.

Bažant, Z. P., and L. Cedolin (2003), *Stability of Structures: Elastic, Inelastic, Fracture, and Damage Theories*, Dover Publications, Inc, Mineola, New York.

Bernick, K. B., T. P. Prevost, S. Suresh, and S. Socrate (2011), Biomechanics of single cortical neurons, *Acta Biomaterialia*, *7*(3), 1210–1219.

Boyce, M. C., and E. M. Arruda (2000), Constitutive models of rubber elasticity: a review, *Rubber Chemistry and Technology*, *73*(3), 504–523.

Bursac, P., G. Lenormand, B. Fabry, M. Oliver, D. A. Weitz, V. Viasnoff, J. P. Butler, and J. J. Fredberg (2005), Cytoskeletal remodelling and slow dynamics in the living cell, *Nature Materials*, *4*, 557–561.

Carin, M., D. Barthès-Biesel, F. Edwards-Lévy, C. Postel, and D. C. Andrei (2003), Compression of biocompatible liquid-filled HSA-Alginate capsules: determination of the membrane mechanical properties, *Biotechnology and Bioengineering*, *82*(2), 207–212.

Charras, G. T., and M. A. Horton (2002), Determination of cellular strains by combined atomic force microscopy and finite element modeling, *Biophysical Journal*, *83*(2), 858–879.

Cross, S. E., Y. Jin, J. Rao, and J. K. Gimzewski (2007), Nanomechanical analysis of cells from cancer patients, *Nature Nanotechnology*, *2*, 780–783.

Cumpson, P. J., P. Zhdan, and J. Hedley (2004), Calibration of AFM cantilever stiffness: a microfabricated array of reflective springs, *Ultra-microscopy*, *100*, 241–251.

Dao, M., C. T. Lim, and S. Suresh (2003), Mechanics of the human red blood cell deformed by optical tweezers, *Journal of the Mechanics and Physics of Solids*, *51*, 2259–2280.

Darling, E. M., S. Zauscher, and F. Guilak (2006), Viscoelastic properties of zonal articular chondrocytees measured by atomic force microscopy, *Ostteoarthritis and Cartilage*, *14*(571).

Darling, E. M., M. Topel, S. Zauscher, T. P.Vail, and F. Guilak (2008), Viscoelastic properties of human mesenchymally-derived stem cells and primary osteoblasts, chondrocytes, and adipocytes, *Journal of Biomechanics*, *41*(2), 454–464.

Dokukin, M. E., N. V. Guz, and I. Sokolov (2013), Quantitative study of the elastic modulus of loosely attached cells in AFM indentation experiments, *Biophysical Journal*, *104*(10), 2123–2131.

Dong, C., and R. Skalak (1992), Leukocyte deformability: finite element modeling of large viscoelastic deformation, *Journal of Theoretical Biology*, *158*(2), 173–193.

Drury, J. L., and M. Dembo (2001), Aspiration of human neutrophils: effects of shear thinning and cortical dissipation, *Biophysical Journal*, *81*(6), 3166–3177.

Elbez, R. (2013), *personal communication*, Graduate Student in Applied Physics, Department of Chemistry, University of Michigan, Ann Arbor, MI.

Evans, E., and A. Young (1989), Apparent viscosity and cortical tension of blood granulocytes determined by micropipette aspiration, *Biophysical Journal*, *56*, 151–160.

Faria, E. C., N. Ma, E. Gazi, P. Gardner, M. Brown, N. W. Clarke, and R. D. Snook (2008), Measurements of elastic properties of prostate cancer cells using AFM, *The Analyst*, *133*(11), 1498–500, doi:1039/b803355b.

Feng, W. W., and W. H. Yang (1973), On the contact problem of an inflated spherical nonlinear membrane, *Journal of Applied Mechanics*, *40*, 209–214.

Fernandes, P. A. L., M. delcea, A. G. Skirtach, H. Mohwald, and A. Fery (2010), Quantification of release from microcapsules upon mechanical deformation with AFM, *Soft Matter*, *6*, 1879–1883.

Forrester, A., A. Sóbester, and A. Keane (2008), *Engineering Design via Surrogate Modelling: a Practical Guide*, John Wiley & Sons Ltd.

Fu, Y. B., and R. W. Ogden (2001), *Nonlinear Elasticity: Theory and Applications*, Cambridge University Press (LMS Lecture Note Series).

Fung, Y. C. (1981), *Biomechanics: Mechanical Properties of Living Tissues*, Springer-Verlag Newyork Inc.

Green, A. E., and J. E. Adkins (1970), *Large Elastic Deformation, 2nd edn*, Oxford: Clarendon Press.

Guck, J., et al. (2005), Optical deformability as an inherent cell marker for testing malignant transformation and metastatic competence, *Biophysical Journal*, *88*(25), 3689–3698.

Gustafson, P. A., and A. M. Waas (2009), The influence of adhesive constitutive parameters in cohesive zone finite element models of adhesively bonded joints, *International Journal of Solids and Structures*, *46*, 2201–2215.

Harouaka, R. A., M. Nisic, and S.-Y. Zheng (2013), Circulating tumor cell enrichment based on physical properties, *J Lab Autom*, *18*(4), doi:10.1177/2211068213494391.

Heinrich, C., and A. M. Waas (2009), Measuring the in-situ matrix properties in fiber reinforced composites, Proceedings of the ASME 2009 International Mechanical Engineering Congress & Exposition.

Hertz, H. (1882), On the contact of elastic solids, *J. Reine und angewandte Mathematik*, *92*, 156–171.

Ji, W., A. M. Waas, and Z. P. Bažant (2013), On the importance of work-conjugacy and objective stress rates in finite deformation incremental finite element analysis, *Journal of Applied Mechanics*, *80*(4), doi:10.1115/1.4007828.

Jones, D. R., M. Schonlau, and W. J. Weltch (1998), Efficient global optimization of expensive black-box functions, *Journal of Global Optimization*, *13*(4), 455–492.

Karcher, H., J. Lammerding, H. Huang, R. T. Lee, R. D. Kamm, and M. R. Kaazempur-Mofrad (2003), A three-dimensional viscoelastic model for cell deformation with experimental verification, *Biophysical Journal*, *85*, 3336–3349.

Kühtreiber, W. M., R. P. Lanza, and W. L. Chick (1999), *Cell Encapsulation: Technology and Therapeutics*, Birkhäuser, Boston.

Ladjal, H., J.-L. Hanus, A. Pillarisetti, C. Keefer, A. Ferreira, and J. P.Desai (2009), Atomic force microscopy-based single-cell indentation: experimentation and finite element simulation, *IEEE/RSJ International Conference on Intelligent Robots and Systems*, doi:10.1109/IROS.2009.5354351.

Lam, R. H. W., S. Weng, W. Lu, and J. Fu (2012), Live-cell subcellular measurment of cell stiffness using a microengineered stretchable micropost array membrane, *Integrative Biology*, *4*(10), 1289–1298.

Lardner, T. J., and P. Pujara (1980), Compression of spherical cells, *Mech Today*, *5*, 161–176.

Lekka, M., et al. (2012), Cancer cell detection in tissue sections using AFM, *Archivers of Biochemsitry and Biophysics*, *518*, 151–156.

Leporatti, S., D. Vergara, A. Zacheo, V. Vegaro, G. Maruccio, R. Cingolani, and R. Rinaldi (2009), Cytomechanical and topological investigation of mcf-7 cells by scanning force microscopy, *Nanotechnology*, *20*(5), doi:10.1088/0957-4484/20/5/055103.

Li, Q. S., G. Y. H. Lee, C. N. Ong, and C. T. Lim (2008), AFM indentation study of breast cancer cells, *Biochemical and Biophysical Research Communications*, *374*, 609–613.

Li, Q. S., G. Y. H. Lee, C. N. Ong, and C. T. Lim (2009), Probing the elasticity of breast cancer cells using AFM, ICBME 2008, Proceedings 23, pp. 2122–2125.

Lophaven, S. N., H. B. Nielsen, and J. Sondergaard (2002), Dace a matlab kriging toolbox, *Tech. rep.*, Technical University of Denmark.

Matei, G. A., E. J. Thoreson, J. R. Pratt, D. B. Newell, and N. A. Burnham (2006), Precision and accuracy of thermal calibration of atomic force microscopy cantilevers, *Review of Scientific Instruments*, *77*.

MATLAB R2010a (2010), *The Mathworks*.

Mofrad, M. R. K., and R. D. Kamm (2006), *Cytoskeleton Mechanics*, Cambridge University Press, New York.

Moreno-Flores, S., R. Benitez, M. dM Vivanco, and J. L. Toca-Herrera (2010), Stress relaxation and creep on living cells with the atomic force microscope: a means to calculate elastic moduli and viscosities of cell components, *Nanotechnology*, *21*, 445,101–445,108.

Nadler, B. (2010), On the contact of a spherical membrane enclosing a fluid with rigid parallel planes, *International Journal of Non-linear Mechanics*, *45*, 294–300.

Nguyen, N., A. Wineman, and A. Waas (2013a), Contact problem of a non-linear viscoelastic spherical membrane enclosing incompressible fluid between two rigid parallel plates, *International Journal of Non-linear Mechanics*, *50*, 97–108.

Nguyen, N., A. Wineman, and A. Waas (2013b), Indentation of a nonlinear viscoelastic membrane, *Mathematics and Mechanics of Solids*, *18*(1), 24–43.

Nguyen, N., A. Wineman, and A. Waas (2014), Compression of fluid-filled polymeric capsules and inverse analysis to determine nonlinear viscoelastic properties, *International Journal of Solids and Structures*, *Under Review*.

Olivera, W. C., and G. M. Pharr (1992), An improved technique for determining hardness and elastic modulus using load and displacement sensing indentation experiments, *Journal of Materials Research*, *7*, 1564–1583.

Pipkin, A. C., and T. G. Rogers (1968), A non-linear representation for viscoelastic behavior, *Journal of the Mechanics and Physics of Solids*, *16*, 59–72.

Prabhune, M., G. Belge, A. Dotzauer, J. Bullerdiek, and M. Radmacher (2012), Comparisons of mechanical properties of normal and malignant thyroid cells, *Micron*, *43*(12), 1267–1272.

Prevost, T. P., A. Balakrishnan, S. Suresh, and S. Socrate (2011), Biomechanics of brain tissue, *Acta Biomaterialia*, *7*, 83–95.

Queipo, N. V., R. T. Haftka, W. Shyy, T. Goel, R. Vaidyanathan, and P. K. Tucker (2005), Surrogate-based analysis and optimization, *Progress in Aerospace Sciences*, *41*, 1–28.

Radmacher, M. (2007), Studying the mechanics of cellular processes by atomic force microscopy, *Cell Mechanics*, *83*(347).

Roca, H., et al. (2013), Transcription factors ovol1 and ovol2 induce the mesenchymal to epithelial transition in human cancer, *PLoS ONE*, *8*(10), doi: 10.1371/journal.pone.0076773.

Sacks, J., W. J. Welch, T. J. Mitchell, and H. P. Wynn (1989), Design and analysis of computer experiments, *Statistical Science*, *4*(4), 409–423.

Selvadurai, A. P. S. (2006), Deflections of a rubber membrane, *Journal of the Mechanics and Physics of Solids*, *54*, 1093–1119.

Selvadurai, A. P. S., and Q. Yu (2006), On the indentation of a polymeric membrane, *Proceedings of the Royal Society A*, *462*, 189209.

Shao, Y. (2014), *personal communication*, Integrated Biosystems and Biomechanics Laboratory, Department of Mechanical Engieering, University of Michigan, Ann Arbor, MI.

Shaw, J. (2013), *personal communication*, Bio Applications Scientist, Bruker Nano Surfaces Division (BNS), Goleta, CA 93117.

Simo, J. C., and T. J. R. Hughes (1998), *Computational Inelasticity*, Springer-Verlag New York, Inc.

Suresh, S. (2006), Mechanical response of human red blood cells in health and disease: Some structure-property-function relationships, *Journal of Material Research*, *21*(8), 1871–1877.

Suresh, S. (2007), Biomechanics and biophysics of cancer cells, *Acta Biomaterialia*, *3*(413).

Suresh, S., J. Spatz, J. P. Mills, A. Micoulet, M. Dao, C. T. Lim, M. Beil, and T. Seufferlein (2005), Connections between single-cell biomechanics and human disease states: gastrointestinal cancer and malaria, *Acta Biomaterialia*, *1*(1), 15–30.

Taatjes, D. J., and B. T. Mossman (2005), *Cell Imaging Techniques: Methods and Protocols*, Totowa, NJ: Humana Press.

Titushkin, I. (2013), *personal communication*, Technical Support Engineer, Bruker Nano Surfaces Division, Santa Barbara, CA.

Veeco Instruments Inc. (2010), *Dimension Icon Instruction Manual-G*, Veeco Instruments Inc., Plainview, NY, USA.

Wineman, A., and K. Rajagopal (2000), *Mechanical Response of Polymers*, Cambridge Universigy Press.

Wineman, A., D. Wilson, and J. Melvin (1979), Material identification of soft tissue using membrane inflation, *Journal of Biomechanics*, *12*, 841–850.

Wineman, A. S. (2007), Nonlinear viscoelastic membranes, *Computers and Mathematics with Applications*, *53*, 168–181.

Yang, W. H., and K. H. Hsu (1971), Indentation of a circular membrane, *Journal of Applied Mechanics*, *38*, 227–230.